Charles University in Prague
Faculty of Mathematics and Physics

DOCTORAL THESIS

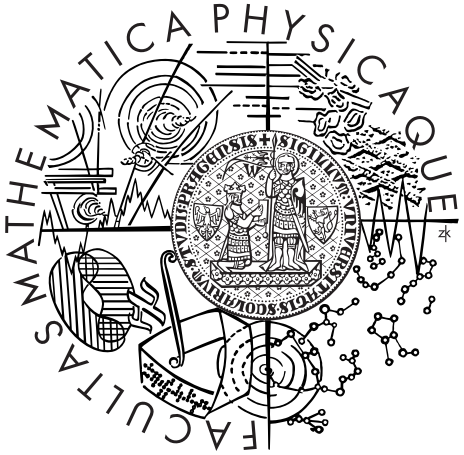

Mgr. Filip Janky

Design and implementation of the plasma control system for the COMPASS tokamak

Department of Surface and Plasma Science

Supervisor of the doctoral thesis:	Mgr. Jan Horacek, Dr ès sc.
Study programme:	Physics
Specialization:	4F2 Physics of plasmas and ionised media

Prague 2016

First of all, I would like to thank my family and all of my friends who were always supporting me and standing by me during my studies, work and while writing this thesis.

I would like to thank RNDr. Radomír Pánek PhD. for the great opportunity to work for COMPASS and for creating good work conditions.

I would like to thank Martin Hron and Jan Horáček for guiding me during my work.

I would like to thank Josef Havlíček for our discussions, his comments, suggestions and help.

I would like to thank František Žáček for his comments and explanations of the electron density measurement.

I would like to thank my colleagues from COMPASS for the warm and friendly atmosphere, especially to Jan Stöckel, for the Friday meetings in his office and for reading books with us.

I would like to thank Prof. RNDr. Šafránková DrSc. and Prof. RNDr. Němeček DrSc. for their patience and help during my doctoral studies, especially with English exam.

I would like to thank AUG CODAC team for supporting me and giving me enough time to write this thesis.

My very special thanks belongs to Wolfgang Treutterer for his help, for his open door, fruitful comments and ideas how to improve this thesis.

To my family
To my friends
To colleagues I met at COMPASS
To Wolfgang Treutterer

I declare that I carried out this doctoral thesis independently, and only with the cited sources, literature and other professional sources.

I understand that my work relates to the rights and obligations under the Act No. 121/2000 Coll., the Copyright Act, as amended, in particular the fact that the Charles University in Prague has the right to conclude a license agreement on the use of this work as a school work pursuant to Section 60 paragraph 1 of the Copyright Act.

In ..... date ..... signature of the author

Název práce: Návrh a implementácia systému kontroly plazmy
pre tokamak COMPASS
Autor: Mgr. Filip Janky
Katedra: Katedra Fyziky povrchů a plazmatu
Vedoucí disertační práce: Mgr. Jan Horáček Docteur ès sciences.
Ústav fyziky plazmatu AV ČR, v.v.i.

Abstrakt: Tokamak COMPASS po opätovnom uvedení do prevádzky v roku 2007 potreboval nový digitálny kontrolný systém pre svoj experimentálny výskum. Táto dizertačná práca prezentuje návrh a implementáciu kontroly hlavných parametrov plazmy ako prúd, poloha, tvar a elektrónová hustota. Vylepšená kontrola prúdu plazmy s resetovaním referenčných hodnôt potlačuje oscilácie, zabraňuje prekmitu a tak predlžuje trvanie plazmy. Opísaná metóda na určovanie polohy plazmy, vyladenie kontroléru a skrátenie oneskorenia, zvýšila stabilitu polohy plazmy a znížila výskyt dizrupcií. Tvar plazmy je kotrolovaný doprednou väzbou s metódou na potlačovanie oscilácií spôsobených vzájomnou indukčnosťou medzi zdrojmi a tiež tým, že využívajú spoločné vinutie. Priemerná elektrónová hustota je v reálnom čase korigovaná podľa dĺžky trasy vlny interferometru plazmou a nelineárnosťou merania. Prezentované kontroléry a ich vylepšenia zohrali kľúčovú úlohu k dosiahnutiu H-módu a naplneniu experimentálneho programu.

Klíčová slova: tokamak, kontrola prúdu plazmy, kontrola polohy plazmy, kontrola tvaru plazmy, kontrola elektrónovej hustoty

Title: Design and implementation of the plasma control system
for the COMPASS tokamak
Author: Mgr. Filip Janky
Department: Department of Surface and Plasma Science
Supervisor: Mgr. Jan Horacek Docteur ès sciences.
Institute of Plasma Physics AS CR, v.v.i.

Abstract: The COMPASS tokamak was recommissioned in 2007 and it needed new digital controllers for its experimental research. This thesis presents the design and implementation of control of main plasma parameters such as plasma current, plasma position, plasma shape and electron density. Improved plasma current control with resetting set points suppresses overshooting and thus increases the length of the flat top phase. A method for estimating the plasma position, gain tuning for the controller and decreasing latencies and delays to obtain robust position control are presented. Lower delays improve plasma stability and decrease the frequency of disruptions. The plasma shape controller is a feedforward controller with a method to suppress oscillations which are coming from mutual inductance between power supplies controlling plasma horizontal position, plasma shape and plasma current, which all use the same coil. Averaged electron density is corrected in real-time according to the interferometer line of sight and a non-linearity of measurement. Controllers and their improvements described here, played a major role in achieving H-mode scenario and fulfilling the experimental program.

Keywords: tokamak, plasma current control, plasma position control, plasma shape control, electron density control

Contents

1. Introduction

Tokamaks [1] are the most promising type of devices for nuclear fusion research in present. In thermonuclear fusion research, the flagship experiment is a tokamak called ITER [2] which is still under construction, with first plasma scheduled for the 3rd decade of this century. ITER should demonstrate 500 MW thermal power production from thermonuclear fusion reactions in a 150×10^6 °C hot plasma of a deuterium and tritium mixture. A tokamak keeps plasma in a toroidal vessel with a strong magnetic field of the order of a few Tesla. Plasma current on the biggest machines reaches several Mega Amperes.

Different types of instabilities can develop in a plasma, they may grow and make the plasma unstable [3]. Unstable plasma in a tokamak can end up with a violent disruption of the plasma current channel which can cause melting damage of in-vessel components and also produce heavy mechanical loads on the magnetic coils and the support structure. These loads can be in the order of dozen Mega Newtons at ITER [4]. As the potential damage on the machine can be severe, proper control of plasma parameters during all discharges has to be implemented. This thesis shows how real-time control during discharges is implemented on a small-size tokamak COMPASS.

Moreover, without active control system the plasma discharge would not last for more than few milliseconds. However, important plasma properties evolve on much longer time scales (confinement time, current diffusion time). Therefore, the relevant research needs to explore behaviour for longer - up to steady state - operation.

1.1 COMPASS

COMPASS (COMPact ASSembly) is a small size tokamak [5] with shape geometry like ITER [2] (diverted plasma with high triangularity and tokamak vessel with divertor, see Fig. 1.1) which is important for scaling of the pedestal or confinement time [6]. It scales 1:10 in every dimension with respect to ITER.

Major radius	$0.56\ m$
Minor radius	$0.18\ m - 0.23\ m$
Plasma current	$<\ 400\ kA$
Magnetic field	$0.9\ T\ -\ 2.1\ T$
Triangularity	$0.5 - 0.7$
Elongation	1.8
Pulse length	$< 0.5\ s$
P_{NBI}	$2 \times 0.3\ MW$
Plasma shape	SND[1], SNT[2], Elliptical, circular

Table 1.1: COMPASS parameters

COMPASS was designed in 1980's in the Culham Science Centre in the Unit-

[1]Single Null Divertor (SND)
[2]Single Null Divertor with high Triangularity (SNT)

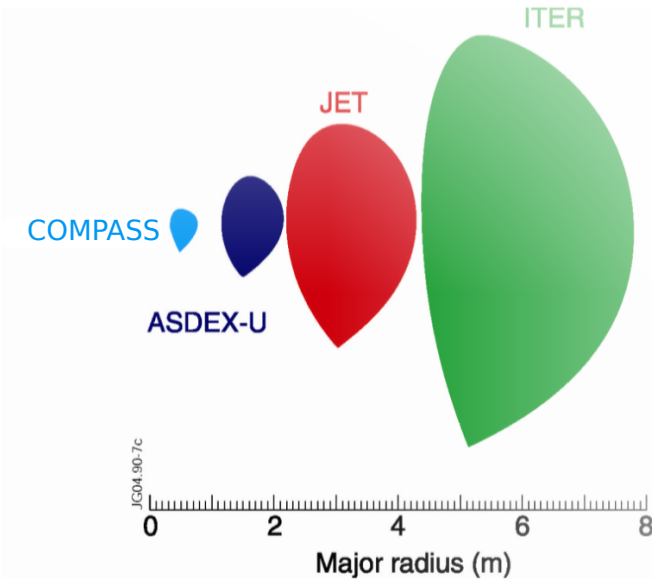

Figure 1.1: Linear scaling of ITER-like plasma shaped tokamaks. Courtesy of EFDA JET [7]

ed Kingdom. COMPASS was transported to Prague in 2006 where it was commissioned and put back to operation [5]. First plasma after reinstallation was achieved in 12th Dec. 2008. First plasma was obtained without feedback, using only pre-programmed waveforms for currents. Final commissioning of most diagnostics [8], control systems and power supplies were done between the years 2009 and 2011.

COMPASS typically operates in three regimes. Ohmic regime, L-mode and H-mode [9, 10]. Ohmic regime is ordinary mode where plasma is heated only with induced current. In L-mode, plasma at COMPASS is heated by Neautral Beam Injection (NBI) [11]. H-mode has with better energy confinement and it can be characterised by particle transport barrier developed at the plasma edge. This barrier can be seen at electron density and electron temperature. At COMPASS, H-mode can be achieved in ohmic heated regime [12, 13, 14] as well as in NBI heated regime [14].

Research programme at COMPASS is focused on:

- H-mode physics
  - Pedestal width physics which can provide additional data into the scaling database for ITER
  - L-H power threshold, isotope effects, height of X-point[3].
  - Edge Localised Modes (ELMs) [15, 16], their control by magnetic perturbation (using Resonant Magnetic Perturbation (RMP) field coils) and their triggering by vertical kicks (induced by Vertical Kick Power Supply (VKPS)). Studying ELM energy losses and the spatial distribution. Achieving type I ELM using NBI.
  - Quasi-coherent modes studies

[3]A saddle point for the flux function ψ (point of zero magnetic field). It creates boundary between closed and open field lines

  - Measurement of transport in edge plasma and Scrape of Layer (SOL), including the transition between resistive ballooning to drift-Alvén wave turbulence.

- Turbulent structures and intermittency in edge plasma – experiment and modelling
- MHD equilibrium and instabilities
- Plasma-wall interaction as studying erosions, re-deposition of eroded material and removal of re-deposited layers of the samples of advanced first-wall materials exposed to the plasma
- Measurement of SOL width for extrapolation to ITER design of in-vessel panels
- Physics of runaways their generation, losses and mitigation methods and physics of disruptions
- Development of advanced diagnostic methods
- Participation in the Integrated Tokamak Modelling (ITM) activity [17]
- Benchmarking experiment with 3D simulations of heat deposition into divertor gaps

To fulfil all experimental requirements, main plasma parameters (plasma current, electron density, plasma shape and vertical and horizontal position) have to be controlled, easily changeable, and monitored during the discharge. Typically, during a dedicated campaign focused on one of the research topics, demands from a responsible physicist are scans across different plasma currents, electron densities and at different plasma positions. Therefore, real-time control has to be easily configurable and changeable between two discharges typically between 10 to 20 minutes. In addition, real-time control has to be robust to avoid disruptions.

COMPASS-D at Culham was operating with analogue control. During reinstallation of COMPASS at Prague, the final decision was to make a new, fully digital control. Benefits of digital control are:

- scalability - adding more signals, increasing complexity
- modularity - changing formulas, models
- reusability - control algorithms can be easily transferred to another devices

1.1.1 Goals of the Thesis

The original aim of this thesis was to develop vertical plasma position control system. This task was later extended to built a plasma control system which will make tokamak COMPASS operational and available to provide experimental research. This extension includes plasma current control, plasma position control (vertical and horizontal), plasma shape control and electron density control. The thesis is focused on how the control of the plasma parameters is designed and

implemented together with results and achievements which were able to do only because of the work done for this thesis.

Plasma position calculation [18] (Attachment: I) and first working feedback at radial position in circular plasma was fully functional in July 2011 (#1847). In November 2011 feedback for plasma current was operational. Vertical position feedback was commissioned in November 2012 (discharge #4073). This vertical position controller worked with D-shaped plasma with big cross-section and close to the tokamak vessel. Speeding up of the data acquisition system, calculation and changing calculation method significantly helped and smaller plasma further from the vessel could be vertically stabilised [19] (Attachment: II). This improvement together with electron density real-time control and calculation electron density along the interferometry chord [20] (Attachment: III) enable to reach ITER-relevant plasma mode with higher confinement (H-mode) at COMPASS since its re-installation at Prague.

1.2 Overview of the Systems Necessary for Plasma Control and Operation at COMPASS

For operation and for controlling plasma during experiments, a tokamak needs power supplies, fuelling and heating systems, data acquisition systems, synchronisation and timing units, control system and software, diagnostics, and subsystems like vacuum system, glow discharge system, baking system, and so on. Systems related with plasma control are briefly described in this part.

1.2.1 Data Acquisition Systems

Acquiring data on COMPASS is implemented by several Data Acquisition Systems (DASs) from D-tAcq, National Instruments or based on Advance Telecommunications Computing Architecture (ATCA) [22] with different sampling rates (varying from 20 kSs/s up to 1 GS/s), input ranges and input parameters (see Fig 1.2). Overview of DAS and its connection and triggering, and timing is described in detail in [21].

Data Acquisition System based on ATCA is used for plasma control systems at COMPASS [23] and also at Joint European Torus (JET) for vertical stabilisation [24, 25] and processing system for gamma-ray cameras [26]. IST-TOK uses it for plasma position control with a real-time tomographic reconstruction [27, 28, 29]. Also a prototype of a fast plasma controller system for ITER is based on ATCA [30, 31].

The ATCA crates at COMPASS can have up to 12 Digitizer-Generator-Processor (DGP) boards each equipped with 32 analog input channels acquiring data with 2 MS/s, 8 digital inputs, 8 RS485 outputs, 8 analog outputs and one Field Programmable Gate Array (FPGA) [32], and one RAM memory for storing data.

One of the ATCA crates, called "ATCA1", is equipped with one Real-Time Board (RTB). Data at the RTB are down-sampled to 20 kS/s by a FPGA[4] and

[4]At the beginning of COMPASS operation, down-sampling together with Finite Input Response (FIR) filter of high order was used which caused delays. This FIR filter was later

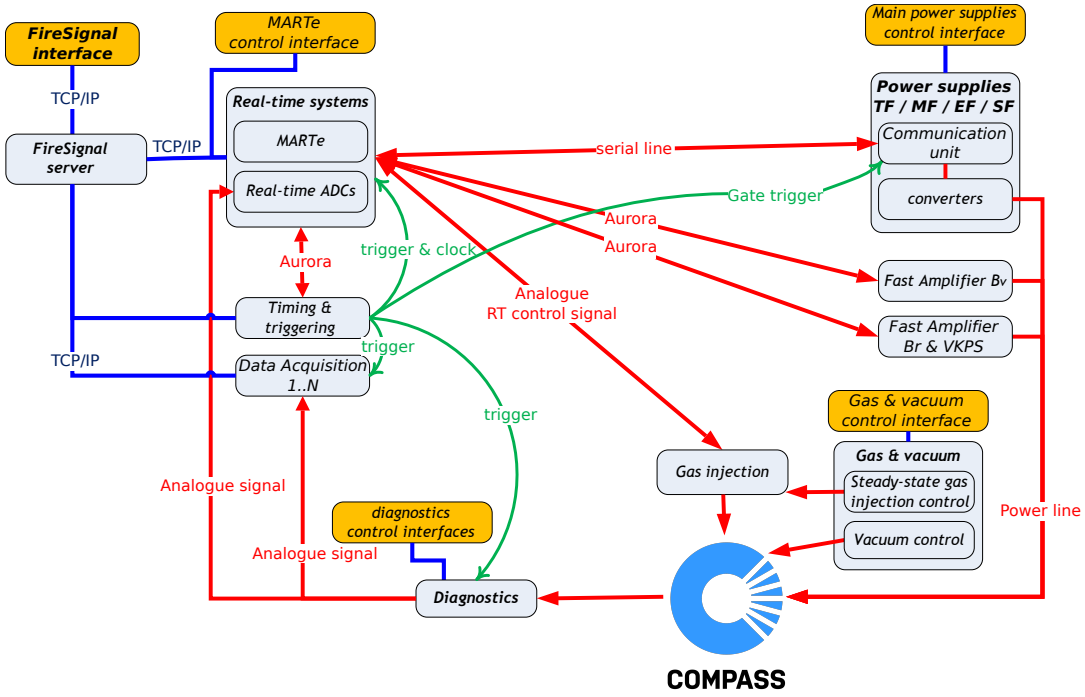

Figure 1.2: Control and communication: grey boxes represent the elements of the COMPASS CODAC system (central FireSignal server, ATCA data acquisition and real-time system, other ADCs, timing and triggering node) and actuators (power supplies, gas injection, and auxiliary NBI heating). Yellow boxes denote the operator's interfaces; for completeness, it should be noted here that FABV, FABR and VKPS, and gas injection control set-up is done using configuration files uploaded to MARTe through its control interface before the shot. Ethernet (marked "TCP/IP", blue lines) is used to set-up the systems before the discharge, trigger and clock are distributed via optical links ("trigger", green lines). Real-time loop including signals from the tokamak, communication links from the real-time system to the actuators, and action links from the actuators to the tokamak are marked in red [21].

are available in real-time for real-time calculations. Data are read by real-time framework called MARTe [33, 34] described in Sec. 1.3. RTB is DGP without the RAM memory and automatic Direct Memory Access (DMA) transfers are used to obtain better data transport time latency.

Each ATCA crate has one board equipped with Rear Transition Module (RTM) with clocks (for boards synchronisation) and triggers (to start acquiring data) receiver attached to that RTM. Triggers and clocks are broadcasted through the back plane using the full-mesh connections between all other boards plugged inside the crate. If RTB is present in the ATCA crate, RTM with clock and trigger receiver is attached to it.

Synchronisation between all different DASs, fuelling, heating system and diagnostics and plasma discharge is performed by Timing Unit (TU) [35] which distributes clocks and triggers to them.

removed (see 3.4.2).

1.2.2 Power Supplies

Main power supplies (also called ČKD energetics or main energetics): Toroidal Field Power Supply (TFPS), Magnetising Field Power Supply (MFPS), Equilibrium Field Power Supply (EFPS) and Shaping Field Power Supply (SFPS) described in [36, 37, 38], are connected to ČKD Communication Unit (ČKD-CU) which communicates with MARTe using RS232 protocol [39, 40].

TFPS creates a toroidal magnetic field up to 2.1 T at the centre of the vessel which corresponds to 92 kA in the Toroidal Field (TF) coils. Usually COMPASS operates with 1.2 T which is 52 kA. *Standard* toroidal field orientation at COMPASS is *negative*. It means looking from the top on COMPASS field direction is *clockwise*. This field is axisymmetric, $B_{\mathrm{T}}(\Phi) = B_{\mathrm{T}}$ with maximum on inner side of the coils which is called High Field Side (HFS). This field decays to outer side of coils, called Low Field Side (LFS) according to the following equation:

$$B_{\mathrm{T}}(R) = \frac{\mu_0 I_{\mathrm{T}}}{2\pi R} = B_{\mathrm{T}}^0 \cdot \frac{R_0}{R}, \tag{1.1}$$

where R_0 is distance from tokamak axis to the plasma centre, B_{T}^0 is the toroidal magnetic field at $R = R_0$ and R is the plasma major radius.

MFPS creates loop voltage using Magnetising Field (MF) coils (Fig. 1.3) and drives plasma current and heats plasma via Ohmic Heating (OH) (see Chap. 2). Typically operates between −16 kA to 14 kA. The current flowing in the Central Solenoid (CS) has *negative* direction from −16 kA to 0 kA and creates downward oriented magnetic field in the CS. Then MFPS changes polarity and the current flowing in CS has *positive* direction which creates upward oriented magnetic field. MFPS current rises from −16 kA to 14 kA, creating *positive* derivation, which creates *negative* plasma current (clockwise).

EFPS current is positive. To MB coil (in CS) is connected negative and to the coils at the LFS is connected in positive direction. This connection creates a vertical magnetic field oriented upwards. Vertical magnetic field with negative plasma current density $\vec{j}$ creates a $\vec{j} \times \vec{B}$ force directed inward i.e. to the HFS and establishes the equilibrium at a chosen position. The Equilibrium Field (EF) coils keep the plasma horizontally at requested position and the vertical magnetic field acts against outward expansion forces (see Chap. 3). Current in EFPS is approximately 25 times smaller than plasma current. The exact ratio between plasma current and equilibrium field $I_{\mathrm{EFPS}}/I_{\mathrm{p}}$ sets plasma horizontal position. Higher ratio $I_{\mathrm{EFPS}}/I_{\mathrm{p}}$ moves equilibrium towards HFS.

SFPS elongates plasma and creates diverted plasma. Shaping Field (SF) coils are hardwired and exact shape cannot be changed automatically, only with reconnection of the coils. Therefore, plasma elongation $\kappa = 1.8$ is the same for all diverted COMPASS discharges. By increasing SFPS current the plasma becomes smaller but with the same elongation (see Chap. 4). SFPS current is positive.

The connection of the main power supplies with the tokamak windings is in Fig. 1.4 and their position in the poloidal cross-section is in Fig. 1.3. All the coils (marked with the same symbol) belong to one of the power supply. The current in the central solenoid drives plasma current and is responsible for OH. The CS is composed of MA and MB coil which are winded together next to each other. Coil MA is fed only by MFPS. However, the MB coil is fed also by MFPS, EFPS and SFPS supplies. MFPS and SFPS have the same polarity which is in opposite

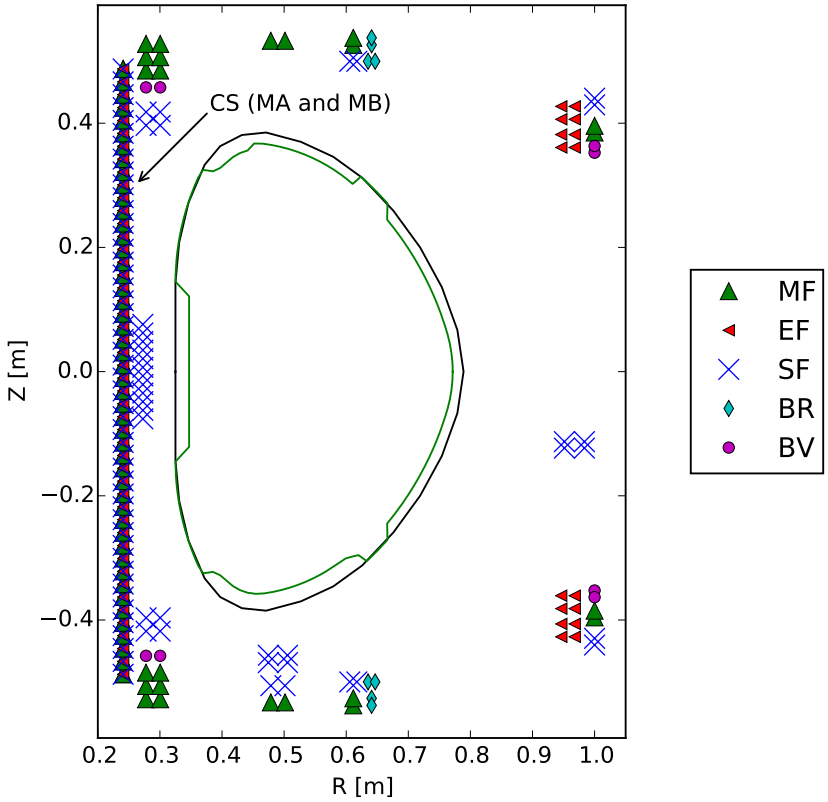

Figure 1.3: Scheme of tokamak vessel with poloidal field coils in poloidal cross-section. The Central Solenoid (CS) is composed of two coils MA and MB. The MB coil is shared by MFPS, EFPS and SFPS (see Fig. 1.4). The coils marked with the same marker belong to one power supply. This figure does not display exact number of the turns of the coils, only their position.

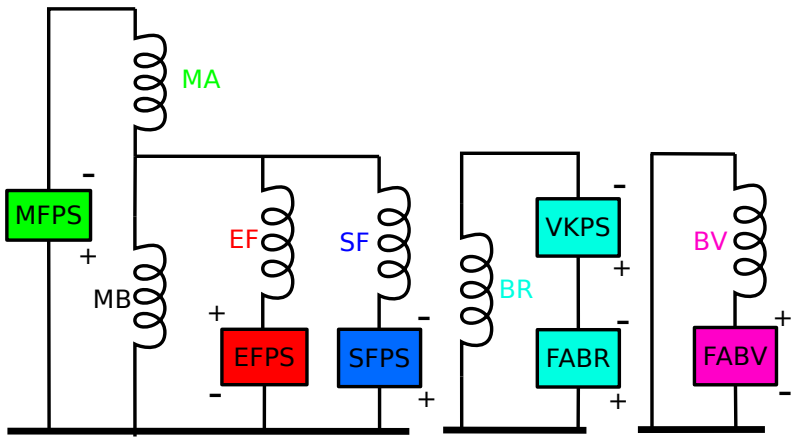

Figure 1.4: Simplified scheme of connection of the tokamak coils with the power supplies.

direction to EFPS. Therefore, combination of three power supplies acting on the same coil together with inductance between corresponding windings cause oscillations of plasma current, vertical and radial position, and plasma shape. To suppress these oscillation averaging of measurement is performed (Sec. 3.4.1 and

Sec. 4.4).

Two other power supplies were designed later to stabilise plasma in horizontal (Fast Amplifier for Vertical Magnetic Field (FABV)) and vertical direction (Fast Amplifier for Radial Magnetic Field (FABR)). Both are operating in $-5\,\mathrm{kA}$ to $5\,\mathrm{kA}$ with switching frequency $40\,\mathrm{kHz}$. They are based on MOSFET transistors modules [41] connected together to the H-bridge operating with $\pm 100\,\mathrm{V}$ supplying $\pm 5\,\mathrm{kA}$ [42]. They have low inductance due to sandwich design with copper plates.

Positive current from FABV power supply creates magnetic field in the same direction as positive current from EFPS. FABV field is 5 times smaller then the field from EFPS for unit current. FABV drives current in Vertical Field (BV) coils and stabilises plasma mainly during plasma breakdown when EFPS response is slow (see Chap. 3).

Vertical stability is controlled with FABR power supply. FABR power supply drives current in Radial Field (BR) coils and is necessary especially for stabilising plasma when plasma is vertically elongated and D-shape profile is created. Positive FABR current with standard negative current creates upward force. Poloidal magnetic fields created by above mentioned power supplies are displayed in Fig. 1.5.

To study ELM triggering with fast vertical movement of plasma column called *kick*, the VKPS is connected in series with FABR. VKPS is also constructed

	FABR	VKPS
maximal current	$\pm 5\,\mathrm{kA}$	$\pm 3.6\,\mathrm{kA}$ (per IGBT) / $\pm 5\,\mathrm{kA}$
maximal survivable voltage	$\pm 150\,\mathrm{V}$	$\pm 1.7\,\mathrm{kV}$
nominal working voltage	$\pm 100\,\mathrm{V}$	$\pm 1.2\,\mathrm{kV}$
switching frequency	$40\,\mathrm{kHz}$	$< 5\,\mathrm{kHz}$
experimental results		
$\mathrm{d}I_{\mathrm{BR}}/\mathrm{d}t$ for $I_{\mathrm{BR}} < -1\,\mathrm{kA}$	$0.5\,\mathrm{kA}$ /ms	$7.5\,\mathrm{kA}$ /ms and $-9.2\,\mathrm{kA}$ /ms
$\mathrm{d}B_{\mathrm{hor}}/\mathrm{d}t$ at top, bottom	$1.7\,\mathrm{mT}$ /ms	$26\,\mathrm{mT}$ /ms and $-32\,\mathrm{mT}$ /ms
$\mathrm{d}B_{\mathrm{hor}}/\mathrm{d}t$ at midplane	$1\,\mathrm{mT}$ /ms	$15\,\mathrm{mT}$ /ms and $-18\,\mathrm{mT}$ /ms

Table 1.2: Comparison of parameters between FABR and VKPS. Parameters of FABV are the same as FABR for switching frequency and maximal, and nominal voltage, current.

as the H-bridge but from IGBT modules [43]. Positive polarity of the VKPS creates magnetic field oriented in the same way as positivity polarity of FABR power supply. FABR power supply and VKPS are controlled together with one controller. Comparison between FABR and VKPS power supply is in Tab. 1.2.

1.2.3 Fuelling and Plasma Heating Systems

A gas puff valve is used for fuelling plasma usually with deuterium gas. Fuelling and controlling the electron density is described in Chap. 5

External heating of plasma is performed with two NBIs [11]. Each of them can deliver $300\,\mathrm{kW}$ and can be located as co-injection or counter-injection.

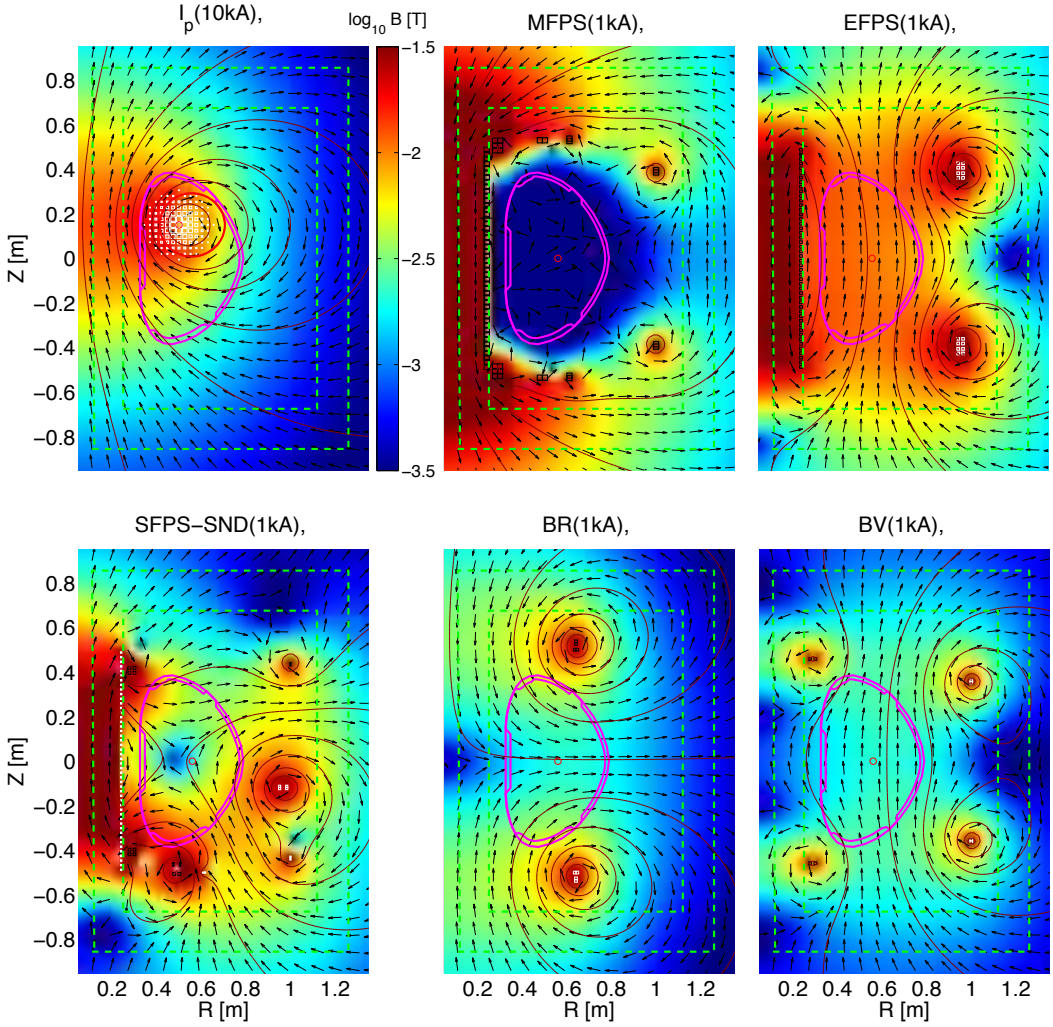

Figure 1.5: Magnetic poloidal fields are created with different power supplies and with different poloidal field coils; the field structure is given by coil locations and number of turns. Colour bar is valid and the same for all the poloidal fields. All fields plotted in this figure are created by positive direction of current in the corresponding coils. Plasma current in first plot is also in the positive direction, nevertheless, at COMPASS standard direction of plasma current is negative.

1.2.4 Synchronisation and Timing, and Control Systems

The Event and Pulse Node (EPN) [35] is responsible for main synchronisation and trigger distribution to the diagnostics and to the DAS at COMPASS. This unit is called TU and it is based on TMS320C6415 [44] Digital Signal Processor (DSP) [45] and XC2PV7 FPGA. The DSP and the FPGA are responsible for managing events. Events are preprogrammed before the experiment. These events are triggers and events that are happening according to giving time or process during the discharge. All signals are spread using optical fibres. EPN provides 12 triggers (max 2 s long), 8 clocks (up to 2 Mhz), 4 event dependant digital outputs (controlled by MARTe in real-time) and has 8 digital inputs.

The control system is built on a Personal Computer (PC) Advanced Technology eXtended (ATX) motherboard [46] connected to a carrier module by the Pe-

ripheral Component Interconnect Express (PCIe™) [47] with a ×16 full duplex link directly connected to the NorthBridge (directly to a processor) [25]. This unit is connected to the backplane of the ATCA crate. At COMPASS, the real-time system, MARTe, runs as above mentioned at ATCA1 crate. It is equipped with a Central Processing Unit (CPU) (Intel® CoreTM 2 Quad CPU Q9550 @2.83 GHz).

Every DAS and also MARTe and TU is controlled by its own node. A node is piece of code which operates concrete DAS (therefore, is hardware dependant) and connects to a FireSignal server [48]. FireSignal is modular software designed to control and operate physics experiments. Communication between FireSignal server and DAS nodes is performed with Common Object Request Broker Architecture (CORBA) [49] protocol. FireSignal has Graphical User Interface (GUI) controlled by a human operator. From this GUI, operator can change configuration of every node (typically time of acquisition and start of acquisition) and start experiment.

There is also one board assembled with one Microchip® dsPIC30F4013 [50]. This board synchronises the Thomson Scattering (TS) laser and the Li-beam diagnostic with the Transistor–transistor logic (TTL) triggers and resets triggers before every discharge. Its synchronisation is performed via serial communication with MARTe. The whole sequence is described in Sec. 1.5.

1.3 MARTe

Real-time systems are usually developed for a particular system or hardware. Therefore, they are strongly depended on an Operating System (OS) or that specific hardware. To design COMPASS control system it was essential that system was modular, fast and easily portable. Therefore, Multi-Threaded Real-Time executor (MARTe) has been adopted as real-time solution for the COMPASS tokamak.

MARTe is a real-time framework based on BaseLib2 library which is OS independent. It has clear boundaries between hardware, algorithms and system configuration. This clear division enables commissioning the system in separate phases when some components are replaced by models or simulations where data input can be used from stored data. Also it enables software-in-loop testing and separated blocks can be tested with other components.

MARTe with BaseLib2 provides portability (already ported and tested at Wind River VxWorks, Linux, Linux/RTAI, Solaris and MS Windows), modularity (built from blocks, which can be easily changed, added, replaced or combined) and re-usability.

MARTe in present is used at many systems for different purposes[5], tokamaks [51] and fusion related devices. MARTe is used at Instituto Superior Técnico TOKamak (ISTTOK) for the real-time tomography equilibrium reconstruction [28] and for plasma current and plasma position, and plasma density control also during AC operation [27, 52, 29]. Frascati Tokamak Upgrade (FTU) uses MARTe for plasma density, plasma current and plasma density control [53, 54, 55, 56], and Electron Cyclotron Resonant Heating (ECRH) real-time

[5]MARTe running on Raspberry Pi™is also used for controlling beer production.

control [57]. SPIDER, the ion source test bed of the ITER neutral beam test facility, uses MARTe for fast control of the power supply systems with particular reference to special asynchronous events, such as the breakdowns [58]. Reversed Field eXperiment (RFX) controls the plasma position and of the MagnetoHydro-Dynamic (MHD) [59, 60]. MARTe at JET is implemented for the Error Field Current Coils (EFCC) and JET vertical stabilisation system and plasma current control [61, 62, 63], hard X-ray and gamma rays control [64] and wall load monitoring system for ITER-like wall (ILW) [65].

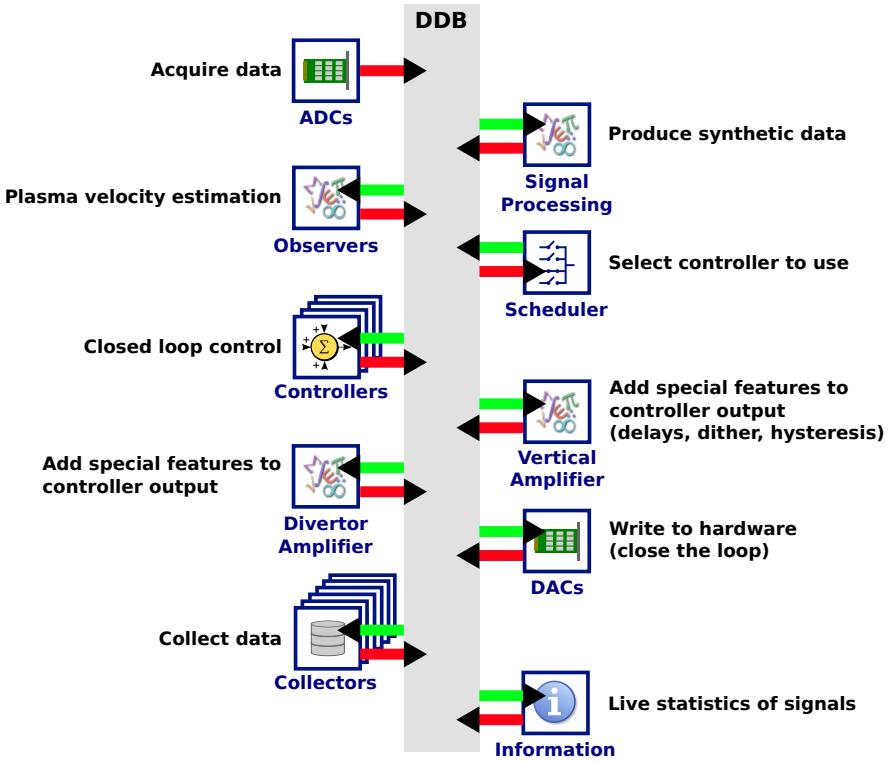

Figure 1.6: Example of GAMs for vertical stability system at JET. Figure is taken from MARTe manuals [66].

MARTe is composed with blocks of code called Generic Application Modules (GAMs) sorted in a specific order providing their functionalities (for example as displayed in Fig. 1.6). Every GAM has three access points: inputs, outputs and configuration file. In the configuration file inputs and outputs are specified. Inputs can be files, constants or data. According to an algorithm written in the GAM, inputs are processed and produces defined outputs. These outputs can be used again in different GAMs as inputs. GAMs are sorted in order specified in configuration file loaded at the beginning of MARTe execution and run in the cycle with certain speed specified also in the configuration file with respect to hardware capabilities.

Standard GAMs' functionalities involve data processing necessary for controlling and communicating with the systems, executing algorithms, taking decisions according to actual plant or subsystem state, providing live information or storing acquired and calculated data (see Fig. 1.7).

Specific set of GAMs providing a high-level interface to hardware is called Input Output Generic Application Modules (IOGAMs) (labelled as hardware input and hw output in Fig. 1.7). The connection between low-level code (driver)

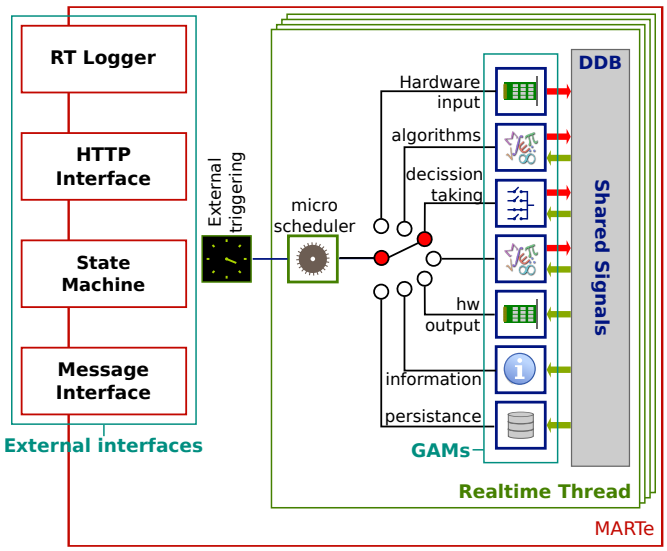

Figure 1.7: MARTe schema overview. Figure is adapted from MARTe manuals [67].

controlling specific hardware and IOGAMs is performed with a high-level class named *generic acquisition module*. This interface requires reading, and writing functions depending on every single piece of interfacing hardware and requires to specify the number of hardware inputs and hardware outputs. IOGAMs provide unique high-level interaction with any kind of hardware. When hardware is changed these low-level pieces of code has to be rewritten and higher level do not need to be changed to keep the same functionality.

Data between GAMs (also IOGAMs) are transferred by memory buffer called Dynamic Data Buffer (DDB). DDB ensures coherency across the system. During start up of MARTe, DDB verifies and checks if every signal requested by all the GAMs is produced by one module. If signal is not produced, error is raised and MARTe will not start.

GAMs are executed in a cycle sequence according to the *real-time thread*. The real-time thread acts like a micro-scheduler and executes GAMs in correct order, tracks execution times and keeps a series of internal timing information about each of the GAMs for which is responsible (e.g. time of execution of the GAM, runtime of GAM). It can be set to run on specific processor and be assign to a specific priority. If loop cycle exceeds time specified for one cycle, all rest GAMs are executed as are written in configuration file and then real-time thread is waiting for execution to the next cycle (see Fig. 1.6, 1.7).

MARTe needs at least one timing source. Usually time is updated by an external source, nevertheless, the CPU clock can be used. A shared variable in the real-time thread tracks the absolute time in microseconds. Control cycle starts when the absolute time is a multiple of the requested period cycle.

MARTe can handle a set of real-time threads running on the same CPU or in parallel. Exchanging data between threads is possible only with a special IOGAM. Outputs from one thread has to be connected as the inputs to the acquisition module of the other thread.

The framework provides also a logging protocol, RT Logger, to show information, warning, errors, etc.

Each GAM can create HyperText Markup Language (HTML) interface. This gives opportunity for configuration, exchanging information or changing internal MARTe states from outside.

1.4 Timing, triggering and synchronisation

In this part, sequence of time events of COMPASS discharge together with applications executed in correct order are described.

At the very beginning, operator has to close tokamak hall for personal protection reasons [68]. If the tokamak hall is not closed correctly, signal from interlock system blocks main power supplies.

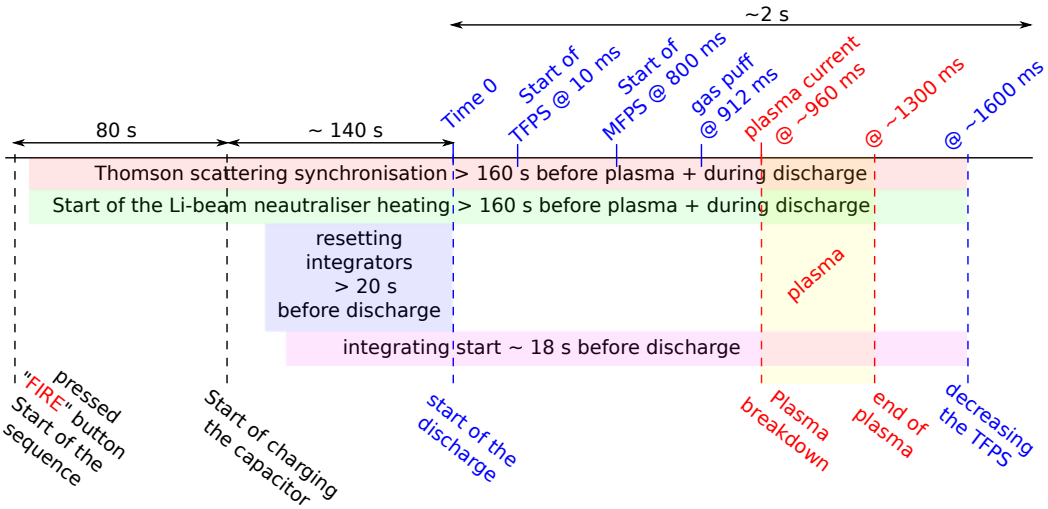

Figure 1.8: Sequence of time events at COMPASS. Time distances are not drawn in real proportions.

Operator sets plasma current, plasma position, electron density, toroidal magnetic field and plasma shape parameters required according to the experimental program in the configuration file. The file is loaded and read during MARTe startup. If MARTe is started and all the nodes are connected to FireSignal, operators press "Fire" button in FireSignal GUI to start a new discharge.

FireSignal sends command to so called MARTeNode, which controls MARTe internal states and acquires data from real-time and changes MARTe internal status from "Offline" to "Online". At this time MARTe sends message about its internal state to the so-called PreTriggering Unit. PreTriggering unit's outputs are configured during MARTe startup. This unit is used to start synchronisation [69] of TS diagnostic [70, 71, 72], heating up Lithium beam neutraliser [73] and resetting the integrators of the magnetic coils.

When 80 s (set in FireSignal by operator in MARTeNode) passes, MARTeNode changes MARTe status again. MARTe sends "start" command to charge capacitor, C (Fig. 2.3 in Sec 2.3), command to ČKD-CU to charge capacitor used for plasma breakdown (see Sec. 2.3)[6] and also sends command to PreTriggering unit. Charging of the capacitor takes approximately 140 s. When capacitor is charged, ČKD-CU sends command to MARTe that main power supplies are

[6]Detailed description of communication between MARTe and ČKD-CU is in [74].

ready. MARTe sends command to TU to reset a cycle counter. When zero at the cycle counter is set, MARTe sends command to start discharge and DASs receive the triggers to start acquiring data. Acquisition of data can be postponed according to the trigger delay settings. This can be set via FireSignal. Detailed description of timing sequence, together with MARTe states and connections are written in App. A

1.5 Typical COMPASS discharge

Typical COMPASS plasma discharge lasts from 250 ms to 500 ms. First power supply which starts is TFPS. TFPS starts rising 10 ms after time zero. Toroidal field reaches usually 52 kA at time ≈ 500 ms which corresponds to 1.2 T and is flat until 1600 ms then is exponentially decreasing.

MF for OH starts decreasing typically to values between -8 kA to -16 kA at time 800 ms (top Fig. 1.9). Time window between time when TF reaches requested value and MF starts decreasing (typical length of the window is 300 ms) is used for calculation of drifts of magnetic measurements (Sec. 2.2) which come from inherent electronic properties of analog integrators for the magnetic sensors. MF reaches requested value (black dashed line of top Fig. 1.9) usually at 900 ms and is kept at requested value for certain time usually 50 ms. Level of requested value influences plasma current level before polarity of MFPS is changed (see Tab. 2.2).

Fuelling of vessel with deuterium gas starts at 912 ms at 950 ms pressure inside vessel is around 4×10^{-3} Pa to 3×10^{-2} Pa which is pressure needed for plasma breakdown [75]. Then at time 950 ms breakdown is requested. Detailed description is written in Chap. 2.

Plasma usually starts between 955 ms to 960 ms. Loop voltage U_{loop} necessary for breakdown is typically between 12 V to 21 V (fifth graph from the top). Plasma current at the beginning of the discharge rises fast and at the time of 965 ms has already 85 kA (top Fig. 1.9) and has always circular shape. Its horizontal position has to be controlled with EF. Because EF rises slowly and has slow response, EFPS waveform request is before plasma starts and FABV power supply is necessary to stabilises plasma at the beginning of discharge (centre part of Fig. 1.9)

When diverted (D-shaped) plasma scenario is requested current in SF coils is driven by SFPS (see third graph of Fig. 1.9). Usually it starts at 980 ms. To stabilise D-shaped plasma, feedback on vertical plasma position is necessary. The vertical plasma position is stabilised with FABR power supply. FABR power supply is connected in series with VKPS used in experiments with fast vertical plasma movement. Detailed description and results are written in Chap. 2 and Chap. 3.

If plasma current is high enough (typically higher than 180 kA for COMPASS) and the electron density is higher than $4 \times 10^{19}\,\mathrm{m}^{-3}$, and other conditions are fulfilled, plasma scenario will jump to the H-mode (mode with better plasma confinement). This jump can be seen at H_α line at last graph of Fig. 1.9. COMPASS can have ohmic H-mode or NBI assisted H-mode [14].

Discharge at COMPASS ends with changing D-shaped plasma to circular shape and decreasing plasma current, and electron density to $2 \times 10^{19}\,\mathrm{m}^{-3}$. Exact

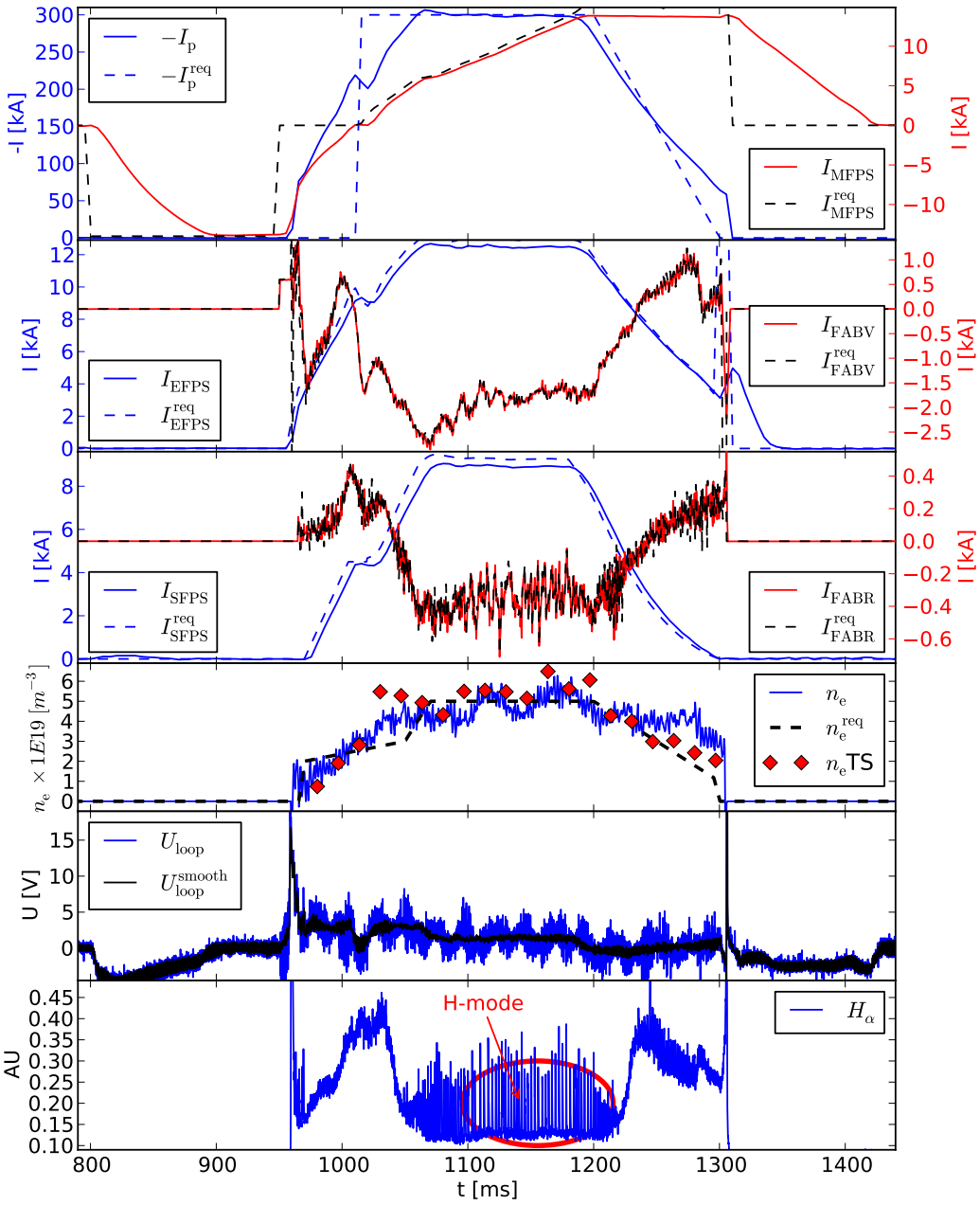

Figure 1.9: Typical plasma discharge with ELMs in H-mode. First graph is plasma current (blue) with magnetising current (red). Second is current in equilibrium field coils (blue) with I_{FABV} current (red). Third graph is current in the shaping field coils (blue) and current created by FABR (red) for vertical stability. Forth graph shows the electron density measured by an interferometer (blue line) and by Thomson Scattering laser diagnostic (red diamonds). Fifth shows loop voltage (blue) at flux loop 1 and smoothed loop voltage (black) from the same flux loop. Last graph shows H_α with labelled regime when plasma was in H-mode with ELMs. The requested values are drawn with dashed lines.

time is programmed by operator in MARTe configuration file.

1.6 Control Theory

Control theory has been developed to formalise how the behaviour of dynamical systems (often called plants) can be changed by re-adusting its inputs based on the behaviour of one or more measured plant system target quantities.The typical aim of control theory is to control a system, so its output follows a desired signal, called the *reference* or the set point. The reference may be a fixed or changing value. The difference between measured signal (*control variable* or *process variable*) and the reference is called *control error*. The relationship between input and output is represented by a *process*. The input signal is processed to provide the output signal.

There are two common types of control system, open loop control system and close loop control system. In the *open-loop system* (Fig. 1.10) there is no measurement of the system output taken into account to alter the actuator. It

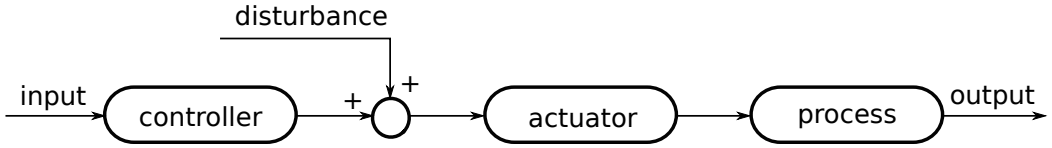

Figure 1.10: Open loop controller

does not use feedback to determine if its output has achieved the desired goal of the input. It means that the plant output has no influence or effect on the control action of the input signal (i.e. the output is neither measured nor "fed back" for comparison with the input). The open-loop system has no knowledge of the output condition so cannot self-correct any errors it could make when the preset value drifts, even if this results in large deviations from the preset value and open-loop systems are poorly equipped to handle disturbances or changes in the conditions which may reduce its ability to complete the desired task.

Example of the open-loop control can be controlling the speed of a car by setting engine's throttle position, which determines how much power the engine delivers. In this case the speed of the car is changed according to the road if it is up hill or down hill (disturbance).

A close-loop control, also known as a *feedback control system* (Fig. 1.11) is a system where the controlled signal (output from sensor) is compared to a desired reference signal and the discrepancy is used to compute corrective control action. For example speed of the car is controlled according to speedometer. If actual

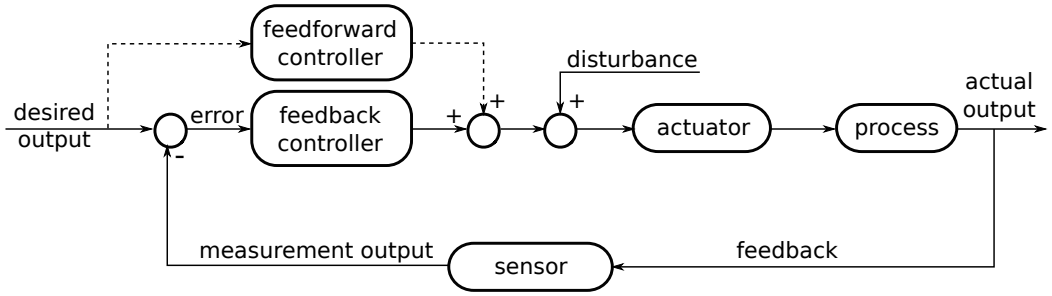

Figure 1.11: Feedback controller

speed is lower than requested engine output power is increased and if actual speed is higher than requested engine output power is decreased.

In some systems, disturbance can be measured and feedback control can be improved with respect to the disturbance. This controller acting according to the disturbance is called *feedforward*.

Processes at the COMPASS tokamak are controlled mostly with feedback controller such as plasma current (Sec. 2.4), vertical plasma position (Sec. 3.4.2) and electron density (Sec. 5.4) or with feedforward controller such as plasma shape (Sec. 4.4). Combination of feedforward and feedback controller can be see in radial plasma position control in Sec. 3.4.1.

At COMPASS as a feedback controller is used Proportional Integral (PI) controller. PI controller continuously calculates an error $e(t)$ between requested value (set-point - $r(t)$) and actual measured value - $y(t)$ (processed variable). The controller attempts to minimise the error of a control variable such as the plasma current (Sec. 2.4) by adjustment MFPS current to a new value $u(t)$ determined by a weighted sum:

$$u(t) = K_\mathrm{p} e(t) + K_\mathrm{i} \int_0^t e(\tau)\mathrm{d}\tau, \tag{1.2}$$

where K_p is proportional constant, K_i denotes integral constant, $e(\tau)$ is integrat-

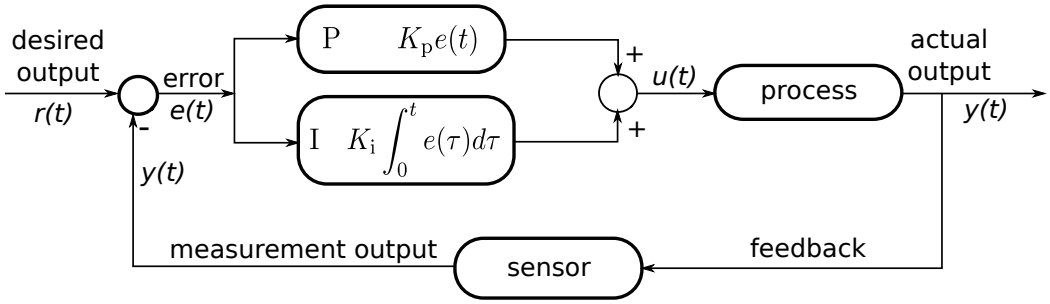

Figure 1.12: Schema of PI controller

ed error time since beginning of calculation of integral component of the controller to present time t. First term will be assigned as P-proportional and second term as I-integral. P calculates value according to present states. I integrates all past errors. For example if output from P is not sufficient to reduce the error, I term will accumulate over time and thus error will be reduced. Usually, PI controller is part of Proportional-Integral-Derivative (PID) controller, where *derivative term* $D = K_\mathrm{d}\dfrac{\mathrm{d}e(t)}{\mathrm{d}t}$ is used, but this term is not used in any controller at COMPASS. I term is important to reach target value but D term is very sensitive to measurement noise but a potential advantage is its quick reaction to changes of the controlled variable. At COMPASS, continuous integral term is discretise to the following form:

$$K_\mathrm{i} \int_0^{t_k} e(\tau)\mathrm{d}\tau = K_\mathrm{i} \sum_{i=1}^{k} e(t_i)\Delta t = \frac{K_\mathrm{p}}{T} \sum_{i=1}^{k} e(t_i)\Delta t, \tag{1.3}$$

where Δt at COMPASS is always in µs and can be 50 or 500 depending on the MARTe thread (slow or fast thread). Typically K_i at COMPASS is chosen

that way, that I term will be equal P term after certain amount of time T. Therefore, $K_\mathrm{i} = K_\mathrm{p}/T$. Wrong settings of PI constants can lead to oscillations and overshooting of the set-point.

2. Plasma Current Real-time Control

In the tokamaks toroidal field is stronger on the inner vessel side called High Field Side (HFS) than on the outer side called Low Field Side (LFS). Toroidal magnetic field decays as $1/R$. Therefore, gradient of magnetic field is created. This gradient is responsible for charge particle separation. If toroidal field is positive (counterclockwise) ions are drifting upwards while electrons are drifting downwards as it pictured in Fig. 2.1. This separation creates electrostatic field $\vec{E}$ downwards which together with gradient of magnetic field creates outward force $\vec{F} = \vec{E} \times \vec{B}$. This force causes drift of charged particles.

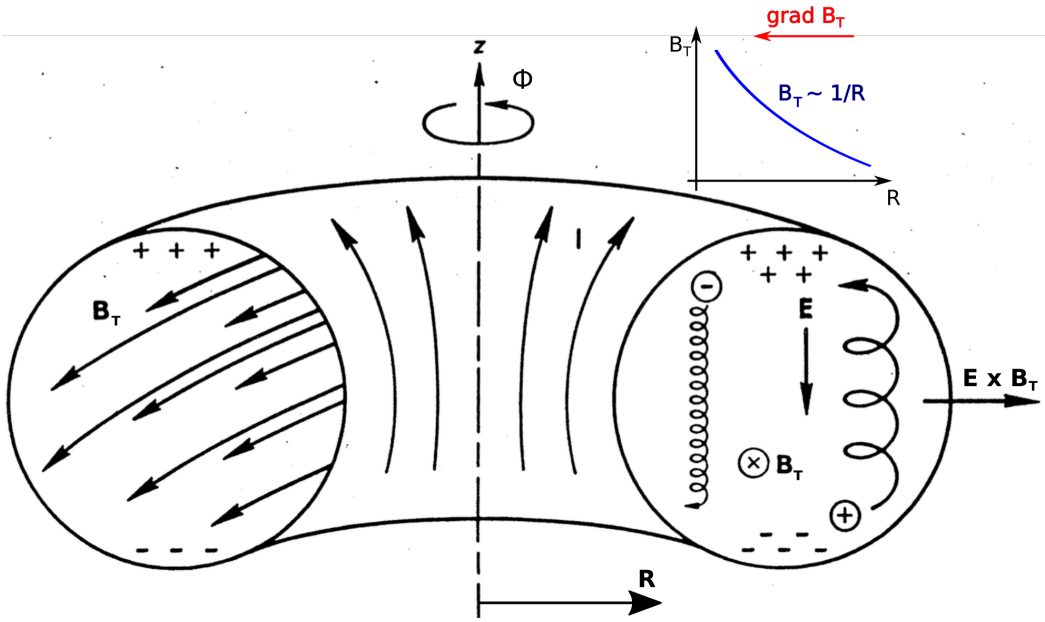

Figure 2.1: Drift of particles due to $\vec{E} \times \vec{B}$ force created by separation of ions and electrons due to gradient of magnetic field. Adapted from [76].

This omnipresent force from together with centrifugal force is compensated in tokamaks with plasma current I_p . Plasma current twists magnetic field lines and they become helical. This effect shortcuts electrostatic field $\vec{E}$ and compensates centrifugal force. Simply said particles on the HFS move up following helically shaped magnetic field lines and then to the LFS and so on. After certain amount of toroidal turns, particle, respectively magnetic field line, is at the same starting poloidal position. This plays very important role in tokamak stability theory. Ratio between number of the turns in toroidal direction m to the turns poloidal direction n is know as safety factor, q:

$$q = \frac{m}{n} \tag{2.1}$$

The safety factor q determines stability. Higher safety factor value leads to better stability. Typically $q = 1$ close to the magnetic axis and increases to 3-4 to the plasma edge.

Plasma current is driven and controlled by Magnetising Field Power Supply (MFPS) feeding current in the Magnetising Field (MF) coils which are Central Solenoid (CS) (MA and MB) and few other coils (see coils labelled "MF" in Fig. 1.3). Current changes in these coils change plasma current. It can be expressed as:

$$\frac{\mathrm{d}I^{\mathrm{MA+MB}}}{\mathrm{d}t} \sim \frac{\mathrm{d}I_{\mathrm{p}}}{\mathrm{d}t} \tag{2.2}$$

$$\frac{\mathrm{d}I_{\mathrm{MFPS}}}{\mathrm{d}t} + \frac{\mathrm{d}I^{\mathrm{MB}}_{\mathrm{SFPS}}}{\mathrm{d}t} - \frac{\mathrm{d}I^{\mathrm{MB}}_{\mathrm{EFPS}}}{\mathrm{d}t} \sim \frac{\mathrm{d}I_{\mathrm{p}}}{\mathrm{d}t}, \tag{2.3}$$

where superscripts denote the name of the coils and subscripts denote names of power supplies.

In order to get the longest plasma discharge with constant I_{p} , MFPS current goes to negative values ($-8\,\mathrm{kA}$ to $-16\,\mathrm{kA}$) before the gas puff and stays there for few milliseconds to stop inducing currents in the vessel. Loop voltage stronger than 12 V[1] has to be created to breakdown the neutral gas to form plasma. To create this loop voltage, capacitor is discharged during first 40 ms to 60 ms. During this time, MFPS reaches zero current. After that, polarity of MFPS is changed and MFPS starts rising. Except time necessary for polarity change, MFPS current is rising. If MFPS rises slower than certain value (this value depends on external heating, impurities and using Shaping Field Power Supply (SFPS) (see Eq. 2.3)) plasma current is decreasing. Decreasing speed of MFPS cannot be bigger than few hundred kA per ms (Sec 2.4), otherwise negative loop voltage is created and plasma current is driven in opposite direction which leads to disruptions. Therefore, limits for rising and decreasing MFPS speed are set in plasma current controller (Sec. 2.4). Detailed description of how MFPS is working is in (Sec. 2.3).

In this chapter, plasma current model will be described in Sec. 2.1. After that, description of diagnostics (Sec. 2.2) and actuators (Sec. 2.3) is described.

2.1 Plasma Current Model

Plasma discharge at COMPASS starts after hydrogen or deuterium is injected in the tokamak vessel to pressure between $4 \times 10^{-3}\,\mathrm{Pa}$ to $3 \times 10^{-2}\,\mathrm{Pa}$ (Sec. 5) and the external electric field $U_{\mathrm{loop}}/[2\pi R_0]$ ionises the deuterium (or hydrogen) gas Fig. 1.9.

Results from breakdown studies depending on both timing of the gas puff and amount of the injected gas at COMPASS are described in the article [75].

Plasma current in the COMPASS tokamak is created and driven by flux change in MF coils (i.e. in the central solenoid), acting like primary winding of a non-iron core transformer at COMPASS. Current changes in MF coils induce toroidal electric field inside the vessel (called the loop voltage - U_{loop}) which accelerates ions and electrons which first ionise the neutral gas into plasma. After ionisation, it generates strong toroidal plasma current - I_{p}

$$I_{\mathrm{p}} = \frac{U_{\mathrm{loop}}}{R_{\mathrm{p}}} - \frac{L_{\mathrm{p}}}{R_{\mathrm{p}}}\frac{\mathrm{d}I_{\mathrm{p}}}{\mathrm{d}t}, \tag{2.4}$$

[1] experimental results from COMPASS

which both suppresses the omnipresent basic toroidal instability and secondly heats up the plasma. This plasma heating is called Ohmic Heating (OH) and its source is toroidal plasma current I_p flowing in resistive plasma. Plasma resistance R_p is caused by collisions between ions and electrons. Ohmic heating power P_OH can be expressed according to $P_\mathrm{OH} = R_\mathrm{p} I_\mathrm{p}^2$

High plasma inductance $L_\mathrm{p} \approx 1\,\mu\mathrm{H}$ [77] sets up the maximum rise time of I_p at the very beginning of discharge (see Fig. 1.9) as:

$$\frac{\mathrm{d}I_\mathrm{p}}{\mathrm{d}t} = \frac{\mathrm{d}I_\mathrm{MF}}{\mathrm{d}t}\frac{L_\mathrm{MF,Ip}}{L_\mathrm{p}} = \frac{U_\mathrm{loop} - U_\mathrm{p} I_\mathrm{p}}{L_\mathrm{p}} \approx \frac{12\,\mathrm{V}}{1\,\mu\mathrm{H}} = 12\,\mathrm{kA/ms}, \tag{2.5}$$

where $L_\mathrm{MF,Ip} = 22\,\mu\mathrm{H}$ [77] is the mutual inductance between the central solenoid and the plasma current. At the beginning plasma resistivity is high and plasma current is low but plasma resistivity decreases fast. During flat top phase $\frac{\mathrm{d}I_\mathrm{p}}{\mathrm{d}t} = 0$ and $U_\mathrm{loop} = 1\,\mathrm{V}$ to $2\,\mathrm{V}$ giving $R_\mathrm{p} = 3\,\mu\Omega$ to $6\,\mu\Omega$

Higher changes of MF rises plasma current faster (Eq. 2.2). If plasma current rises too fast, the skin effect will cause flat or even hollow current profile $j(r)$ (Fig. 2.2) with highest gradient of $j(r)$ at the plasma edge ($r = 0$ at central magnetic axis, $r \approx 20\,\mathrm{cm}$ at the edge, Last Closed Flux Surface (LCFS)). Hollow profiles are associated with a central region of inverse safety factor profile, $\mathrm{d}q/\mathrm{d}r < 0$, implicating bursts of MagnetoHydroDynamic (MHD) activity associated with surface kink modes [3], localised near the edge of plasma. These modes can result in the so-called *locked mode* and develop into a violent disruption [78, 79]. At the JET tokamak, amount of disruptions caused by fast current ramp-up is 5.9% [80] and with ITER-like wall (ILW) 1.1% [81] and AUG is 10.2% [81]. There is no such statistics at COMPASS, but occurrence of disruptions during fast current ramp-up was observed and therefore the current ramp-up has been slowed down (see Sec. 2.3). On the other hand, these inverse safety factor profiles are the basis of modes with confinement even better than the H-mode thanks to the so-called *edge transport barrier* formation during fast I_p ramp-up phase, stabilised by localised lower-hybrid current drive [82].

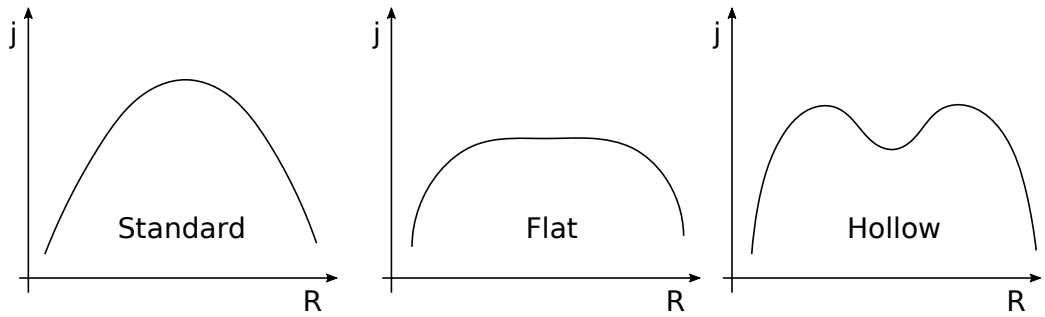

Figure 2.2: Schema of different plasma current profiles.

2.2 Plasma Current Diagnostic

Plasma current is measured with Rogowski coil wired inside the tokamak vessel in poloidal direction. This signal ($U_\mathrm{Rogowski} \propto \mathrm{d}I_\mathrm{p}/\mathrm{d}t$) is then integrated with

an analogue integrator and connected to an acquisition board for MARTe measurement. Due to analogue integration, plasma current measurement drifts (given by a random voltage offset) which can be written as:

$$I_{\mathrm{p}} = \int (U_{\mathrm{Rogowski}} + U_{\mathrm{offset}})\mathrm{d}t = I_{\mathrm{p}} + U_{\mathrm{offset}} \cdot t + c, \tag{2.6}$$

where U_{offset} is offset at input of the integrator and c is offset at input at Analog Digital Converter (ADC) at Data Acquisition System (DAS). Therefore, this drift and offset has to be subtracted. The drift is removed using the linear least squares method using measurements before plasma breakdown with simple linear equation $y = kx + q$, calculated according to following equation:

$$\begin{aligned}
\overline{x} &= \frac{1}{N}\sum_{t_s}^{t_e} t_i \\
\overline{y} &= \frac{1}{N}\sum_{t_s}^{t_e} s_i \\
xx_s &= \sum_{t_s}^{t_e} t_i^2 \\
xy_s &= \sum_{t_s}^{t_e} t_i \cdot s_i \\
S_{xx} &= xx_s - N \cdot \overline{x}^2 \\
S_{xy} &= xy_s - N \cdot \overline{x} \cdot \overline{y} \\
k &= \frac{S_{xy}}{S_{xx}} \\
q &= \overline{y} - k \cdot \overline{x},
\end{aligned} \tag{2.7}$$

where $t_s = 500\,\mathrm{ms}$ is start time and $t_e = 850\,\mathrm{ms}$ is end time of counting drift from the plasma current signal s. s_i is a value of the signal at actual discharge time t_i, N is number of samples of signal s and time t. Using Eq. 2.7 drift from signal s after time t_e can be calculated using the following equation:

$$o_i = s_i - (k \cdot t_i + q) \tag{2.8}$$

where o_i is drift compensated output signal with subtracted drift from the integrators at current discharge time. Start of subtracting is after calculating drift at 900 ms and ends after plasma discharge at 2200 ms.

The same algorithm is used for removing drift for all other integrated magnetic measurements used in real-time (see Sec. 3.4) and for plasma density offset removing (Sec. 5.4) with different time settings. Start and end of calculation as well as start and end of correction of drift from the plasma current measurement is specified in the LinearDriftRemoverGAM configuration in the configuration file loaded at MARTe startup.

The integrator after disruption may tear from real values and output signal is neither zero nor the same linear function as was before plasma and its disruption,

because integration process is corrupt. Therefore, plasma current measurement is not zero after subtracting drift calculated before plasma. This effect may affect request from MFPS that way, that MFPS is requested to ramp-up despite the fact that plasma current is not present any more. Therefore, feedback is applied only if plasma current is higher than 15 kA for discharge after 1000 ms.

2.3 Plasma Current Actuator

Plasma current is driven and controlled by MFPS - a thyristor power supply which operates between −16 kA to 14 kA. Firstly, MFPS current is ramped to starting negative value (polarity shown in Fig. 2.3 labelled by blue mark) between −8 kA and −16 kA and stays there for few milliseconds until eddy currents in the vessel have decayed (Fig. 2.5). The current is flowing through the thyristors TV1 and

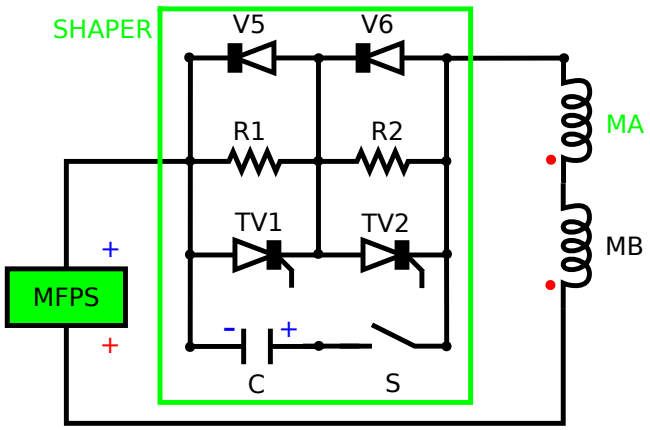

Figure 2.3: Schema of MFPS connection with thyristors TV1 and TV2 and capacitor C necessary for plasma breakdown.

TV2 to the tokamak coils. The thyristors are open by discharging capacitor C into them. Then the current flows through R1 and R2, changing time constant of the whole circuit L/R, allowing large $\mathrm{d}I_{\mathrm{MFPS}}/\mathrm{d}t$ to start plasma. L is inductance of MFPS windings and inductively connected short circuit created by the vacuum vessel. R is resistivity of R1, R2 and the MFPS winding resistance. The thyristors TV1 and TV2 can be switched on during MFPS current going to 0 A, effectively decreasing $\mathrm{d}I_{\mathrm{MFPS}}/\mathrm{d}t$ (and loop voltage on the plasma column) by increasing L/R time constant. This can be set only before the discharge and cannot be controlled during plasma discharge. Therefore, they were heuristically optimised to rise plasma current reasonably fast to avoid instabilities or fast enough to fulfil experimental program (e.g. creating runaway electrons). The most used setting is listed in Tab. 2.1.

When MFPS reaches zero current, polarity of power supply changes and positive current starts flowing in the opposite direction through the V5 and V6 diodes (red polarity marks). Changing of the polarity takes approximately 10 ms. During this time, MFPS current stays zero and therefore, plasma current is falling as $\mathrm{d}I_{\mathrm{p}}/\mathrm{d}t = -I_{\mathrm{p}}\, R_{\mathrm{p}}/L_{\mathrm{p}}$. Till this time plasma current is uncontrolled. After the polarity of power supply is changed MFPS current can be controlled in real-time. Therefore, plasma current can be feedback controlled only after MFPS crosses

	D-shape plasma	runaway electron campaign	circular plasma
delay TV1 [ms]	5	0	4
delay TV2 [ms]	8	0	8

Table 2.1: Time delay of resistors used for breakdown.

0 kA current and starts rising to positive values. Speed of MFPS ramping up, determines rising speed of plasma current. Positive requested current after crossing zero has to come before polarity is changed, otherwise MFPS current stays zero longer time than necessary due to delays in the whole system.

Delay between MFPS current request and MFPS current response is ≈ 8 ms and is estimated from vacuum shot #7333 (Fig. 2.4).

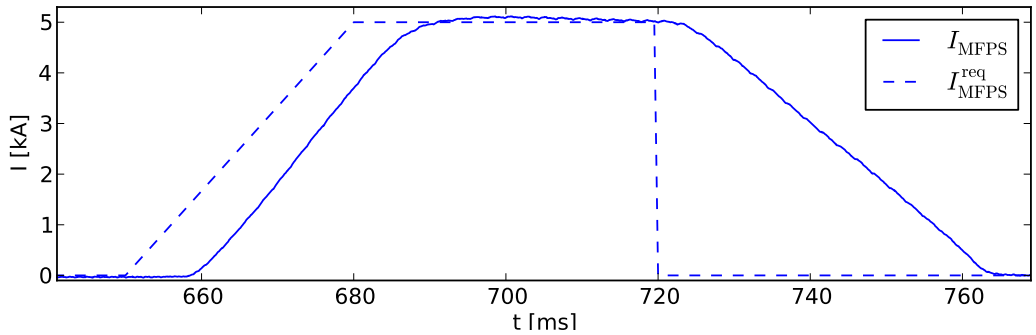

Figure 2.4: Vacuum shot #7333 with MFPS current. Solid line is measured current and dashed line is requested.

Changes of setting different time for TV1 and TV2 are visible in Fig. 2.5. The top figure illustrates MFPS current in *vacuum shot* (ie. without plasma) in time corresponding the plasma breakdown. Requested current is drawn with dashed-line and is -12 kA, -14 kA and -16 kA. Depending on starting level, loop voltage, exact time of plasma breakdown and also plasma current before MFPS changes polarity vary. Different U_{loop} during breakdown, time of plasma breakdown and the plasma current value reached before feedback starts to control are listed in Tab. 2.2. Plasma start time can vary depending on the controlled

MFPS requested current [kA]	-8	-10	-12	-14	-16
U_{loop} during breakdown [V]	12	13	16	18	21
plasma start time [ms] ± 0.5 ms	954.5	955.5	957.1	959.2	961.4
$\approx I_{\mathrm{p}}$ b. MFPS pol. ch. [kA] $\pm 10\,\%$	90	135; 115	145	210	245

Table 2.2: Empirically found loop voltage, plasma breakdown time and plasma current before MFPS polarity change according to requested waveform for different level of MFPS. Blue numbers show when SFPS was used and red number is without SFPS. Loop voltage, plasma start time and plasma current before polarity is changed were averaged values over shots with different wall conditions and different settings of TV1 and TV2. Also loop voltage signal is very noisy, therefore, values are not accurate.

neutral gas pressure and (poorly controlled) vessel internal surface cleanness (impurity content). Values marked blue show plasma current when SFPS power supply was used. Red value shows when SFPS was not used, therefore, current is lower. SFPS helps MFPS to drive plasma current because they have the same polarity in coil MB (Fig. 1.4).

Plasma breakdown start varies in few ms and causes problem to establish equilibrium in very first ms of plasma discharge (see Sec. 3.4.1). The lower MFPS current (e.g. $-16\,\mathrm{kA}$) is requested, higher plasma current is reached before MFPS changes polarity, higher loop voltage is created and plasma current rises faster because of the voltage drop over the resistors which is proportional to MFPS current. Also, plasma current flat top phase can be longer due to increasing Vs (VoltSeconds) of MFPS.

The total budget of VoltSeconds $U_{\mathrm{loop}} \cdot t_{\mathrm{discharge}}$ is the most limiting hardware factor for our tokamak: worse condition of the first wall means lower plasma temperature, so lower conductivity, yielding to higher U_{loop} for the desired I_p current and thus shorter discharge. According to Eq. 2.4 and Eq. 2.5, the VoltSeconds budget is determined by the maximum and minimum current driven in the central solenoid. At COMPASS, its value is mostly limited by the mechanical strength of the solenoid copper insulation layers (the engineering safe value is $\pm 16\,\mathrm{kA}$), secondly by available energy in the flywheel generators and third the copper coil resistive heating. Plasma is created easier when starting from higher absolute value of negative current. Loop voltages corresponding to starting level of MFPS current are listed in Tab. 2.2 as well as approximate plasma starting time.

Different time settings of TV1 and TV2, together with different starting point, are in Fig. 2.5. MFPS rises the fastest when MFPS starts at $-16\,\mathrm{kA}$ and TV1 and TV2 are set to 0 (the blue line at the bottom graph). The fastest ramp up at positive current is $150\,\mathrm{A/ms}$ when step at MFPS current is requested (blue line). Green line has the same trend as the requested line (the green dashed line) and is delayed approximately 8.5 ms. Ramp-up speed is $140\,\mathrm{A/ms}$. Another two MFPS current ramp-ups are $60\,\mathrm{A/ms}$ and $100\,\mathrm{A/ms}$ and are slow enough that MFPS current follows and is stabilised at requested values. Requested currents in top and bottom graph are plotted with dashed line with corresponding colour.

Coil MB, as mentioned above, is used for MFPS, SFPS and Equilibrium Field Power Supply (EFPS) current. Therefore, effect of SFPS was investigated on rising of plasma current and is displayed in Fig. 2.6. Due to the same polarity of SFPS and MFPS in CS, increasing SFPS current increases plasma current as well (see Eq. 2.3). For testing effect of SFPS current at plasma current starting TV1 and TV2 is same (4 ms and 7 ms) and starting level of MFPS is $-14\,\mathrm{kA}$. SFPS current is starting at different time (middle graph). Plasma current rises the fastest when SFPS starts earlier (cyan colour) and slowest if SFPS is not used at all (red colour). Therefore, early start of SFPS can save Vs of MFPS and thus prolongate plasma discharge or plasma current can reach higher values.

Note that also external heating (Neautral Beam Injection (NBI) in case of COMPAS) has positive effect of saving Vs due to the fact it heats up plasma and therefore decreases plasma resistivity. Since external heating is not real-time controlled, it is not investigated in this thesis.

Another necessary field is the *equilibrium field* EFPS which stabilises plasma in the horizontal direction by compensating the plasma expansion hoop force with

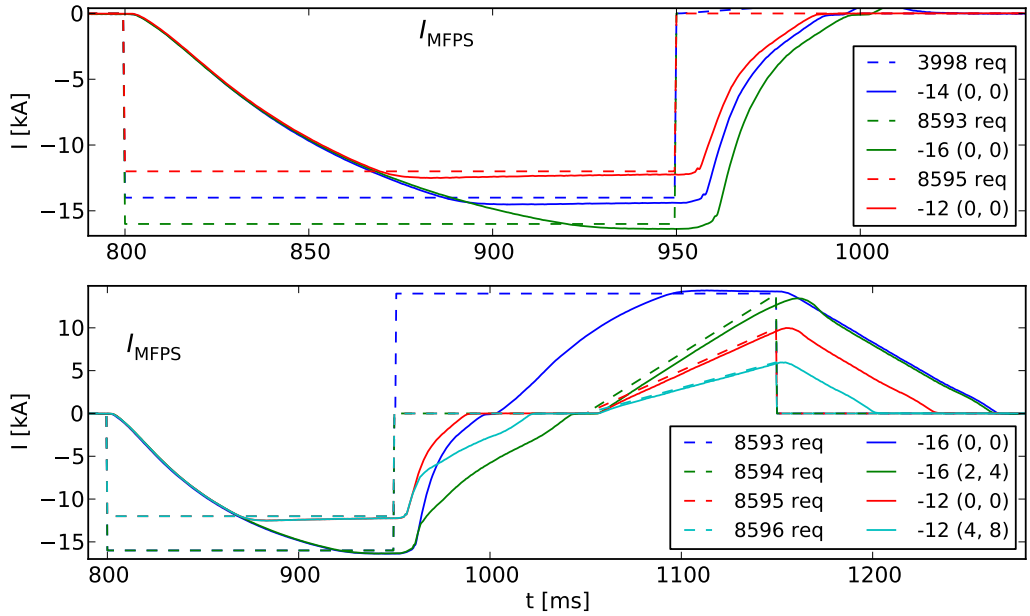

Figure 2.5: Top window shows different starting point of MFPS for plasma current breakdown. Bottom graph displays different MFPS currents evolution according to time settings of switching off of the thyristor TV1 (first number in the brackets) and TV2 (second number in the brackets) before crossing zero. After crossing zero, there are different current requests (dashed lines) to see difference MFPS current (solid lines) rising speed.

a vertical magnetic field (see Fig. 3.2b). Effect of EFPS is also not consider in this thesis because EFPS current is simply directly proportional to the plasma current during whole discharge (see Sec. 3.4.1).

2.4 Plasma Current Controller

Plasma real-time control starts at fast thread with 50 µs loop cycle with acquiring data by ATCAAdc Generic Application Module (GAM) as it is drawn in Fig 2.7.

Plasma current measurement is integrated signal, so drift and offset from integrator and measurement is subtracted in LinearDriftRemoverGAM according to Eq. 2.7 and 2.8. Plasma current signal is used in other GAMs for activating another controllers usually to control position, horizontal Sec. 3.4.1 and vertical - Sec. 3.4.2, shape (Sec. 4.4) and electron density (Sec. 5.4) only if plasma current exists. Plasma current measurement is transferred from fast thread to slow thread (2 kHz) using OutputGAM and InputGAM. During this transfer every 10th sample is copied from fast to slow thread. Then calculation of requested MFPS current is calculated in MFPSCurrentControllerGAM according to the following equation:

$$I^{\mathrm{req}}_{\mathrm{MFPS}} = P_{\mathrm{I_p}} e_{\mathrm{I_p}} + I_{\mathrm{I_p}} \sum_{j=0}^{k} e^{j}_{\mathrm{I_p}} \Delta t \tag{2.9}$$

where $P_{\mathrm{I_p}} = -120$ is proportional constant, $I_{\mathrm{I_p}} = -0.006$ is integral constant in µs and $e_{\mathrm{I_p}} = SP - MV$ is difference between requested value (setpoint) SP

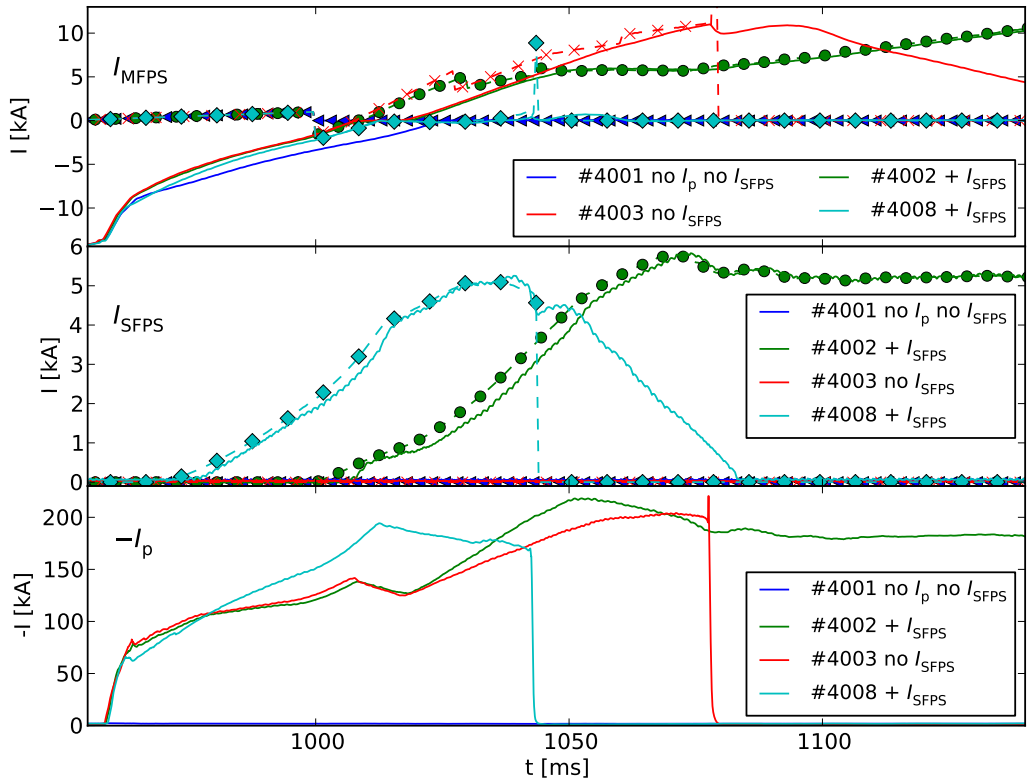

Figure 2.6: Effect of using SFPS current for plasma rising speed. Top graph is MFPS current. Middle graph is SFPS current and bottom graph is plasma current in corresponding shots. Dashed lines are requested values. Markers are for better distinguishing between the lines.

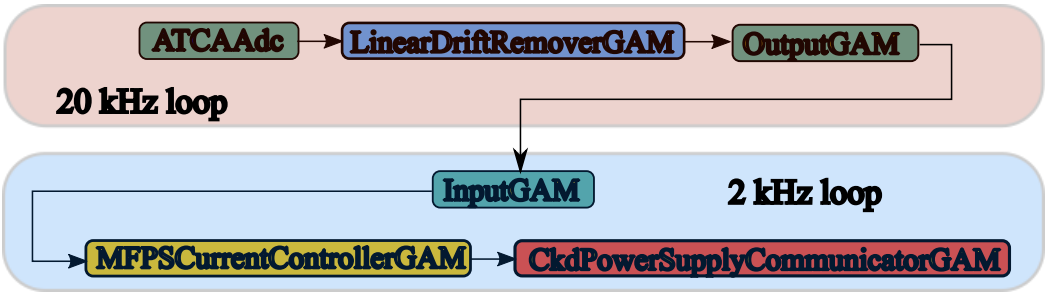

Figure 2.7: Sequence of GAMs for plasma current control.

and measured value MV. One step of integration is $\Delta t = 500\,\mu s$ and because of the fact that MARTe based time is in µs value 500 is used instead of 500E-6. k is the actual step of integration since beginning of plasma current $j(0) = 0$. That means $k\Delta t$ is actual time of discharge since plasma breakdown.

Plasma current controller is Proportional Integral (PI) controller in slow thread executing each 500 µs as can be seen from Eq. 2.9. Requests after calculation are sent to CkdPowerSupplyCommunicatorGAM where are translated according to Current Control Protocol (CCP) [74] to data packets. These packets are then sent via RS232 [39] link through communication link to the MFPS control unit.

2.4.1 Plasma Current Controller Optimisation

Plasma current feedback controller gains were tuned by the trial-and-error method starting at $P_{I_p} = -15$ and doubling it every next step up to $P_{I_p} = -240$, and keeping integral gain set to zero. After that integral constant $I_{I_p} = -0.012$ was added. Integral constant was chosen, that in 20 ms will be same as proportional (time is counted in µs). Results from tuning feedback constants are in Fig. 2.8. Plasma current has the same requested value −120 kA for constant $P_{I_p} = -15$, −30, −60, −120 and −240. Therefore, requested lines (dash lines) are overlapping and only magenta colour is visible. −130 kA plasma current is requested for experiment with constants $P_{I_p} = -240$ and $I_{I_p} = -0.012$ (black line).

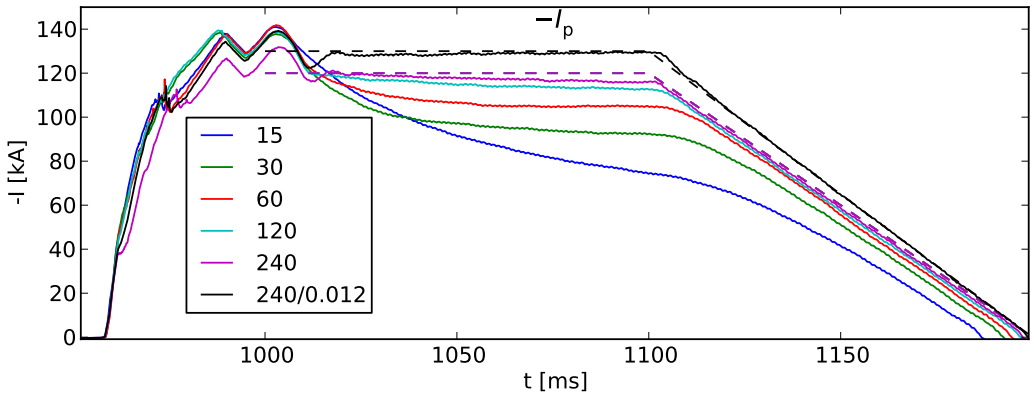

Figure 2.8: Tuning of feedback constants for plasma feedback controller. Requested currents are in dashed lines with corresponding colours (All requested currents except $P_{I_p} = -240$, $I_{I_p} = -0.012$ has same request, therefore, colours are overlapped). First number is P_{I_p}, number behind "/" is I_{I_p}.

Plasma current follows the requested value better when the proportional constant P_{I_p} increases. Doubling constant from -120 to -240 has no significant effect but starting integral part of regulator helps to keep plasma current to follow the requested value (−130 kA black line). $P_{I_p} = -240$ and $I_{I_p} = -0.012$ were bit strong when plasma was shaped using SFPS (as aforemationed, they share one coil) and it created oscillations. Therefore, these constants were lowered later (discharge #3505)to $P_{I_p} = -120$ and $I_{I_p} = -0.006$.

Note that plasma current is most of the time, in COMPASS tokamak, in negative direction, but for better overview and better look at graphs, plasma current is plotted as positive but is marked with labels on y-axis and in the legend with correct sign. For the same reason and better understanding, following explanation is written in the way like plasma is in positive direction (respectively like describing plasma current amplitude).

The mentioned controller (with both settings of PI gains) was used for approximately 900 discharges, however, improvement was necessary. The main reason to improve the controller was that after crossing zero $I_{\mathrm{MFPS}} = 0$ kA, plasma current could be at a very different value than the requested value. Then either very fast ramp up was requested (which caused overshooting and it prolonged the time necessary to obtain the flat top phase) or the current after crossing zero was higher than requested current. Then MFPS current started decreasing into

negative values, negative loop voltage was created and plasma current was driven in opposite direction. When plasma was below requested value, MFPS current started to rise, MFPS reached zero current again then polarity was changed and only then plasma current was fully controlled. This leaded to disruptions. To avoid overshooting and creating negative loop voltage plasma current controller has been changed in the following way.

If plasma current is greater more than 15 kA over requested current, then new set point is calculated as plasma current minus 0.3 kA. This defines maximal plasma current ramp down as 0.6 kA/ms. Slower current decreasing is to avoid negative loop voltage and driving plasma current in opposite direction as mentioned before.

On the other hand, when plasma current is lower more than 15 kA below requested value then new set point is set which is actual measured plasma current plus 1 kA in every cycle. Therefore, plasma current ramp up is limited to 2 kA/ms. These limits were obtained from experiments and observation of plasma current rising and decreasing speed. Limits at rising and decreasing plasma current requests were implemented firstly in the discharge #3881 with slightly different values. Starting with discharge #3892 are in above presented format.

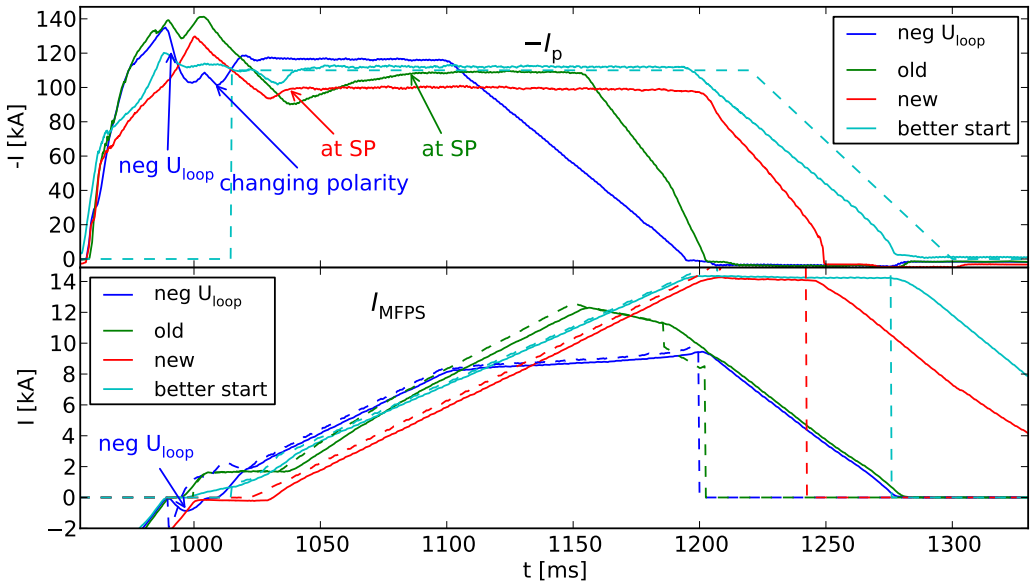

Figure 2.9: Different types of plasma current control approaches. New algorithm with limiting current ramp-up and current ramp down are plotted with red and cyan colour. Cyan colour has already optimised shaping current to be close to the requested plasma current before MFPS changes polarity. MFPS current plotted with blue colour creates negative loop voltage. Plasma current plotted with green line has limit on plasma current ramp-down but it is after calculation of PI regulator. Therefore, integral component creates overshoot at 1040 ms, which prolong time necessary to reach flat-top phase.

In Fig. 2.9 are results showing comparison between the discharges when plasma current ramp-up and ramp-down is limited and when they are not limited. Top graph shows plasma current in different discharges while bottom graph shows corresponding MFPS current. Blue line shows when plasma current is not lim-

ited and feedback on plasma current starts before magnetising field crosses zero current. Because TV1 and TV2 or starting point of breakdown at MFPS are set the way that MFPS rises fast, plasma current has almost 140 kA when feedback starts to control. Nevertheless at this point MFPS has not changed polarity. Lower MFPS current is requested (bottom graph blue dashed line) and MFPS is falling (bottom graph blue solid line), and plasma current starts decreasing for the first time to 100 kA which is 20 kA bellow requested value. Then, MFPS current starts rising reaching zero and plasma rises as well. After that MFPS is changing polarity and plasma is falling again. When polarity is changed MFPS rises again and plasma current is easily controlled.

First limit was performed in the following way. MFPS was set to previous value, if controller calculated request for MFPS lower than previous value. Negative loop voltage was not created, however, disadvantage of this approach was that integral component was increasing error and therefore, it overshoots (top graph green line at 1040 ms). Requests as well as MFPS current are not decreasing but error is accumulating. Due to overshooting plasma current reaches requested point at 1080 ms (labelled with green mark "at SP").

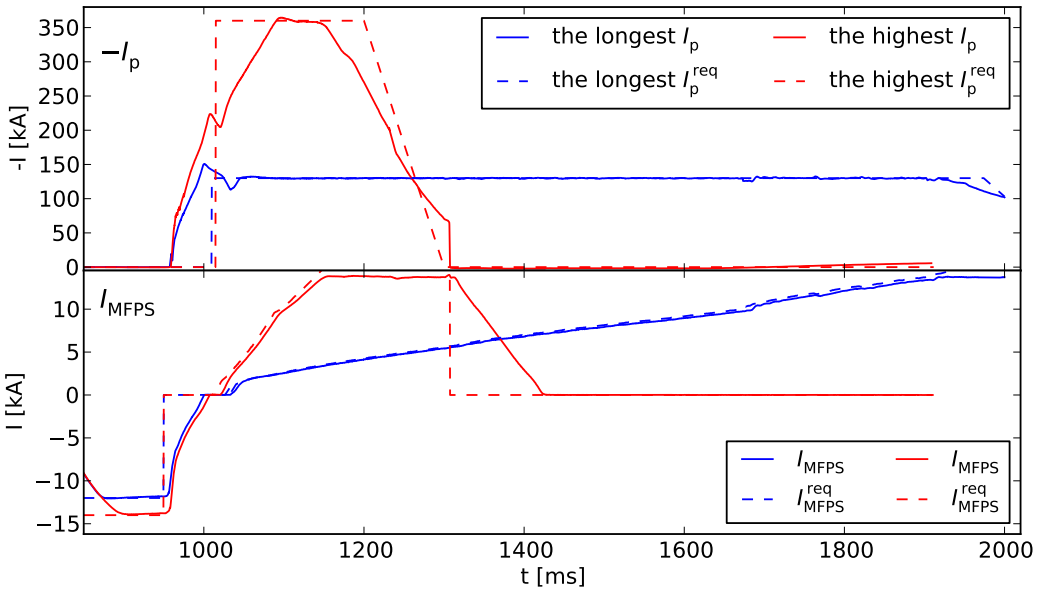

Figure 2.10: Plasma current (top figure) plotted together with magnetising current (bottom figure) from the longest discharge and from the discharge with highest plasma current. Both discharges were performed with plasma control algorithms and improvements described in this thesis.

Results with limit on rising and decreasing plasma current as was described above are drown with red colour. Plasma current is decreasing slower than for green line and also does not overshoot so much. Therefore plasma current reaches requested value 50 ms earlier than if set point is not being reseted.

Best approach is when MFPS starting level for breakdown is optimised. Cyan colour shows starting point at −10 kA of MFPS current and thus, plasma current goes only to 120 kA and after MFPS current crosses zero plasma current is already at requested current 110 kA. Oscillations at plasma current are caused by SFPS current and changing from circular shape to elongated shape and back

(see Chap. 4). For circular plasma shape, elongated plasma is used at the beginning of discharge until MFPS crosses zero to suppress creating of magnetic islands which are created at COMPASS typically between 80 kA to 140 kA in pure circular plasma. When plasma decreases due to polarity switching of MFPS rotation of islands slows down which leads to lock mode and disruption. If plasma is elongated these islands are not created.

Bottom part of Fig. 2.9 shows also limit at MFPS current which is 14 kA. When MFPS reaches maximum and current request is requested to be flat or rising, MFPS stays flat at 14 kA but plasma current is decreasing due of ohmic loses (collisions between charge particles).

Plasma current controller with resetting the set point and correct settings of MFPS current level before breakdown prolongs plasma flat top phase, reduces disruption during MFPS changing polarity and plasma ramp up phase. With this controller the longest shot > 1050 ms and highest current was reached 364 kA (see Fig. 2.10).

3. Plasma Position Real-Time Control

Magnetic confined plasma and it's behaviour from macroscopic point of view can be described as a model of a single electrically conductive fluid using MagnetoHydroDynamic (MHD) theory. Plasma is represented with current density $\vec{j}$, a fluid velocity $\vec{v}$, a local mass density ρ, a plasma kinetic pressure $p = n \cdot T$, where n is the plasma density and T is plasma temperature. These quantities are connected together with the mass conservation law:

$$\frac{\partial}{\partial t}\rho = -\nabla \cdot (\rho \vec{v}) \tag{3.1}$$

and Newton's law applied to an infinitesimal plasma element:

$$\rho \frac{\mathrm{d}\vec{v}}{\mathrm{d}t} = \vec{j} \times \vec{B} - \nabla p, \tag{3.2}$$

where $\vec{j} \times \vec{B}$ is Lorentz force and $\vec{B}$ is magnetic field. Eq. 3.2 tells basic condition for equilibrium which means that the overall forces acting on an infinitesimal plasma volume is zero. For steady-state solution of the MHD theory, $\partial / \partial t = 0$, the plasma pressure and Lorenz force are in equilibrium:

$$\nabla p = \vec{j} \times \vec{B} \tag{3.3}$$

The electromagnetic field satisfies also Maxwell's equations:

$$\nabla \cdot \vec{B} = 0 \tag{3.4}$$

$$\nabla \times \vec{B} = \mu_0 \vec{j} \tag{3.5}$$

Equation 3.4 is Gauss's law for the magnetic induction field, Eq. 3.5 is Ampere's law giving the relationship between the current density $\vec{j}$ and magnetic field intensity $\vec{H}$. Relation between $\vec{B}$ and $\vec{H}$ is defined as $\vec{B} = \mu_0 \vec{H}$, where μ_0 is permeability of free space. From Eq. 3.3 it can be directly obtained:

$$\vec{B} \cdot \nabla p = \vec{B} \cdot (\vec{j} \times \vec{B}) = 0 \tag{3.6a}$$

$$\vec{j} \cdot \nabla p = \vec{j} \cdot (\vec{j} \times \vec{B}) = 0 \tag{3.6b}$$

Eq. 3.6a implies that there is no pressure gradient along the magnetic field lines and Eq. 3.6b shows the current lines lie on the magnetic surfaces (Fig 3.1). Magnetic field lines and current density lines lie on isobaric surfaces where the magnetic pressure is constant. The isobaric surfaces are toroidally nested around the maximum of the pressure near the centre (R_0) of poloidal cross-section of the plasma.

As tokamaks are axisymmetric toroidal devices, it is convenient to transfer MHD equations to the cylindrical coordinates system (R, ϕ, z), where the axis $R = 0$ is the rotational axis of the tokamak. Due to tokamaks' toroidal symmetry it is possible to assume that all the quantities do not depend on the toroidal angle

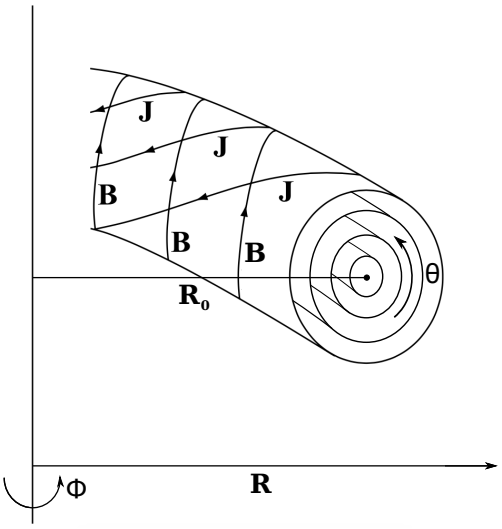

Figure 3.1: Plasma toroidally nested magnetic surfaces

ϕ. With this assumption the Gauss's law Eq. (3.4) in cylindrical coordinates can be written as:

$$\frac{1}{R}\frac{\partial}{\partial R}RB_{\mathrm{R}} + \frac{\partial}{\partial z}B_{\mathrm{z}} = 0 \tag{3.7}$$

To study tokamak equilibria it is convenient to introduce poloidal magnetic flux function ψ so the magnetic (isobaric) surfaces also coincide with the constant poloidal flux surfaces:

$$\vec{B} \cdot \nabla\psi = 0 \tag{3.8}$$

Therefore, the magnetic induction, the pressure and the current density are constant on each level of the poloidal flux function ψ on the poloidal plane. The poloidal magnetic field in cylindrical coordinates is:

$$B_{\mathrm{R}} = \frac{1}{R}\frac{\partial\psi}{\partial z} \tag{3.9a}$$

$$B_{\mathrm{z}} = -\frac{1}{R}\frac{\partial\psi}{\partial R} \tag{3.9b}$$

Plasma position control can be divided in two separate problems. First, horizontal (radial) plasma position control. Plasma is horizontally stable and is in equilibrium with external magnetic forces. Changing these forces moves equilibrium and therefore horizontal position to another stable position. Second, vertical plasma is stable only in circular shape and its vertical position can be controlled in open loop mode. Elongated - D-shaped plasma has better confinement of plasma energy and particles, however, it is vertically unstable [83]. Therefore, D-shaped plasma has to be controlled by feedback closed loop.

At COMPASS, plasma position in horizontal direction is controlled with two different current power supplies. First, Equilibrium Field Power Supply (EFPS) controls the main stabilizing field but it is slow and drives currents in Equilibrium Field (EF) coils (see Fig. 1.3) with many turns. Second is Fast Amplifier for Vertical Magnetic Field (FABV) which is fast power supply with lower current-turns (see Sec 3.3) and thus varying fast current in the Vertical Field (BV) coils.

Using EF, Magnetising Field (MF), BV coils, COMPASS has circular plasma shape. D-shaped or elongated plasma is driven by Shaping Field (SF) created by Shaping Field Power Supply (SFPS). When SF is used, plasma has to be vertically stabilised with radial magnetic field - Radial Field (BR) created by Fast Amplifier for Radial Magnetic Field (FABR). FABR has similar construction as FABV.

Fig. 1.3 shows localisation of each circuit; each symbol represents a poloidal coil (without showing the actual number of turns). Note that MF, EF and SF coils are using the same coils in central solenoid.

Plasma position has to be stabilised and controlled during the whole discharge. Techniques of real-time estimation of plasma position are described in Sec. 3.2. Real-time control algorithms are written in Sec. 3.4. Section 3.4.1 shows detailed implementation and usage of horizontal plasma position controller as a mixture of two different power supplies EFPS and FABV. Specific improvements for vertical plasma position are written in Sec. 3.4.2.

Further suggestions for improving plasma position real-time control are depicted in last Chap. 6.

3.1 Plasma Position Model

Poloidal fields in tokamak determines plasma position. Poloidal field is created as a sum of the five poloidal fields from the five different current power supplies EFPS, Magnetising Field Power Supply (MFPS), SFPS, FABR, FABV and plasma current. Poloidal field B_{pol} can be expressed as a linear combination of hardware-fixed fields:

$$\begin{aligned}\vec{B}_{\mathrm{pol}}(R,Z) = \vec{B}_{\mathrm{MFPS}}(R,Z)\cdot I_{\mathrm{MFPS}} + \vec{B}_{\mathrm{SFPS}}(R,Z)\cdot I_{\mathrm{SFPS}} + \\ + \vec{B}_{\mathrm{EFPS}}(R,Z)\cdot I_{\mathrm{EFPS}} + \vec{B}_{\mathrm{FABV}}(R,Z)\cdot I_{\mathrm{FABV}} + \\ + \vec{B}_{\mathrm{FABR}}(R,Z)\cdot I_{\mathrm{FABR}} + \vec{B}_{\mathrm{I_p}}(R,Z)\cdot I_{\mathrm{p}},\end{aligned} \tag{3.10}$$

where $\vec{B}_{\mathrm{MFPS}}$, $\vec{B}_{\mathrm{EFPS}}$, $\vec{B}_{\mathrm{SFPS}}$, $\vec{B}_{\mathrm{FABR}}$, $\vec{B}_{\mathrm{FABV}}$ are magnetic fields in [T/kA] as were shown in Fig. 1.5 and I_{MFPS}, I_{EFPS}, I_{SFPS}, I_{FABR}, I_{FABV} are currents from corresponding power supplies which can be varied.

Lorentz's force acting on plasma is given as:

$$\vec{f}\,(R,Z) = \vec{j}_{\,\mathrm{p}}(R,Z) \times \vec{B}_{\mathrm{pol}}(R,Z), \tag{3.11}$$

when relation between current density $\vec{j}_{\,\mathrm{p}}(R,Z)$ and total plasma current I_{p} is:

$$I_{\mathrm{p}} = \int_R \int_Z \vec{j}\,(R,Z)\mathrm{d}r\mathrm{d}z. \tag{3.12}$$

The total force is then given by integral over the entire plasma cross-section:

$$\vec{F} = \int_R \int_Z \vec{f}\,(R,Z)\mathrm{d}r\mathrm{d}z. \tag{3.13}$$

Plasma position in horizontal direction is in equilibrium with expansion forces and vertical plasma position has to be actively stabilised. Vertically elongated plasma is generated by the SF field, simply pulling the bottom part of plasma downwards and the top part upwards. Since the force non-linearly rises the closest the plasma is to one of those coils, this makes it naturally vertically unstable.

3.1.1 Plasma Equilibrium

Two qualitatively different types of forces are involved in producing an MHD equilibrium. *Radial expansions forces* Fig. 3.2a (from plasma point of you) and *outward expansion forces* Fig. 3.2b. Radial expansion forces are due to a natural

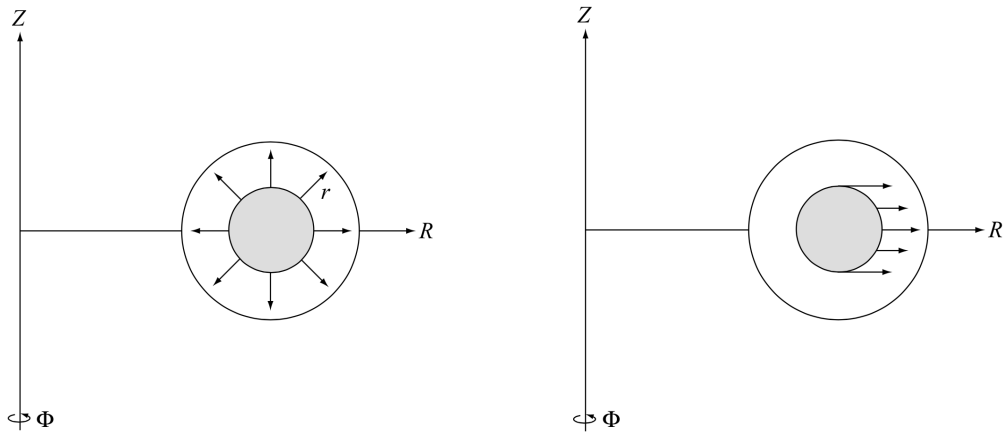

(a) Radial expansion forces created by expansion of the hot gas [84] p. 260.

(b) Othward expansion forces due to the toroidal geometry of tokamaks [84] p. 260.

Figure 3.2: Expansion forces in tokamaks.

expansion of a hot gas. Outward forces come from the toroidal geometry of tokamaks. They tend to expand the plasma ring outwards to increase the major radius. Here, stabilising of these forces will be separately discussed.

Radial expansion forces

If a toroid is cut in poloidal plain and narrowed to the cylinder, Z-pinch (Fig. 3.3a) or θ-pinch (Fig. 3.3b) can be created. Radial expansion forces are in balance for

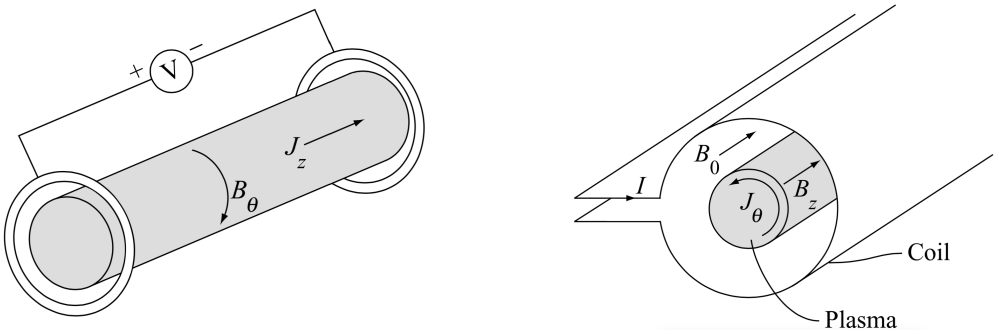

(a) Z-pinch [84] p. 266.

(b) θ-pinch [84] p. 265.

Figure 3.3: Cylindrical plasma configurations.

Z-pinches, if we consider expansion of the hot gas against the plasma pressure gradient p according to equation:

$$\nabla p = \overrightarrow{J_z} \times \overrightarrow{B_\theta} \tag{3.14}$$

As we can see inward force $\overrightarrow{J_z} \times \overrightarrow{B_\theta}$ pushes plasma to the centre of cylinder. This inward force in tokamak is created by plasma current. Same way oriented inward force is also produce in θ-pinches:

$$\nabla p = \overrightarrow{J_\theta} \times (\overrightarrow{B_0} + \overrightarrow{B_z}) \tag{3.15}$$

Magnetic field B_0 corresponds to toroidal magnetic field B_T in tokamak. These two forces are combined in so called screw pinch which is valid for tokamaks.

As was shown, radial expansion forces can be balanced with toroidal or poloidal magnetic field. Cylinder configurations like θ-pinches or Z-pinches suffer from end losses. However, toroidally bent plasma in toroidal configured devices avoid these losses.

Outward expansion forces

Bending a straight cylinder into a torus generates three new outward forces directed outwardly alongside of the major radius R (see: Fig. 3.2b). These three forces are *the hoop force*, *the tire tube force* and *the* $1/R$ *force*.

The hoop force comes from toroidally bent plasma current which is analogous to outwards expansion force of current flowing in a circular loop of wire. If the loop is split into the small elements, then current on the each element of the loop flows in opposite direction in the opposite element. This creates repulsive hoop force. It can be explained also this way: magnetic field B_1 created by plasma current I_p on inner side of the loop is stronger than magnetic field B_2 on the outer side due to toroid configuration (see Fig. 3.4). Therefore, force $\frac{B_1^2}{2\mu_0} S_1 > \frac{B_2^2}{2\mu_0} S_2$ which

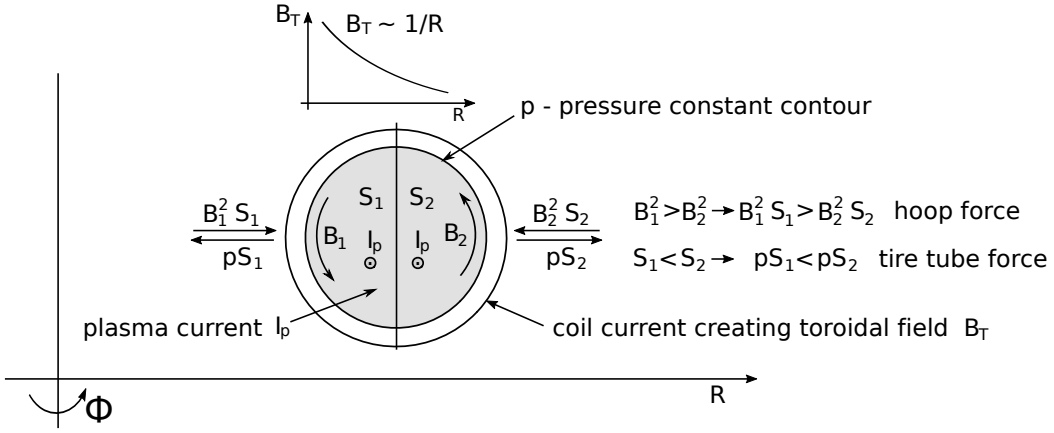

Figure 3.4: Outward forces cause by hoop force and tire tube force, and $1/R$ force

creates force expanding the ring to outside.

The tire tube force is named according to a tire filled with air. Air creates constant pressure on the tire surface. Force from air pressure is similar to plasma pressure and is given by $F = pS$ but outer side of tire respectively vessel has bigger surface S_2 than inner side S_1, therefore $pS_2 > pS_1$ which creates outward force.

Lastly mentioned $1/R$ *force* is due to toroidal magnetic field B_T, which decreases as $1/R$. This outward force is created similar way as hoop force created by plasma current, because B_T is bigger on the inner side of the torus. These

three outwards forces are counteracted only with poloidal magnetic field. To keep outward forces balanced, helical magnetic field lines wrapping around the vessel are necessary. These helical magnetic fields lines are created with toroidal plasma current. Also external vertical field is applied to establish equilibrium.

The outward expansion forces are compensated with $\vec{B}_{\mathrm{EFPS}} \cdot I_{\mathrm{EFPS}} + \vec{B}_{\mathrm{FABV}} \cdot I_{\mathrm{FABV}}$ and so plasma is in equilibrium. Ratio between outward expansion forces and compensating forces determine the plasma horizontal position.

3.1.2 Plasma vertical stability

Variations of all poloidal forces with plasma vertical movement were computed together to obtain forces on which vertical plasma position depends on. All the forces (Eq. 3.10) vary quite linearly with vertical displacement and can be simplified into:

$$F_{\mathrm{z}}(z) = I_{\mathrm{p}} \cdot \left(F_{\mathrm{E}} I_{\mathrm{EFPS}} \cdot (z - z_{\mathrm{E}}^0) + F_{\mathrm{S}} I_{\mathrm{SFPS}} (z - z_{\mathrm{S}}^0) + F_{\mathrm{BR}} I_{\mathrm{BR}} \right), \tag{3.16}$$

where

$$z_{\mathrm{E}}^0 = 4\,\mathrm{mm}, \qquad z_{\mathrm{S}}^0 = -18\,\mathrm{mm}$$

$$F_{\mathrm{E}} = -31.3\,\mathrm{N\,m^{-1}\,kA^{-2}}, \quad F_{\mathrm{S}} = 71.4\,\mathrm{Nm^{-1}kA^{-2}}, \quad F_{\mathrm{BR}} = 7.5\,\mathrm{Nm^{-1}kA^{-2}}$$

Here the vertical force F_{z} acting on plasma is proportional to both plasma current and currents in the external poloidal coils. The EFPS field stabilises (due to its concave shape, corresponding to $F_{\mathrm{E}} < 0$), while SFPS destabilises because $F_{\mathrm{S}} > 0$). Contribution from all the other fields is negligible, as COMPASS tokamak has been designed. If plasma is at vertical position $z = z_{\mathrm{E}}^0$ then there is not vertical stabilising force created by I_{EFPS} analogous it is for shaping field if $z = z_{\mathrm{S}}^0$ there is not destabilising force. These different values come from geometry of the poloidal coils at COMPASS.

Motion of vertically shaped plasma can be expressed with equation:

$$m_{\mathrm{p}} \frac{\partial^2 z}{\partial t^2} = F_{\mathrm{z}}(z) - F_{\mathrm{stab}}, \tag{3.17}$$

where $m_{\mathrm{p}} = 2\pi^2 R a^2 m_{\mathrm{D}} \bar{n}_{\mathrm{D}} \approx 100\,\mu\mathrm{g}$ and F_{stab} is stabilising force generated in the tokamak vessel as the plasma moves and eddy currents are induced in the vessel. This force acts in opposite direction as plasma movement. This stabilising force is:

$$F_{\mathrm{stab}} = I_{\mathrm{v}} \frac{\partial M_{\mathrm{vp}}}{\partial z} I_{\mathrm{p}}, \tag{3.18}$$

where M_{vp} is mutual inductance between plasma current and the tokamak vessel and I_{v} is induced current in the vessel. To estimate induced vessel current, the vessel was divided into 30 virtual toroidal segments (loops) where the ports were not taken into account. Resistivity R of every segment i was calculated according to:

$$R_i = \frac{2\pi r_i \rho}{d} \frac{N}{L_{\mathrm{pol}}}, \tag{3.19}$$

where r_i is radius of i^{th} segment, $\rho = 1.29 \times 10^{-6}\,\Omega\,\mathrm{m}$ is resistivity of inconel, $d = 3\,\mathrm{mm}$ is vessel width, $N = 30$ is number of segments and $L_{\mathrm{pol}} = 1.98\,\mathrm{m}$

is length of the vessel in poloidal cross-section. Vessel was modelled in loops with 3 mm x 66 mm. Induced current was calculated in every segment, that each of these segments was divided in 22 segments, so each segment was thick 3 mm x 3 mm. Next approximation was that are not squared loops but loops with 3 mm diameter. Mutual inductances were calculated between each of these loops as well self-inductances of each of these loops. Then inductances were summed for each coil and averaged. Averaged values were used to calculated inductance between 30 segments. Detailed description is written in Kudlacek's master thesis [85]. The plasma-vessel mutual inductance was estimated as $L_{\mathrm{v}}^{\mathrm{p}} \approx 1\,\mu\mathrm{H\,m^{-1}}$. The vessel toroidal voltage is generated by plasma movement and can be written as:

$$U_{\mathrm{v}}^{\mathrm{p}} = I_{\mathrm{p}} \frac{\mathrm{d}L_{\mathrm{v}}^{\mathrm{p}}}{\mathrm{d}t} = I_{\mathrm{p}} \frac{\partial L_{\mathrm{v}}^{\mathrm{p}}}{\partial z} \frac{\mathrm{d}z}{\mathrm{d}t} \tag{3.20}$$

Same way as for plasma-vessel, mutual inductance between stabilising coils and vessel was calculated. For the total vessel current Ohm's law can be written as:

$$R_{\mathrm{v}} I_{\mathrm{v}} + L_{\mathrm{v}} \frac{\mathrm{d}I_{\mathrm{v}}}{\mathrm{d}t} = I_{\mathrm{p}} \frac{\partial L_{\mathrm{v}}^{p}}{\partial z} \frac{\mathrm{d}z}{\mathrm{d}t} + L_{\mathrm{v}}^{\mathrm{BR}} \frac{\mathrm{d}I_{\mathrm{BR}}}{\mathrm{d}t}, \tag{3.21}$$

where $L_{\mathrm{v}}^{\mathrm{BR}} \frac{\mathrm{d}I_{\mathrm{BR}}}{\mathrm{d}t}$ corresponds to the penetration of the external active stabilising radial field through the vessel. Computed value for inductances are:

$$R_{\mathrm{v}} = 1\,\mathrm{m\Omega}, \qquad L_{\mathrm{v}} = 1.5\,\mu\mathrm{H}, \qquad L_{\mathrm{v}}^{\mathrm{BR}} = 1.6\,\mu\mathrm{H} \tag{3.22}$$

Computer simulation performed for COMPASS by Dr. Horacek shows that with $I_{\mathrm{BR}} = 0$ (which corresponds to a plasma without conductive vessel) the plasma would hit vessel due to Vertical Displacement Event (VDE) [86] in 5 µs. Inside a conductive vessel of 3 mm thickness (providing a passive stabilization), the plasma would disappear in 500 µs. This is in good agreement with experimental result obtained here [87]. Therefore, plasma has to be further stabilised by fast modification of the BR current in the feedback vertical loop.

Current I_{BR} in stabilising coil has to be actively changed to stabilise vertical plasma movements:

$$I_{\mathrm{BR}} = \frac{U_{\mathrm{BR}}}{R_{\mathrm{BR}}} - \frac{L_{\mathrm{BR}}}{R_{\mathrm{BR}}} \frac{\mathrm{d}I_{\mathrm{BR}}}{\mathrm{d}t}, \tag{3.23}$$

where $R_{\mathrm{BR}} = 30\,\mathrm{m\Omega}$ and $L_{\mathrm{BR}} = 92\,\mu\mathrm{H}$. The maximum voltage delivered by FABR is $\pm 100\,\mathrm{V}$. The corresponding current rise is $\pm 1.1\,\mathrm{A/\mu s}$. Detail description of power supply is in Sec 3.3.

Desired BR-current in the model was obtained using the Proportional Integral (PI) controller (Eq. 1.2) according to equation:

$$I_{\mathrm{FABR}}^{\mathrm{req}} = P e_{\mathrm{z}}(t) + I \int_0^t e_{\mathrm{z}}(t) \mathrm{d}t, \tag{3.24}$$

where $e_{\mathrm{z}}(t)$ is difference between requested vertical position in model and vertical value obtained from model.

$$P = -2 \times 10^4\,\mathrm{A\,m^{-1}}, \qquad I = -1 \times 10^{-8}\,\mathrm{A\,m^{-1}\,s^{-1}} \tag{3.25}$$

These values were obtained for $I_{\mathrm{EFPS}} = 8\,\mathrm{kA}$, shaping field $I_{\mathrm{SFPS}} = 5\,\mathrm{kA}$ and plasma current $I_{\mathrm{p}} = 150\,\mathrm{kA}$.

Delay of the system was not included within this estimation.

3.2 Plasma Position Diagnostic

COMPASS is very well equipped with magnetic sensors. It has 16 Internal Partial Rogowski (IPR) coils and 16 External Partial Rogowski (EPR) at one toroidal position, 8 Flux Loop (FL) coils and 3 times 24 of Mirnov coils at three different toroidal positions. Effect of plasma current in different position and different type of shapes and profiles was computed for set of IPR coils, FL coils and Mirnov coils. Algorithm for plasma detection was obtained using IPR coils and FL coils and plasma current measurement.

Plasma current and FABV current measurement, are necessary for position control. Both are used in the control algorithms.

3.2.1 Plasma Diagnostic Model

Plasma current was simulated in the mesh of 50×50 current filaments to estimate effect of plasma current at the positions of diagnostic IPR, Mirnov and FL coils (Fig. 3.5). Plasma shape was computed in three different configurations to

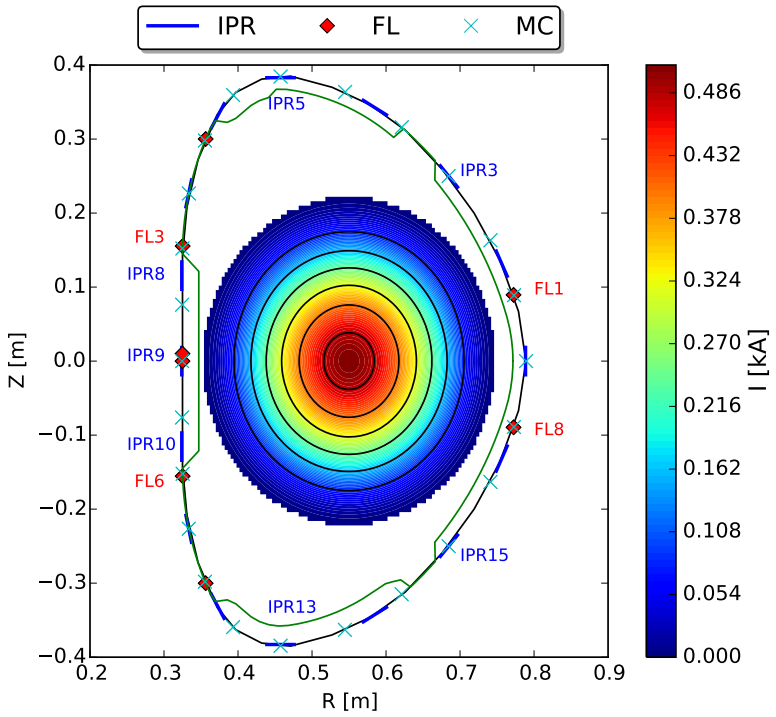

Figure 3.5: Schema of diagnostic model and IPR coils and Mirnov coils (MC), and flux loops (FL) at their location. Labelled IPR coils and FLs are used for estimation plasma position.

a larger database. The circular shape with $\kappa = 1.0$ and two elliptical shapes with elongation $\kappa = 1.5$ and 2.0. These shapes were chosen before Equilibrium and Reconstruction Fitting Code (EFIT) [88] at COMPASS was working. Real plasma elongation according to results from EFIT, when plasma is fully elongated, is $\kappa = 1.8$.

Plasma position was calculated in "limiter" and "divertor" configurations. In the "limiter" configuration plasma size was chosen always so big that was touching

the closest limiter.[1] In the divertor configuration, plasma size was modelled with three different minor radii a =16 m, 15 m and 14 m. If plasma current filaments exceeded the inner limiter radius in model, plasma shape was modelled smaller just to touch the limiter (similar as "limiter configuration").

Current profile for filaments in circular shape was assumed according to the following equation (see also [15] Chap. 2) when Shafranov shift [89] was not considered:

$$j(r) = j_0 \left(1 - \left(\frac{r}{a}\right)^2\right)^p, \tag{3.26}$$

where $j(r)$ is current profile at position r from plasma centre, j_0 is current in the plasma centre, a is minor radius and $p = 2$ and 3 is peaking factor. For elliptical plasma, Eq. 3.26 was adapted to:

$$j(r,\theta) = j_0 \left(1 - r^2 \frac{1 - \varepsilon \cos^2\theta}{b^2}\right)^p, \tag{3.27}$$

where θ is poloidal angle, ε is eccentricity given by $\varepsilon = \sqrt{1 - \frac{1}{\kappa^2}}$ and $\kappa = \frac{b}{a}$ is elongation. Current profile of 1 kA distributed current for elongation $\kappa = 2$, minor radius $a = 0.15$ m and peaking factor $p = 2$ is shown in Fig. 3.6. All

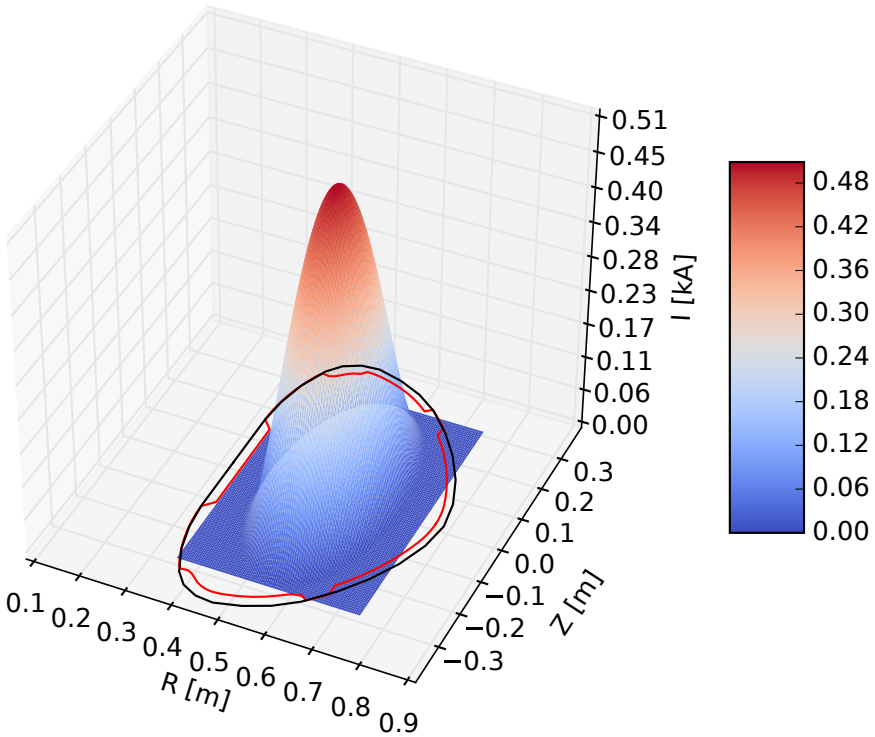

Figure 3.6: Plasma current profile with elongation $\kappa = 2$ and peaking factor $p = 2$, and position $R = 0.55$ m, $Z = 0$ m, minor radius $a = 0.15$ m

mentioned plasma current profiles were then normalised to 1 kA and moved with 1 mm steps in the area from 0.4 m to 0.7 m in radial direction and -0.25 m to 0.25 m in vertical direction with grid 300 X 500 points.

[1] Configuration either is of limiter or a divertor type. A non-divertor configuration that does not touch any limiter does not exist.

3.2.2 Calculating Magnetic Field in IPR coils

Magnetic field at all 16 IPR coils is calculated using Biot-Savart law 3.28 from every current filament for all plasma positions (see Fig. 3.5 and Fig. 3.7).

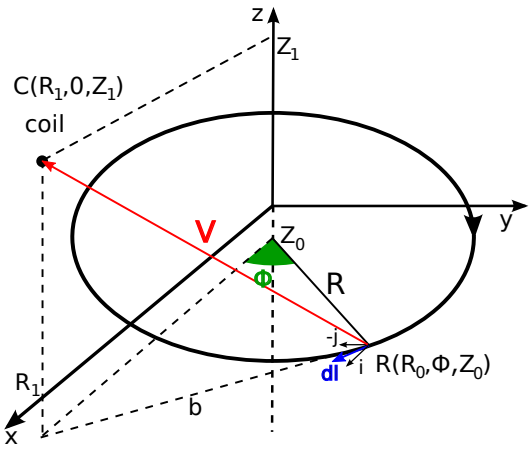

Figure 3.7: Biot-Savart schema.

Current I in thin wire of infinitesimal length $\vec{dl}$ in distance V from coil creates magnetic field in coil at position $C = (R_1, \phi = 0, Z_1)$ described by the Biot-Savart law:

$$\vec{B} = \frac{\mu_0 \cdot I}{4 \cdot \pi} \int_L \frac{\vec{dl} \times \vec{R}}{|V^3|}, \tag{3.28}$$

where $\mu_0 = 4\ \pi \times 10^{-7}\,\mathrm{T\,A^{-1}}$ is the permeability of free space and integration is over total length L of the wire.

Transforming cylindrical coordinates to cartesian (Fig. 3.7) gives position of point where $\vec{B}$ is computed. Position of wire element in cartesian will be:

$$\vec{R} = (R_0 \cos\phi, R_0 \sin\phi, Z_0), \tag{3.29}$$

where R_0 and Z_0 are thin wire coordinates toroidally symmetric around z-axis. Unit vector of wire element is given:

$$\vec{dl} = dl \cdot (-\sin\phi, \cos\phi, 0) = \frac{2\pi R_0}{N} \cdot (-\sin\phi, \cos\phi, 0)\,, \tag{3.30}$$

where N is number of division of the wire. Vector $\vec{R}$ is given as:

$$\vec{V} = \vec{C} - \vec{R} = (R_1 - R_0\cos\phi, -R_0\sin\phi, Z_1 - Z_0) \tag{3.31}$$

Distance between a thin wire element and a point for B calculation can be calculated according to the following equations:

$$\begin{aligned} b^2 &= R_0^2 + R_1^2 - 2R_0R_1\cos\phi \\ V^2 &= b^2 + (Z_1 - Z_0)^2 = R_0^2 + R_1^2 - R_0R_1\cos\phi + (Z_1 - Z_0)^2 \\ |V| &= \sqrt{R_1^2 + R_0^2 - 2R_1R_0\cos\phi\ + (Z_1 - Z_0)^2} \end{aligned} \tag{3.32}$$

Cross product between unit vector of wire element $\vec{dl}$ Eq. 3.30 and vector $\vec{R}$ Eq. 3.31 is placed together with distance between them Eq. 3.32 to Biot-Savart law Eq. 3.28. Then magnetic poloidal $\vec{B}$ field in $[B_{\mathrm{R}}, B_{\mathrm{Z}}]$ in cartesian coordinates can be computed numerically:

$$B_{\mathrm{R}} = \frac{\mu_0 I dl}{4\pi} \cdot (Z_1 - Z_0) \cdot \sum_{i=0}^{N-1} \frac{\cos\phi_i}{|V^3|} \tag{3.33}$$

$$B_{\mathrm{Z}} = \frac{\mu_0 I dl}{4\pi} \cdot \sum_{i=0}^{N-1} \frac{R_0 - R_1 \cos\phi_i}{|V^3|} \tag{3.34}$$

where $\phi_i = \dfrac{2\pi i}{N}$ and N is number of samples of the wire with total length L with current I and radius R. The resulting matrix of calculated magnetic field from all plasma current filaments at all plasma positions at coils IPR #9 is at left side of Fig. 3.8 .

3.2.3 Calculating Poloidal Flux in Flux Loop Coils

Plasma position can be estimated also using FL coils and for that purpose poloidal flux has to be calculated. Poloidal flux ψ in every FL coil was calculated with mutual inductance $L_{m,n}$ between current filaments (Sec. 3.2.1) and FL coils (Eq. 3.35):

$$L_{m,n} = \frac{\mu_0}{4\pi} \oint_{C_m} \oint_{C_n} \frac{\overrightarrow{dx_m} \cdot \overrightarrow{dx_n}}{|\overrightarrow{x_m} - \overrightarrow{x_n}|}, \tag{3.35}$$

where $\overrightarrow{dx_m}$, $\overrightarrow{dx_n}$ are unit tangential vectors of wires and FL and $|\overrightarrow{x_m} - \overrightarrow{x_n}|$ is distance between them.

$$\psi = \int_R \int_Z j(R,Z) L_{m,n}(R,Z) \mathrm{d}R\mathrm{d}Z, \tag{3.36}$$

where j is toroidal plasma current density, $L_{m,n}$ is the mutual inductance between the plasma filament and the flux loop. the product of the mutual inductance and the toroidal current density is integrated over the area inside the separatrix. The result for FL #5 is shown at the right side of Fig. 3.8. Centre of the vessel is labelled with black diamond.

3.2.4 Estimation of Vertical and Horizontal Position Using IPR coils

Left side of Fig. 3.8 show sensitivity of IPR #9 coil to magnetic field. Sensitivity is localised around the coil. Therefore, set of IPR coils to obtain better results in estimation of plasma position in horizontal or vertical position were chosen.

It is worth combining specific IPR coils such that the horizontal position becomes independent from vertical position as much as possible. We found such a combination as:

$$B_{\mathrm{hor}} = 3 \cdot \mathrm{IPR}_5 + \mathrm{IPR}_3 - 3 \cdot \mathrm{IPR}_{13} - \mathrm{IPR}_{15}. \tag{3.37}$$

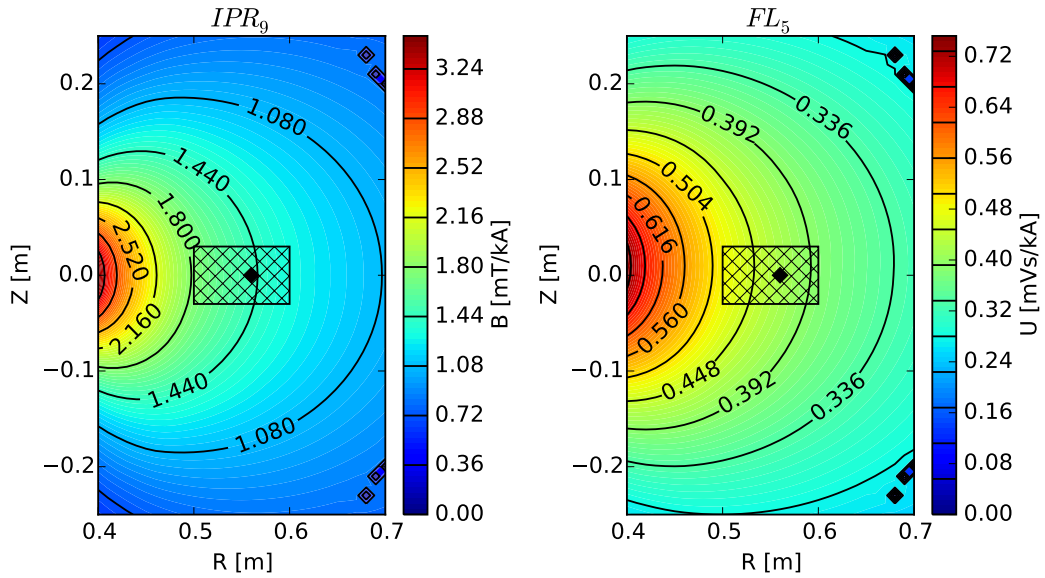

Figure 3.8: Left: Signal from plasma current filaments calculated at position of coil IPR #9. Right: Signal from plasma current filaments calculated at position of FL #5. Plasma centre is marked with black diamond mark. Calculation was done with parameters $a = 0.15\,\mathrm{m}$, elongation $\kappa = 1.5$ and peaking factor $p = 3$.

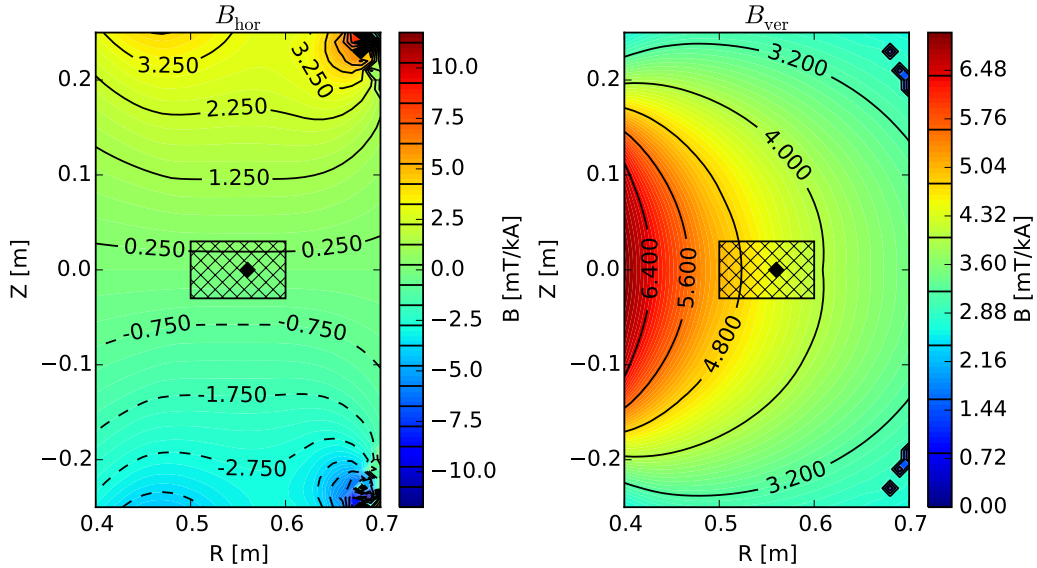

Figure 3.9: Magnetic fields calculated to estimate plasma position. Field is normalised to centre of plasma column $R, Z = [0.56\,\mathrm{m}, 0\,\mathrm{m}]$. Left: vertical position according to 3.37. Right: horizontal position according to 3.38

Such signal mostly sensitive on plasma vertical movements is shown at left side of Fig. 3.9).

Another set of IPR coils creates mostly vertical magnetic field B_{ver} signal which is changing mostly in horizontal direction:

$$B_{\mathrm{ver}} = 1.2 \cdot \mathrm{IPR}_8 + \mathrm{IPR}_9 + 1.2\mathrm{IPR}_{10} \tag{3.38}$$

Signal created with this equation is shown at right side of right Fig. 3.9. This

signal is sensitive in horizontal movement of plasma current.

Equations 3.37 and 3.38 are calculated as $B_{\mathrm{hor}}(R,Z)$ and $B_{\mathrm{ver}}(R,Z)$, where R and Z are parameters describing plasma centre. For real-time calculation these equations are transformed to look-up tables (plotted at Fig. 3.10) $R(B_{\mathrm{hor}},B_{\mathrm{ver}})$ and $Z(B_{\mathrm{hor}},B_{\mathrm{ver}})$ in this way.

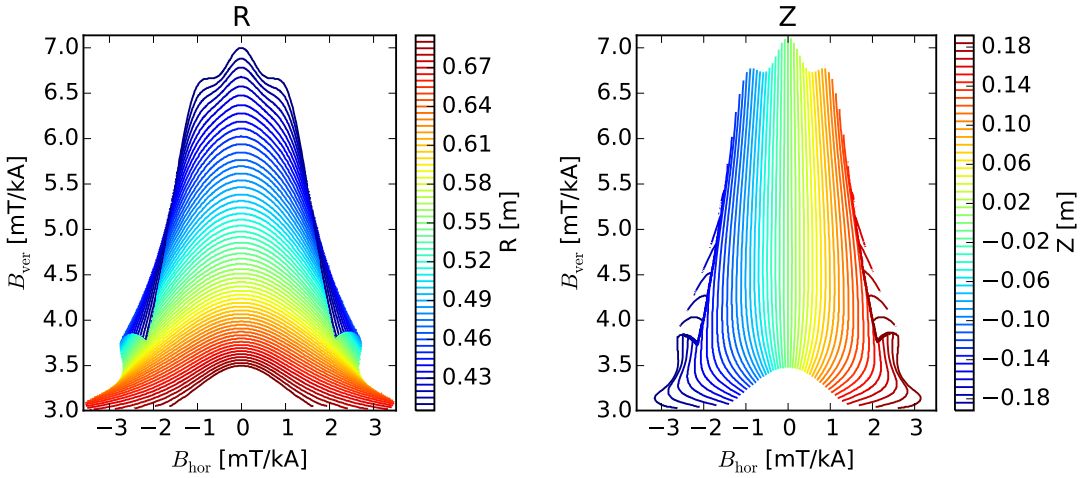

(a) Look up table for radial position from IPR coils

(b) Look up table for vertical position from IPR coils

Figure 3.10: R and Z position stored in the look up tables

Both matrices $B_{\mathrm{hor}}(R,Z)$ and $B_{\mathrm{ver}}(R,Z)$ were reduced only to region inside the vessel. Maximum and minimum for every matrix was found. In the loop for 500 levels between maximum and minimum of matrix $B_{\mathrm{hor}}(R,Z)$ is in new matrix $Aux_1(\mathrm{R},\mathrm{Z})$ marked a line with 1 at place where plasma can exists. The same way matrix $Aux_2(\mathrm{R},\mathrm{Z})$ is created for $B_{\mathrm{ver}}(R,Z)$. Both matrices have resolution 1 mm. Line in matrix $Aux_1(\mathrm{R},\mathrm{Z})$ has to be thicker to ensure cross-section with $Aux_2(\mathrm{R},\mathrm{Z})$. Therefore, ones are filled at one index to the left side and to the right side from existing line (in R index). Small groups (clouds) of ones at cross-section of both lines appear once are matrices multiplied in single elements (not matrix multiplication). These clouds show possible plasma position. Position of the two furthest ones in surrounding $\epsilon \approx 1$ mm is averaged. This way one or two possible position of plasma can be obtained for chosen $B_{\mathrm{hor}}(R,Z)$ and $B_{\mathrm{ver}}(R,Z)$. Then one element of $R_1(B_{\mathrm{hor}},B_{\mathrm{ver}})$ and $R_2(B_{\mathrm{hor}},B_{\mathrm{ver}})$, $Z_1(B_{\mathrm{hor}},B_{\mathrm{ver}})$ and $Z_2(B_{\mathrm{hor}},B_{\mathrm{ver}})$ can be filled in look-up table. From experiments we received that for every plasma position $R_1(B_{\mathrm{hor}},B_{\mathrm{ver}}) = R_2(B_{\mathrm{hor}},B_{\mathrm{ver}})$ and $Z_1(B_{\mathrm{hor}},B_{\mathrm{ver}}) = Z_2(B_{\mathrm{hor}},B_{\mathrm{ver}})$.

These look-up tables are essential for real-time plasma position control (see Sec. 3.4) and were used in experiments up to shot #5668 when this plasma position determination algorithm was replaced by the algorithm using flux loops coils according to Eq. 3.39 (see Sec. 3.2.5).

Comparison of the left and the right side of Fig. 3.9 shows that error in estimation of horizontal position is bigger than vertical position. Centre of plasma column is labelled with black diamond. One can notice B_{ver} around centre is not as straight as for B_{hor}. Therefore, better and more precise estimation has been developed[2]. Comparing results between Fig. 3.8 show flux loops are more suitable

[2]difference in control of plasma using IPR or FL are described in Sec. 3.4.1

for estimation of plasma position because they are not so localised around the coil which is explained in detail in the master thesis [85].

3.2.5 Estimation of Horizontal Position Using Flux Loop coils

Set of FL coils to estimate horizontal position was chosen same way as set of IPR for horizontal respectively vertical position[3]. The position of flux loops is in Fig. 3.5. Combination of FL S_{FL} sensitive dominantly in movement of plasma current in horizontal direction is according to the following equation:

$$S_{\mathrm{FL}} = \left(2.5 \cdot (\mathrm{FL}_3 + \mathrm{FL}_6) - (\mathrm{FL}_1 + \mathrm{FL}_8)\right), \tag{3.39}$$

Result is at right side of Fig. 3.11. Comparing the left and the right side of the fig-

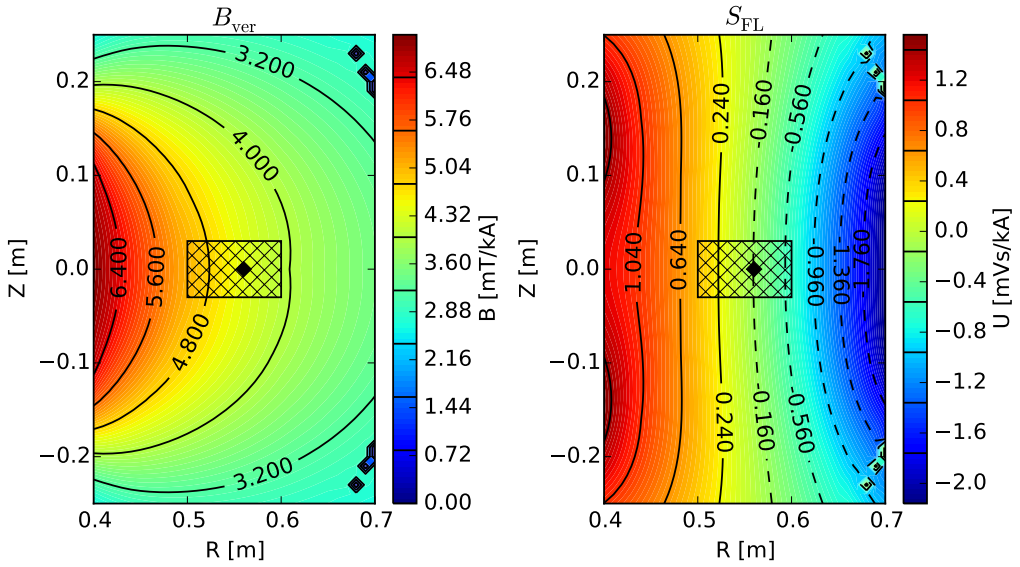

Figure 3.11: Left: Magnetic field calculated according to Eq. 3.37 to estimate vertical position of the plasma centre. Right: Magnetic field calculated according to Eq. 3.39 to estimate horizontal position of the plasma centre. The central rectangle corresponds to region of typical plasma centre positions; outside this region, the plasma becomes very small (limited by the vessel) that it becomes unstable. The left frame uses IPR coils; the magnetic field gradient in the right frame (using FL) is visibly much more homogeneous in space which implicates uniform (thus better) resolution of the plasma position.

ure one can notice that magnetic field lines around the vessel centre ($R = 0.56\,\mathrm{m}$) are narrower for FL combination (right) than for IPR combination (left). Therefore, combination according to Eq. 3.39 is better and more suitable to estimate radial position of plasma column.

Fig. 3.12 displays results in estimation of horizontal plasma position for all twelve combination (plasma current profile, radius, limiter/divertor configuration and elongation mentioned in Sec. 3.2.1). Left figure shows error of 31 mm between

[3]Work described in this section was done by Ondrej Kudlacek in his master thesis [85]. Here it is written because this part is then implemented in real-time by author of this thesis.

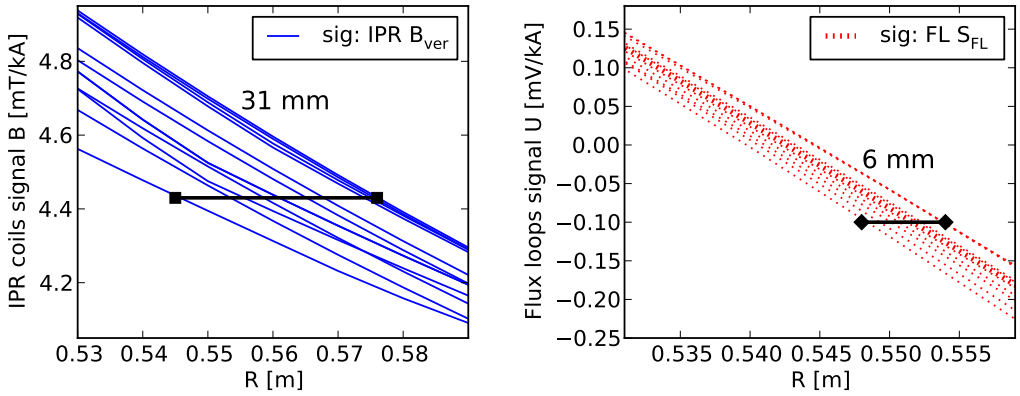

Figure 3.12: Left: sensitivity to movement in horizontal direction with algorithm using IPR coils according to Eq. 3.38. Right: sensitivity to movement in horizontal direction for estimating position using flux loops with Eq. 3.39. Different lines show different plasma scenarios like peaking profile, elongation, limiter, divertor configuration and plasma size. Different x-axis on left and right plot are to cover real values of plasma horizontal position during plasma discharge (see Fig. 3.15).

different configuration when IPR coils are used according to Eq. 3.38. Right figure shows error 6 mm when flux loops are used according to Eq. 3.39. Therefore, FL coils have been used since shot #5668. Error in estimation of horizontal position has been decreased by a factor of 5. When IPR coils for horizontal position was used, operators had to adapt plasma position according to EFIT post processed data to keep plasma position during the shaping process at the same position. This correction is not necessary anymore when FL coils are used. Differences between both algorithms in real-time and other benefits of using FL coils are described in Sec. 3.2.6.

3.2.6 Calculation of horizontal and vertical position in real-time

During start-up of MARTe, the look-up tables (i.e. Fig 3.10) for estimation of plasma position are read. At the beginning of each control loop cycle, data from magnetic diagnostics IPR, FL coils, loop voltage and poloidal currents from EFPS, SFPS, MFPS, FABV, FABR and plasma current are acquired with ATCAAdc GAM.

Acquired signals from magnetic pick-up coils are essentially $\mathrm{d}B/\mathrm{d}t$ and so must be integrated by analogue integrators. Therefore, drift and offset from every signal must be subtracted in the same way as it is done for the plasma current. The drift is calculated using linearisation method (based on signal at the beginning of the discharge) according to Eq. 2.7. Start and end of drift calculation is at 500 ms respectively 790 ms. Then, subtraction of the drift from the measured signal is performed according to Eq. 2.8; it starts at 900 ms and ends after plasma discharge at 2200 ms. List of signals and starting and ending time are written in MARTe configuration file and are loaded during MARTe startup.

After removing the drifts, the signals necessary for plasma position calculation are read in PlasmaPositionCalculationGAM. Calculation of the plasma position estimation is described in Sec. 3.2.5 and 3.2.4. In real experiments, IPR coils

and FL coils are sensitive also to the all other fields (magnetising, equilibrium, shaping etc). These pick-up signals from other fields have to be subtracted.

To remove pick-up signal from combination of IPR coils for horizontal (Eq. 3.37) and vertical position (Eq. 3.38), vacuum shot, where poloidal field was created by a sequence of different poloidal field coil currents, was done. Then these signals were fitted by hand to find proper constants for removing signals from poloidal fields typically as some constant c multiplied by current from some of the power supplies (e.g. $c_{\mathrm{E}} \cdot I_{\mathrm{EFPS}}$ for current from EFPS). As it can be seen in Fig. 3.13 for combination for B_{hor} for determining vertical position, different poloidal fields are visible with different amplitudes (blue line at top graph). While I_{MFPS} and I_{EFPS}

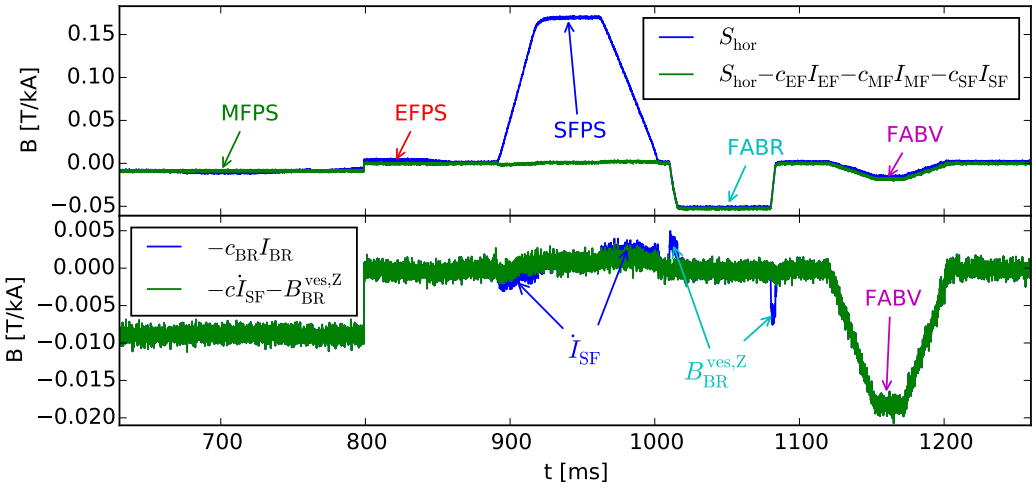

Figure 3.13: Top graph vacuum field measured according to Eq. 3.37 (blue line). Green line shows same combination of coils after the direct contributions of I_{MFPS} and I_{EFPS}, and I_{SFPS} have been subtracted. Bottom graph shows subtracting of derivative components and induced currents during fast changes of poloidal currents.

have small impact on these set of coils, I_{SFPS}, I_{FABR} and I_{FABV} have big influence. Green line shows when I_{MFPS} and I_{EFPS}, and I_{SFPS} are removed. Bottom graph shows that after removing these parts, still small peaks are visible. They are caused by magnetic signal from current induced in the vacuum vessel generated by fast changes of current in the circuits MF, EF, SF, BR, BV and Resonant Magnetic Perturbations (RMPs). It is beneficial to remove the signal from vacuum vessel current. A different levels of approximation can be used. In case of EFPS and SFPS subtracting of $\mathrm{d}I/\mathrm{d}t$ was deemed satisfactory. However, this is not sufficient for BR, BV and RMP because their current changes are faster. Therefore, solution of an equation for one inductive coil has to be subtracted according to Eq. 3.44.

For any current when derivative component has to be subtracted we will write:

$$\dot{I}_{\mathrm{source}} = \frac{I_{\mathrm{source}}(t_\tau) - I_{\mathrm{source}}(t_{\tau-1})}{\Delta t}, \tag{3.40}$$

where the **source** is any current created by an external current power supply (for example EFPS, FABR) and are shortened to EF and BR. The current driven by RMP power supplies are named as RMP1 and RMP2. Also these constants to

remove derivative component were fitted by hand and can be written as $c \cdot \dot{I}_{\text{source}}$. t_τ is the actual discharge time, $t_{\tau-1}$ is the time of the previous loop cycle and $\Delta t = t_\tau - t_{\tau-1} = 50\,\mu\text{s}$. $\dot{I}_{\text{source}} = \dfrac{\mathrm{d}I_{\text{source}}}{\mathrm{d}t}$ is derivation over one time step.

In the two specific cases, for current driven by EFPS and for SFPS, derivation over longer period was used for EFPS ($N_{\text{EF}} = 60$ samples which corresponds to 3 ms) and SFPS ($N_{\text{SF}} = 50$ samples which is 2.5 ms) according to the following equation:

$$\dot{I}_{\text{SF}} = \frac{I_{\text{SF}}(t_\tau) - I_{\text{SF}}(t_{\tau - N_{\text{SF}}-1})}{\Delta t \cdot (N_{\text{SF}} - 1)} \tag{3.41}$$

$$\dot{I}_{\text{EF}} = \frac{I_{\text{EF}}(t_\tau) - I_{\text{EF}}(t_{\tau - N_{\text{EF}}-1})}{\Delta t \cdot (N_{\text{EF}} - 1)}, \tag{3.42}$$

where $I_{\text{SF}}(t_\tau)$ and $I_{\text{EF}}(t_\tau)$ are currents from EFPS and SFPS power supplies at actual discharge time $t = \tau$ and $I_{\text{SF}}(t_{\tau - N_{\text{SF}}-1})$ and $I_{\text{EF}}(t_{\tau - N_{\text{EF}}-1})$ are currents 50 respectively 60 samples before. Number of samples can be configured with the configuration file.

For the rest of the power supplies (FABV, FABR, RMPs) approximation with $\mathrm{d}I/\mathrm{d}t$ is not precise enough. Therefore, when $c_{\text{source}} \cdot I_{\text{source}}$ are subtracted, induced currents in the vessel from the power supplies have to be subtracted. They are subtracted from combination of IPR coils according to following equations:

$$\begin{aligned} U^{\text{ves}} = I^{\text{ves}} R^{\text{ves}} &= -L\frac{\mathrm{d}I^{\text{ves}}}{\mathrm{d}t} - M\frac{\mathrm{d}I_{\text{source}}}{\mathrm{d}t} \rightarrow \\ &\rightarrow I^{\text{ves}} = -\tau^{\text{ves}}\frac{\mathrm{d}I^{\text{ves}}}{\mathrm{d}t} - \tau^{\text{mut}}\frac{\mathrm{d}I_{\text{source}}}{\mathrm{d}t} \\ &\rightarrow \tau^{\text{ves}}\frac{\mathrm{d}I^{\text{ves}}}{\mathrm{d}t} = -I^{\text{ves}} - \tau^{\text{mut}}\frac{\mathrm{d}I_{\text{source}}}{\mathrm{d}t} \\ &\rightarrow \mathrm{d}I^{\text{ves}} = \frac{1}{\tau^{\text{ves}}}\mathrm{d}t(-I^{\text{ves}} - \tau^{\text{mut}}\frac{\mathrm{d}I_{\text{source}}}{\mathrm{d}t}) \end{aligned} \tag{3.43}$$

in descretised form it can be rewritten as aa:

$$\rightarrow I^{\text{ves}} = \frac{1}{\tau^{\text{ves}}}\Delta t \sum_{t=0}^{t=T}(-I^{\text{ves}}(t) - \tau^{\text{mut}}\dot{I}_{\text{source}}). \tag{3.44}$$

However, magnetic sensors measure magnetic field created by this current, thus, multiplying this equation with constant converting induced current into magnetic field - c_1 it can be obtained:

$$\begin{aligned} B^{\text{ves}} &= c_1 \cdot \frac{1}{\tau^{\text{ves}}}\Delta t \sum_{t=0}^{t=T}(-I^{\text{ves}}(t) - \tau^{\text{mut}}\dot{I}_{\text{source}}) \\ &\rightarrow B^{\text{ves}} = \frac{1}{\tau'^{\text{ves}}}\Delta t \sum_{t=0}^{t=T}(-I^{\text{ves}}(t) + \tau'^{\text{mut}}\dot{I}_{\text{source}}), \end{aligned} \tag{3.45}$$

where in our case $\tau'^{\mathrm{mut}} = -\tau^{\mathrm{mut}}$.

$$B_{\mathrm{BR}}^{\mathrm{ves,Z}} = \frac{\Delta t}{\tau'^{\mathrm{ves}}_{\mathrm{BR}}} \sum_{t=0}^{t=T} \left(\tau'^{\mathrm{mut}}_{\mathrm{BR}} \dot{I}_{\mathrm{BR}} - I_{\mathrm{BR}}^{\mathrm{ves,Z}}(t) \right) \tag{3.46}$$

$$B_{\mathrm{BV}}^{\mathrm{ves,R}} = \frac{\Delta t}{\tau'^{\mathrm{ves}}_{\mathrm{BV}}} \sum_{t=0}^{t=T} \left(\tau'^{\mathrm{mut}}_{\mathrm{BV}} \dot{I}_{\mathrm{BV}} - I_{\mathrm{BV}}^{\mathrm{ves,R}}(t) \right) \tag{3.47}$$

$$B_{\mathrm{RMP1}}^{\mathrm{ves,Z}} = \frac{\Delta t}{\tau'^{\mathrm{ves,Z}}_{\mathrm{RMP1}}} \cdot \sum_{t=0}^{t=T} \left(\tau'^{\mathrm{mut,Z}}_{\mathrm{RMP1}} \dot{I}_{\mathrm{RMP1}} - I_{\mathrm{RMP1}}^{\mathrm{ves,Z}}(t) \right) \tag{3.48}$$

$$B_{\mathrm{RMP2}}^{\mathrm{ves,Z}} = \frac{\Delta t}{\tau'^{\mathrm{ves,Z}}_{\mathrm{RMP2}}} \cdot \sum_{t=0}^{t=T} \left(\tau'^{\mathrm{mut,Z}}_{\mathrm{RMP2}} \dot{I}_{\mathrm{RMP2}} - I_{\mathrm{RMP2}}^{\mathrm{ves,Z}}(t) \right) \tag{3.49}$$

$$B_{\mathrm{RMP1}}^{\mathrm{ves,R}} = \frac{\Delta t}{\tau'^{\mathrm{ves,R}}_{\mathrm{RMP1}}} \cdot \sum_{t=0}^{t=T} \left(\tau'^{\mathrm{mut,R}}_{\mathrm{RMP1}} \dot{I}_{\mathrm{RMP1}} - I_{\mathrm{RMP1}}^{\mathrm{ves,R}}(t) \right) \tag{3.50}$$

$$B_{\mathrm{RMP2}}^{\mathrm{ves,R}} = \frac{\Delta t}{\tau'^{\mathrm{ves,R}}_{\mathrm{RMP2}}} \cdot \sum_{t=0}^{t=T} \left(\tau'^{\mathrm{mut,R}}_{\mathrm{RMP2}} \dot{I}_{\mathrm{RMP2}} - I_{\mathrm{RMP2}}^{\mathrm{ves,R}}(t) \right), \tag{3.51}$$

where $\tau'^{\mathrm{mut}}_{\mathrm{source}}$ are the fitted constants which represent how the current from the 'source' is induced in combination of set of IPR coils, including the sign. It is not only the vessel time constant between the vessel and the source but it also includes conversion from current to magnetic field in the set of the coils. The vessel time constant for the current source is named as $\tau'^{\mathrm{ves}}_{\mathrm{source}}$. The number behind index RMP shows which source is used and upper index R and Z tells in which direction of position estimation the RMP coils have effect (R for horizontal and Z for vertical). If the configuration of RMP coils is changed, the constants for RMP coils can be rewritten in the MARTe configuration file and there is no need to recompile the source code. The values of these constants are listed in Tab. 3.1

$\tau'^{\mathrm{mut}}_{\mathrm{BR}}$	$\tau'^{\mathrm{mut}}_{\mathrm{BV}}$	$\tau'^{\mathrm{ves}}_{\mathrm{BR}}$	$\tau'^{\mathrm{ves}}_{\mathrm{BV}}$	$\tau'^{\mathrm{mut,R,Z}}_{\mathrm{RMP1,2}}$	$\tau'^{\mathrm{ves,R,Z}}_{\mathrm{RMP1,2}}$
0.006	-0.003	0.5	0.5	0	1

Table 3.1: Fitted constants for subtracting induced currents from RMPs and FABR, and FABV power supplies. All constants $\tau'^{\mathrm{ves,mut,R,Z}}_{\mathrm{RMP1,2}}$ are set up the way that all $B_{\mathrm{RMP1,2}}^{\mathrm{ves,R,Z}} = 0$. Fitted constants for RMPs are for one specific configuration. Another configurations have different constants.

When all derivative components and induced currents in vessel are calculated,

subtraction of them for vertical position is done according to:

$$\begin{aligned}
B_{\mathrm{hor}} &= \frac{1}{I_{\mathrm{p}}} \cdot \left(B_{\mathrm{hor}}^{\mathrm{meas}} - B_{\mathrm{hor}}^{\mathrm{pick-up}} \right) = \\
&= \frac{1}{I_{\mathrm{p}}} \cdot (3 \cdot IPR_5 + IPR_3 + 3 \cdot IPR_{13}/1.09 + IPR_{15} + \\
&+ 0.000429 \cdot I_{\mathrm{MFPS}} - 0.00015 \cdot U_{\mathrm{loop}} - 0.000677 \cdot I_{\mathrm{EFPS}} - \\
&- 0.0004465 \cdot I_{\mathrm{BV}} - 0.18/4.9 \cdot I_{\mathrm{SFPS}} \cdot 0.938 + \\
&+ 0.018190403/1.212285 \cdot 1.14 \cdot B_{\mathrm{BR}} - B_{\mathrm{BR}}^{\mathrm{ves,Z}} + \\
&+ 0.0006 \cdot \dot{I}_{\mathrm{SF}} - C_{\mathrm{RMP1}}^{\mathrm{Z}} \cdot I_{\mathrm{RMP1}} - \\
&- C_{\mathrm{RMP2}}^{\mathrm{Z}} \cdot I_{\mathrm{RMP2}} - B_{\mathrm{RMP1}}^{\mathrm{ves,Z}} - B_{\mathrm{RMP2}}^{\mathrm{ves,Z}}),
\end{aligned} \tag{3.52}$$

where $B_{\mathrm{hor}}^{\mathrm{meas}}$ is signal measured by combination of coil Eq. 3.37 and $B_{\mathrm{hor}}^{\mathrm{pick-up}}$ is a signal from the other poloidal fields measured by this set of coils. Multiplying constants are fitted constants from vacuum shot (see Fig. 3.13). Constant 1.09 comes from later recalibration of IPR coils.

With same analogy, the signal for the horizontal position using IPR coils can be obtained as:

$$\begin{aligned}
B_{\mathrm{ver}} &= \frac{1}{I_{\mathrm{p}}} \cdot \left(B_{\mathrm{ver}}^{\mathrm{meas}} - B_{\mathrm{ver}}^{\mathrm{pick-up}} \right) = \\
&= \frac{1}{I_{\mathrm{p}}} \cdot (1.2 \cdot IPR_8 + IPR_9 + 1.2 \cdot IPR_{10} + \\
&+ \frac{(0.0204 + 0.0473 + 0.0204) \cdot 2.5}{1000} \cdot I_{\mathrm{MFPS}} - \\
&- \frac{(1.2 \cdot 12.63 + 12.45 + 1.2 \cdot 12.63) \cdot 1.036}{1000} \cdot I_{\mathrm{EFPS}} - \\
&- 0.004876 \cdot I_{\mathrm{BV}} + 0.285/4.9 \cdot I_{\mathrm{SFPS}} \cdot 1.012 + \\
&+ 0 \cdot I_{\mathrm{BR}} - B_{\mathrm{BV}}^{\mathrm{ves,R}} + 0.0051 \cdot U_{\mathrm{loop}} - \\
&- 0.034 \cdot \dot{I}_{\mathrm{SF}} + 0.031 \cdot \dot{I}_{\mathrm{EF}} - C_{\mathrm{RMP1}}^{\mathrm{R}} \cdot I_{\mathrm{RMP1}} - \\
&- C_{\mathrm{RMP2}}^{\mathrm{R}} \cdot I_{\mathrm{RMP2}} - B_{\mathrm{RMP1}}^{\mathrm{ves,R}} - B_{\mathrm{RMP2}}^{\mathrm{ves,R}}),
\end{aligned} \tag{3.53}$$

where $B_{\mathrm{ver}}^{\mathrm{meas}}$ is signal measured by combination of coil Eq. 3.38 and $B_{\mathrm{ver}}^{\mathrm{pick-up}}$ is picked up signal from poloidal fields. For the actual configuration of the RMP coils, the constants $C_{\mathrm{RMP1,2}}^{\mathrm{R,Z}} = 0$. B_{hor} and B_{ver} are normalised to plasma current I_{p} . Equations 3.52 and 3.53are written in detail exactly as in the C++ code actually used on COMPASS. Somehow complicated multiplications are here kept for historical reasons when calibration constants were progressively changed and backwards compatibility and also history are preserved this way. Also anyone who is reading C++ source code can see evolution in calibration constants and compared them with the COMPASS DataBase (CDB) [90] and the COMPASS logbook.

For finding position R and Z, cross-section between S_{hor} and S_{ver} has to be found in the look-up tables (Fig 3.10). To find the plasma position as exactly as possible, bilinear fitting (Fig. 3.14) method is used. Firstly, interpolation in x domain is calculated. This yields to:

$$\begin{aligned}
R_1 = f(x, y_1) &\approx \frac{x_2 - x}{x_2 - x_1} f(Q_{11}) + \frac{x - x_1}{x_2 - x_1} f(Q_{12}) \\
R_2 = f(x, y_2) &\approx \frac{x_2 - x}{x_2 - x_1} f(Q_{21}) + \frac{x - x_1}{x_2 - x_1} f(Q_{22})
\end{aligned} \tag{3.54}$$

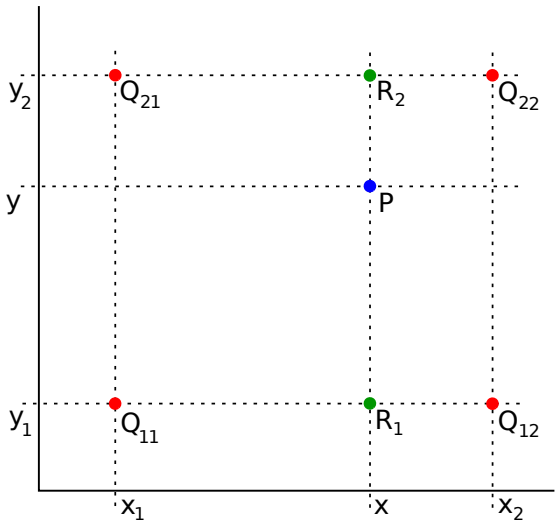

Figure 3.14: Schema of bilinear interpolation used for determination of the plasma position [91].

Then same way in y-direction

$$
\begin{aligned}
P = f(x,y) &\approx \frac{y_2 - y}{y_2 - y_1} f(x, y_1) + \frac{y - y_1}{y_2 - y_1} f(x, y_2) \\
&\approx \frac{y_2 - y}{y_2 - y_1} \left(\frac{x_2 - x}{x_2 - x_1} f(Q_{11}) + \frac{x - x_1}{x_2 - x_1} f(Q_{12}) \right) + \\
&+ \frac{y - y_1}{y_2 - y_1} \left(\frac{x_2 - x}{x_2 - x_1} f(Q_{21}) + \frac{x - x_1}{x_2 - x_1} f(Q_{22}) \right) \qquad (3.55) \\
P = f(x,y) &= \frac{1}{(x_2 - x_2)(y_2 - y_1)} \Big(f(Q_{11})(x_2 - x)(y_2 - y_1) \quad + \\
&+ f(Q_{21})(x - x_1)(y_2 - y_1) + f(Q_{12})(x_2 - x)(y - y_1) \quad + \\
&+ f(Q_{22})(x - x_1)(y - y_1) \Big)
\end{aligned}
$$

In our case for determining horizontal position, magnetic field B_{hor} calculated according to Eq. 3.52 (x-axis) and magnetic field B_{ver} calculated according to Eq. 3.53 (y-axis) represent point P from Fig. 3.14 in our look-up table in Fig. 3.10a. Then x and y are converted to indexes of matrix. x_1 and y_1 are the largest values less than or equal to calculated x, respectively y as indexes from corresponding matrix. x_2 and y_2 are the smallest values equal or bigger than x respectively y. Then Q_{mn} are values from look-up table (Fig. 3.10a) corresponding to indexed from $x_{1,2}$ and $y_{1,2}$. This way R-position is obtained. Same way only using look-up table for vertical position (Fig. 3.10b), vertical position Z is obtained.

This way calculated plasma position has systematic error in calculating horizontal position during shaping. Plasma shape in COMPASS, is determined as ratio between shaping current I_{SFPS} and plasma current I_{p} (see Chap. 4). Therefore, plasma position was adapted according to EFIT with operators before each shot. Difference, between EFIT reconstruction and real-time methods, in plasma position estimation during shaping can be seen in Fig. 3.15. Deviation in

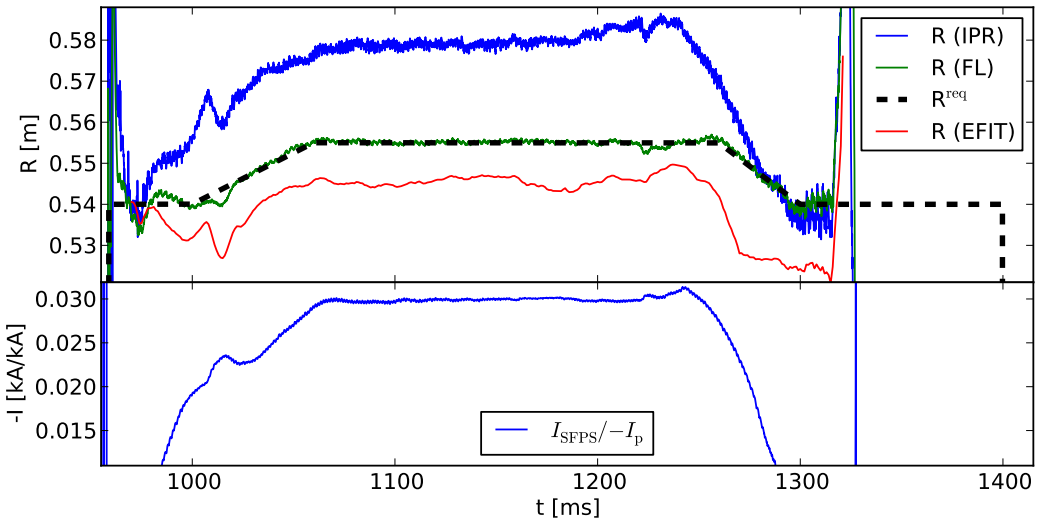

Figure 3.15: Top: Comparison of horizontal position calculation between IPR coils and FL coils and EFIT. Requested position is labelled as R^{req}. Bottom: Ratio between I_{SFPS} and I_p determining plasma shape, influences horizontal position using mainly IPR coils, calculated according to equation Eq. 3.38.

estimation of horizontal position using IPR coils (top graph: blue line) is changing at the end of the flat-top phase (approximately after 1220 ms) because ratio I_{SFPS}/I_p is changing. This deviation with position estimation using set of IPR coils was reduced when IPR coils for estimation of horizontal plasma position were replaced by the algorithm using the flux loops. Horizontal position using FL coils (green line) is constant during this phase. There is some offset between EFIT (red colour) and algorithm using FL during the entire discharge. Reason behind can be that real-time algorithm used at COMPASS does not include Shafranov shift [89] and real-time method is based on simple diagnostic model.

To calculate horizontal position using flux loops external fields have to be subtracted. Subtraction of all the external field including its' derivations is done with the same way as for IPR coils.

$$\begin{aligned} U'_{FL1} = U^{pick-up}_{FL1} - (&0.022033 \cdot I_{MFPS} + 0.00963528 \cdot I_{EFPS} + \\ &+ 0.0100927 \cdot I_{SFPS} - 0.000794556 \cdot I_{BR} + \\ &+ 0.0036218 \cdot I_{BV} + C_{RMP1} \cdot I_{RMP1} + C_{RMP2} \cdot I_{RMP2}) \end{aligned} \tag{3.56a}$$

$$\begin{aligned} U'_{FL3} = U^{pick-up}_{FL3} - (&0.0220654 \cdot I_{MFPS} - 0.00653242 \cdot I_{EFPS} + \\ &+ 0.0117974 \cdot I_{SFPS} - 0.000426559 \cdot I_{BR} + \\ &+ 0.000316906 \cdot I_{BV} + C_{RMP1} \cdot I_{RMP1} + C_{RMP2} \cdot I_{RMP2}) \end{aligned} \tag{3.56b}$$

$$\begin{aligned} U'_{FL6} = U^{pick-up}_{FL6} - (&0.0218689 \cdot I_{MFPS} - 0.00648446 \cdot I_{EFPS} + \\ &+ 0.0115928 \cdot I_{SFPS} + 0.000447446 \cdot I_{BR} + \\ &+ 0.000330135 \cdot I_{BV} + C_{RMP1} \cdot I_{RMP1} + C_{RMP2} \cdot I_{RMP2}) \end{aligned} \tag{3.56c}$$

$$\begin{aligned} U'_{FL6} = U^{pick-up}_{FL6} - (&0.0221238 \cdot I_{MFPS} + 0.00970142 \cdot I_{EFPS} + \\ &+ 0.0126111 \cdot I_{SFPS} + 0.000848655 \cdot I_{BR} + \\ &+ 0.00364527 \cdot I_{BV} + C_{RMP1} \cdot I_{RMP1} + C_{RMP2} \cdot I_{RMP2}), \end{aligned} \tag{3.56d}$$

where the multiplying constants $C_{RMP1,2} = 0$ for recent configuration of RMP coils. These constants are also configurable with MARTe configuration file. For

subtracting all external currents from flux loops, the mutual inductance between each flux loops and coil is calculated according to Eq. 3.43 in the discreate form (Eq. 3.44). The following constants are analogous of the constant c_1 from equation Eq. 3.45. Different is they convert measured signal to volts. Then for each flux loop the following equation can be written as:

$$\begin{aligned}
U^{\text{mut}}_{\text{FL1}} = \Delta t \cdot (&-0.97536 \sum_{t=0}^{t=T} I^{\text{ves}}_{\text{MF}}(t) + 0.0143663 \cdot \dot{I}_{\text{MF}} - \\
&- 0.30752 \cdot \sum_{t=0}^{S} t = T I^{\text{ves}}_{\text{EF}}(t) + 0.00369737 \cdot \dot{I}_{\text{EF}} - \\
&- 0.51888 \cdot \sum_{t=0}^{t=T} I^{\text{ves}}_{\text{SF}}(t) + 0.00765356 \cdot \dot{I}_{\text{SF}} - \\
&- 1.37599 \cdot \sum_{t=0}^{t=T} I^{\text{ves}}_{\text{BR}}(t) - 0.000545697 \cdot \dot{I}_{\text{BR}} - \\
&- 2.47999 \cdot \sum_{t=0}^{t=T} I^{\text{ves}}_{\text{BV}}(t) + 0.00320179 \cdot \dot{I}_{\text{BV}} - \\
&- C^{\text{ves}}_{\text{RMP1}} \cdot \sum_{t=0}^{t=T} I^{\text{ves}}_{\text{RMP1}}(t) + C^{\text{mut}}_{\text{RMP1}} \cdot \dot{I}_{\text{RMP1}} - \\
&- C^{\text{ves}}_{\text{RMP2}} \cdot \sum_{t=0}^{t=T} I^{\text{ves}}_{\text{RMP2}}(t) + C^{\text{mut}}_{\text{RMP2}} \cdot \dot{I}_{\text{RMP2}})
\end{aligned} \tag{3.57a}$$

$$\begin{aligned}
U^{\text{mut}}_{\text{FL3}} = \Delta t \cdot (&-1.96 \cdot \sum_{t=0}^{t=T} I^{\text{ves}}_{\text{MF}}(t) + 0.00389783 \cdot \dot{I}_{\text{MF}} - \\
&- 0.1152 \cdot \sum_{t=0}^{t=T} I^{\text{ves}}_{\text{EF}}(t) + 0.0006682 \cdot \dot{I}_{\text{EF}} - \\
&- 0.798999 \cdot \sum_{t=0}^{t=T} I^{\text{ves}}_{\text{SF}}(t) + 0.0080184 \cdot \dot{I}_{\text{SF}} - \\
&- 1.34399 \cdot \sum_{t=0}^{t=T} I^{\text{ves}}_{\text{BR}}(t) - 0.000384215 \cdot \dot{I}_{\text{BR}} - \\
&- 0.258 \cdot \sum_{t=0}^{t=T} I^{\text{ves}}_{\text{BV}}(t) - 0.000425978 \cdot \dot{I}_{\text{BV}} - \\
&- C^{\dot{\text{I}}}_{\text{RMP1}} \cdot \sum_{t=0}^{t=T} I^{\text{ves}}_{\text{RMP1}}(t) + C^{\text{mut}}_{\text{RMP1}} \cdot \dot{I}_{\text{RMP1}} - \\
&- C^{\dot{\text{I}}}_{\text{RMP2}} \cdot \sum_{t=0}^{t=T} I^{\text{ves}}_{\text{RMP2}}(t) + C^{\text{mut}}_{\text{RMP2}} \cdot \dot{I}_{\text{RMP2}})
\end{aligned} \tag{3.57b}$$

$$\begin{aligned}
U^{\text{mut}}_{\text{FL6}} = \Delta t \cdot (&-1.6919999 \cdot \sum_{t=0}^{t=T} I^{\text{ves}}_{\text{MF}}(t) + 0.00512287 \cdot \dot{I}_{\text{MF}} - \\
&- 0.0929999 \cdot \sum_{t=0}^{t=T} I^{\text{ves}}_{\text{EF}}(t) + 0.000409273 \cdot \dot{I}_{\text{EF}} - \\
&- 0.728 \cdot \sum_{t=0}^{t=T} I^{\text{ves}}_{\text{SF}}(t_i) + 0.0073502 \cdot \dot{I}_{\text{SF}} - \\
&- 0.5017599 \cdot \sum_{t=0}^{t=T} I^{\text{ves}}_{\text{BR}}(t_i) + 0.000215878 \cdot \dot{I}_{\text{BR}} - \\
&- 0.353999 \cdot \sum_{t=0}^{t=T} I^{\text{ves}}_{\text{BV}}(t_i) - 0.000517855 \cdot \dot{I}_{\text{BV}} - \\
&- C^{\text{ves}}_{\text{RMP1}} \cdot \sum_{t=0}^{t=T} I^{\text{ves}}_{\text{RMP1}}(t_i) + C^{\text{mut}}_{\text{RMP1}} \cdot \dot{I}_{\text{RMP1}} - \\
&- C^{\text{ves}}_{\text{RMP2}} \cdot \sum_{t=0}^{t=T} I^{\text{ves}}_{\text{RMP2}}(t_i) + C^{\text{mut}}_{\text{RMP2}} \cdot \dot{I}_{\text{RMP2}})
\end{aligned} \tag{3.57c}$$

$$
\begin{aligned}
U^{\mathrm{mut}}_{\mathrm{FL8}} = \Delta t \cdot (&-1.01504 \cdot \sum_{t=0}^{t=T} I^{\mathrm{ves}}_{\mathrm{MF}}(t) + 0.0143039 \cdot \dot{I}_{\mathrm{MF}} - \\
&- 0.30628 \cdot \sum_{t=0}^{t=T} I^{\mathrm{ves}}_{\mathrm{EF}}(t) + 0.00369559 \cdot \dot{I}_{\mathrm{EF}} - \\
&- 0.513884 \cdot \sum_{t=0}^{t=T} I^{\mathrm{ves}}_{\mathrm{SF}}(t) + 0.00740187 \cdot \dot{I}_{\mathrm{SF}} - \\
&- 0.687999 \cdot \sum_{t=0}^{t=T} I^{\mathrm{ves}}_{\mathrm{BR}}(t) - 0.000375863 \cdot \dot{I}_{\mathrm{BR}} - \\
&- 2.45599 \cdot \sum_{t=0}^{t=T} I^{\mathrm{ves}}_{\mathrm{BV}}(t) + 0.00310156 \cdot \dot{I}_{\mathrm{BV}} - \\
&- C^{\mathrm{ves}}_{\mathrm{RMP1}} \cdot \sum_{t=0}^{t=T} I^{\mathrm{ves}}_{\mathrm{RMP1}}(t) + C^{\mathrm{mut}}_{\mathrm{RMP1}} \cdot \dot{I}_{\mathrm{RMP1}} - \\
&- C^{\mathrm{ves}}_{\mathrm{RMP2}} \cdot \sum_{t=0}^{t=T} I^{\mathrm{ves}}_{\mathrm{RMP2}}(t) + C^{\mathrm{mut}}_{\mathrm{RMP2}} \cdot \dot{I}_{\mathrm{RMP2}}),
\end{aligned}
\tag{3.57d}
$$

where again $C^{\mathrm{ves}}_{\mathrm{RMP1,2}} = C^{\mathrm{mut}}_{\mathrm{RMP1,2}} = 0$ for current setup and $I_{\mathrm{mut}}(FL_{1,3,6,8})$ are mutual inductances between flux loops coils and poloidal coils. Signal only from plasma current measured with flux loops can be get combining Eq. 3.56 and Eq. 3.57.

$$U_{\mathrm{FL1}} = U'_{\mathrm{FL1}} - U^{\mathrm{mut}}_{\mathrm{FL1}} \tag{3.58a}$$

$$U_{\mathrm{FL3}} = U'_{\mathrm{FL3}} - U^{\mathrm{mut}}_{\mathrm{FL3}} \tag{3.58b}$$

$$U_{\mathrm{FL6}} = U'_{\mathrm{FL6}} - U^{\mathrm{mut}}_{\mathrm{FL6}} \tag{3.58c}$$

$$U_{\mathrm{FL8}} = U'_{\mathrm{FL8}} - U^{\mathrm{mut}}_{\mathrm{FL8}} \tag{3.58d}$$

This way created signals are combined in the following equation which creates signals as is at right side of the Fig. 3.11 and is used to estimate horizontal position:

$$S_{\mathrm{FL}} = \frac{1}{I_{\mathrm{p}}} \left(2.5 \cdot (U_{\mathrm{FL3}} + U_{\mathrm{FL6}}) - (U_{\mathrm{FL1}} + U_{\mathrm{FL8}})\right) \tag{3.59}$$

3.3 Plasma Position Actuator

Plasma position is controlled with three different power supplies. Two of them (FABR and FABV) are fast reacting with current $\pm 5\,\mathrm{kA}$ with low self-inductance; third one EFPS is slower but provides current up to I_{EFPS}=16 kA

Horizontal plasma position is controlled with two different types of power supplies EFPS and FABV. Self-inductance of EF coils is $L_{\mathrm{EF}} = 1450\,\mu\mathrm{H}$ and voltage $U_{\mathrm{EFPS}} = 300\,\mathrm{V}$ [77] which gives $\approx 210\,\mathrm{A/ms}$ according to:

$$\frac{\mathrm{d}I_{\mathrm{EFPS}}}{\mathrm{d}t} = \frac{U_{\mathrm{EFPS}}}{L_{\mathrm{EF}}} = \frac{300}{1.45 \cdot 10^{-3}} \approx 210\,\mathrm{kA/s}, \tag{3.60}$$

The BV circuit has smaller inductance $L_{\mathrm{BV}} = 61\,\mu\mathrm{H}$ and voltage is $U_{\mathrm{FABV}} = 100\,\mathrm{V}$. Applying Eq. 3.60 to FABV gives rising speed $\approx 1.6\,\mathrm{kA/ms}$.

Coils connection of EF gives five times stronger field than connection for BV. It means 5 kA of FABV corresponds 1 kA of EFPS. But in contrary, current ramp up speed of the BV circuit is much faster comparing to EFPS. Therefore, FABV is essential for controlling plasma at the beginning of the discharge when plasma current rises very quickly (12 kA/ms, Eq. 2.5 and Fig. 1.9) while EFPS rises only

0.5 kA/ms (Fig. 1.9) during first 5 ms of the discharge (MFPS current induces voltage in EFPS circuit and thus increasing current ramp up speed in them) and thus reaction of the horizontal control system has to be fast.

Communication between FABV and central real-time control system MARTe is performed with serial communication link RS-232 [92] set to 921 600 bit s^{-1}. The protocol is composed with 2 bytes, corresponding to the requested current. Time needed for sending one current request is approximately 20.3 µs. When current request is received by FABV controller then reaction of the FABV to start driving current in the coils is less than 1 µs.

Vertical plasma position is stabilised with FABR power supply. The FABR power supply was completely the same construction as FABV power supply at the beginning. Inductance of BR coils is bit higher $L_{BR} = 92\,\mu H$ and thus current ramp up is close to 1 kA/ms. Nowadays FABR has new way of communication which increased total reaction speed. FABR is controlled with controller based on ML405 board assembled with Field Programmable Gate Array (FPGA) [32] Virtex 4. Controller communicates via AURORA serial link [93] with main real-time controller system MARTe [19].

Vertical Kick Power Supply (VKPS) and FABR have the same controller unit and they are connected in series [42] (as aforementioned at Sec. 1.2.2 see Fig. 1.5). Therefore, AURORA communication protocol [94] has been adjusted to communicate between MARTe and VKPS as well. At the layer of communication, special command is sent to activate kick at exact time in µs for specified duration. Setting of time and length and number of kicks and enabling them is loaded during MARTe startup using configuration file. Also these settings can be changed via MARTe generated web page between the discharges without restarting MARTe.

When kicks are enabled, plasma is vertically kicked upwards or downwards depending on the sign of the preset time in µs . When kick is active, the FABR power supply is switched off. Then FABR is switched on for a short time (usually a few tens of µs). After that, a new kick is performed by VKPS in opposite direction to move plasma column down to its previous position. Usually the second kick must be a bit longer because plasma had already accelerated vertically towards unstable position. Then FABR is switched on again and plasma is stabilised only by the FABR power supply. The FABR power supply is switched on also between upward destabilising kick and downward stabilising kick. Results from vertical kick experiments are visible in Fig. 3.31 and 3.32.

Protocol for communication between MARTe and VKPS and FABR controller is in document [94].

3.4 Plasma Position Controller

Plasma position control is divided in two separate parts. One part controls horizontal plasma position, other controls vertical plasma position. Both controls are essential for reaching research goals and providing plasma stability.

3.4.1 Horizontal Plasma Position Controller

Horizontal plasma position is controlled with two different power supplies (EFPS and FABV) controlled separately in different threads. EFPS is controlled in slow

thread with repetition cycle 500 µs. FABV is controlled in fast thread with repetition cycle of 50 µs. If plasma equilibrium has to be shifted towards High Field Side (HFS) then EFPS and FABV current has to be increased with comparison to plasma current.

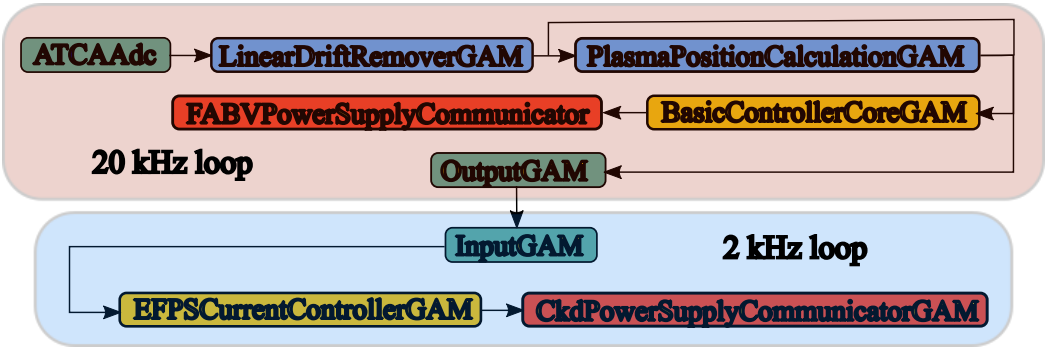

Figure 3.16: A sequence of Generic Application Modules (GAMs) for horizontal position control.

Whole horizontal control process starts with ATCAAdc GAM which collects all the data (see Fig. 3.16). Signals here are converted from levels to physics units. Then linear drift and offset is removed (Eq. 2.7 and 2.8) from the magnetic sensors which have their signal integrated. From these signals plasma position is calculated (Eq. 3.59) and is used together with plasma current to calculate request for FABV according to Eq. 3.62 using a BasicControllerCoreGAM. Calculated currents are then transferred to the FABVPowerSupplyCommunicator GAM which converts currents to the packets (messages) which are then sent to the FABV controller via RS232 link. Data necessary for EFPS current controller are transferred via OutputGAM to InputGAM (every tenth sample) from 50 µs thread to 500 µs thread. At the slower thread current for EFPS is calculated according to Eq. 3.61. This current is then transferred using CkdPowerSupply-CommunicatorGAM via RS232 link to communication unit and here are data changed and transferred to EFPS current controller. Protocol for communication with main power supplies is described in document [74].

At the very beginning, when FABV was not built and commissioned, plasma position was controlled only with EFPS. Requested output current was obtained with feedforward on plasma current. This plasma was unstable and chances to obtain longer pulses than 20 ms were around few percents. FABV is essential at the beginning of plasma discharge mainly up to first 20 ms when EFPS does not react fast enough.

Difference in plasma horizontal position control with and without FABV are in Figures 3.17, 3.18, 3.19. Figure 3.17 shows that despite the fact current for FABV was requested, current was not driven at discharge #5327 (blue line is zero).

Figure 3.18 shows horizontal position evolution since plasma starts at 960 ms. Without FABV plasma reached position bellow 0.52 m (more than 4 cm out off the requested position) and EFPS reacted on it but is not fast enough to control plasma on requested position (see Fig. 3.19). At the time around 965 ms current request for plasma position from EFPS significantly dropped but EFPS still rises (lower EF or BV causes plasma moving to Low Field Side (LFS)).

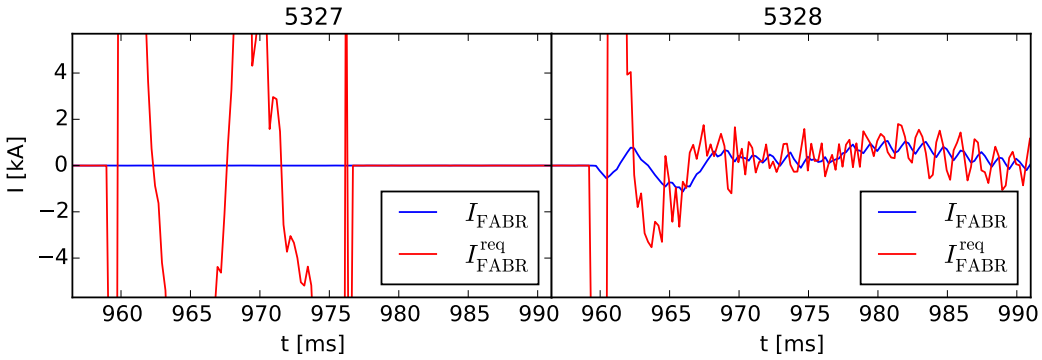

Figure 3.17: Requested and realised current for FABV power supply. At discharge #5327 FABV power supply did not work while in discharge #5328 worked.

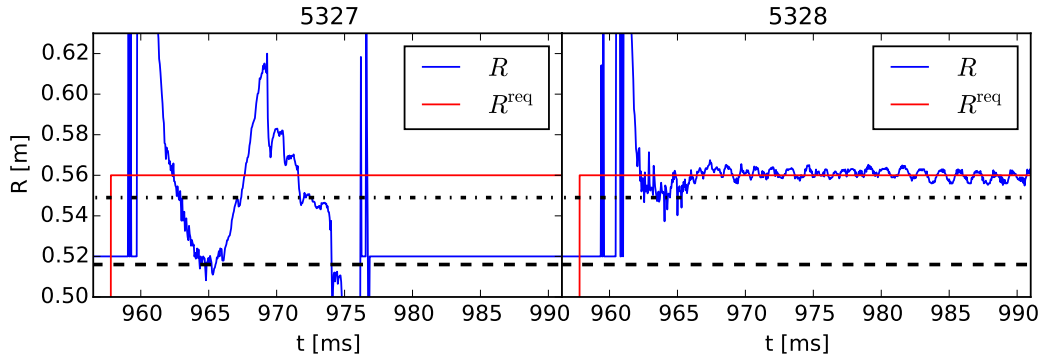

Figure 3.18: Requested and obtained horizontal position. Left: discharge #5327, FABV power supply did not work. Right: discharge #5328, FABV power supply worked. Dashed black line shows minimum of controlled position when FABV did not work. Dash-dot line shows minimum of controlled position when FABV worked.

With FABV (#5328) plasma at time 965 ms moves only to 0.55 m, 1 cm off the requested position and at the time of 967 ms is already at the requested position.

Comparing left and right side of Fig 3.19 once can notice that I_{EFPS} has the same value at 965 ms which also shows EFPS does not react fast enough. Therefore, faster power supply with fast control is necessary.

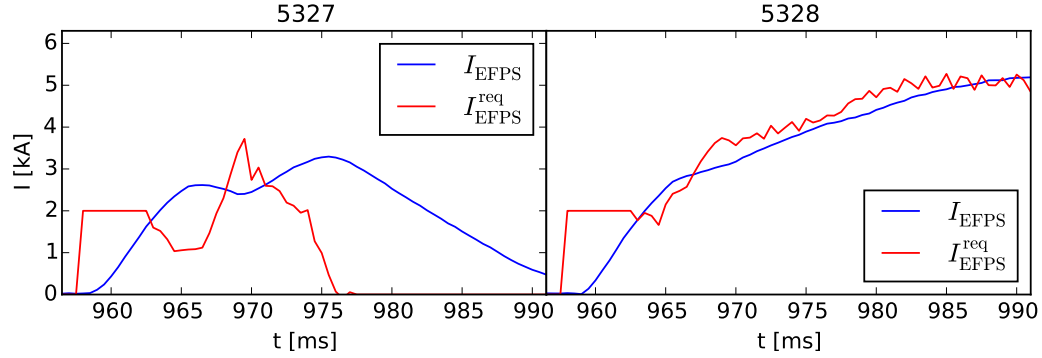

Figure 3.19: Requested and obtained current in EFPS. Left: discharge #5327, FABV power supply did not work. Right: discharge #5328, FABV power supply worked. We can notice the slow reaction of EFPS.

Same important as FABV, is correct starting time of EFPS (see Fig. 3.20). As mentioned in Chap. 2, depending on starting request level of MFPS (blue

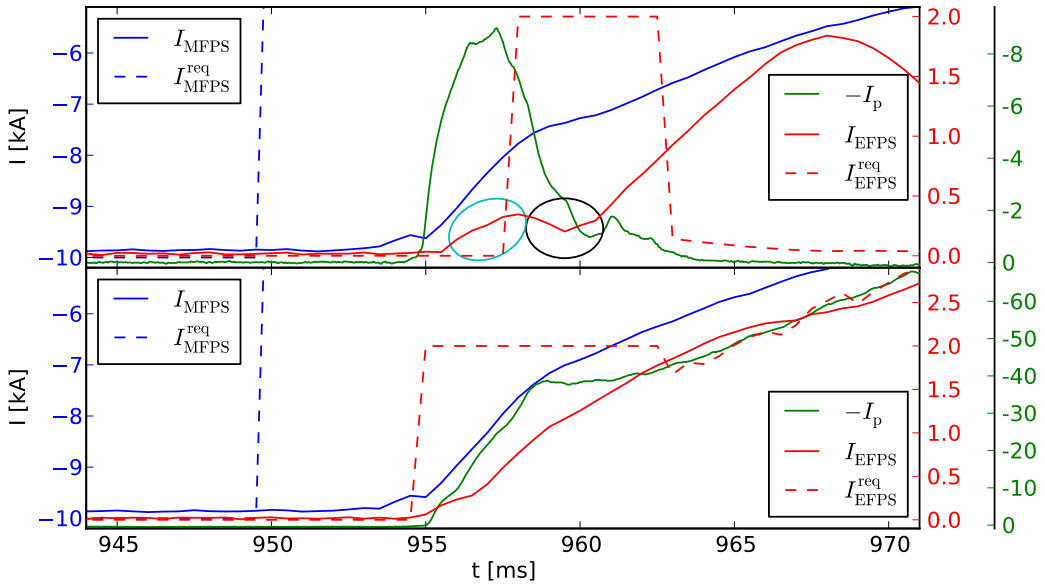

Figure 3.20: Top graph: At discharge #6523 EFPS starts late and plasma horizontal position is not stabilised. At discharge #6536 EFPS start is shifted 3 ms earlier and plasma is succesfully stabilised. Blue curves has y-axis at left side and all other have at right side. From plasma current (green line) only ramp up is visible.

dashed line), plasma current (solid green line) starts at different time. This makes necessary to change different start time of EFPS current (red solid lines) because it is slow power supply and is unable to react fast enough as plasma current rises. Plasma horizontal position is then uncontrollable. Starting of EFPS is done with requested current waveform step to 2 kA. This starting value request is optimal for all plasma currents.

At the top of Fig. 3.20 induced current from MFPS (blue solid line) is seen in EF current windings measurement marked with magenta ellipse. This induced current in EF coils creates vertical magnetic field which has been later compensated by 600 A starting at 950 ms driven by FABV creating vertical magnetic field in opposite direction. This can be seen at third graph of Fig. 3.22. However, significant improvement at optimising start up phase was not observed.

When EFPS (red solid line) starts late, drop and rising step at EFPS current is visible (marked with black ellipse) and plasma column is not stabilised and ends on LFS. If EFPS starts early it creates vertical field and plasma is pushed to HFS. Therefore (see bottom Fig. 3.20), EFPS current request (red dashed line) is slightly before plasma current start to start rising EFPS current together with plasma current. As optimal solution was found to keep steep of induced current in EFPS so difference between start of EFPS current and induced current is not visible. Which is done with 2 kA waveform request before plasma current start rising. Starting time of EFPS was experimentally shifted to obtain following table for MFPS levels and start time for EFPS.

After optimising of start of EFPS, the Proportional-Integral-Derivative (PID) controller was tuned. Several approaches were tried. Firstly, proportional con-

MFPS requested current [kA]	-8	-10	-12	-14	-16
start of EFPS [ms]	955	956	958	958	961

Table 3.2: Starting time of EFPS request waveform for different level of MFPS requests current

troller and proportional and integral controller on plasma current, which was enough to obtain equilibrium but to set equilibrium on desired position was not possible. Second approach was proportional controller on plasma position but this controller oscillates and did not work correctly. Main reason behind this is that the smaller error requests, the smaller EFPS current is requested too. But from experiments we know there has to be always current approximately 20 times smaller than plasma current. Also equilibrium depends on plasma current. Therefore there has to be binding between EFPS current and plasma current, not only the error in horizontal position.

As the best solution to have plasma in equilibrium is combination of feedforward controller on plasma current, feedback on plasma position and feedforward controller for FABV current. The following equation describes optimised controller:

$$\begin{aligned} I_{\mathrm{EFPS}}^{\mathrm{req}} = & P_{\mathrm{I_p}} I_{\mathrm{p}} + \\ & + P_{\mathrm{pos}} e_{\mathrm{pos}} + I_{\mathrm{pos}} \sum_{j=0}^{k} e_{\mathrm{pos}}^{j} \Delta t + \\ & + P_{\mathrm{FABV}} \frac{1}{N} \sum_{j=0}^{N} I_{\mathrm{FABV}}^{j} \end{aligned} \tag{3.61}$$

where total EFPS current request is $I_{\mathrm{EFPS}}^{\mathrm{req}}$ is calculated as a proportional component of plasma current with $P_{\mathrm{I_p}} = 0.046$, proportional $P_{\mathrm{pos}} = 0.5$ and integral $I_{\mathrm{pos}} = 0.00002$ component of plasma horizontal position $\Delta t = 500\,\mu\mathrm{s}$. e_{pos}^{j} is error between set-point (requested horizontal position) and measured value (calculated horizontal position) at time j since beginning of plasma current. The very last term of this equation is the proportional component of averaged FABV during the last 19 ms which means $N = 38$ and $P_{\mathrm{FABV}} = 0.2$. This component requests 5 times smaller current in EFPS than is requested by FABV averaged over 19 ms. It is used also to help FABV to reduce load by driving current in EFPS. The constant 5 is chosen because, as mentioned before field generated by FABV is 5 times smaller than from EFPS. Looking at Eq. 3.61 from control point of view, first and last term are open loop terms at plasma current and smoothed current from FABV. Closed loop (feedback) part of equation is done using plasma position (second and third term in equation).

When constant P_{FABV} in EFPS was set two times bigger to help FABV to reduce load even more, horizontal position started to oscillate. In Fig. 3.21 the feedforward on the measured FABV (blue line) is doubled (marked with 2×). Top graph shows EFPS current oscillations together with total (all component together including waveform) requested values compared with non-oscillating current and request when feedforward constant P_{FABV} is halved. The same oscillations are at plasma current (second graph). To see oscillations better, plasma current is zoomed between 95 kA to 155 kA. Oscillations on plasma current are due to mutual inductance between plasma current and EFPS current and also between MFPS coils and EFPS coils. Third graph shows oscillations on FABV current

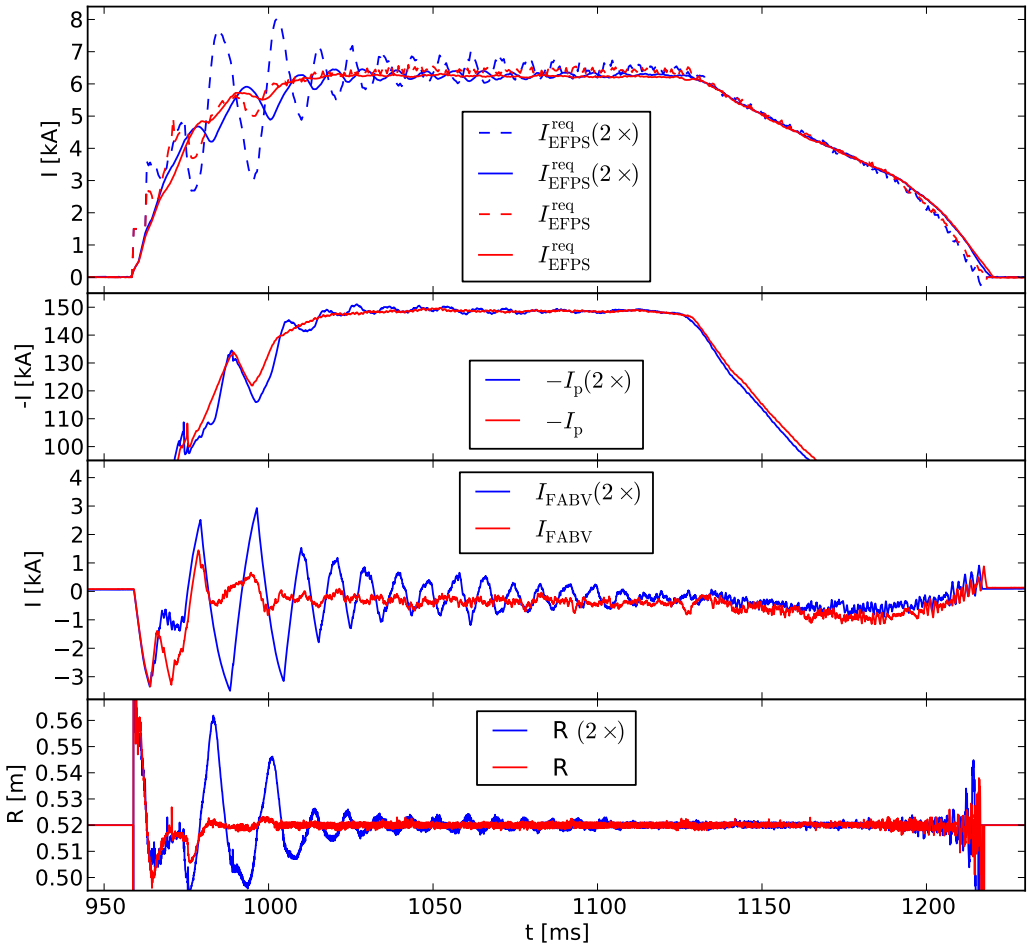

Figure 3.21: Analysing of effect when constant P_{FABV} is doubled for shot #3733 (labelled with '2×')and for shot #3738 is correct. Oscillations are visible on top graph: at requested (dashed blue) and measured (solid blue) EFPS current. Second graph same for plasma current. Third FABV current and bottom graph shows plasma position and oscillations when constant is doubled.

which are more than three times bigger comparing to correct set constant. Bottom graph displays these oscillations on horizontal position. With correct set constant plasma is in equilibrium at correct position at time 980 ms with doubled constant plasma horizontal position oscillates at level of 6 cm.

In Fig. 3.22 single current's components of EFPS control are plotted so effect of all parts of controller from Eq. 3.61 are clearly visible. In this shot plasma is horizontally moved for 3 cm to the LFS and back (bottom graph). During this movement effect of every component can be seen better. At top graph we can see that component of from plasma current $I^{\mathrm{req}}_{\mathrm{EFPS}}(I_{\mathrm{p}})$ is dominant. Before time 1100 ms component from horizontal position $I^{\mathrm{req}}_{\mathrm{EFPS}}(\mathrm{R})$ and from component from FABV $I^{\mathrm{req}}_{\mathrm{EFPS}}(I_{\mathrm{FABV}})$ (second graph) is decreasing as well as I_{FABV} at third graph. Then is plasma moved back. Comparing flat phase of horizontal position around time 1200 ms and 1100 ms one can notice that only 200 A of I_{EFPS} and 1 kA of I_{FABV} is needed to move plasma horizontally in 3 cm.

Control algorithm for FABV is based on PID controller which uses only pro-

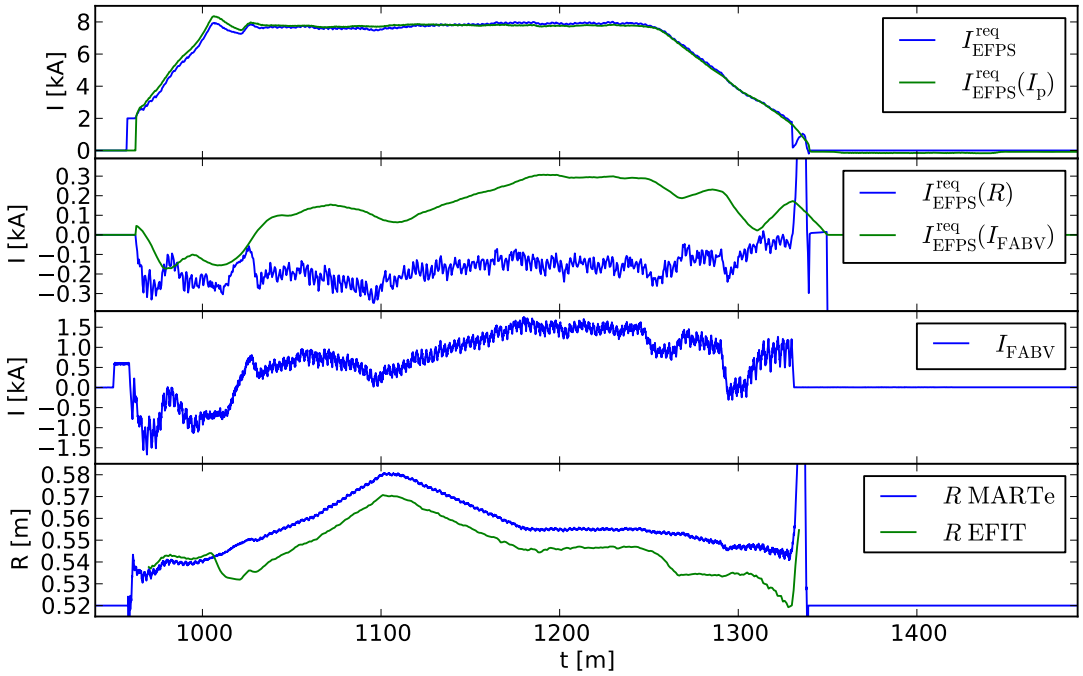

Figure 3.22: Different current's components of EFPS and current of FABV during moving plasma position in horizontal direction in discharge #9691

portional and integral component. The algorithm is described by:

$$I^{\mathrm{req}}_{\mathrm{FABV}} = P_{\mathrm{pos}} e_{\mathrm{pos}} + I_{\mathrm{pos}} \sum_{j=0}^{k} e^{j}_{\mathrm{pos}} \Delta t \tag{3.62}$$

where $P_{\mathrm{pos}} = -300000$ is proportional constant, $e_{\mathrm{pos}} = SP - MV$ is error between set point (requested value) SP and measured value (process variable) MV. This means that proportional part of the controller requests for each 1 cm error a current change by 3 kA. Integral part is computed with constant $I_{\mathrm{pos}} = -60$ and $\Delta t = 50\,\mu\mathrm{s}$. P_{pos} and I_{pos} constants were obtain trial error method which is describe in text below.

Tuning constants for horizontal position was very difficult because many different aspects played role and was difficult to see which effect is responsible for non successful breakdown. Aspects which played the role were plasma current start and speed of plasma current rising (Sec. 2.4) and amount of gas injected at the beginning of discharge (Sec. 5.4). FABV was freshly built and suffers on child problems. The same was with control and data acquisition systems, hydraulics and crowbars which were commissioned at the same time. Also operations of tokamak was new for us and many errors were done by operators. This all together slowed down the whole process. Plasma breakdown optimisation, gas puff and constants for EFPS current controller and FABV current controller were adjusting during the same period.

Nevertheless in this part, tuning of system will be described as much as possible. Tests started for $I^{\mathrm{req}}_{\mathrm{FABV}}$ at values $P_{\mathrm{pos}} = -60000$ which means 600 A every 1 cm error (Eq. 3.62). This was later increased to $P_{\mathrm{pos}} = -80000$. This constant was kept, whilst the constants at EFPS current controller (Eq. 3.61) were altered. Firstly $P_{\mathrm{I_p}}(= 0.04)I_{\mathrm{p}}$ and $P_{\mathrm{FABV}}(= 0.2)I_{\mathrm{FABV}}$ were implemented. Then also feed-

back component at horizontal position was added $P_{\text{pos}}e_{\text{pos}}$ for $P_{\text{pos}} = 0.25$, 0.3, 0.4 and 0.5.

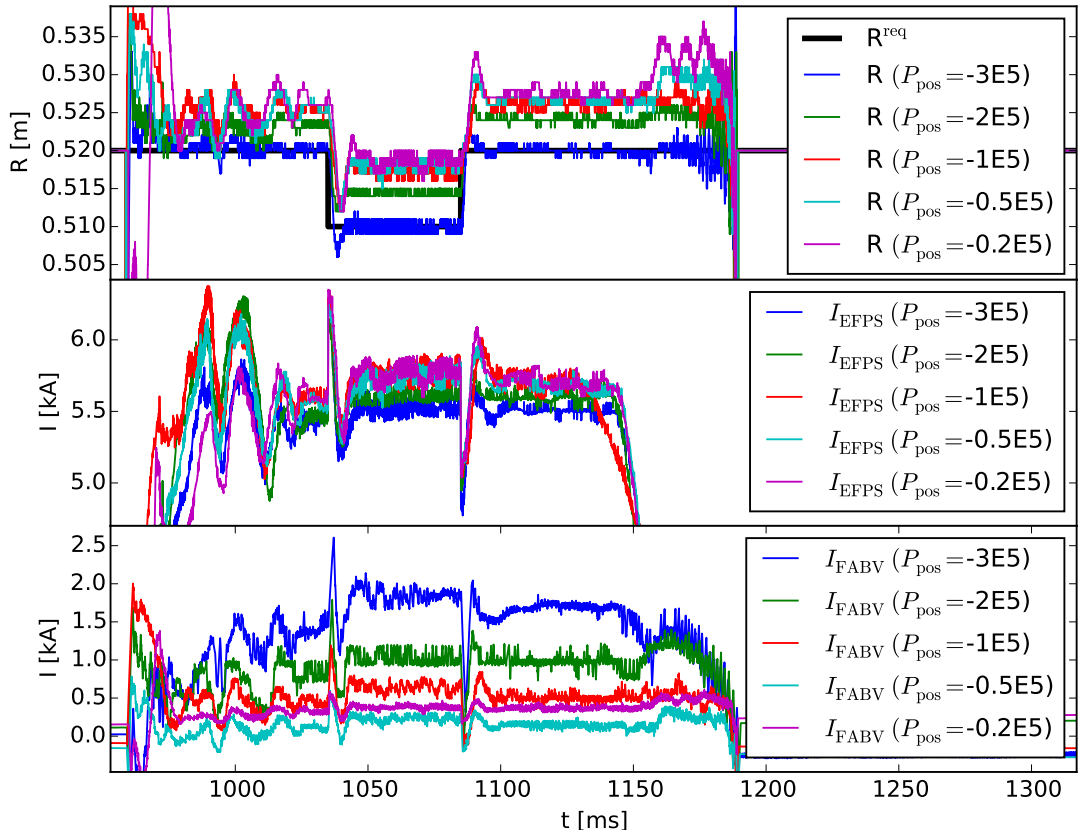

Figure 3.23: Tuning P_{pos} constant for FABV current supply. Values on constant are written in legend. Top: response at horizontal position. Middle: response at I_{EFPS}. Bottom: response at I_{FABV}

Lastly P_{pos} for Eq. 3.62 was optimised. 1 cm jump on horizontal position to HFS was requested at 1035 ms and then back to HFS at 1085 ms. Programmed jump (black line) with horizontal position response at jump for different value of constant (Tab. 3.3) are at top of Fig. 3.23. It is clearly visible that with

discharge number	2655	2649	2650	2651	2654
P_{pos}	$-3E5$	$-2E5$	$-1E5$	$-0.5E5$	$-0.2E5$

Table 3.3: Different constants for optimising feedback control for horizontal position in different discharges.

increasing P_{pos} constant horizontal position is better followed. When $P_{\text{pos}} = -300000$ then plasma position followed requested value very well. Overshooting visible at position is cause by EFPS (middle graph). Bottom graph shows FABV current currents for different constansts. EFPS and FABV power supply create biggest changes mainly during moving plasma. When P_{pos} was set then integral component was designed to gain same amount of current with constant error in 5 ms so $P_{\text{pos}} = -60$.

Comparing results obtained with new algorithm for horizontal position calculation according to Eq. 3.59 using bilinear extrapolation Eq. 3.54 and Eq. 3.55 (red

solid line R (S_{FL})) with comparison between controller using IPR coils R(S_{hor}) calculating position according to Eq. 3.53 (blue solid line R (S_{hor})) and horizontal position compared with EFIT reconstruction (green line R (EFIT)) are at the top of Fig. 3.24. Estimation using R (S_{FL})) is more accurate with respect to EFIT reconstruction during whole phase, is less sensitive on plasma shape as above-mentioned and position calculated from flux loops is less noisy which has also benefit in estimation of vertical position because oscillations are smaller. This comes from the fact that both positions, R and Z, are functions of B_{hor} and B_{ver}, therefore noise reduction in estimation B_{hor} leaded to improvement of vertical stability, because the oscillations at vertical positions were reduced too.

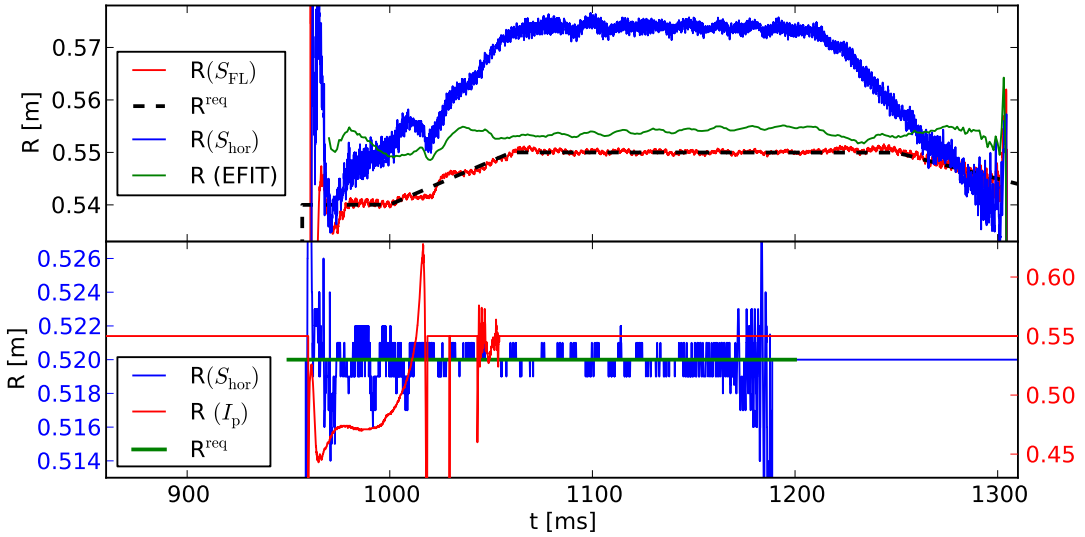

Figure 3.24: Top graph: Comparison between different calculation of horizontal position for shot # Horizontal position calculated using flux loop is in better agreement with EFIT reconstruction. Bottom graph: comparison between old controller when horizontal position was controlled only according to plasma current $R(I_{\mathrm{p}}$) and plasma feedback according to position. At the top graph R(S_{hor}) is calculated with bilinear interpolation whilst at the bottom grap R(S_{hor}) is calculated only in linear interpolation.

Bottom graph shows two old controller. Red line is the oldest algorithm which used only feedforward component at plasma current. Keeping equilibrium at certain horizontal position using only plasma current was not possible as it is seen from R (I_{p}). Every time plasma touched LFS plasma current was reduced by limiter and EFPS current pushed plasma on the HFS. When EFPS current rose slower than plasma current, then plasma expanded to LFS where ended (as seen red curve in Fig. 3.24). The speed of rising of plasma current is uncertain so using only EFPS did not result at stable equilibrium because plasma was pushed at the beginning of every discharge at inner side (if EFPS was strong - started early) or outer wall (if EFPS was weak - started late).

Blue curve shows algorithm using IPR coils but only with linear interpolation, therefore sharp peak like digital noise are visible. Green line shows requested horizontal position for S_{hor} algorithm

3.4.2 Vertical Plasma Position Controller

Vertical plasma position control is essential for elongated and D-shaped plasma. Vertical plasma position controller is easier than horizontal control with respect to number of controllers, real-time threads, power supplies, total current needed and precise timing of starting EFPS. On the other hand its reaction speed is more critical to obtain stable vertical position due to effect that elongated plasma is naturally unstable. Therefore, fast detection, precise estimation and reaction speed of the system is crucial in success of suppressing VDEs. COMPASS control system faced this problem because of transport delay. Description of determining delays, suppressing them and also controller algorithm and optimisation of controller is described in the following part.

At the Fig. 3.25 there is a sequence of the GAMs needed for vertical plasma control. All control is done in fast thread with 20 kHz frequency cycle. Firstly,

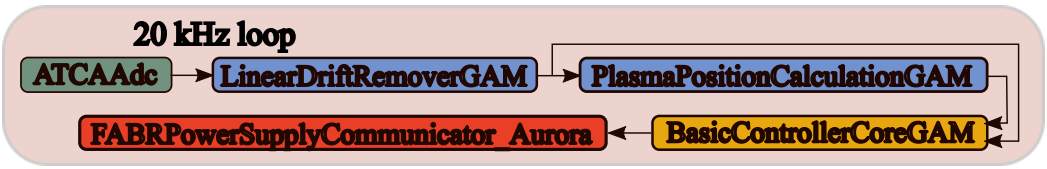

Figure 3.25: A sequence of GAMs for vertical position control.

data are collected using ATCAAdc GAM. Then drift is removed from all magnetic signals which are integrated in LinearDriftRemoverGAM according to Eq. 2.8. Afterwards, vertical plasma position is calculated as it was described in previous sections. Plasma current and calculated position together with requested position read from configuration file are used to compute requested current using PI controller according to:

$$I_{\mathrm{FABR}}^{\mathrm{req}} = P_{\mathrm{pos}} e_{\mathrm{pos}} + I_{\mathrm{pos}} \sum_{j=0}^{k} e_{\mathrm{pos}}^{\mathrm{j}} \Delta t, \tag{3.63}$$

where P_{pos} is proportional constant, I_{pos} is integral constant, $e_{\mathrm{pos}} = Z_{\mathrm{req}} - Z_{\mathrm{meas}}$ is error between requested vertical position Z_{req} and measured vertical position Z_{meas}. P_{pos} and I_{pos} constants for vertical controller were roughly taken from model described in Sec. 3.1 (Eq. 3.25). This model does not include any delays. Model described in the thesis [95] calculates with delay and estimates $P_{\mathrm{pos}} = 7.5 \times 10^4$.

Before transport delay was reduced, plasma was stable only if was kept close to the LFS. Constant was set $P_{\mathrm{pos}} = 8 \times 10^4$ and was obtained experimentally starting with bang bang regulator at $P_{\mathrm{pos}} = 50 \times 10^4$ and then decreasing value through stable regime around $P_{\mathrm{pos}} = 8 \times 10^4$ to again unstable constant when $P_{\mathrm{pos}} < 6 \times 10^4$.

After shortening delay, P_{pos} constant were getting empirically around value $P_{\mathrm{pos}} = 8 \times 10^4$. To obtain the best values, plasma poloidal cross-section size was decreased and kept further from the vessel to increase sensitivity to VDE. In Fig. 3.26 there is comparison between standard plasma size (blue) and shrunk plasma size (green). Shrunk plasma is also moved downwards. For finding correct constants plasma current scan from -120 kA to -300 kA with steps -30 kA were

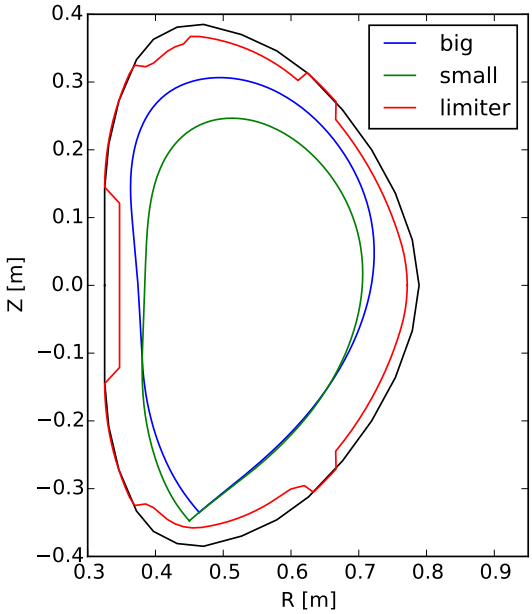

Figure 3.26: Comparison between standard plasma size and position (blue) and smaller plasma size shifted 2 cm below standard position. Smaller plasma was used for tuning vertical position controller.

done. Then minimum and maximum of P_{pos} for every current was searched to find window where P_{pos} stabilises small plasma. Every discharge was repeated at least twice to see if that discharge is repeatable with the same results. I_{pos} has been chosen to provide same current as P_{pos} in 5 ms. Correct and incorrect P_{pos} constants together with linear fit are in Fig 3.27. Linear fit can be described by

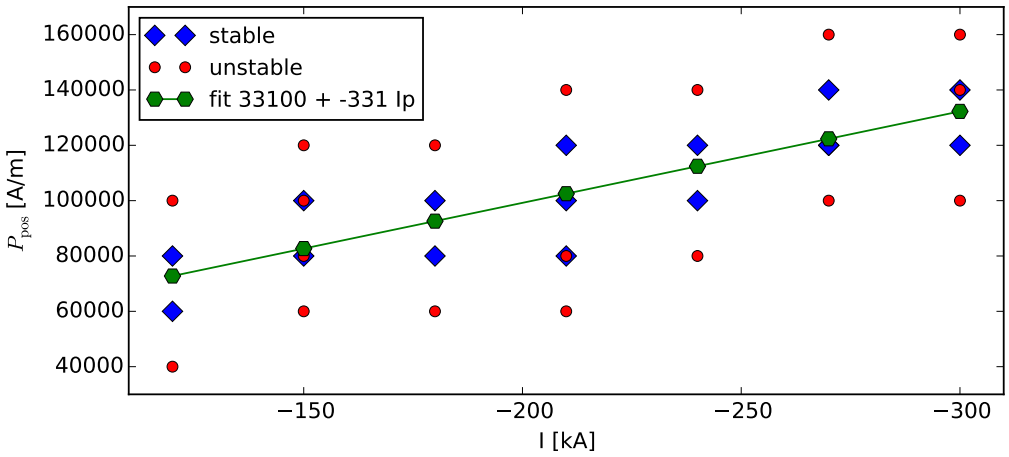

Figure 3.27: Stable (blue diamonds) and unstable (red circles) P_{pos} constants and fitting curve for stable constants changing according to plasma current (green).

function

$$P_{\mathrm{pos}} = 33100 - 330 \cdot I_p \tag{3.64}$$

When plasma current $I_{\mathrm{p}} = -150\,\mathrm{kA}$ and $I_{\mathrm{p}} = -300\,\mathrm{kA}$ results for P_{pos} are not clear and reason is unknown.

Total transport delay was caused by four separate issues and had to be fixed to obtain vertically stable plasma. As mentioned in Sec. 1.3, MARTe executes

GAMs in loops - cycles. If total execution time of all GAM in sequence exceeds loop cycle, MARTe executor continue with predefined orders of GAMs until all of them are executed. Then it will wait to next cycle. At the beginning MARTe running cycles not rarely exceeded 50 µs when control loop cycle was expected at 50 µs. Which means that in these cases, vertical control action were performed only once per 100 µs instead of 50 µs planned. This was mainly fixed by compiling all the GAMs and the libraries with parameter "-O3" for optimisation on speed. Before optimisation during plasma discharge around 1% of cycle time exceeded 50 µs. After "-O3" optimisation and changing protocol and communication link to control FABR with Aurora these longer cycles are not present.

At top Fig. 3.28 there is comparison between runtime of the GAM sending data to FABV via RS-232 link and the GAM using Aurora to sending information to FABR both with "-O3" optimisation. Maximal time for Aurora is 13 µs while

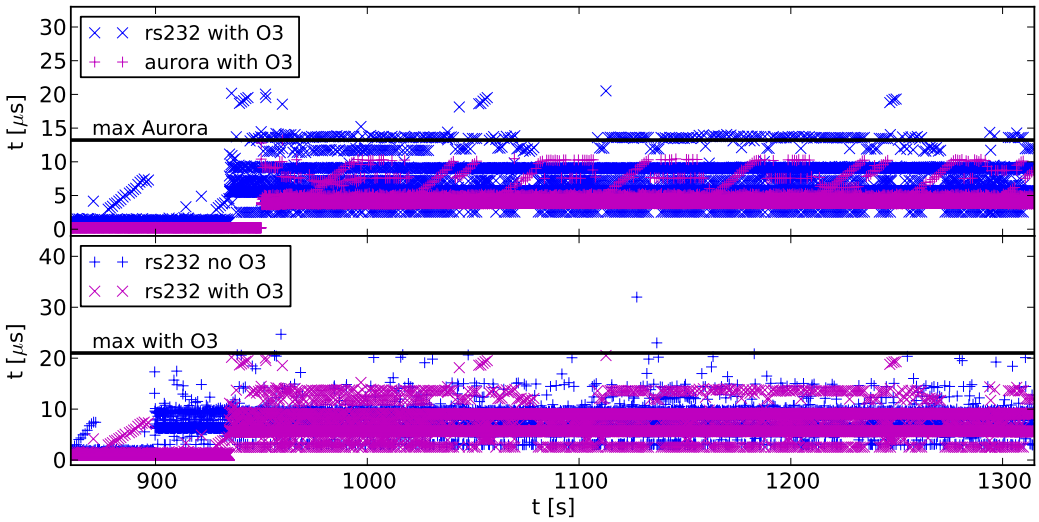

Figure 3.28: Comparing execution time of GAMs for communication using Aurora or RS232 protocol compiled with and without speed optimising. Top: comparing RS232 and Aurora protocol compiled with "O3" optimisation. Bottom: Comparing RS232 protocol compiled and not compiled with "O3" optimisation.

for RS232 it is ≈ 21 µs. At bottom of that figure there is comparison of same RS232 protocol before and after "-O3" compilation. Without "O3" optimisation runtime can go up to 25 µs. At present only on fast power supply is controlled can be done using Aurora. At the beginning only RT card were able to communicate via Aurora. Firmware at fast data acquisition card were not design to communicate via Aurora. Therefore, upgrade of the firmware and the driver for this cards has been done. Also MARTe can use Aurora connection on Rear Transition Module (RTM) connected on RT cards or fast data acquisition card. That gave us opportunity to us 12 Aurora communication link on each Advance Telecommunications Computing Architecture (ATCA) crate. If communication link on the controller unit of FABV will be converted to Aurora extra 8 µs to 12 µs can be saved. Data showing maximal, median and mean values of different communication link and compilations are listed in Tab. 3.4

Second issue causing delay was filter at acquisition module programmed on the FPGA [32]. This firmware was using high pass order filter for filtering 100

Communication and optimisation	max	median	mean
Aurora relative with "O3"	13 µs	4 µs	4 µs
RS232 relative with "O3"	20.5 µs	5.5 µs	6.5 µs
RS232 relative without "O3"	24.5 µs	6.5 µs	7 µs
whole cycle (absolute) with "O3"	42 µs	19.5 µs	21.5 µs
whole cycle (absolute) without "O3"	63 µs	32.5 µs	33.5 µs

Table 3.4: Main statistical data from using different communication link and optimisation.

samples of data which caused shifting data by around 50 µs. The filter was removed and last measured sample is used for all measurements at MARTe.

Third part of total delay was caused by communication between FABR and real-time software. First communication was done on serial link RS-232 with speed 921 600 bit/s. Two bytes were transferred in approximately 24 µs 2× (8 + 1 start + 1 parity + 1 stop) [bit] / 921600 [bit/s] = 23.87 µs. With new update of firmware on FPGA, serial communication link based on Aurora [93] protocol has been used. Using Aurora 4bytes are transferred in 1 µs. Comparing total execution time for all GAMs in sequence before and after "O3" optimisation together with changing of communication way is in Fig. 3.29. This includes only

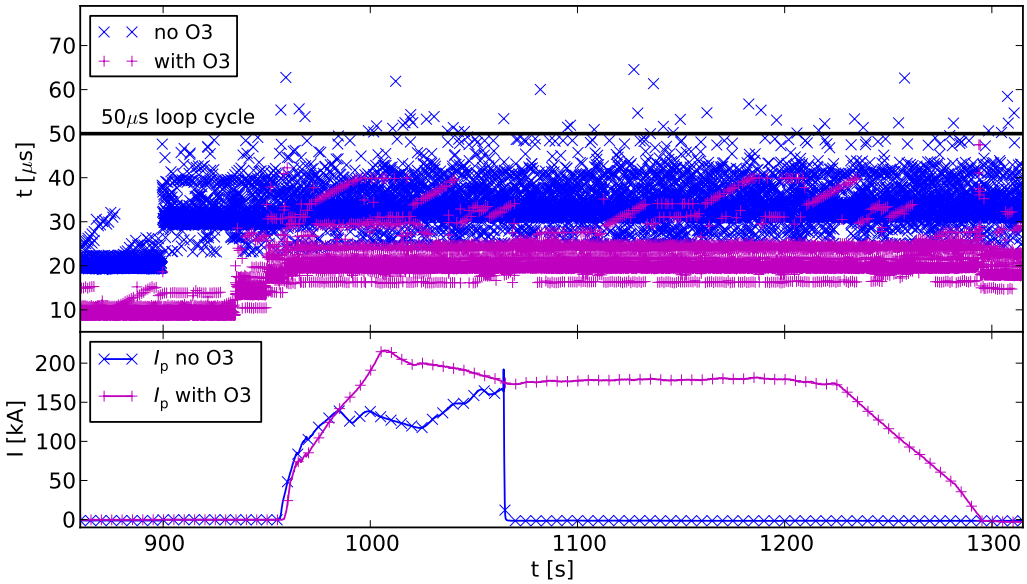

Figure 3.29: Comparing execution time of all GAMs in whole cycle with communication using Aurora or RS232 protocol compiled with and without speed optimising. Top: comparing execution of all GAMscommunicating with RS232 or Aurora protocol compiled with "O3" optimisation or without "O3" optimisation. Bottom: Plasma current during discharges.

delays caused directly with GAMs execution. Data transferred by the serial link or data delayed by the filter are not considered because they are before or after GAM's execution. From bottom figure one can see that when plasma current starts longer execution time starts also. It is caused mainly by the communication with FABV and FABR power supplies which starts slightly before plasma current.

Last part of the delay was caused by asynchronous operation between MARTe and FABR. MARTe operates at 20 kHz as a whole cycle but concrete message is never sent in exact time. FABR operates at 40 kHz. So depending on which time of cycle message is received by FABR, delay can vary between 0 µs to 25 µs. New controller which communicates with AURORA has the same speed but depending on the MARTe communication it can start in interval ±7 µs of internal 25 µs cycle.

When delay was shortened vertical stability increased that way, that new experiments were able to perform. Especially two of them will be mentioned here together with results.

Firstly, due to construction limit of edge Thomson Scattering (TS) diagnostic at COMPASS [72] (edge TS optic does not see to the very top of the vessel where is plasma edge), pedestal during H-mode was not visible. Therefore, scenario with smaller plasma moved 4 cm downwards has been developed (see Fig. 3.26). In this scenario the pedestal was observed at COMPASS for the first time (see Fig. 3.30).

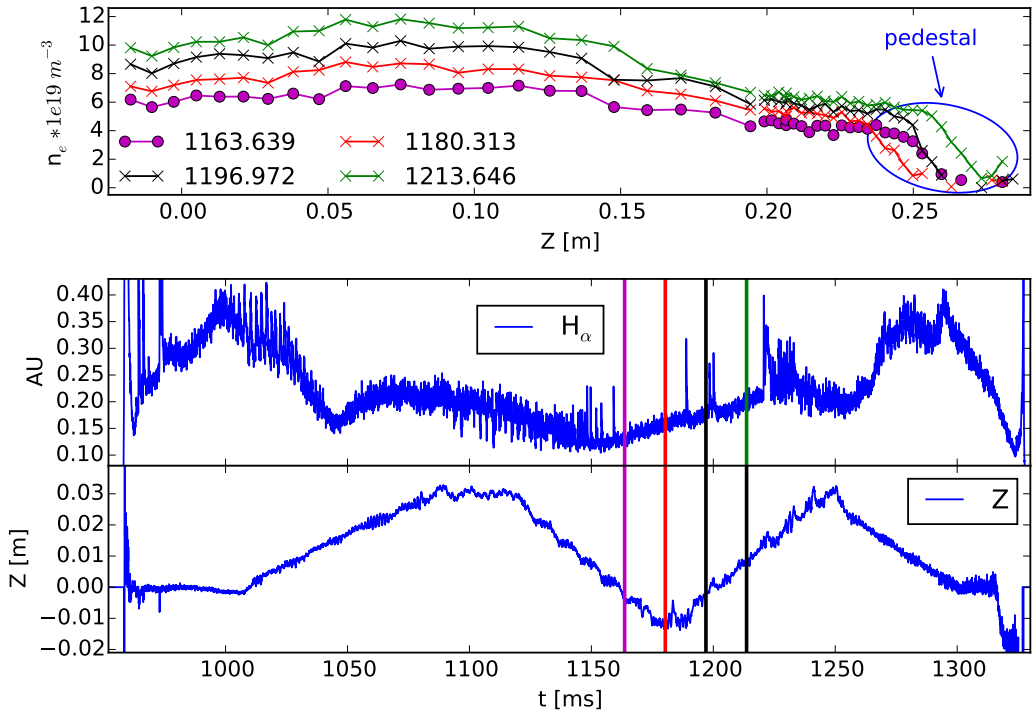

Figure 3.30: Top graph shows four different density profiles from TS diagnostic. Colours corresponds the vertical lines from bottom graphs. Labels show time when TS measured. Pedestal is visible at the edge of plasma and is labelled with blue ellipse. Middle graph shows H_α line with. Bottom graph shows vertical position. Bottom graph tells that H-mode is achieved when plasma column is moved downwards.

Top figure shows the electron density profiles from discharge #8172 from TS diagnostic at four different times. Last closed surface of this discharge at time 1185 ms is in Fig. 3.26 marked as small. Pedestal together with measurement of upper points of TS are clearly visible. At next two graphs of the same figure H_{alpha} and vertical position is plotted. H-mode, according to H_{alpha} measurement, starts around time 1150 ms when plasma centre is around 0.0 cm which is 2 cm

to 3 cm bellow standard operation. The vertical lines and their colours match the electron density profiles from TS diagnostic at corresponding time.

Second big achievement was Edge Localised Modes (ELMs) triggered experiments. Plasma was "kicked" (vertical fast movement of plasma) by VKPS and stabilised afterwards to trigger the ELM [96]. Confirmation of ELM triggered by kick is not clear. In Fig. 3.31 four kicks are made and all of them are stabilised. Vertical dotted lines show request time of every kick. All the kicks were per-

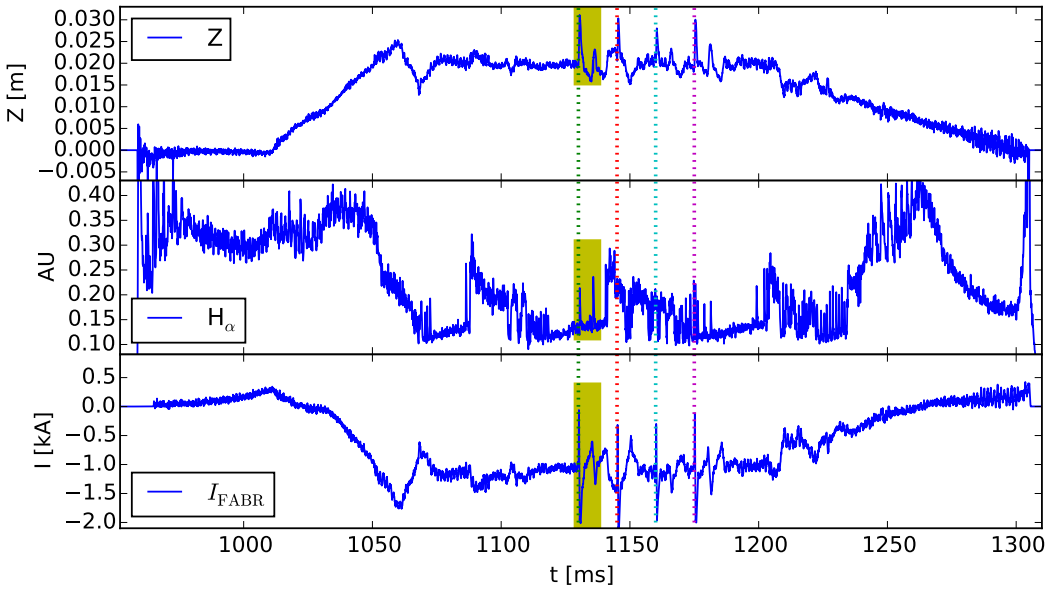

Figure 3.31: Experiment performed with VKPS. At top graph, the vertical position is drawn. Spikes correspond to fast movement of plasma column induced by VKPS. The second graph shows H_α with ELMs. Bottom graph shows current driven by VKPS and FABR in BR coils. Up spikes show current driven by VKPS to kick plasma upwards and downwards spikes are used to move plasma back. Green, red, cyan and magenta vertical dot lines show time when kicks were active. The yellow boxes show zoomed area in Fig. 3.32.

formed upwards. Top graph shows vertical position. During vertical kick plasma moves fast by more than 1 cm. Then it is kicked back downwards to stabilise the position. At the middle graph, H_α line is plotted. H-mode starts around 1120 ms stops around 1140 ms and then later starts again around 1180 ms. Few ELMs are visible. Bottom graph shows measured current in FABR circuit. Sharpest spikes upwards and downwards are kicks. Data marked by yellow rectangle are zoomed in detail around two ELMs in Fig. 3.32.

Zoomed data show two ELMs in sequence. First ELM has smaller amplitude and comes 0.3 ms after kick. Second ELM is bigger and comes before kick. It cannot be clearly told that first ELM is triggered by kick but also cannot be clearly said that is not. Nevertheless, without vertical stable system with some reserves this vertical kick experimental campaign would not be possible at all.

As one of the COMPASS experimental topics is the L-H transition, experiments with observing L-H and H-L transition depending on X-point distance from the divertor were performed. During these experiments plasma was moving slowly downwards to less stable position and then back. Clear dependence on

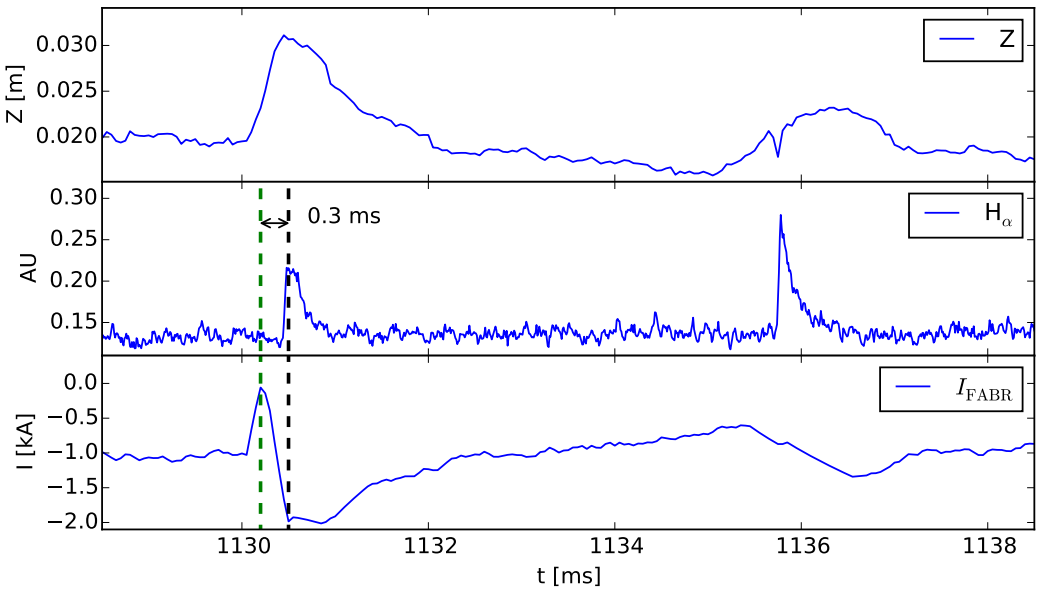

Figure 3.32: The top graph shows vertical position slightly before and after the vertical kick and two ELMs. Second graph shows H_α line with two ELMs. First one is only 0.3 ms after the kick and is smaller than second ELM which is before vertical kick. Bottom graph shows current driven by VKPS and FABR in BR coils. This graph shows zoomed yellow regions from Fig. 3.31

X-point high from divertor was observed [97]. L-H transitions occured typically at lower position of X-point.

Improvements in controlling and estimation of vertical and horizontal plasma position allowed running stable plasma with significantly larger gap from the LFS wall. This especially allowed running small circular plasmas in 2012-2013. This was crucial in order to measure with infra-red cameras as far as possible away from the plasma HFS contact point [98, 99]. This task was requested by the ITER International Tokamak Physics Activity. This yielded finally to a new design of the ITER enhanced heat flux panels, including the observed steep heat flux gradients [99, 100].

All these types of experiments were possible only due to improved calculation of position using FLs, subtracting induced currents in the vessel and derivative components of external currents, shortening delays with removing filters, changing communication and speed optimisation during compilation of all source codes and improved controller of EFPS.

4. Plasma Shape Control

Plasma in tokamaks is naturally in circular shape in poloidal cross-section. Circular plasma has to be always limited by a limiter from a material which can sustain high heat flux. Sputtering or melting of limiter releases material into plasma. These impurities undesirably cool down the plasma. Therefore, diverted plasma shape has been developed for tokamaks. Particles, that leave the plasma, flow along the magnetic field lines and hit the target tiles of the so-called divertor, far from the plasma. In comparison with the limiter plasma, impurities released from the plates have smaller chance to end up inside the confined plasma.

In this section, different benefits of elongated respectively D-shaped plasma will be summarised. One of the important improvement of elongated plasma is phenomena when plasma goes from L-mode (low confinement mode) to H-mode (high confinement mode) which is possible only at diverted plasma. H-mode is characterised by steep pressure profile at the plasma edge called pedestal as it is visible in Fig. 1.9. Confinement can be improved by a factor 2 or more [10, 101].

The confinement efficiency of plasma pressure p by the magnetic field B can be expressed as:

$$\beta = 2\mu_0 \frac{p}{B^2}, \tag{4.1}$$

where β is a MagnetoHydroDynamic (MHD) parameter expressing the efficiency of confinement of plasma pressure p by the magnetic field B. β is limited due to MHD instabilities driven by pressure gradient. Maximum achievable value of β is given essentially by the tokamak geometry (a, R_0, κ, δ) and additional heating systems. Higher β limit [102] can be obtained with increased elongation and triangularity [103]. Since the desired thermonuclear fusion power rises as $P \propto \beta^2 B_0^4 V$ whilst large fraction of the tokamak construction cost is given by the toroidal magnetic field volume B^2V, increasing β is the way to increase the power/cost ratio.

Other benefit of D-shaped plasma (diverted plasma) is increase of the safety factor q which allows higher plasma current. The safety factor q determines the magnetic field line twist: how many toroidal turns m a magnetic field line performs within one poloidal n turn, $q = m/n$. For circular plasma, the Maxwell equations yield to a simple formula:

$$q(r) = \frac{2\pi r^2 B_\phi}{\mu_0 I_\mathrm{p}(r) R}, \tag{4.2}$$

where r is small radius, B_ϕ is toroidal magnetic field, $I_\mathrm{p}(r)$ is plasma current inside r and R is tokamak major radius. For the circular plasma with radius a, Eq. 4.2 can be rewritten as:

$$q(a) = \frac{2\pi a^2 B_\phi}{\mu_0 I_\mathrm{p} R} = q_\mathrm{circ}, \tag{4.3}$$

where I_p is entire plasma current. Safety factor for elongated plasma with elongation $\kappa = \frac{b}{a}$ can be rewritten this way:

$$q_\mathrm{el} = \frac{2\pi a b B_\phi}{\mu_0 I_\mathrm{p} R} = \frac{2\pi a^2 \kappa B_\phi}{\mu_0 I_\mathrm{p} R}. \tag{4.4}$$

Therefore, for the same q, plasma current can be higher in elliptically shaped plasma.

Experimental results show that the thermal energy confinement time τ_E increases with elongation as $\kappa_\chi^{0.8\pm0.3}$ [1], where κ_χ is separatrix elongation. H-mode is also possible only in diverted plasma.

However, there is a practical limit to the maximum achievable elongation due to the excitation of an n = 0 axisymmetric mode. Typically, it is very difficult to achieve elongations greater than a factor of height/width = 2.

Tokamaks with elongated, non-circular cross sections are capable of stably confining reactor grade plasma pressures without the need of a perfectly conducting wall.

4.1 Plasma Shape Model

Plasma cross section shape at COMPASS is configured by manual connections of Shaping Field (SF) coils at the link-board. COMPASS can operate with the following shapes: circular (Shaping Field Power Supply (SFPS) current is zero), elliptical (SFPS current is typically lower than 2 kA), Single Null Divertor (SND), Single Null Divertor with high Triangularity (SNT) and Double Null Divertor (DND). COMPASS operates mainly in SNT or circular shape. Plasma shape at COMPASS is determined as a funtcion between plasma current I_p and shaping current I_SFPS. When increasing SFPS current, circular plasma shape vertically elongates to elliptical and then with SFPS current above 0.025 times plasma current (for example $I_\mathrm{SFPS} = 3.25\,\mathrm{kA}$ for $I_\mathrm{p} = 130\,\mathrm{kA}$), the magnetic X-point penetrates inside the vessel and forms diverted plasma with maximum elongation $\kappa = 1.8$. Further increase of SFPS current does not increase elongation but shrinks plasma area from $0.175\,\mathrm{m}^2$ to $0.14\,\mathrm{m}^2$ as it can be seen in Fig. 4.1. Plasma current in this discharge (#8335) was kept constant 200 kA during changing ratio $I_\mathrm{SFPS}/I_\mathrm{p}$.

4.2 Plasma Shape Diagnostic

Diagnostic of plasma shape is not performed as on other devices using real-time reconstruction codes because plasma shape at COMPASS is predefined with hardware connections and cannot be changed in real-time. Therefore, COMPASS uses only feedforward shape control. Measurement is performed using plasma current as it was described in Sec. 2.3. Nevertheless, shaping current in SF coils is also measured using Rogowski coil, but it is not used for plasma shape control.

4.3 Plasma Shape Actuator

Plasma shape is changed at COMPASS using SF coils fed by current from SFPS. Maximal current which can be delivered by SFPS is $I_\mathrm{SFPS} = 12\,\mathrm{kA}$. The inductance of the SF coils in SNT in configuration is ($L_\mathrm{SF-SNT} = 1.23\,\mathrm{mH}$) and voltage ($U_\mathrm{SFPS} = 580\,\mathrm{V}$). Therefore, ramp up speed of SFPS is $\mathrm{d}I_\mathrm{SF-SNT}/\mathrm{d}t = U_\mathrm{SFPS}/L_\mathrm{SF-SNT} = 580\,\mathrm{V}/1.23\,\mathrm{mH} \approx 475\,\mathrm{A/ms}$.

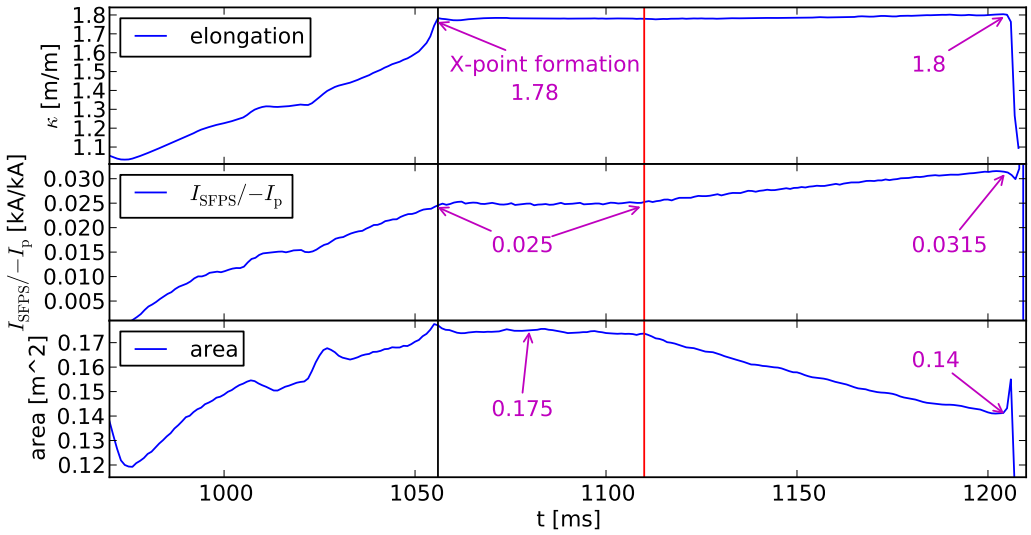

Figure 4.1: Top: elongation calculated by EFIT. Middle: ratio between shaping current and plasma current, which at COMPASS determines plasma shape. Bottom: plasma area calculated by EFIT. Black line show time when X-point is in the vessel. Red line shows time when ratio between shaping field and plasma current increases.

4.4 Plasma Shape Controller

Controller of SFPS starts with pre-programmed waveform without feedback typically to values between 2 kA to 6.5 kA. After Magnetising Field Power Supply (MFPS) crosses zero current, feedforward on plasma current is activated with waveform request starting typically slightly higher than ratio I_{SFPS}/I_p at the time when MFPS crosses zero (this value is typically between 0.019 to 0.024) and goes linearly up to 0.028 for large plasma or 0.031 for small plasma in next 50 ms.

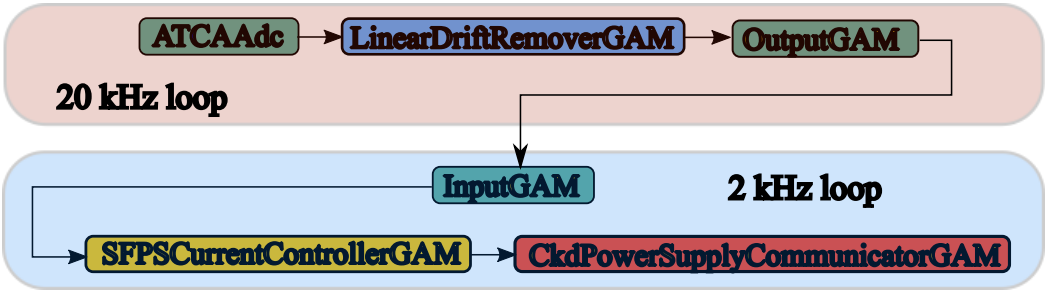

Figure 4.2: Schema of GAMs running in sequence for controlling plasma shape.

Pre-programmed waveform is used to increase plasma current before MFPS crosses zero current and thus saving volt-seconds of MFPS.

Control sequence of plasma shape is similar to other controllers. Firstly, data are collected in ATCAAdc Generic Application Module (GAM), then the drift and offset are removed according to Eq. 2.7 and 2.8 in LinearDriftRemoverGAM and data are transferred from fast thread to slow thread using OutputGAM and InputGAM. In the slow thread, request to SFPS current is calculated according to plasma current using feedforward controller in SFPSCurrentControllerGAM. After that, current request is transferred to packets, according to the document [74],

in the CKDCommunicatorGAM GAM and from there is sent via RS-232 protocol to ČKD Communication Unit (ČKD-CU).

A plasma shape controller is a simple feedforward controller on plasma current. Ratio between plasma current and shaping current determines the elongation. The controller can be described with the following equation:

$$I_{\mathrm{SFPS}}^{\mathrm{req}} = P_{\mathrm{SFPS}} I_{\mathrm{p}} \ , \tag{4.5}$$

where $I_{\mathrm{SFPS}}^{\mathrm{req}}$ is the requested SFPS current and P_{SFPS} is a constant multiplying plasma current I_{p} . As mentioned above, currents in SFPS, MFPS, Equilibrium Field Power Supply (EFPS) and plasma current strongly influence each other through mutual inductances and using same coil MB (see Fig. 1.4). This strong cross-coupling creates oscillations. Therefore, plasma current, which is used as feedforward input signal, is smoothed over last $N = 26$ samples which in slow thread (executing each 500 µs) makes smoothing over 13 ms.

$$I_{\mathrm{SFPS}}^{\mathrm{req}} = P_{\mathrm{SFPS}} \frac{1}{N} \sum_{j=t-26}^{t} I_{\mathrm{p}}^{j}, \tag{4.6}$$

where P_{SFPS} for large plasma is typically 0.028 and for small plasma is 0.031. Level of P_{SFPS} and smoothing time can be set in the configuration file.

In Fig. 4.3 one can see differences between smoothed signal for SFPS current and without smoothing. Oscillations are mainly visible at I_{SFPS} (blue line top

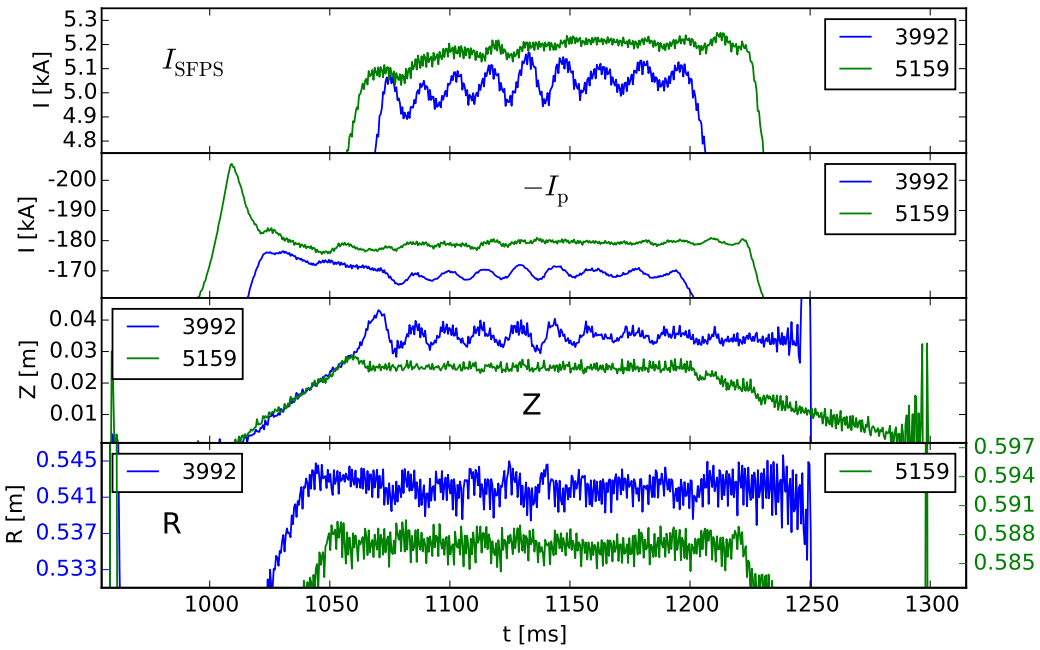

Figure 4.3: Top graph: Oscillations at I_{SFPS} comparing non oscillated when smoothing over 13 ms is used. Second graph: comparing plasma current when oscillations at SFPS current are suppressed by smoothing. Third graph: vertical position when smoothing at I_{SFPS} is not used and when is used. Fourth graph shows horizontal position. Oscillations are slightly visible as well.

graph of Fig. 4.3) itself but also at plasma current (second graph blue line).

Most dangerous are oscillations at vertical position Z (third graph blue line) because these oscillations can cause Vertical Displacement Event (VDE). Slightly visible oscillations are at horizontal position as well (blue line). When smoothing is applied oscillations are suppressed. Smoothing causes also delay in control, therefore, P_{SFPS} has to be configured to start decreasing faster than I_{p} and also it has to start decreasing before I_{p} starts decreasing, otherwise ratio $I_{\mathrm{SFPS}}/I_{\mathrm{p}}$ starts increasing. This leads to smaller and less stable plasma and it can be followed by disruption triggered by VDE. Therefore, operator has to set proper P_{SFPS} constant in the MARTe configuration file. However, if operator does not set decreasing time properly, plasma will disrupt. Therefore, new controller is suggested in Sec. 6.1.

Using D-shaped plasma in SNT configuration allowed reach H-mode at COMPASS as well as reach higher current and fulfilling experimental plans.

5. Electron Density Real-Time Control

Plasma can be characterised by temperature T, pressure p and density n. In plasma, pressure, density and temperature are related together according to following equation:

$$p = T \cdot n \tag{5.1}$$

Plasma density is defined as the number the charged particles (electrons n_e and ions n_i) in a unit volume. Thus $n = n_\mathrm{e} + n_\mathrm{i}$ and in the most cases $n_\mathrm{e} \approx n_\mathrm{i}$. Typical averaged electron density in tokamak devices are in the range of $1 \times 10^{19}\,\mathrm{m}^{-3}$ to $1 \times 10^{20}\,\mathrm{m}^{-3}$. Comparison of temperatures and electron density pressures for various plasma types are in Fig. 5.1

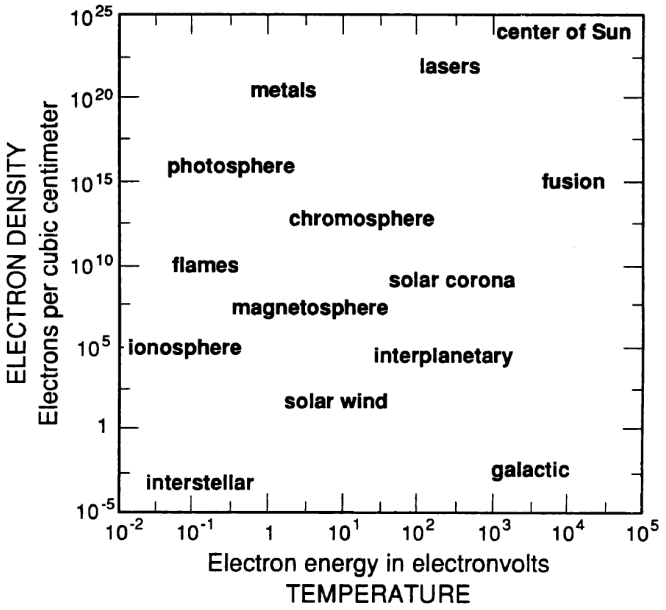

Figure 5.1: Plasma temperatures and electron densities for various types of plasmas [104].

In tokamaks, there is very important empirical electron density limit called *Greenwald limit*, n_GW, [105]. It says what is maximal density which can be reached for particular average plasma current density $\overline{j}$ without disruption. It is defined as:

$$n_\mathrm{GW} = \kappa \overline{j}, \tag{5.2}$$

where n_GW is measured in $1 \times 10^{20}\,\mathrm{m}^{-3}$ and κ is plasma elongation. Plasma current density $\overline{j}$ is total plasma current I_p in area, measured in $\mathrm{MA/m^2}$. This equation for elliptical machines can be rewritten to:

$$n_\mathrm{GW} = \frac{I_\mathrm{p}}{\pi a^2}, \tag{5.3}$$

where a is plasma minor radius in m and I_p is in MA. This is hard limit and typically averaged electron density $\overline{n_\mathrm{e}}$ has to be lower than n_GW [106]. However,

there is possibility to exceed the Greenwald fraction, f_{GW}, defined as:

$$f_{\mathrm{GW}} = \frac{\overline{n_{\mathrm{e}}}}{n_{\mathrm{GW}}} \tag{5.4}$$

for highly peaked electron density profile. As it is shown, the density limit is an edge phenomena. Particles can be added to the core with no deleterious effects as long as MagnetoHydroDynamic (MHD) modes are not destabilised by the peaked pressure profiles [106]. This can be done using pellets injection to the plasma centre or density reduction at the plasma edge [107, 108, 109].

At COMPASS, the electron density is measured with a 2 mm microwave interferometer described in Sec. 5.2 and density can be controlled only with gas puff valve placed at Low Field Side (LFS) as it is written in Sec. 5.3. Beginning of the chapter describes the electron density model 5.1 and the description of the electron density controller with results is in Sec 5.4.

5.1 Electron Density Model

The electron density can be changed by control processes like gas puff or pellet injection and also indirectly with uncontrollable processes such are: recombination of charged particles on the wall, escaping particles, ionisation of neutrals coming to plasma from the vessel or Neautral Beam Injection (NBI) heating system. Changes of the electron density can be evaluated from the following equation:

$$\frac{\mathrm{d}n_{\mathrm{e}}}{\mathrm{d}t} = \phi(t) + f_{\mathrm{rec}} - f_{\mathrm{neut}} \tag{5.5}$$

where $\phi(t)$ is controlled input of gas or pellets. At COMPASS, gas flow controlled by one piezo-electric valve. n_{e} is electron density, f_{rec} represents recycling of neutrals from the vessel and ionised atoms from external heating NBI. f_{neut} is neutralisation process of ions on the wall and also particles carried out with Edge Localised Modes (ELMs) from plasma discharge.

The amount of gas coming into the plasma during a discharge does not depend only at the requested electron density. Vessel condition like cleanness (clean/not so clean/time after last boronisation) has significant impact on the amount of gas needed to reach requested electron density. Vessel condition is not measurable so prediction how much gas vessel will pump or how much gas will be recycled from vessel back to plasma is not possible. Cleaning processes before every campaign and single discharge are the only way how to keep similar conditions for plasma discharges.

Plasma size and plasma position has also effect on the electron density. If plasma is bigger and closer to the vessel recycling f_{rec} of neutrals from the wall has bigger impact as if plasma is smaller and further from the wall. Other effects important for the electron density are penetration of the gas to the centre of the plasma column with and without transport barrier, ionisation and recombination processes, diffusion, self cleaning effect via ELMs, etc. For example during H-mode, due to edge transport barrier at the edge, density and temperature, and thus plasma pressure in the plasma edge is higher, flattening density profile and increasing total density. One of the reason behind creating transport barrier can be that at high auxiliary power levels, strongly sheared flow velocities develop

near the plasma edge that act to stabilise micro-turbulence. However, transition into H-mode from ohmic mode or L-mode is not yet fully understood. Further increasing of the density can even violate Greenwald limit and thus cause disruption. Density can be reduce by ELMs which carry out impurities and lowering density. However, COMPASS does not have any ELM control developed yet.

Control electron density in real-time is crucial to reach the H-mode because L-H transition depends also on the density. Even more, some plasma parameters or processes in plasma depend on the electron density like Alfén waves [110]. Therefore, real-time control of the electron density has been developed to perform electron density scans and to fulfil experimental program. Without electron density feedback control (using only feedforward or pre-programmed gas puff waveform) it is not possible to keep the density constant at requested value or to change the electron density to different desired values during the discharge or to performed controlled electron density ramp-up.

The most important reason is usually the unknown density influx and pumping of the wall. It strongly depends on the number of discharges since last boronisation or glow-discharge cleaning procedure and quality of vacuum. This influences different ratio of recycling and ionisation particles from the wall. Other reason is that behaviour of gas puff valve depends on the reservoir pressure as it discussed at Sec. 5.3.

Electron density control schema for the COMPASS tokamak is drawn in Fig. 5.2. The electron density at COMPASS is measured with a microwave

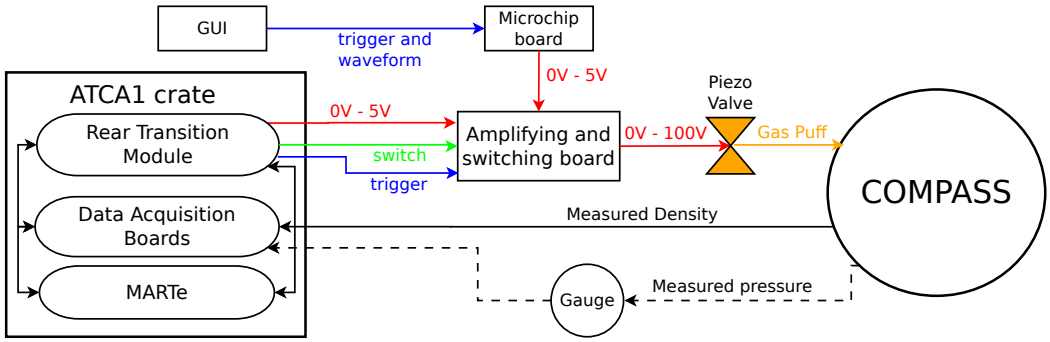

Figure 5.2: Schema of electron density measurement and real-time control. Measured gas pressure in the vacuum vessel is not used in real-time control, therefore, connection is draw with dashed line.

interferometer as it is described in Sec. 5.2. Increasing of density is done by one piezo-electric valve (see Sec. 5.3). However, there are no controlling options how to decrease electron density. For example speed of turbo pumps can not be changed on time scales comparing plasma discharge at the COMPASS tokamak. Gas pressure is measured by a gauge PKR 251 [111]. This signal is measured in real-time but it is not used in control purposes only for monitoring after the discharge to check if there was correct pressure for plasma break down. The gauge was also used for calibrating of the valve.

The electron density control has two obstacle at COMPASS tokamak. First, density cannot be actively decreased as mentioned above. Second, delay in system is big which causes oscillations and overshooting. Delay in control is caused by stickiness of the piezo-electric valve (Sec. 5.3.1), spreading of gas in the vacuum

vessel and non-linearity of the valve (Sec. 5.3). It was also influenced by filtering of measured signal (Sec. 5.4.2) but filter was removed. This, however, causes increasing of noise at electron density measurement.

5.2 Electron Density Diagnostic

The electron density can be measured with a microwave interferometer. Microwave interferometry diagnostic in principle compares phase shift between two electromagnetic waves. One wave *probing wave* is going through plasma and second wave is reference one. A phase shift that appears between probing wave passing through the plasma and a reference wave corresponds to changes of the electron density according to:

$$\varphi = \int_L (k_0 - k_x) dx = k_0 \int_L \left[1 - \left(1 - \frac{\omega_p^2}{\omega^2} \right)^{1/2} \right] \mathrm{d}x, \tag{5.6}$$

where the integral is along the interferometer chord through plasma where L gives length of the chord (therefore, it is line integrated measurement), k_0 and k_x are vacuum and plasma angular wavenumbers ω is microwave frequency and ω_p is plasma frequency given by:

$$\omega_p^2 = \frac{n_e e^2}{\epsilon_0 m}, \tag{5.7}$$

where n_e is electron density, e is electron charge, electron mass is m and ϵ_0 is the vacuum permittivity. The electron density is given as:

$$n_\mathrm{e} = \frac{C}{L} f(n_\mathrm{p}) \varphi, \tag{5.8}$$

where C is conversion from signal measured in volts to electron density, L is length of the interferometer chord (line of sight) through plasma. For circular plasma discharge at COMPASS $L = 0.35\,\mathrm{m}$. Chord length L changes during shaping and plasma movements. Therefore, a correction should be calculated according to chord length L (see Sec. 5.2.3). $f(n_\mathrm{p})$ is function which calculates the electron density according to non-linearity effect of the interferometer and non-homogenous electron density profile. $f(n_\mathrm{p}) = 1$ for the electron density $n_\mathrm{e} < 0.2 \cdot n_\mathrm{crit}$. For the electron density close to the critical density n_crit (see Eq. 5.9) is $f(n_\mathrm{p})$ non-linear. Therefore, non-linearity has to be taken into account as it is described in Sec. 5.2.4.

The critical plasma density can be calculated according to following equation:

$$n_\mathrm{crit} = \frac{\epsilon_0 m_\mathrm{e}}{e^2} \omega^2 = \frac{\epsilon_0 m_\mathrm{e}}{e^2} (2\pi f)^2 = 1.24 \cdot 10^{-2} f^2, \tag{5.9}$$

where $\epsilon_0 = 8.854 \times 10^{-12}\,\mathrm{F/m}$ is vacuum permittivity, $m_\mathrm{e} = 9.1 \times 10^{-31}\,\mathrm{kg}$ is electron mass, $e = 1.602 \times 10^{-19}\,\mathrm{C}$ is charge of electron, ω is angle frequency given as $2\pi f$, where f is frequency of wave passing through plasma.

COMPASS has two different interferometers but can operate only one at the time. Each of them operates with two different electromagnetic waves with frequencies close to each other with wavelength $\lambda = \approx 2\,\mathrm{mm}$. The first and older

interferometer [8, 112] operates at 131 GHz and 133 GHz. The second one, newer, works at 139.3 GHz and 140 GHz. Each of them uses same measuring principle.

Both interferometers utilise two probing waves *S1* and *S2* with slightly different frequencies. The older one, with frequency difference 2 GHz, is shown at

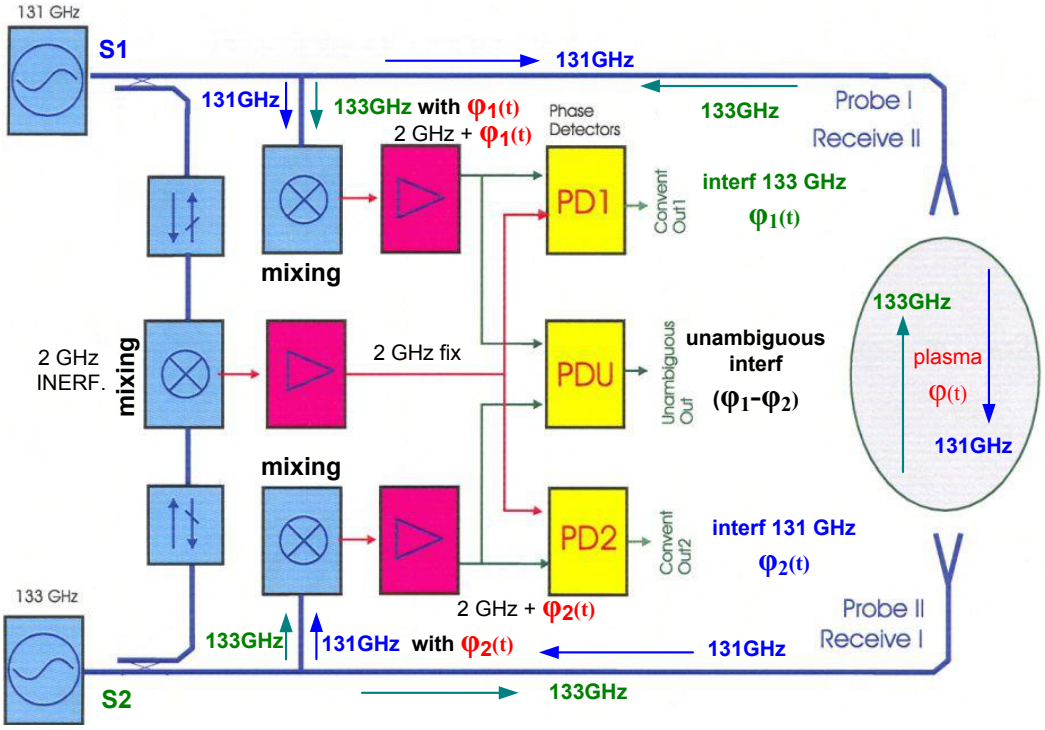

Figure 5.3: Schema of 2 mm microwave interferometer diagnostic. Blue lines show waveguides. Figure is changed from original source Annual Report of the EURATOM/UKAEA Fusion Programme 2000/01, p.109.

Fig. 5.3. The small parts of the both waves, before they enter the plasma, are used to form a reference wave on the first intermediate frequency 2 GHz (note that for so called unambiguous interferometer discussed below this reference wave is not needed). It may be seen from the figure that the main powers of *S1* and *S2* waves are propagating through the same tract including the measured plasma, only in the opposite direction. After the passage through the plasma the both waves are carrying information about the same plasma, but on the own frequency (i.e. phase shifts $\varphi_1 \neq \varphi_2$). Using the two mixers, similarly to formation of the reference 2 GHz intermediate frequency mentioned above (i.e. using another small parts of *S1* and *S2* generators, see figure as well), we can transfer information about the phase shifts φ_1 and φ_2 of the both *S1* and *S2* waves on the two waves with the same intermediate frequency 2 GHz. Because of a small S1 and S2 frequency differences, the difference of the both waves phase shift $\varphi_1 - \varphi_2$ can be so small, that never exceeds the value 2π (one phase jump), unlike to the absolute value of the phase shifts φ_1 and φ_2, reaching during the plasma existence usually several tens of phase jumps (as it is in the case phase detectors PD1 and PD2 utilizing the 2 GHz reference wave, see lower part of Fig. 5.4). Fringe jump for each of the wave occurs at $n_e = 2.4 \times 10^{18}\,\mathrm{m}^{-3}$. Therefore, if we measure directly this phase difference $\varphi_1 - \varphi_2$, then even if one of the probing signals *S1* or *S2* disappears for a short time, after its recovery the absolute phase difference $\varphi_1 - \varphi_2$,

carrying an unambiguous information about the instant plasma density, is measured again. For this reason such interferometer can be called unambiguous, see phase detector PDU in the figure. The situation is demonstrated in the Fig. 5.4.

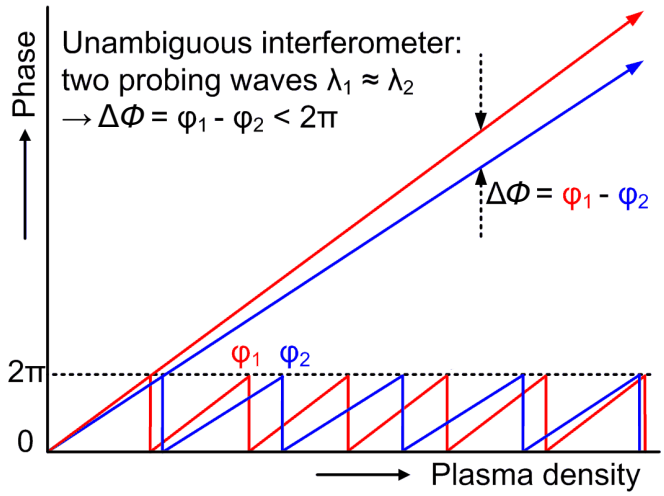

Figure 5.4: A phase shift between two different interferometry waves $S1(\varphi_1)$ and $S2(\varphi_2)$ [113]

Unambiguous phase shift is processed by measuring circuits, which have a voltage output. The obtained line integrated electron density n_e is for $n_e < 0.2 \cdot n_{crit}$ given as:

$$n_e = \frac{C}{L}\Delta\phi\frac{f_1 + f_2}{2(f_2 - f_1)} = \frac{C}{L}(\varphi_1 - \varphi_2)F \tag{5.10}$$

where C is calibration constant converting voltage output from phase shift to the electron density. φ_1 and φ_2 are given according to Eq. 5.6 for source $S1$ and $S2$ and $F = \frac{f_1 + f_2}{2(f_2 - f_1)}$. This measurement for both interferometers is valid to density $n_e < \approx 4.5 \times 10^{19}\,\mathrm{m}^{-3}$.

To obtain correct electron density at COMPASS three things have to be taken into account. The fringe jumps have to be summed if they occur and the electron density has to be stitched as it can be seen in Fig. 5.5. This can be done with software in real-time as it is described in Sec. 5.2.1. Then chord length L has to be calculated according to plasma shape and plasma position. This is described in Sec 5.2.3. Electron density measurement is linearised with Eq. 5.10, however, for electron densities higher than $0.2 \cdot n_{crit}$ this equation gives wrong results. Therefore, non-linear effect has to be taken into the account and the electron density has to be estimated with respect of it (see Sec. 5.2.4). If this correction is not calculated, measurement can lead to unrealistic values higher than critical density.

Main difference between these two interferometers is the range of measurement without fringe jump. The fringe jump at the old interferometer occurs typically around $n_e = 15.8 \times 10^{19}\,\mathrm{m}^{-3}$ while new interferometer measures up to $n_e = 24 \times 10^{19}\,\mathrm{m}^{-3}$ without fringe jump. Detailed comparison is written in Sec. 5.2.1 and Sec. 5.2.2

New interferometer is installed on the same position as older one. Older one can be used in case of malfunction of newer one. Measured electron density

signal from both interferometers can be used in real-time control for controlling electron density. Only calibration constant C has to be changed in the MARTe configuration file.

5.2.1 Interferometer with the Fringe Jumps

Each wave (*S1*(φ_1), *S2*(φ_1)) measures electron density up to $\approx 2.4 \times 10^{18}\,\mathrm{m}^{-3}$ and then fringe jump occurs. Whenever the electron density increases, phase shift between two electromagnetic waves ($\Delta\phi = \varphi_1 - \varphi_2$) passing through plasma increases too until phase shift reaches 360°. This is represented by maximal voltage on the output and fringe jump at electron density measurement occurs also at unambiguous signal. Then, the output voltage immediately drops to zero. In case the electron density keeps rising, the output voltage increases from 0 V again. Vice versa, if density decreases, the phases shift goes towards 0° (corresponding to 0 V at the output) and when the phase shift crosses 0° then the output voltage jumps to maximum. Applying Eq. 5.10 for $\Delta\phi$ maximal density before fringe jump occurs is $n_\mathrm{e} = 2.4 \times 10^{18}\,\mathrm{m}^{-3} \cdot F = 2.4 \times 10^{18}\,\mathrm{m}^{-3} \cdot 66 = 15.8 \times 10^{19}\,\mathrm{m}^{-3}$. Fringe jumps can be caused also by pellet injection, rotation of magnetic islands or ELMs [114]. However, it is not case of COMPASS because COMPASS has higher measurement range till fringe jump occurs.

These jumps have to be counted together and the phase has to be reconstructed to obtain the temporal evolution of the electron density, see Fig. 5.5. Blue lines

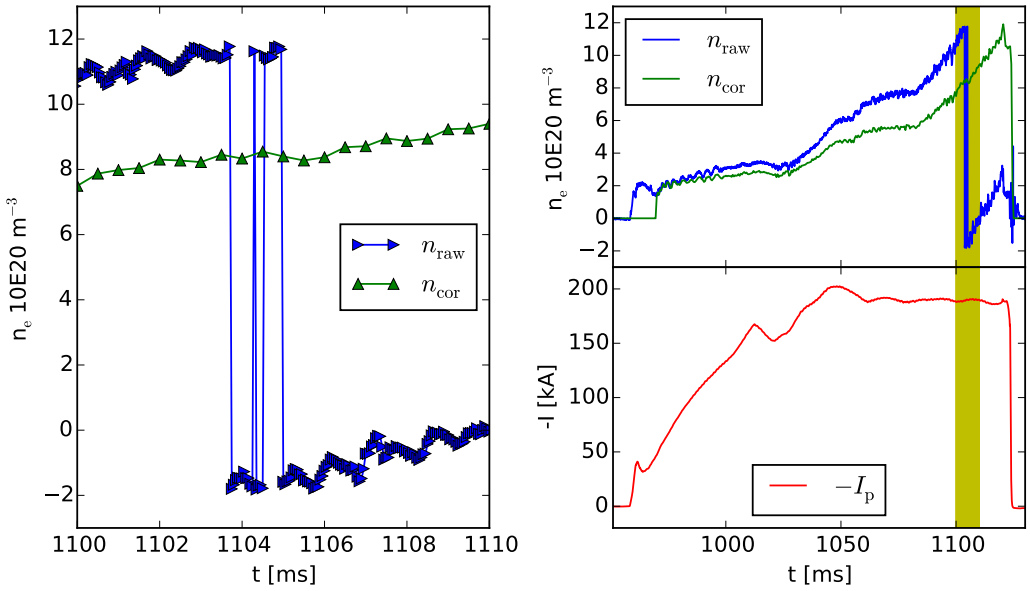

Figure 5.5: The raw electron density signal measured with the fringe jumps and the reconstructed electron density after a correction on the plasma shape.

on the graph show obtained electron density n_e. Sudden drop and sudden rise of the electron density is visible on the blue lines. Yellow region shows area of occurred fringe jumps. That region is zoomed in left part of figure. Plasma current I_p (red line) is stable during jumps on electron density and there is no physical reason for such behaviour. Rising of electron density from −2 V is observed after fringe jump. This offset is caused by an electronic circuit in the interferometer when before the discharge offset of 2 V is used. This offset is removed the same

way as drift at magnetics are removed using Eq. 2.7 and Eq. 2.8. This $-2\,\mathrm{V}$ corresponds with above mentioned 0 V. A real-time algorithm has to count these fringes and to stitch density together. Corrected electron density n_{cor} is without jumps and keep rising during whole discharge (green lines).

Unfortunately, there are more effects visible together. First effect is that density is measured in fast thread 50 µs but density fringe jump calculation is in slow thread 500 µs cycle. Therefore, corrected electron density (green line) has ten time less data. Second effect is that the obtained electron density is higher because corrected electron density is recalculated according to chord length for diverted plasma shape.

5.2.2 Interferometer without the Fringe Jumps

Secondly mentioned microwave interferometer is working at higher frequencies 139.3 GHz and 140 GHz. Smaller difference between frequencies gives approximately 3 times higher density measurement than older one. The electron density can be measured up to critical density $n_{\mathrm{crit}} = 24 \times 10^{19}\,\mathrm{m}^{-3}$. This theoretical value is higher than real electron densities (see Sec. 5.2.3 and Sec. 5.2.4). Typical electron densities reached during experiments at COMPASS are in the range of 4×10^{19} m^{-3} to 8×10^{19} m^{-3}. In dedicated experiments for density disruption mitigation electron densities can go up to $12 \times 10^{19}\,\mathrm{m}^{-3}$. These densities are fully covered with new interferometer measurement range.

5.2.3 Influence of the Plasma Shape and the Plasma Position on the Electron Density Measurement

The microwave interferometers measure the line integrated electron density along the chord passing through the plasma at COMPASS at position $R = 0.56\,\mathrm{m}$ (Fig. 5.6 vertical black dashed line). Measured signal is normalised to standard circular plasma size with radius $r = 0.2\,\mathrm{m}$ (red curve). Every time when plasma moves in radial direction (blue and green curves) or plasma shape is changed the electromagnetic wave from the interferometer measures electron density across different plasma length. Therefore, the electron density has to be calculated according to real chord length L where electromagnetic wave crosses plasma instead of the normalisation at $r = 0.2\,\mathrm{m}$. The length of the chord on the position where the electromagnetic wave crosses plasma can be calculated off-line from the EFIT reconstruction [88]. However, EFIT data are not available during the plasma discharge and COMPASS does not have any type of the plasma shape real-time reconstruction. Therefore estimation of plasma length at interferometer position has to be calculated in real-time from signals which are available in real-time system.

First approximation of chord length L from Eq. 5.11 is assumed as L_1:

$$L_1 = 1 - C \cdot \frac{I_{\mathrm{SFPS}}}{I_{\mathrm{p}}}, \tag{5.11}$$

where $C = \dfrac{0.35}{0.031}$ comes from ratio between $\dfrac{I_{\mathrm{SFPS}}}{I_{\mathrm{p}}}$ for diverted plasma and chord length $L = 0.35\,\mathrm{m}$ in circular shape at the interferometer chord for typical plasma

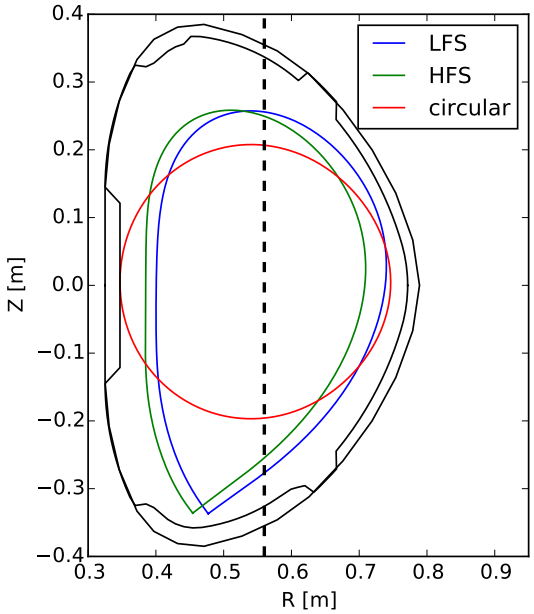

Figure 5.6: Comparison of different plasma current profile and positions.

position. After observation, that with increasing ratio $I_{\mathrm{sfps}}/I_{\mathrm{p}}$ after certain values plasma does not increase elongation, but becomes smaller (see Sec. 4.1). As can be seen from Fig. 5.6, the length of the chord depends on plasma elongation and plasma position.

Therefore, in the scope of this thesis, plasma length was estimated for real-time calculation, using R and Z position (see Chap. 3), plasma current I_{p} (Chap. 2), and shaping current I_{SFPS} (Chap. 4). For this purpose, function was searched which fits these inputs to match the interferometry chord length calculated from EFIT reconstruction. Function was chosen in the following form to obtain best results:

$$L_{\mathrm{EFIT}}(t) = f\left(R^i(t), Z^j(t), \left(I_{\mathrm{SFPS}}/I_{\mathrm{p}}\right)^k(t)\right), \tag{5.12}$$

where L_{EFIT} is plasma length at the place of interferometer chord calculated from EFIT, and $i, j = 1, \cdots, 5$ and $k = 1, \cdots, 10$. Several discharges for this purpose were developed. Especially, when plasma is moving vertically Z (discharge #8171) (Fig. 5.7) and radially R (#8256) (Fig. 5.8), and plasma shape (i.e. elongation κ) is changing significantly (#8335) (Fig. 5.9) or H-mode was achieved (#8238) and also L-mode discharges (#8338, #9114) were added (see Fig. 5.10). Approximation was calculated with time stamps every 5 ms in all these discharges to cover the most extreme positions and shapes with enough amount of the points.

Good agreement between length obtained from EFIT and fitted function gives following equation:

$$L_2 = \sum_{1=0}^{5} C_i \left(\frac{I_{\mathrm{SFPS}}}{I_{\mathrm{p}}}\right)^i + C_R \cdot R + C_Z \cdot Z + C, \tag{5.13}$$

where constants are listed in Tab. 5.1. When plasma moves vertically (bottom graph of Fig. 5.7) function L_2 and L_{EFIT} reconstructed from EFIT are in good agreement almost during whole discharge. Some disagreement can be seen around time 1000 ms and at the end of discharge, but also at time when plasma is at

C_1	C_2	C_3	C_4	C_5	C_R	C_Z	C
-12.04	-3.039e3	-3.334e5	-1.3e7	$-1.634e8$	1.182	-0.287	-0.234

Table 5.1: Fitted constants for subtracting induced currents from Resonant Magnetic Perturbations (RMPs) and Fast Amplifier for Radial Magnetic Field (FABR), and Fast Amplifier for Vertical Magnetic Field (FABV) power supplies.

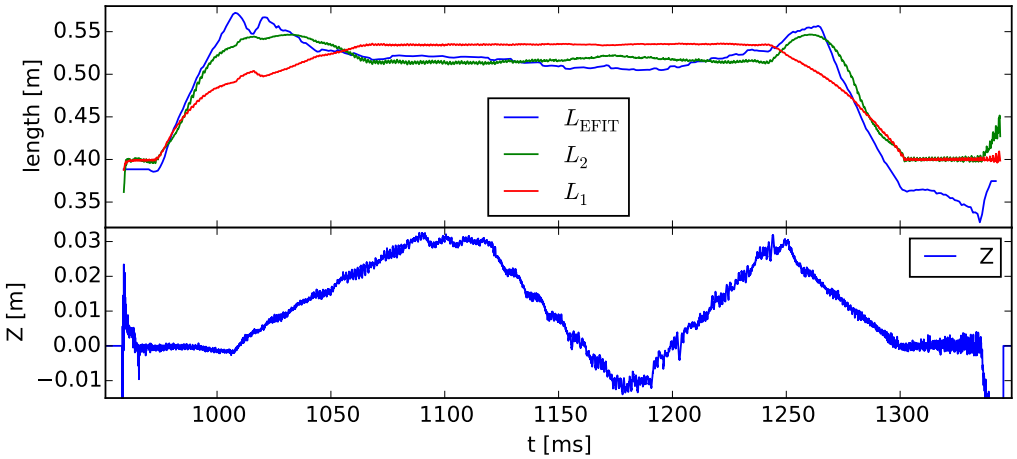

Figure 5.7: Comparison of estimated plasma length according to equation 5.11 and 5.13 with EFIT reconstructed chord length L_{EFIT} for ohmic mode discharge when plasma was moved 4 cm in vertical direction. Bottom graph shows vertical position.

the most down position. Estimated length chord L_1 gives higher error during plasma current rise and current ramp-down phase.

In the case, plasma moves radially (see Fig. 5.8), same conditions can be observed. Also, estimated length L_2 agrees better with EFIT calculated length

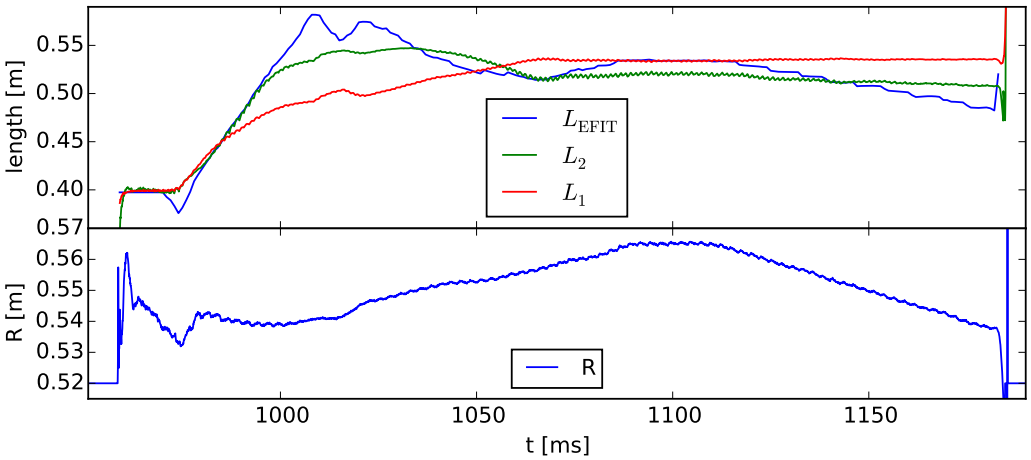

Figure 5.8: Comparison of estimated plasma length according to equation 5.11 and 5.13 with EFIT reconstructed length L_{EFIT} for ohmic mode discharge when plasma was moved 3 cm in the horizontal direction. Bottom graph shows horizontal position.

L_{EFIT} than L_1, especially at the beginning of the discharge. However, same two peaks are visible at L_{EFIT} but there are not visible in none of fitting function.

These peaks can be cause by fast changes of plasma current, shaping field and Magnetising Field Power Supply (MFPS) current. Also, it can be caused, that fifth order of polynomial function is not sufficient. However, significantly better results were not observed even when polynomials for $I_{\mathrm{SFPS}}/I_{\mathrm{p}}$ was increased to 10th order and R and Z were polynomials off 5th order. Also magnetic current from Internal Partial Rogowski (IPR) coils were used. However, IPR coils added big noise, and did not bring any benefit either.

The biggest difference between behaviour of L_1 and L_2 is visible in Fig. 5.9 when ratio $I_{\mathrm{SFPS}}/I_{\mathrm{p}}$ was changing. As it can be seen at bottom graph, the elonga-

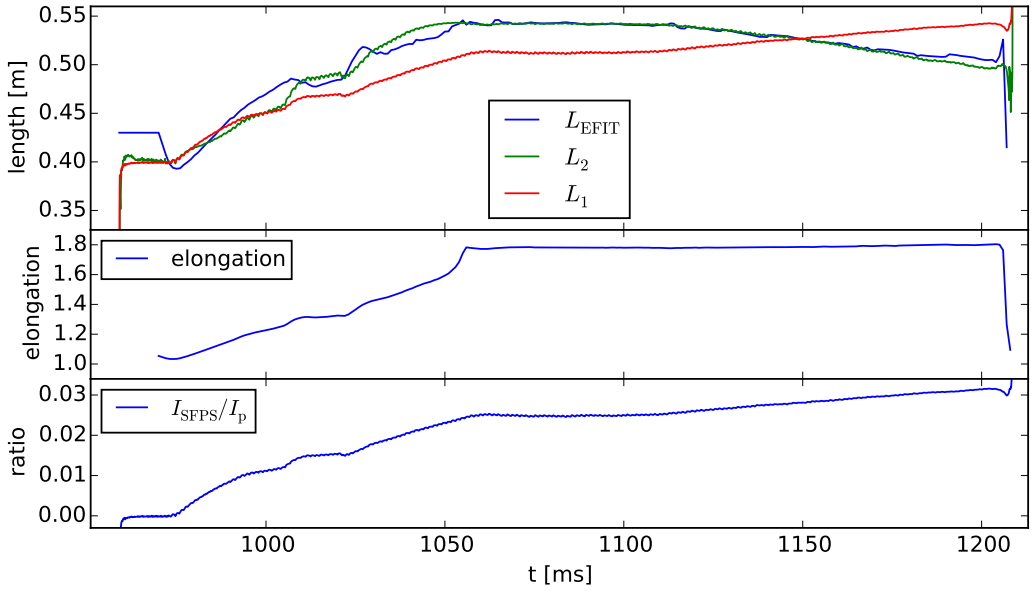

Figure 5.9: Comparison of estimated plasma length according to equation 5.11 and 5.13 with L_{EFIT} for ohmic mode discharge when ratio $I_{\mathrm{SFPS}}/I_{\mathrm{p}}$ determining plasma elongation was changed. Middle graph shows plasma elongation calculated by EFIT. Bottom graph shows ratio $I_{\mathrm{SFPS}}/I_{\mathrm{p}}$.

tion is constant during the discharge, the ratio $I_{\mathrm{SFPS}}/I_{\mathrm{p}}$ is increasing. However, plasma length is decreasing as it can be seen from L_{EFIT} and L_2 but L_1 follows the increasing ratio.

In Fig. 5.10 length approximation is calculated for L-mode and H-mode discharges. It can be seen that H-mode makes no different in changing chord length estimation using approximation and fits on EFIT calculated length during the flat top phase.

Comparing results for different discharges we can state that newly fitted function is in good agreement during the flat top phase. Discrepancies may occur during fast changes in the ramp-up and ramp-down phase. Also discrepancy is visible when plasma is moved horizontally. Reason behind can be that plasma also shrinks while moving and it is not detectable using signals available in real-time.

Eq. 5.13 is used in real-time calculation. It is in good agreement in most cases with EFIT calculation especially in plasma flat-top phase[1].

[1]For the old interferometer only function calculated length of plasma is used according to: $n_{\mathrm{e}}(L_1) = n_{\mathrm{e}}(L_1, f(n_{\mathrm{p}}))$. This is coming from historical reason when reconstruction to non-linearity of interferometer was consider only after new interferometer was built-in.

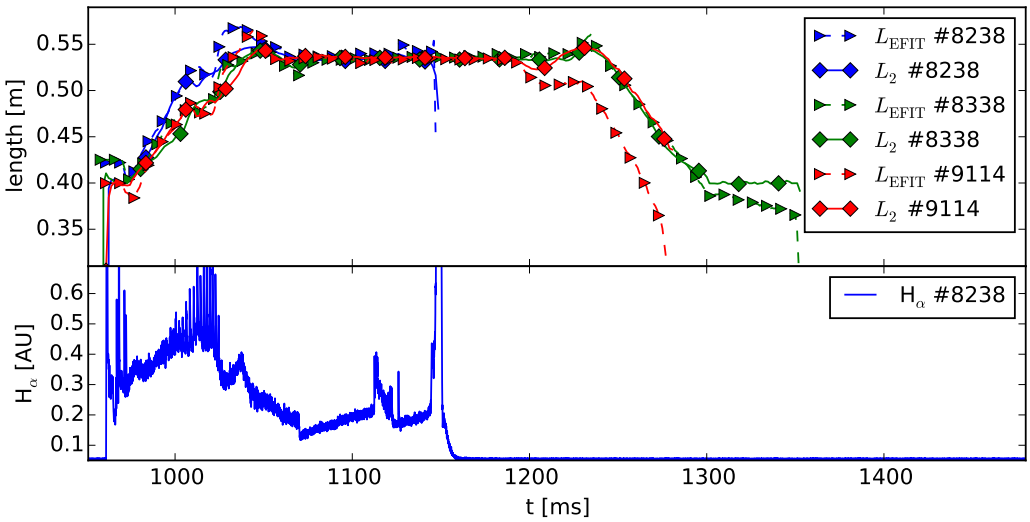

Figure 5.10: Comparison estimated length according to equation 5.13 with L_{EFIT} for H-mode and ohmic mode discharges. Bottom graph shows H_α for H-mode discharge

The line averaged electron density, $n_{\mathrm{L}}^{\mathrm{cor}}$, corrected to the estimated length L_2 is then calculated according to following equation:

$$n_{\mathrm{L}}^{\mathrm{cor}} = \frac{n_{\mathrm{avg}}}{L_2} \cdot 0.4, \tag{5.14}$$

where n_{avg} is the averaged electron density obtained from the interferometer for circular plasma shape with diameter 0.4 m.

5.2.4 Influence of the Non-Linearity Effect of the Electron Density Measurement

As aforementioned, Eq. 5.10 is valid only for small electron densities compared to critical density. Densities higher than $n_{\mathrm{e}} > 0.2 \cdot n_{\mathrm{crit}}$, typically reached at COMPASS, have to be corrected according to phase, which is non-linearly dependant on electron density. Density at COMPASS is measured with two different frequencies f_1 and f_2 where $f_1 < f_2$. Let us denote: obtained electron density from the interferometer n_{o}, $a = (f_1/f_2)^2 < 1$, $b = f_2/f_1 > 1$ and refractive index given as:

$$r = \sqrt{1 - n_{\mathrm{o}}/n_{\mathrm{crit}}}, \tag{5.15}$$

Now we will denote normalised density n_{norm} to critical density n_{crit_1} with lower frequency and used introduced notation, and Eq. 5.9 one can write:

$$n_{\mathrm{norm}} = \frac{n_{\mathrm{o}}}{n_{\mathrm{crit}_1}} \rightarrow \frac{n_{\mathrm{o}}}{n_{\mathrm{crit}_2}} = n_{\mathrm{norm}} \frac{n_{\mathrm{crit}_1}}{n_{\mathrm{crit}_2}} = n_{\mathrm{norm}} \left(\frac{f_1}{f_2}\right)^2 = n_{\mathrm{norm}} a \tag{5.16}$$

Combing Eq. 5.15 with Eq. 5.16 can be written for refractive index of wave f_1: $r_1 = \sqrt{1 - n_{\mathrm{norm}}}$ and for wave with f_2: $r_2 = \sqrt{1 - n_{\mathrm{norm}} \cdot a}$. A phase φ of a wave with wavelength $\lambda = c/f$ in vacuum, expressed in 2π, is after crossing plasma with length L and refractive index r defined as:

$$\varphi = \frac{L}{\lambda} r = \frac{L}{c} f r \tag{5.17}$$

Phase difference $\Delta\varphi$ of wave crossing plasma with refractive index r with wave going through vacuum is:

$$\Delta\varphi = \frac{L}{c} f(1-r) \tag{5.18}$$

From here for two waves with two different frequencies f_1 and f_2 phase difference can be expressed as:

$$\Delta\varphi_1 = \frac{L}{c} f_1(1-r_1) = \frac{L}{c} f_1 \left(1 - \sqrt{1 - n_{\mathrm{norm}}}\right) \tag{5.19}$$

$$\Delta\varphi_2 = \frac{L}{c} f_2(1-r_2) = \frac{L}{c} f_2 \left(1 - \sqrt{1 - n_{\mathrm{norm}} \cdot a}\right) \tag{5.20}$$

The unambiguous interferometer at COMPASS measures phase difference $\Delta\phi$ as between $\Delta\varphi_1$ and $\Delta\varphi_2$:

$$\begin{aligned} \Delta\phi_{\mathrm{cor}} &= \frac{L}{c} f_1 \left(1 - \sqrt{1 - n_{\mathrm{norm}}}\right) - \frac{L}{c} f_2 \left(1 - \sqrt{1 - n_{\mathrm{norm}} \cdot a}\right) = \\ &= \frac{L}{c} f_1 \cdot \left(1 - \sqrt{1 - n_{\mathrm{norm}}} - b \left(1 - \sqrt{1 - n_{\mathrm{norm}} \cdot a}\right)\right) \end{aligned} \tag{5.21}$$

Measured phase shift $\Delta\phi_{\mathrm{cor}}$ between two phases is linearised with Eq. 5.22 using first approximation of Taylor series $\sqrt{1 - n_{\mathrm{norm}}} = 1 - 0.5 \cdot n_{\mathrm{norm}}$:

$$\begin{aligned} \Delta\phi_{\mathrm{lin}} &= \frac{L}{c} f_1 \left(1 - 1 + 0.5 \cdot n_{\mathrm{norm}}\right) - \frac{L}{c} f_2 \left(1 - 1 + 0.5 \cdot n_{\mathrm{norm}} \cdot a\right) = \\ &= \frac{L}{c} f_1 \cdot \left(0.5 \cdot n_{\mathrm{norm}} - b \left(0.5 \cdot n_{\mathrm{norm}} \cdot a\right)\right) = \\ &= \frac{L}{c} f_1 \cdot 0.5 \cdot n_{\mathrm{norm}} (1 - b \cdot a) \end{aligned} \tag{5.22}$$

Obtained linearised phase shift $\Delta\phi_{\mathrm{lin}}$ is wrongly interpreted as electron density. Therefore, correction to non-linearity has to be taken into account and correct density has to be calculated. Difference between wrongly interpreted density from phase shift $\Delta\phi_{\mathrm{lin}}$ and correct density from phase shift $\Delta\phi_{\mathrm{cor}}$ for homogenous electron density is visible in Fig. 5.11. Vertical line shows that $\Delta\phi = 0.2\,\mathrm{rad}$

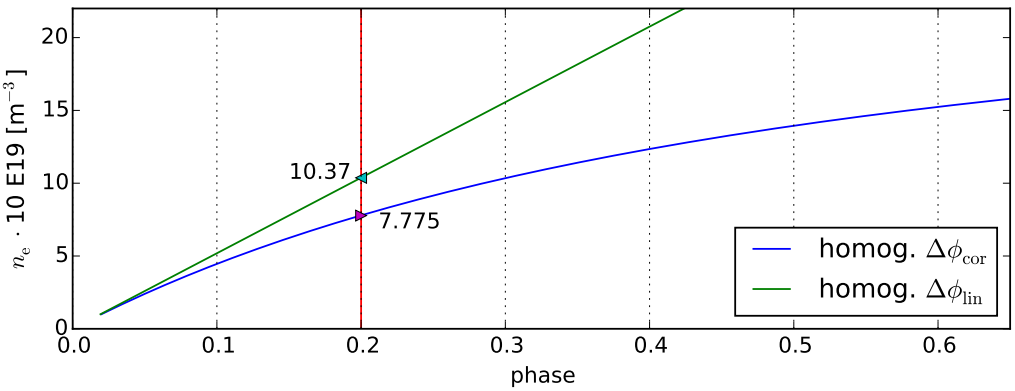

Figure 5.11: Phase shift for homogenous density without correction to non-linearity labelled as homog. $\Delta\phi_{\mathrm{lin}}$ and with non-linearity taken into account labelled as homog. $\Delta\phi_{\mathrm{cor}}$.

wrongly interprets density as $10.37 \times 10^{19}\,\mathrm{m}^{-3}$ while the correct electron density

is only $7.775 \times 10^{19}\,\mathrm{m}^{-3}$. With increasing phase shift difference between linearised density and correct one is increasing.

To obtain correct density, reduction coefficient C_{red} between wrongly interpreted density n_{wi} and real density n_{cor} has to be found in corresponding form: $n_{\mathrm{cor}} = C_{\mathrm{red}}(n_{\mathrm{wi}}) \cdot n_{\mathrm{wi}}$. Pairs of $n_{\mathrm{cor}},\ n_{\mathrm{wi}}$, like it is displayed with vertical line in Fig. 5.11, were got for 24 different values $\Delta\phi$. Reduction coefficient for homogenous electron density can be found analytically.

However, the electron density profile in the tokamak is not homogenous. In this case, analytical solution is not possible. Therefore, the reduction coefficient, $C_{\mathrm{red}}(r/a)$, has to be numerically integrated for given density profile. Density profile is given as:

$$n(r/a)/n_{\mathrm{crit1}} = n_{\mathrm{norm}}(0) \cdot y(r/a), \tag{5.23}$$

where $n_{\mathrm{norm}}(0) = n(0)/n_{\mathrm{crit1}}$ is electron density at the interferometry chord which crosses plasma centre with the highest density. $n(0)$ are 13 different densities from $1 \times 10^{19}\,\mathrm{m}^{-3}$ to $24.1 \times 10^{19}\,\mathrm{m}^{-3}$. Radial profiles are given as $y(r/a) = 1 - (r/a)^p$, where $a = 0.2\,\mathrm{m}$ and $p = 1,\ 3,\ 4,\ 5,\ 9$ are chosen values. These profiles normalised

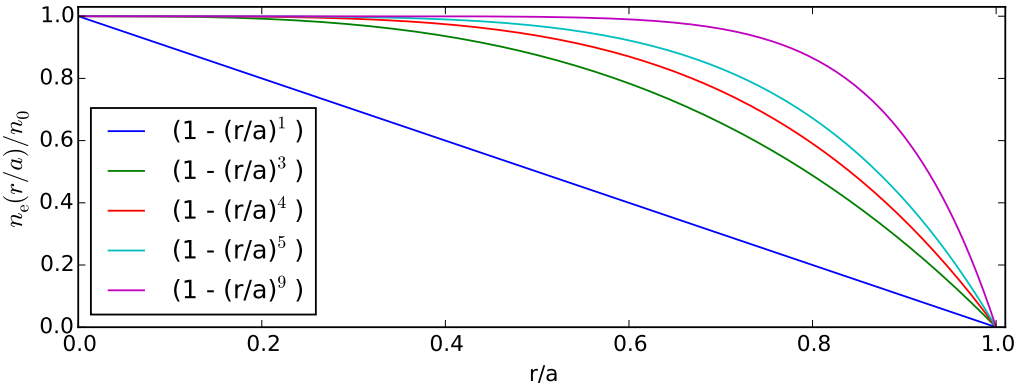

Figure 5.12: Different electron density profiles normalised to maximal density in the centre.

to maximal density in the centre $n(0)$ can be seen in Fig. 5.12.

Each density profile was divided to 300 points and $\Delta\phi_{\mathrm{lin}}$ at every point is calculated according to Eq. 5.22 and $\Delta\phi_{\mathrm{cor}}$ according to Eq. 5.21. This way dependences $\Delta\phi_{\mathrm{cor}}(n_{\mathrm{norm}})$ and $\Delta\phi_{\mathrm{lin}}(n_{\mathrm{norm}})$ are obtained for mentioned density profiles with integration over the profile (interferometer gives line integrated density). Then reduction coefficient is calculated as $\Delta\phi_{\mathrm{lin}}(n_{\mathrm{norm}})/\Delta\phi_{\mathrm{cor}}(n_{\mathrm{norm}})$ for every profile.

The interferometer gives incorrect electron density averaged (this includes correction to the length of line of sight - Eq. 5.14) along the wave path. Therefore, calculated electron density for each of the profile and for all 13 different densities are plotted in Fig. 5.13 at y-axis over real averaged density x-axis. One can see that for linear electron density profile $1 - (r/a)$ the interferometer shows value $42 \times 10^{19}\,\mathrm{m}^{-3}$ while real averaged density is only $12 \times 10^{19}\,\mathrm{m}^{-3}$ which is half of critical density. Non-linearity has higher influence with increasing densities closer to critical density and with increasing p. Said other way, probing wave spends more time in the region of higher densities if total density is higher and profile is flatter - higher p. Therefore, non-linearity effect is not negligible. To obtain

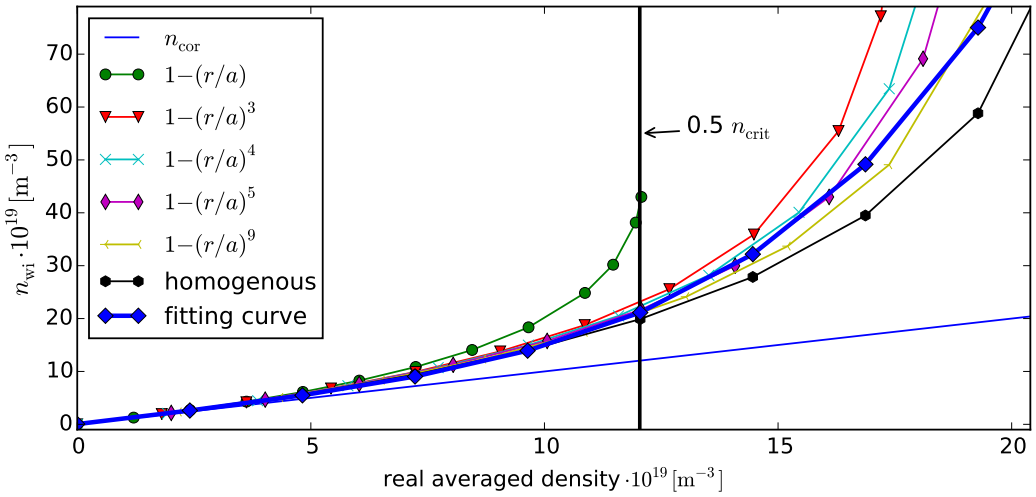

Figure 5.13: Calculated electron density for different profiles. Fitting curve approximates calculated densities for different profiles.

density corrected to non-linearity, the obtained value from the interferometer needs to be corrected with respect to density profile and non-linearity. In Fig. 5.13 can be see, that for curves with $p = 3$ and bigger, there is no high dependence on electron density profile, for the densities up to $0.5 \cdot n_{\mathrm{crit}_1} \approx 12 \times 10^{19}\,\mathrm{m}^{-3}$ which is maximal density obtained at the COMPASS tokamak. Therefore, these curves were approximated with fitting curve according to $n_{\mathrm{fit}} = 1.05 \cdot n_{\mathrm{real}} + n_{\mathrm{crit}_1}(0.35 + n_{\mathrm{real}}/n_{\mathrm{crit}_1})^6$. Then reduction coefficients from fitting curve were obtained as $f_{\mathrm{reduc}} = n_{\mathrm{real}}/n_{\mathrm{fit}}$.

These coefficients were used to create function, which wrongly interpreted averaged density obtained from the interferometer n_{wi} converts to density corrected to non-linearity n_{cor}. This function is given as given as:

$$n_{\mathrm{cor}} = n_{\mathrm{wi}} / \left(1 + 0.8 \frac{n_{\mathrm{wi}}}{n_{\mathrm{crit}_1}}\right) \tag{5.24}$$

This function was fitted by trial-error method. The difference between the wrongly interpreted electron density n_{wi} and corrected density n_{cor} can be seen in Fig. 5.14. The wrongly interpreted density shows $n_{\mathrm{wi}} = 15 \times 10^{19}\,\mathrm{m}^{-3}$, however,

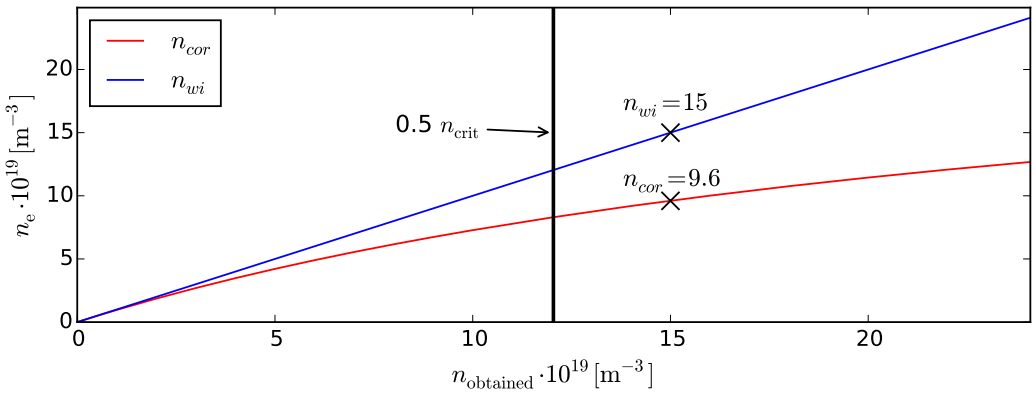

Figure 5.14: Difference between wrongly interpreted density and density corrected to non-linearity.

in reality this value is only $\approx 9.6 \times 10^{19}\,\mathrm{m}^{-3}$. This difference rises with increasing density close to critical density. Wrongly interpreted density could give values much higher than critical density which is not possible. Also it can be seen that there is no big difference between linearised and correct values for densities lower than $0.2 \cdot n_{\mathrm{crit}}$.

To remind, in this section, electron density was taken as averaged density. It means it was calculated according to interferometer line of sight. This means that $n_{\mathrm{wi}} = n_{\mathrm{L}}^{\mathrm{cor}}$ from Eq. 5.14. Therefore, Eq. 5.24 can be rewritten in the following form:

$$n_{\mathrm{cor}} = n_{\mathrm{L}}^{\mathrm{cor}} / \left(1 + 0.8 \frac{n_{\mathrm{L}}^{\mathrm{cor}}}{n_{\mathrm{crit}_1}}\right) \tag{5.25}$$

n_{cor} is then used as input for Proportional Integral (PI) controller for feedback density control.

5.3 Electron Density Actuator

The electron density at COMPASS is controlled with one piezo-electric valve closely attached to the vessel. The valve is connected to a reservoir filled with D_2 gas at a pressure typically between 0.9 bar to 1.1 bar. Depending on the pressure in the reservoir, the vessel is filled to different pressure as it can be seen in Fig. 5.15. In both graphs applied voltage for the valve is same. However, left graph shows reservoir filled to 0.9 bar while the reservoir on right side of the figure is filled up to 1.1 bar. This caused increasing of gas pressure in the vessel by 20% for the same valve opening voltage settings. First vertical line shows when gas puff was started. Second vertical line shows when gas puff was changed. Third line shows when change on pressure was measured by vacuum gauge. Comparing left and right figure one can see that higher pressure in the reservoir does not influence reaction speed of the valve. A time delay between line 2 and 3 shows the delay between opening the valve and measurement. This delay is approximately 45 ms however, this includes also measurement delays by the gauge.

The piezo-electric valve opens with an analog signal between 0 V to 100 V. This signal is amplification of 0 V to 5 V signal which can be provided by two different systems (see Fig. 5.2). First one is an electronic board assembled with a Microchip dsPIC30F4013 (Microchip board) which provides 5 V Pulse Width Modulation (PWM) signal. This signal is filtered to give 0 V to 5 V analogue output[2]. In the second system, output is provided by the Rear Transition Module (RTM) controlled by MARTe in real-time. Real-time control directly gives voltage which is changed every 500 µs.

First system can be used during the experiment and is also used during the glow discharge procedure (used for the vessel cleaning). During the glow-discharge procedure, this valve is used for decreasing breakdown voltage by factor of 10, when D_2 is puffed to the vessel filled with He[3]. The output signal is set as pre-defined waveform in the Graphical User Interface (GUI), transferred to the Microchip board and activated by a trigger. In this system, the valve can

[2]Controlled boards with Microchips, which are typically used at COMPASS, do not have analog outputs. Therefore, PWM modulation was chosen.

[3]D_2 ionisation energy is 15.47 eV [115] and He first ionisation energy is 24.59 eV [116].

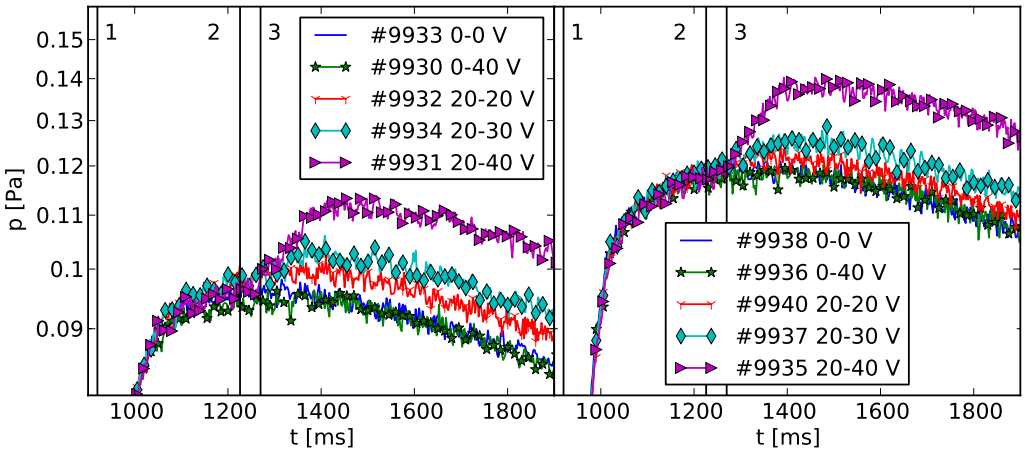

Figure 5.15: Left: Gas pressure in the vessel. Reservoir was filled to 0.9 bar. First number in the legend is discharge number. Second number means voltage applied at the gas puff valve during 300 ms after an initial 6 ms pulse with 100 V. Third number shows voltage applied during next 100 ms. Right graph shows the same voltage and timing of opening valve as left only difference is that reservoir is filled to 1.1 bar. Detail waveforms of voltage applied at the gas puff valve are at the left side of Fig. 5.19. Vertical line labelled with 1 shows when gas puff is started. Second vertical line shows when gas puff was changed. Third line shows when first change was measured by vacuum gauge.

be triggered in two ways. Either with an external trigger from the timing unit (tokamak plasma discharge) or manually triggered by clicking in GUI.

Second system controls the valve in real-time from RTM via MARTe during discharge (Sec. 5.4). Both systems are connected to the specific board with the amplifier, which also selects the input source dependent on another control signal from the real-time system.

5.3.1 Stickiness of the Piezo-Electric Valve

Piezo-electric valves suffer from stickiness especially on the time scales of COMPASS experiment. Every piezo-electric valve is behaving different way, throughput rises non-linearly and also suffers on stickiness. Therefore, calibration of the valve has been done to open and close valve as fast as possible. Characteristic of piezo-electric valve used at COMPASS is in Fig. 5.16. Stickiness depends on the valve usage. After several hours of non-using the valve its time response is different and gas pressure filled in the vessel varies significantly (see the difference in shot #4344 and #4356 in Fig. 5.17).

Firstly, time necessary to open the valve and fill the vessel at desired pressure was tested. Short pulses 5 ms to 10 ms long (see Fig. 5.17 - length of opening is plotted up to 9 ms) at maximum voltage 100 V were used. From experiments' expertise if the valve is open for less than 5 ms, in the vessel will not be enough pressure for plasma breakdown. We can see that first 5 ms opening pulse (blue dashed line - discharge #4344) injected significantly less gas as the second opening pulse at 5 ms (green dashed line marked with circles - discharge #4345). This is caused by stickiness of the valve. Pressure in the vessel increases with longer

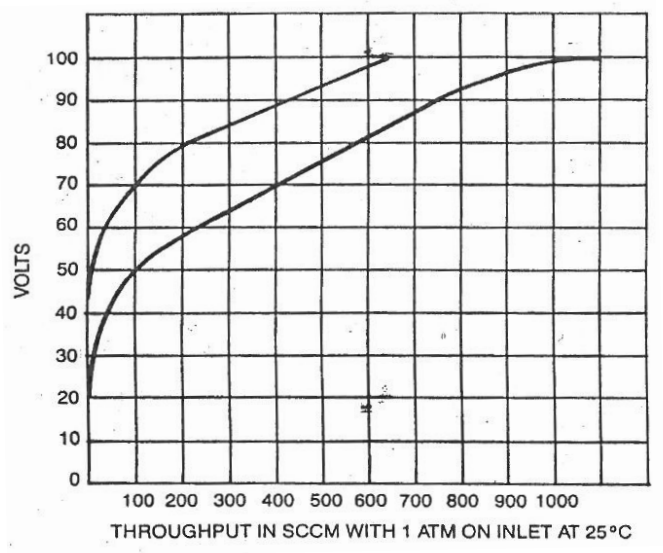

Figure 5.16: The graph depicts throughput in the PEV-1 piezo-electric valve. The two lines represent the low and high end of the scale. All the valves fall between the lines. Unit Standard Cubic Centimeters per Minute (SCCM) has conversion to standard SI units as 1 sccm = 1.67 Pa l /second.

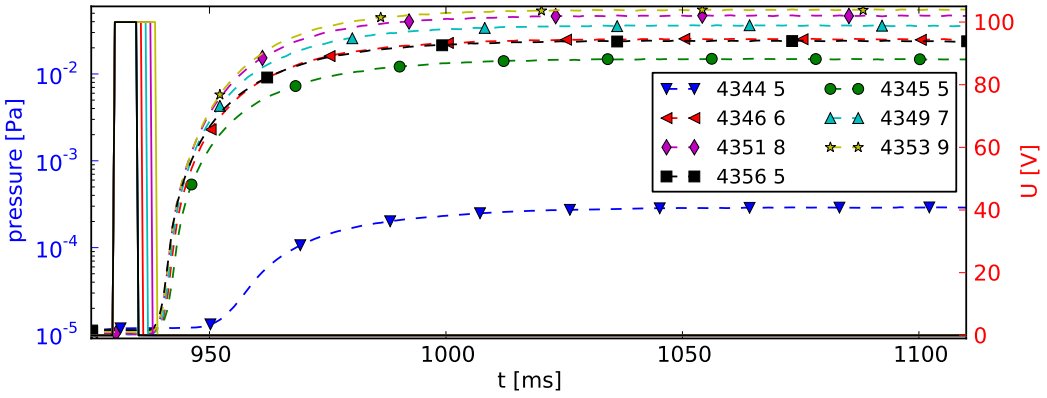

Figure 5.17: Pressure in the vessel depending on opening time of the valve. Solid lines show opening time and voltage applied at the gas puff valve. Dashed lines show pressure evolution inside the vessel corresponding to time how long was gas puff valve open. Pulse length varies from 5 ms to 10 ms.

opening of the valve. Also last 5 ms opening pulse (black dashed line marked with squares - discharge #4356) injects almost same amount of gas as 6 ms pulse (red dashed line marked with left triangles - discharge #4346). This is caused because valve contact is not so sticky as it was in the first opening after few hours of being closed. To avoid this behaviour, the valve is open in the morning and gas is puffed. This is done mainly during glow-discharge procedure. At the figure solid lines show applied voltage for the gas puff valve. Dashed lines show pressure inside the vessel measured by a gauge with an analog output connected to the real-time acquisition board. Time delay between a command for opening the valve and increasing pressure is approximately 10 ms. From this experiments time of 7 ms for fully open valve with 100 V is typically used in the experiments.

5.3.2 Long Term Behaviour of the Piezo-Electric Valve

The piezo-electric valve was calibrated to see how big voltage has to be constantly applied to increase, to decrease and to keep constant pressure. The vessel was filled by D_2 gas during 250 ms long pulse applying different voltage at the valve after the first opening pulse. In Fig 5.18 we can see five 6 ms long pulses open

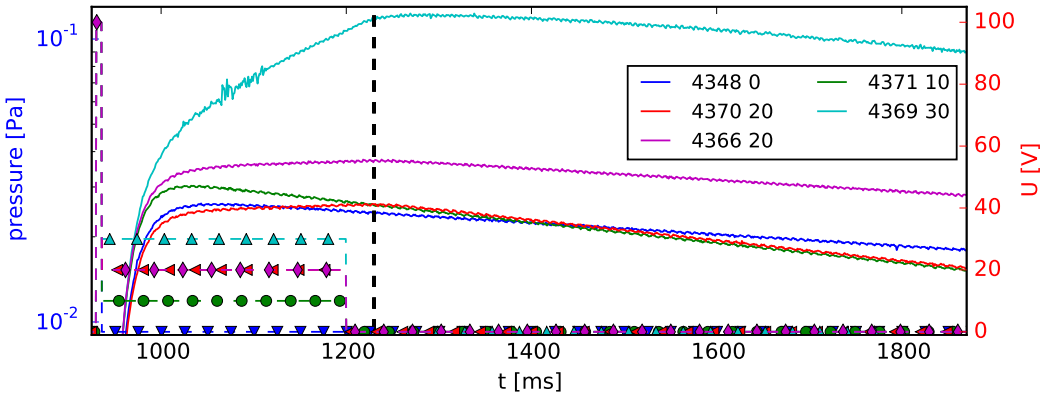

Figure 5.18: Pressure in the vessel depending on the used voltage at gas puff valve. Dashed lines with markers show opening time and voltage applied at the gas puff valve. The solid lines show pressure evolution inside the vessel, corresponding to applied voltage - how much was the gas puff valve open. Blue labelled y-axis shows the pressure for the solid lines and red labelled y-axis shows the voltage for the dashed lines. Starting pulse 6 ms followed by 250 ms pulse with 0 V, 20 V, 30 V, 20 V and 10 V. Vertical black line shows time when the pressure inside the vessel starts decaying in pulses when 20 V and 30 V were used. Pressure started to decrease 30 ms after the valve had been already closed.

with 100 V followed by pulses at three different voltage levels 10 V (shot #4371), 20 V (shots #4366, #4370) and 30 V (shot #4369). Applying 30 V after opening pulse leads to significant increase of the pressure in the vessel. When 10 V or 0 V after opening pulse is used, pressure starts to decrease at the same time around 1000 ms. If 20 V is used, pressure in the vessel is stable or very slightly increases which means that the gas puffed by the valve is very close to the equilibrium with pumping by the wall and by the pumps. This result is reproducible because in shot #9940 (Fig. 5.19), made two years later, the same behaviour was observed.

One can notice that in shot #4371 (10 V pulse) pressure decreases faster than in shot #4348 (0 V) and also that two shots (#4366, #4370) with the same voltage 20 V have different pressure. These two discrepancies can be explained with stickiness of the valve and pumping by the wall. Both cases are caused by the time gap between the shots. The shots from #4345 to #4369 were done in short time gaps typically less than 10 minutes but there were two hours between shots #4369 and #4370. This increased stickiness of the valve in shot #4370 and thus less amount of the gas was puffed in the vessel than in shot #4366 with same voltage applied at the valve. In shot #4371 the wall was cleaner than in shot #4348 because the vessel was pumped for two hours (glow discharge could be possibly done as well). Therefore, the wall was able to pump out more gas and the pressure in shot #4371 decreased faster than in shot #4348.

This dependance on gas-puff valve usage and on vessel condition shows that

only feedforward control can not be sufficient. Feedback control is necessary to compensate stickiness and wall pumping.

In Fig. 5.18 one can see that the pressure started to decrease 30 ms after the valve had been already closed when 20 V and 30 V were applied (time event is marked with black dashed vertical line). Difference between the opening time which is $\approx$ 10 ms and closing the valve $\approx$ 30 ms is caused by the valve behaviour. The opening speed of the valve depends on the applied voltage, while closing of the valve depends on internal resonance frequency of the piezo plate. Therefore, opening of the valve with sufficient high voltage is much faster than closing the valve with 0 V. The open valve is closing with time constant of several ms when 0 V applied.

5.3.3 Short Term Behaviour of the Piezo-Electric Valve

Reaction of the valve on fast voltage changes was tested to optimise the controller. In Fig. 5.19 there is comparison of gas puff valve reaction speed for different voltage applied. For comparison, in all following experiments we can described

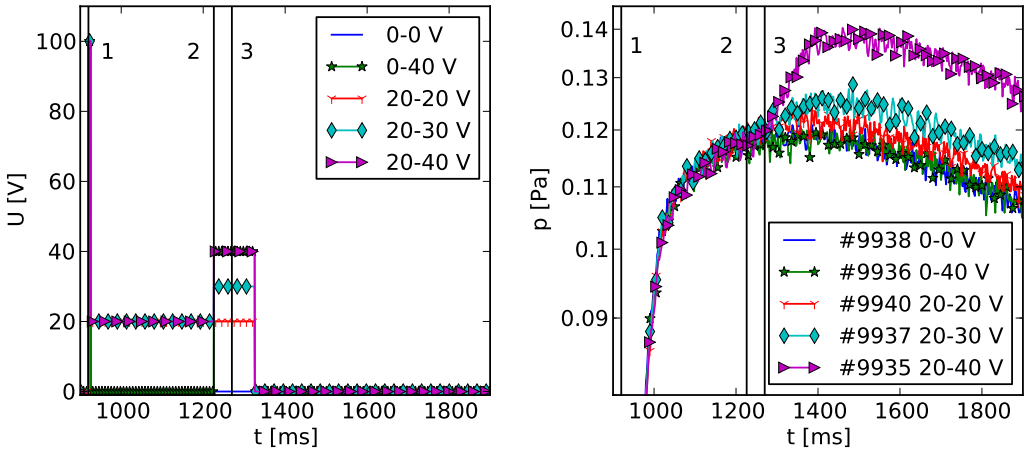

Figure 5.19: Testing and comparing delay in opening after valve was fully closed to valve kept open with 20 V. All pulses start with 6 ms and 100 V pulse. Left: the voltage applied at the gas puff valve. Right: the pressure in the vessel corresponds to opening valve at the left side of the figure. The legend shows voltage following the first 6 ms 100 V pulse. Colours at the left and the right graphs correspond. Vertical line labelled with 1 shows when gas puff is started. The second vertical line shows when gas puff was changed. The third line shows when first change was measured by the vacuum gauge.

pulses with three different steps. All the shots are starting with first 6 ms long and 100 V opening pulse. The second pulse is always 300 ms long after the opening pulse and can be 0 V or 20 V. The third pulse is 100 ms long and can have 0 V, 20 V, 30 V and 40 V. Combination of second and third pulse is used to determine responding speed of the valve.

Firstly, 20 V for 300 ms after the opening pulse was used and followed with 40 V for 100 ms (#9935). In the next shot, again 40 V in the third pulse was used for 100 ms but during the second 300 ms long pulse, the valve was closed (#9936 green line labelled with stars). In shot #9937, 30 V in the third pulse was applied

after the 20 V was applied in the second pulse. During shot #9938, the valve was closed in the second and third pulse. It means, only the first opening pulse was used. In the last shot (#9940), 20 V was used in the second and third pulse.

Results from these experiments are in Fig. 5.19. At the right side of the figure, the gas pressure is plotted which corresponds to the applied gas-puff voltage plotted at the left side. From pressure evolution in these shots we can say that once the valve is closed even 40 V during 100 ms is not enough to open the valve again (#9936 green line marked with stars) and pressure drops the same way as if the valve is closed (blue line). Therefore, the valve needs voltage higher than 40 V to open it again. The similar pressure and result is when the valve is kept at 20 V during 400 ms (red line marked with tri-down marker). The pressure slightly increases if the valve is open with 30 V after 20 V 300 ms long pulse (cyan with diamond markers #9937). Significant increase of the pressure is observed only when 40 V (purple with triangle markers) was applied after 20 V pulse. If the voltage at the valve, after opening pulse, is kept for 20 V, pressure does not increase significantly. If the voltage is then increased to 30 V or 40 V valve responds and pressure increases. For these reasons, the valve during the experimental discharge is always kept at minimal 20 V after first opening pulse.

Vertical line 1 shows starting of the first pulse. Vertical line 2 shows when the third pulse starts. Vertical line 3 shows when the pressure in the vessel increases after the third pulse. The time difference ≈ 45 ms between line 2 and 3 shows the respond time of the system (this includes also spreading gas in the vessel which is few ms and the gauge read out time which is 10 ms). Therefore, the time response of the valve can be estimated to ≈ 30 ms if the valve is not fully closed and is not opening with 100 V.

5.4 Electron Density Controller

The electron density controller can be operated in two different regimes. First one is fully controlled in open loop cycle when predefined waveform is used (typically used in runaway experiment campaigns). Second one, used in the most cases is feedback controlled.

At the beginning of every discharge, the vessel is filled with D_2 at pressure 4×10^{-3} Pa to 3×10^{-2} Pa with predefined waveform. Few milliseconds after plasma breakdown (typically 20 ms), feedback starts to control of the gas puff valve. The corrected density signal from the interferometer, n_{cor} (Eq. 5.25), after corrections is used as an input for feedback control. According to difference between requested and measured electron density, the piezo-electric valve for deuterium gas (Sec. 5.3) is opening or closing. During whole discharge pressure in the vessel is also measured with a gauge, however, gauge measurement is not used in the control.

The electron density is controlled in real-time using MARTe GAMs running in the sequence shown in Fig. 5.20. The electron density signal from the interferometer is acquired in the ATCAAdc GAM. In this GAM measured voltage is converted to the raw electron density. Offset from measurement is removed in DriftRemover_Density (see Eq. 2.8). The electron density signal without drift is processed in PlasmaDensityCalculatorGAM and the electron density is corrected according to estimated length using Eq. 5.13 and 5.14. The in-

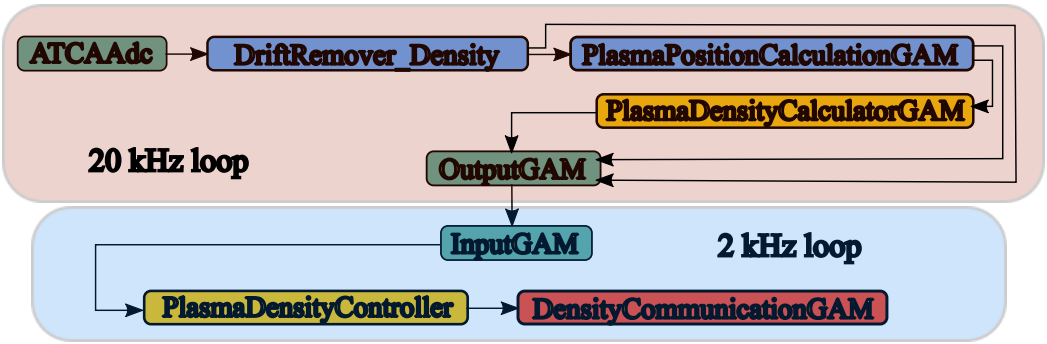

Figure 5.20: A sequence of Generic Application Modules (GAMs) for electron density control.

put values, Shaping Field Power Supply (SFPS) and I_p, for Eq. 5.13 are obtained in DriftRemoverGAM and plasma position used in Eq. 5.13 is calculated in PlasmaPositionCalculationGAM. Also in PlasmaDensityCalculatorGAM non-linearisation effect is calculated according to Eq. 5.24. All these GAMs run in the fast thread. If old interferometer is used and fringe jumps occur, then correction to fringe jumps will be used (see Sec. 5.4.1). Corrected density according to length and non-linearity effects is then transferred from the fast thread to the slow thread via OutputGAM and InputGAM. In the slow thread PlasmaDensityCalculatorGAM calculates voltage request of PI controller. Requested voltage at specific time k is given by following equation:

$$V_\mathrm{req} = P \cdot (n_\mathrm{req} - n_\mathrm{cor}) + I \sum_{j=0}^{k} (n^\mathrm{j}_\mathrm{req} - n^\mathrm{j}_\mathrm{cor}) \Delta t, \tag{5.26}$$

where n_cor is electron density corrected to the length and non-linearity effect at time k of the discharge, $n^\mathrm{j}_\mathrm{req}$ is referenced value requested for the experiment at time $k \cdot \Delta t$, $P = 30$ is proportional constant at time same time, $I = 0.0006$ is integration constant and Δt is time step (for slow thread is 500 µs). Total output from PlasmaDensityCalculatorGAM is sum of predefined waveform in the configuration file and V_req. P and I constants were estimated from expertise gained during the period, when the electron density was controlled in pre-defined waveforms specified before every discharge.

Last GAM in this sequence DensityCommunicationGAM converts requested signal (sum of pre-defined waver and signal calculated from feedback) to volts in range 0 V to 5 V dividing signal $V_\mathrm{req}/20$. It also serves as a protection for the vessel and the gas puff valve. Furthermore, DensityCommunicationGAM prevents to create runaway electrons as it is described in Sec. 5.4.3.

5.4.1 Fringe Jumps Calculation

As was mentioned in Sec. 5.2.1 fringe jumps can occur when old interferometer is used and the measured signal needs to be corrected. To calculate fringe jumps difference between last two measured density is compared with the maximal measurable electron density without fringe jump n_max. If difference is bigger than 80% of maximal value then fringe jump has occurred. Then n_max is added

to the last and all the following samples (Eq. 5.27) until negative fringe jump occurs (Eq. 5.28).

$$\text{if } (n^{\mathrm{n}}_{\mathrm{raw}} - n^{\mathrm{n-1}}_{\mathrm{raw}}) \;<\; -n_{\max} \cdot 0.8 \Rightarrow n^{\mathrm{n}}_{\mathrm{raw}} = n^{\mathrm{n}}_{\mathrm{raw}} + n_{\max} \tag{5.27}$$

$$\text{if } (n^{\mathrm{n}}_{\mathrm{raw}} - n^{\mathrm{n-1}}_{\mathrm{raw}}) \;>\; n_{\max} \cdot 0.8 \Rightarrow n^{\mathrm{n}}_{\mathrm{raw}} = n^{\mathrm{n}}_{\mathrm{raw}} - n_{\max} \tag{5.28}$$

where $n^{\mathrm{n}}_{\mathrm{raw}}$ is last measured electron density value, $n^{\mathrm{n-1}}_{\mathrm{raw}}$ is one before last and $n_{\max} = 8 \times 10^{19}\,\mathrm{m}^{-3}$

5.4.2 Time Delay Estimation in the Control Loop

Estimate time delay in case of measurement of electron density is difficult because many different things play role. Firstly, delay is estimated from gas pressure measurement. As explained in Sec. 5.3 (Fig. 5.15 and Fig. 5.19, time delay between lines 2 and 3 is approximately 50 ms. However, this delay includes also effect of gauge measurement and spreading of the gas inside the chamber and to the port where the gauge is mounted. According to the specification, response time of the gauge is ≈ 10 ms [111]. Gas spreads inside the vessel in the order of milliseconds. Which is not in good agreement with 50 ms measurement. An experiment where the valve is fully open at the beginning of the discharge (see Fig. 5.17) seems to conform with a latency of 10 ms. However, when valve is closed, gas pressure starts decaying only after 30 ms as it is visible in Fig. 5.18. These different results can be caused by non-linear behaviour of gas puff valve during opening and possibly even more during closing. Thus time delay measurable by the gauge, caused by opening and closing valve and spreading gas, can be between 10 ms to 50 ms.

Another delay is caused by a filter at the output signal from the interferometer and is estimated with two different experiments. One is with comparing measurement between Thomson Scattering (TS) n_{e} and the interferometer - n_{cor} (Fig. 5.21). It can be seen, that blue rectangles (measurement with TS) are often in advance in front of the red line, which is measurement with the interferometer. It is hard to estimate the time delay exactly because TS measures data locally and then are data recalculated to the averaged density. The interferometer measures line integrated density (n_{raw}) and then data are recalculated according to the plasma length and non-linearity to line averaged density n_{cor}. However, this delay can be roughly estimated between 10 ms to 20 ms. In the second experiment, estimated time delay is according to electron density evolution after the disruption. In Fig. 5.22 there are two different discharges. One discharge (#9312) when measurement output at interferometer is filtered (green line left side of the figure) and second one (#9314) when filter is removed (blue line). Cyan and red vertical lines correspond to disruptions at plasma current plotted at the right side of the figure. Electron density measurement from discharge #9314 was smoothed for analysing purposes and is plotted with black line. Comparing time when green line and black line reach zero density (magenta line) to disruption time, one can say that time delay for interferometry with filter is 50 ms and without filter is 40 ms.

These results do not agree when plasma current start is compared with start of electron density as it is plotted in Fig. 5.23. In this figure, lines and their colours are plotted the same way as in Fig. 5.22. Delay estimated using start

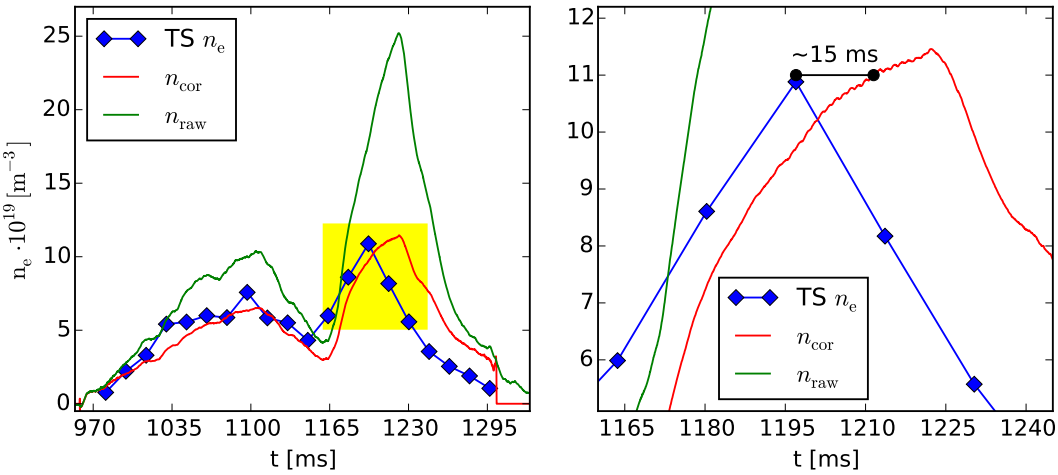

Figure 5.21: Time delay between Thomson Scattering measurement (TS n_e) and corrected electron density (n_{cor}) according to plasma length and non-linearity measured by the interferometer with the analogue filter on its output. Yellow box on the left graphs shows zoomed region of the right graph. Green line shows non-corrected interferometer (n_{raw}) signal. Graph from discharge # 9311.

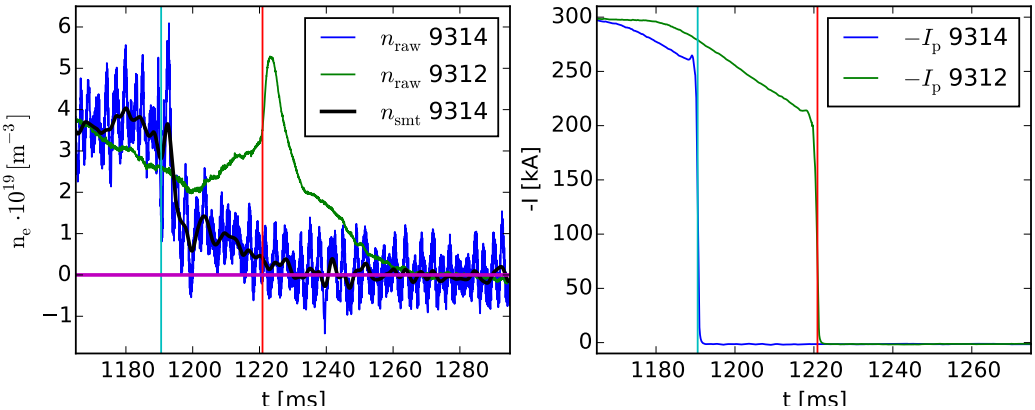

Figure 5.22: Left: the electron density for two different discharges measured during disruption. First one, measured with interferometer with filter (#9312) and second one without filter (#9314). Black line is post-processed smoothing of #9314 used for time delay analysis. The vertical lines show when disruptions occurred. Cyan colour shows time disruption of #9314 and red one of #9312. Magenta line shows zero electron density. Right: plasma current with vertical lines showing disruption time.

of plasma current and the electron density is ≈ 0.5 ms for measurement with the interferometer without the filter and ≈ 2 ms when the filter was used. Reasons for these big disagreement between estimation using start of plasma current and disruption are unknown.

However, removing the filter introduces big error in the measurement as it is visible in Fig. 5.24. Delay between TS diagnostic and interferometry is not visible but noise level in amplitude of the electron density can be bigger than 1.3×10^{19} m^{-3}. Therefore error in measurement can exceed 10% of measured electron density.

System time response and control time response is estimated from step elec-

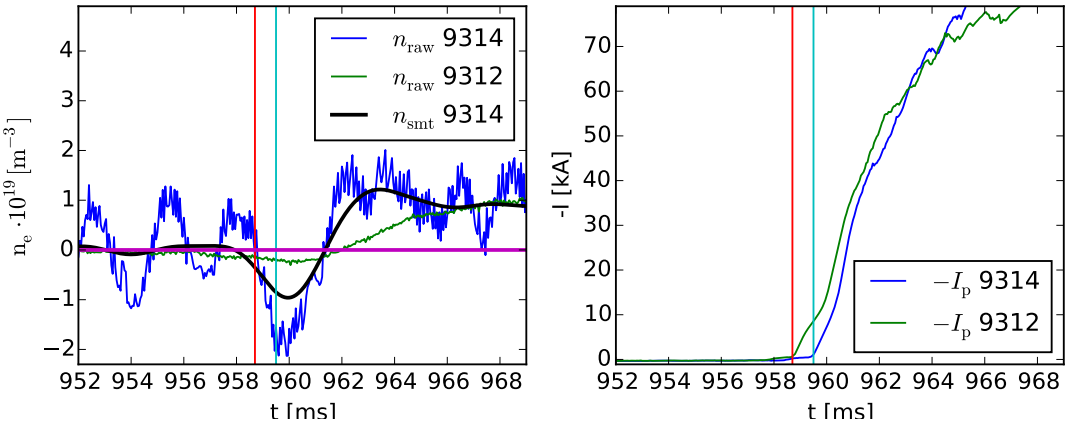

Figure 5.23: Left: the electron density for two different discharges during plasma breakdown. First one measured with interferometer with filter (#9312) and second one without filter (#9314). Black line is post-processed smoothing of #9314 used for time delay analysis. Vertical lines show when plasma current started. Cyan colour shows start time of #9314 and red one of #9312. Magenta line shows zero electron density. Right: plasma current with vertical lines showing plasma current starting time.

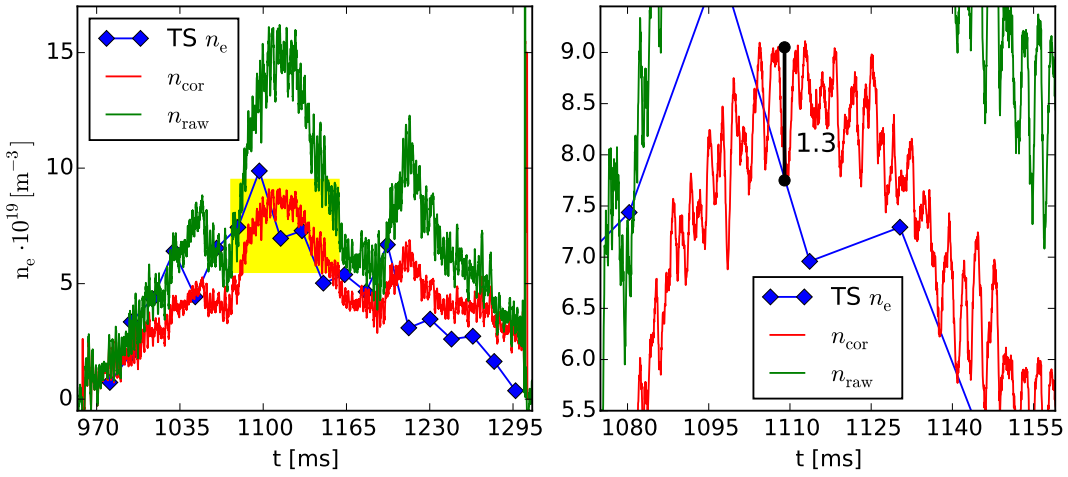

Figure 5.24: Time delay between Thomson Scattering measurement (TS n_e) and corrected electron density (n_{cor}) by the interferometer after the analogue filter on its output was removed. Yellow box on the right graphs shows zoomed region of the left graph. Green line shows non-corrected interferometer (n_{raw}) signal. However, error in measurement labelled with black vertical line can exceed 10% of measured electron density. Graph from discharge # 9326.

tron density request after filter was removed. Results from experiment is shown in Fig. 5.25. Vertical line "1" shows when step was requested (at $t = 1150$ ms). Vertical line "2" shows when when system started to react (at $t = 1170$ ms). Vertical line "3" shows one system was stabilised at new value (at $t = 1178$ ms). From time difference between lines "1" and "2" we can say that system response is approximately 20 ms and control response (time between lines "2" and "3") is approximately 8 ms. Bottom graph with the analogue output shows immediate increasing output voltage to control the valve. However, the electron density starts rising only 20 ms after the voltage was increased which is in good agreement

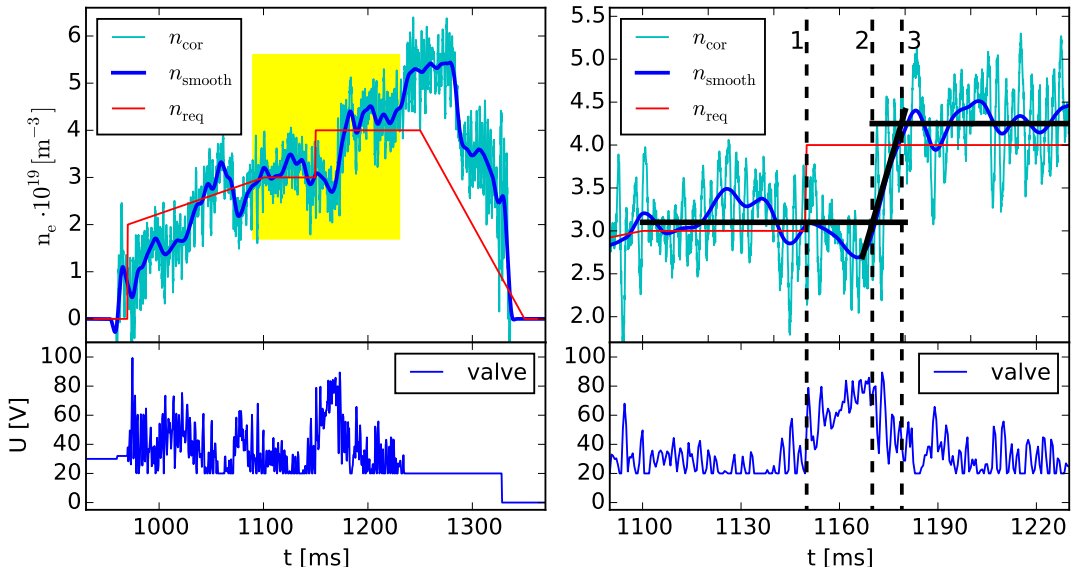

Figure 5.25: Estimation of system response time (1 - 2) and control response time (2 - 3) on the step request. Upper graphs: n_{cor} is corrected and non-smoothed density. Smoothed density is labeled with n_{smooth} and reference value is labeled as n_{req}. Yellow box shows zoomed time domain and data range. Bottom graphs: Shows the analog output used to open the piezo electric valve.

with result obtained from Sec. 5.3. After that feedback control needs 8 ms to stabilise the plasma at newer value. However, this delays whole loop and creates overshooting. Reason for the delay and overshooting can be caused by the D_2 propagation (estimated to approx. 20 ms) and reaction of the valve. The valve is opening fast only if high voltage (100 V) is used. Once electron density is higher than requested, there is no way how to actively decrease the electron density. The electron density can drop only in "natural" way. If the voltage is equal or lower than 20 V density starts to decrease as can be seen from bottom right graph after 1240 ms.

5.4.3 Electron Density Control Protection System

Old interferometer was not always reliable as well as new one during testing period. Therefore for machine protection, several safety measures were added in the final control algorithm. Several things with interferometry could go wrong.

One of the common error was failure of the interferometer signal (closed shutter, malfunction, etc.). For this purpose if plasma current is higher than 50 kA and the electron density is less than 0.3×10^{19} m^{-3} then only predefined waveform will be used. If waveform for gas puff valve is zero then voltage output will be set to 40 V. 40 V corresponds typically to the $n_{\text{cor}} = 2 \times 10^{19}$ m^{-3} to 4×10^{19} m^{-3}. This helps to keep the electron density at some level and dangerous runaway electrons are not created. For runaway electron experiment option without any gas puff was included but this has to be configured in the MARTe configuration file, otherwise 40 V for the valve is used.

Bad calculation of fringe jump can lead to bad interpretation of density.

Therefore, if more than one[4] jump in positive direction occurs in a row or negative fringe jump occurs as a first, the electron density calculation is wrong. Measured electron density is in real-time calculation set to $15 \times 10^{19}\,\mathrm{m}^{-3}$ in PlasmaDensityCalculatorGAM GAM. High density is chosen because when the fringe jump occurs it is typically at high densities. Therefore, there is no need to increase gas puff. If requested density is lower (as always was for early experiments) feedback in PlasmaDensityController GAM will request zero gas puff. If plasma current is higher than 50 kA then 40 V at the output voltage for piezo-electric valve will be set as was described in Sec. 5.4 for the DensityCommunicationGAM.

Another protection becomes active when the interferometer shows the electron density also in the time when there is no plasma current. In Fig. 5.26 we can see reaction of the control system when the interferometer stops measure correctly. Measured electron density n_{raw} (blue line) shows high density long af-

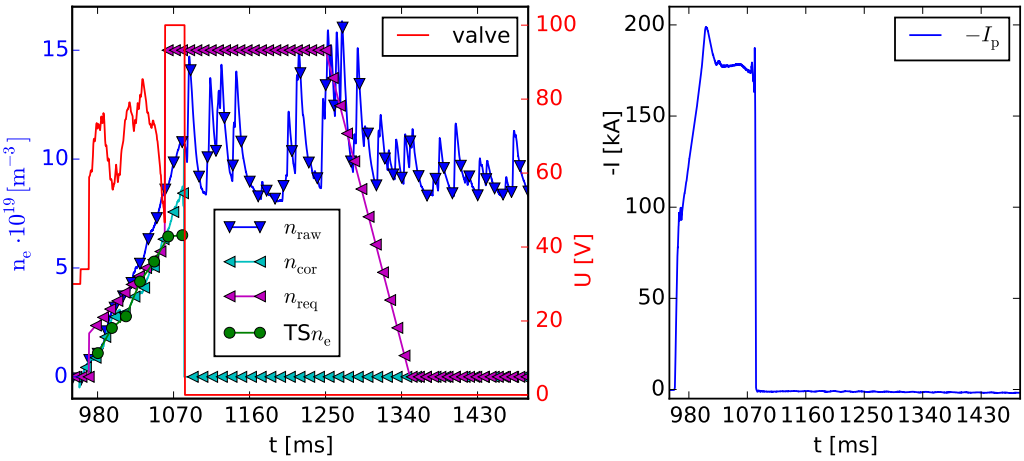

Figure 5.26: Left: n_{raw} is electron density measured directly form interferometer; n_{cor} is corrected density according to shape and evaluated when plasma current exists; TS n_{e} is electron density from Thomson scattering diagnostic; n_{req} - reference electron density value. Right: plasma current

ter plasma current is already zero. Without the protection D_2 would be filled in the vessel, despite the fact there is no real electron density and the measured value is only an error of the interferometer signal. In this concrete example, if there is no plasma current, then PlasmaDensityController GAM will set output from the controller to zero.

The results showing controlled electron density in the typical discharge without interferometer failure and without fringe jump are in Fig. 5.27. The corrected electron density n_{cor} (black line) is controlled according to the requested electron density n_{req} (green line). Signal from the interferometer which is not correcting according to the plasma length and non-linearity effect is plotted with blue line n_{raw}. The voltage applied at the piezo electric gas puff valve, labelled "voltage" is plotted with red line. All densities, including density obtained from TS (TS n_{e} - cyan colour), have their value axis on the right side of the figure (blue). The voltage applied at the gas puff valve has y-axis at the left side (red).

[4]During using old interferometer with fringe jumps COMPASS worked on lower densities lower than $12 \times 10^{19}\,\mathrm{m}^{-3}$.

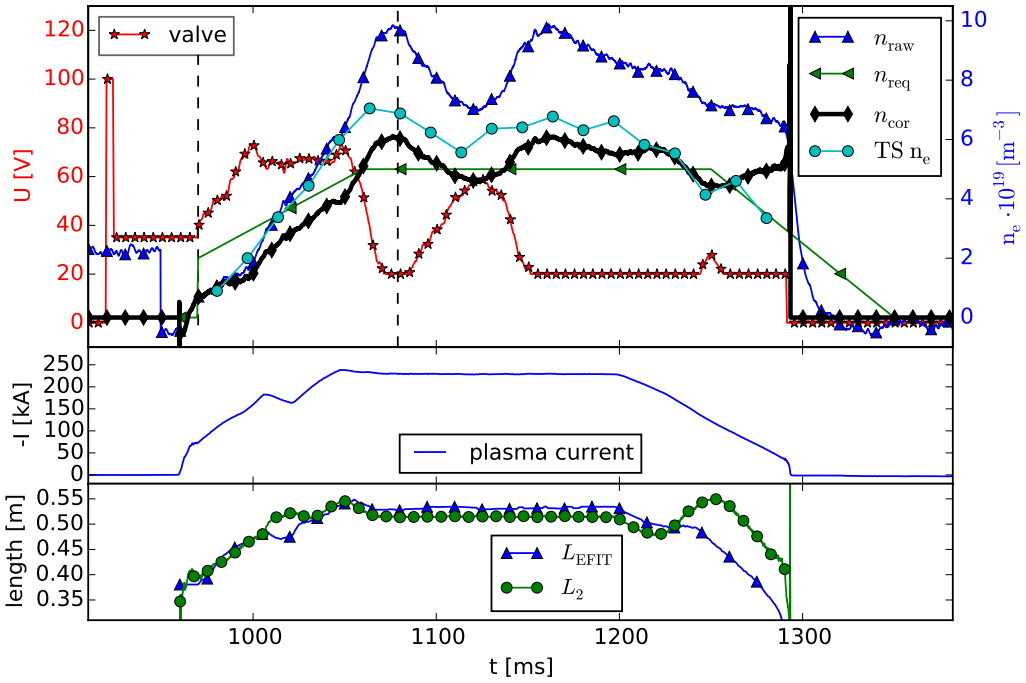

Figure 5.27: Top: Result of density calculation starting with raw measured electron density signal and ending with comparison signal of the real density and the electron density from Thomson Scattering. Centre: Plasma current. Bottom: length comparison between offline post-process calculated L_{EFIT} and real-time calculation in the MARTe GAM. Graphs are from discharge #9114. First vertical dashed line shows when control is changed from predefined waveform to feedback control. Second line shows when in feedback controlled output is 20 V requested instead of 0 V.

In this figure one can see that the measured electron density can be 50% higher than corrected. Comparing requested density to obtained is visible that is easier and faster to increase density, however, decreasing density is slow process which cannot be regulated. It depends only on the vessel condition. Middle graph shows plasma current only for showing characteristic of the discharge. Bottom graph shows comparison between the calculated length in real-time L_2 and L_{EFIT}. Except the current ramp-down phase, real-time calculated length is in the good agreement with EFIT reconstructed length.

First vertical dashed line shows when control is changed from predefined waveform to feedback control. Before vertical line, waveform is used to puff enough D_2 for plasma breakdown. Shortly after plasma is started, feedback control overtakes valve control. Second line shows when in feedback controlled output is 20 V requested instead of 0 V. It is at time when the electron density is higher than requested density. As mentioned above 20 V is used to have fast reaction of the gas puff valve

6. Improvements

COMPASS control system which has been designed and implemented in the scope of this thesis is working sufficiently good enough to fulfil all experimental research activities including reaching H-mode with type I Edge Localised Modes (ELMs) and their studies using Resonant Magnetic Perturbation (RMP) and vertical kicks, measurement of transport in edge plasma and Scrape of Layer (SOL), runaway experiments, and also measurement of SOL width for extrapolation to ITER design of in-vessel panels, etc.

Nevertheless, with the following suggestions the control system could be further improved in future. Improvements can bring higher robustness of controllers, decrease load to operators and decrease possibility of their mistakes, and optimise plasma discharge parameters. These ideas are based on expertise developed during operation of the COMPASS tokamak and designing and improving plasma control.

6.1 Multiple Input Multiple Output Controller

Multiple Input Multiple Output (MIMO) controller suggested here will unify control of plasma current, equilibrium and plasma shape controller. Operator will set waveform for plasma current, horizontal plasma position and plasma shape. According to these setting MIMO controller will set correct negative starting current for Magnetising Field Power Supply (MFPS) to reach requested plasma current without overshooting. Start of Equilibrium Field Power Supply (EFPS) will be adjusted in agreement with starting of plasma current. If divertor shape is requested then Shaping Field Power Supply (SFPS) will start automatically depending on the requested shape and requested current. Functions for optimising start of plasma current and reaching targeted plasma current, position and shape can be obtained from data in Tab. 2.2 and Tab. 3.2.

MIMO controller should be designed with respect to decreasing oscillations caused by using the same coil and mutual inductance between MFPS, SFPS and EFPS.

This needs to design a physical model which includes mutual inductance and forcing power supplies through the same coil. It will help to prolong plasma current flat-top phase, decrease consumption of Volt-seconds and it will suppress oscillations also at plasma position, which will make plasma position more stable. MIMO controller also minimises possible mistakes by operators when wrong start point for EFPS can be set or EFPS and Fast Amplifier for Vertical Magnetic Field (FABV) will have different settings for equilibrium.

Using this MIMO controller, predefined plasma current ramp-down scenarios can be easily designed, programmed and executed. When MFPS reaches its maximal values, divertor shape can be changed to circular plasma decreasing SFPS current according to preprogrammed scenario and keeping equilibrium at the best position during landing. This will help to avoid disruptions when plasma current decreases because of MFPS saturation while SFPS is constant (this can happen because of applied smoothing in controlling SFPS current). Different scenarios can be used for runaway experiments or when circular plasma is used.

Proportional Integral (PI) constants for Fast Amplifier for Radial Magnetic Field (FABR) depend on actual plasma current. Therefore, FABR controller can be also part of MIMO controller. First, PI function described by Eq. 3.64 can be implemented inside FABR controller. This will keep PI constants at proper value in respect to the actual plasma current. Another benefit is when plasma shape is changing, changes of vertical plasma position can be attached to actual plasma shape. Typically, different plasma position is used when plasma shape is circular or diverted, or during transition between these shapes. Therefore, actual vertical plasma position can be predefined in the scenarios. If plasma is vertically unstable, i.e. FABR cannot keep plasma in the requested position, then Vertical Kick Power Supply (VKPS) can be possibly used for stabilising Vertical Displacement Event (VDE). If plasma column will be moving faster than certain critical value, VKPS can generate current which will push plasma in opposite direction and thus help FABR power supply.

6.2 Shortening Delays and Latencies

MARTe communicates with FABR controller card already via Aurora. Delay caused by communication using RS-232 protocol was reduced by $\approx 25\,\mu s$ when Aurora is used. Therefore, Aurora protocol is strongly suggested to be used also for communicating with FABV controller card and also for communicating with ČKD energetics. Communication with ČKD energetics (four power supplies) uses 4×33bits which makes it $132\,\mu s$ only for sending data. Using Aurora, this can be reduced to $4\,\mu s$. Each power supply will need only $1\,\mu s$. Also increasing Generic Application Module (GAM) speed used for communication with energetics according to Tab. 3.4 can possibly shorten the delay by more than $10\,\mu s$. Also, all other communication should be changed from RS-232 protocol to Aurora, such as communication with the Pre-Triggering card. Even though this implicates lot of programming work with Field Programmable Gate Array (FPGA), the benefit would be significant.

6.3 Optimising Electron Density Controller

As mentioned above, noise of electron density measurement is bigger than 10%. In top of Fig. 6.1 one can see how electron density oscillates around requested value. Bottom graph shows applied voltage on the gas puff piezo-electric valve. To improve the electron density control, two different ways are suggested.

First one is to apply low pass filter on the input measurement. This increases delay in measurement and thus in control. However, it is not sure that when filter was removed after discharge #9312 delays was reasonably shorten, but noise level has been increased massively (see Sec. 5.4.2). Therefore, combination of applying filter and predictive control is suggested. Predictive control can be designed using feedforward component reacting on actual request or applying feedback control at time 50 ms in advance. Also implementing fuzzy logic to compensate non-linear dynamics can have good impact on controller performance (e.g. decreasing gain if actual value is 80% of the requested value).

Second option is to reduce proportional gain and increase integral gain which

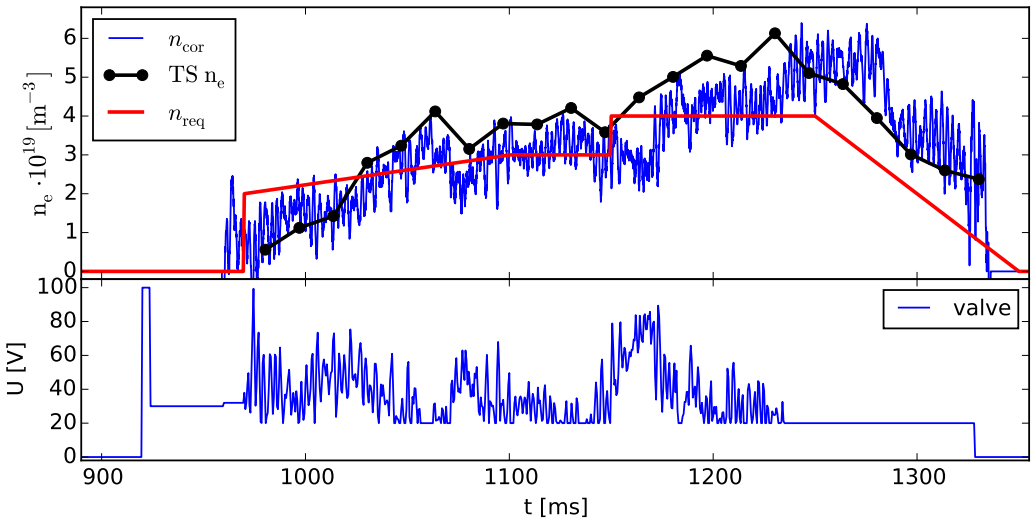

Figure 6.1: Top graph shows chosen different density profiles, including the fitting curve. Bottom graph shows difference between the measured and real density when non-linearity is taken into account.

also increases delay. Since this can create overshoot, methods to ensure that a PI controller correctly compensates for actuator saturation (like anti wind-up) should be considered. Also a combination of feedback controller and predictive control may be useful to try. For the second one, implementing the fuzzy logic is not envisaged due to big noise and to say correctly when density reaches 80% of requested value is not possible without filtering the signal.

As was showed in Sec. 5.3, stickiness of the valve influences total amount of gas puffed in the vessel. That means the same voltage can cause different amount of injected gas. Therefore, the electron density control at COMPASS can be improved with changing recent piezo-electric valve with a valve which has flow meter implemented inside and thus gas flow could be controlled instead of valve opening using simply volts. If the flow is controlled, then there will be always defined amount of the gas injected and influence of stickiness will be suppressed.

Note, that values here are just examples and correct values for controller have to be obtained from models on the trial and error methods.

Conclusion

The original aim of this doctoral thesis was to stabilise plasma vertically in the COMPASS tokamak using digital feedback control. Nevertheless, the control of other plasma parameters such as horizontal position, plasma current, plasma shape and electron density is closely linked to the original task via the used control system and diagnostics as well as physics involved. Therefore, all these topics were included in this work.

Control of the above mentioned quantities has been implemented on the basis of the MARTe real-time framework [34]. Within MARTe, the algorithms, the communication and the controllers are divided into separate blocks called Generic Application Modules (GAMs). These blocks access measured and processed signals and data via the Dynamic Data Buffer (DDB) and calculate control commands. Sequence of GAMs and their configuration is specified in a configuration file.

Determining plasma position was the first task which had to be solved. Sensitivity of Internal Partial Rogowski (IPR) coils to plasma at different positions and in different configurations was calculated. Two sets of IPR coils were selected from these results to obtain horizontal and vertical plasma position. An algorithm which determines the plasma position using these sets has been derived and programmed in one of the GAMs [18]. Implementation of the algorithm included subtracting all poloidal fields together with the current induced in the vacuum vessel by external fields.

Horizontal plasma position control uses two separate power supplies. Equilibrium Field Power Supply (EFPS) is a slow but strong power supply which delivers sufficient amount of vertical field to obtain plasma equilibrium. Fast Amplifier for Vertical Magnetic Field (FABV) power supply stabilises horizontal plasma position at the beginning of the discharge when plasma current rises fast and EFPS does not react fast enough. In this work, controllers for EFPS and FABV have been developed and implemented in MARTe. While FABV is a simple Proportional Integral (PI) controller, the controller for EFPS is composed of three different components. In the first one, the majority of the EFPS current is requested by the feedforward controller according to plasma current. The second part is a feedback controller and it is important for keeping plasma at it requested horizontal position. Last part is used to reduce load of FABV power supply. This new controller was developed together with a new calculation for horizontal plasma position using flux loops which has improved precision in determining horizontal position. Due to the fact that algorithms for calculating vertical and horizontal plasma positions are bound together, the improved precision leads to reduction of the noise in the calculation of the vertical position. The improved precision and the decreased sensitivity to the plasma shape also reduced load to the operators [19].

Vertical plasma position control is essential for elongated and D-shaped plasma scenarios, which are important for today's and also future fusion devices since they enable easier access to the high confinement mode, called H-mode. A D-shaped plasma is vertically unstable. The plasma instabilities significantly faster than the vacuum vessel time constant are stabilised passively by currents induced

in the vessel walls. However, slower events must by controlled actively and, therefore, a fast acting controller had to be developed for COMPASS. Since the time constant of the COMPASS vessel is short, approximately 0.5 ms, the vertical stability control in COMPASS is much more demanding than on other tokamaks. Therefore, this work is focused on tuning the feedback controller, improvement of computing speed and reducing delays in the control loop. Three different delays were identified and then reduced. First one, was a high order low-pass filter causing delays of 50 µs. This filter has been removed. The second delay was reduced by additional ≈ 25 µs when communication link was changed from RS-232 protocol to Aurora which increased the amount of information transferred in one message. This was also used to control new Vertical Kick Power Supply (VKPS) [96] used in Edge Localised Mode (ELM) triggering experiments. The third delay was decreased by optimised compilation of all source codes which decreased delay up to 20 µs [19].

These controllers together with the improvements of their speed and precision helped COMPASS to developed stable scenarios with H-mode [14]. Moreover, plasma scenario with plasma column shifted bellow the mid-plane and low X-point position could be achieved [72]. This scenario, operating further from the vacuum vessel walls, in a less stable position, was necessary to observe pedestal using Thomson Scattering (TS) diagnostic. These developments enable also to perform experiments with L-H transition requiring the X-point close to the divertor.

Plasma current controller was developed and optimised to suppress overshooting and driving plasma current in opposite direction, which was created by negative loop voltage, when Magnetising Field Power Supply (MFPS) current was decreasing [19]. The reference values are restricted to a band close to the most recent measurement of the plasma current. Since the difference between the new reference value and the measurement is always small, then output from the controller is also small. When plasma is above requested value, new requests are set until plasma current reaches the lower value. The speed of plasma ramp-down is set that way, that MFPS current is not decreasing and thus does not create negative loop voltage and does not drive plasma current in the counter direction.

Plasma shape control is simple feedforward controller with adoption to the actual plasma current. Plasma shape is set by ratio between current in Shaping Field (SF) coils driven by Shaping Field Power Supply (SFPS) and plasma current I_p. However, this dependence is not linear and when plasma elongation κ reaches values $\kappa = 1.8$ further increasing ratio of $I_\mathrm{SFPS}/I_\mathrm{p}$ leads to decreasing plasma size, not to increasing plasma elongation. Smoothing of plasma current measurement used as input for feedforward control of plasma shape had to be included to avoid oscillatory behaviour of the plasma shape, plasma current and vertical position. These oscillations are caused by the facts that I_MFPS, I_EFPS and I_SFPS use one common coil and by high mutual inductances between the coils and between the coils and the plasma. This smoothing over 13 ms suppressed all oscillations which were created.

Last developed controller was for the electron density control. This controller can work with two different interferometers. The first - and older one - suffered from fringe jumps. For this device, fringe jump detection and correction was implemented. However, currently it is used only as a replacement in case of malfunction of a newer interferometer measuring without fringe jumps. Both in-

terferometers measure the line integrated density but when the plasma shape is changed also the length of interferometer chord inside plasma is changed. Therefore, correction according to the chord length has been included into the controller. The correction is based on a fifth order polynomial function of the ratio $I_{\mathrm{SFPS}}/I_{\mathrm{p}}$ and it includes a linear dependence on horizontal and vertical positions. At higher values of electron density, the interferometer measurement is not in its linear range anymore. Therefore, recalculation taking into account the non-linear behaviour of the electromagnetic wave propagation at high electron density has been implemented into the real time code [20].

In the last chapter, ideas for further development such as Multiple Input Multiple Output (MIMO) controller, shortening the delays and latencies, and optimisation of the electron density controller are described. They reduce possible human mistakes, optimise plasma control and make plasma control more robust.

A. Appendix: Detailed description of timing sequence and synchronisation

Here description of the sequence is written after operators presses "Fire" button in FireSignal Graphical User Interface (GUI).

FireSignal sends command via CORBA [49] to MARTeNode, which controls MARTe internal states and acquires data, and changes MARTe internal status from *GAMCheck*. At this time MARTe sends message about its internal state using programmed module called PreTriggeringGAM to the so-called PreTriggering Unit.

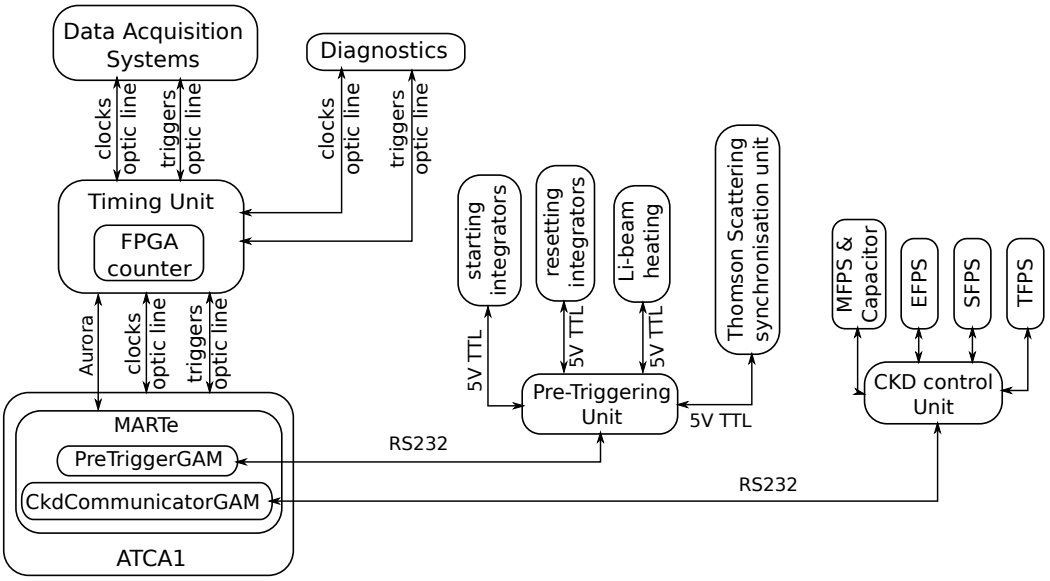

Figure A.1: Schema of connections between MARTe, nodes, Data Acquisition System (DAS) with connection description

PreTriggering unit is based on in-house built circuit board with one Microchip dsPIC30F4013. Its outputs are 5 V signals configured during MARTe startup. There is 1 s counter and according to the settings received from MARTe, unit countdowns correct time and then sets outputs to 5 V and thus the synchronising board [69] starts synchronising of Thomson Scattering (TS) diagnostic [70, 71, 72]. Also with triggers from this board heating up Lithium beam neutraliser [73] and resetting integrators of the magnetic coils are triggered. The PreTriggering unit uses a serial port and RS232 protocol for communication with PreTriggeringGAM.

When 80 s (set in FireSignal by operator in MARTeNode) passes, MARTeNode changes MARTe status from *GAMCheck* to *GAMPrepulse* and "Offline" state to "Online". MARTe sends "start" command to ČKD Communication Unit (ČKD-CU) to start charging the capacitor used for plasma breakdown (see Sec. 2.3) via serial communication link using RS232 protocol from CkdCurrentControl-

lerGAM[1] and also sends command about its update state again to PreTriggering unit. Charging of the capacitor takes approximately 140 s. When capacitor is charged, ČKD-CU sends command to MARTe that main energetic is ready. MARTe sends command via AURORA link [93] to Timing Unit (TU) to reset cycle counter on Field Programmable Gate Array (FPGA). When zero at cycle counter is set, MARTe sends command to start discharge and DASs receive triggers to start acquiring data. Acquisition of data can be postponed according to trigger delay settings. This can be set via FireSignal.

[1]Detailed description of communication between MARTe and ČKD-CU is in document [74].

Bibliography

[1] J. A. Wesson. *Tokamaks*. Clarendon Press, Oxford, U.K., 3rd edition, 2004.

[2] Group of authors. *Summary of the ITER Final Design Report*. ITER EDA Documentation Series. International Atomic Energy Agency, Wien, July 2001.

[3] J. A. Wesson. Hydromagnetic stability of tokamaks. *Nuclear Fusion*, 18(1):87, 1978.

[4] N. Miki, M. Verrecchia, P. Barabaschi, A. Belov, S. Chiocchio, F. Elio, K. Ioki, S. Kikuchi, V. Kokotkov, J. Ohmori, M. Roccella, P. Sonato, P. Testoni, and Y. Utin. Vertical displacement event/disruption electromagnetic analysis for the ITER-FEAT vacuum vessel and in-vessel components. *Fusion Engineering and Design*, 58-59:555–559, 2001. cited By 12.

[5] R. Panek, O. Bilykova, V. Fuchs, M. Hron, P. Chraska, P. Pavlo, J. Stockel, J. Urban, V. Weinzettl, J. Zajac, and F. Zacek. Reinstallation of the COMPASS-D tokamak in IPP ASCR. *Czechoslovak Journal of Physics*, 56(Suppl. B):B125–B137, 2006. 22nd Symposium on Plasma Physics and Technology, Prague, Czech Republic, JUN 26-29, 2006.

[6] E. J. Doyle, W.A. Houlberg, Y. Kamada, V. Mukhovatov, T. H. Osborne, A. Polevoi, G. Bateman, J.W. Connor, J. G. Cordey, T. Fujita, X. Garbet, T.S. Hahm, L.D. Horton, A.E. Hubbard, F. Imbeaux, F. Jenko, J.E. Kinsey, Y. Kishimoto, J. Li, T.C. Luce, Y. Martin, M. Ossipenko, V. Parail, A. G. Peeters, T.L. Rhodes, J.E. Rice, C.M. Roach, V. Rozhansky, F. Ryter, G. Saibene, R. Sartori, A.C.C. Sips, J. A. Snipes, M. Sugihara, E.J. Synakowski, H. Takenaga, T. Takizuka, K. Thomsen, M. R. Wade, H.R. Wilson, ITPA Transport Physics Topical Group, ITPA Confinement Database, Modelling Topical Group, ITPA Pedestal, and Edge Topical Group. Chapter 2: Plasma confinement and transport. *Nuclear Fusion*, 47(6):S18, 2007.

[7] Institute of Plasma Physics, Prague, Czech Republic Association EURATOM/IPP.CR. Application for Preferential Support for Enabling a programme of ITER relevant plasma studies by transferring and installing COMPASS-D to the Institute of Plasma Physics AS CR, Association EURATOM-IPP.CR, 2006.

[8] V. Weinzettl, R. Panek, M. Hron, J. Stockel, F. Zacek, J. Havlicek, P. Bilkova, D. I. Naydenkova, P. Hacek, J. Zajac, R. Dejarnac, J. Horacek, J. Adamek, J. Mlynar, F. Janky, M. Aftanas, P. Bohm, J. Brotankova, D. Sestak, I. Duran, R. Melich, D. Jares, J. Ghosh, G. Anda, G. Veres, A. Szappanos, S. Zoletnik, M. Berta, V. Shevchenko, R. Scannell, M. J. Walsh, H. W. Mueller, V. Igochine, A. Silva, M. Manso, R. B. Gomes, Tsv. Popov, D. Sarychev, V. K. Kiselov, and S. Nanobashvili. Overview of

the COMPASS diagnostics. *Fusion Engineering and Design*, 86(6-8):1227–1231, OCT 2011. 26th Symposium on Fusion Technology (SOFT), Porto, Portugal, SEP 27-OCT 01, 2010.

[9] F. Wagner, G. Becker, K. Behringer, D. J. Campbell, A. Eberhagen, W. Engelhardt, G. Fussmann, O. Gehre, J. Gernhardt, G. v. Gierke, G. Haas, M. Huang, F. Karger, M. Keilhacker, O. Klüber, M. Kornherr, K. Lackner, G. Lisitano, G. G. Lister, H. M. Mayer, D. Meisel, E. R. Müller, H. Murmann, H. Niedermeyer, W. Poschenrieder, H. Rapp, H. Röhr, F. Schneider, G. Siller, E. Speth, A. Stäbler, K. H. Steuer, G. Venus, O. Vollmer, and Z. Yü. Regime of Improved Confinement and High Beta in Neutral-Beam-Heated Divertor Discharges of the ASDEX Tokamak. *Phys. Rev. Lett.*, 49:1408–1412, Nov 1982.

[10] F. Wagner. A quarter-century of H-mode studies. *Plasma Physics and Controlled Fusion*, 49(12B):B1, 2007.

[11] P. Deichuli, V. Davydenko, V. Belov, A. Gorbovsky, A. Dranichnikov, A. A. Ivanov, A. Sorokin, V. Mishagin, A. Abdrashitov, V. Kolmogorov, and A. Kondakov. Commissioning of heating neutral beams for COMPASS-D tokamak. *The Review of scientific instruments*, 83(2):02B114, February 2012.

[12] S. J. Fielding, J. D. Ashall, P. G. Carolan, A. Colton, D. Gates, J. Hugill, A. W. Morris, M. Valovic, the COMPASS-D, and ECRH teams. The H-mode in COMPASS-D. *Plasma Physics and Controlled Fusion*, 38(8):1091, 1996.

[13] P. G. Carolan, S. J. Fielding, S. Gerasimov, J. Hugill, A. W. Morris, D. C. Robinson, T. N. Todd, M. Valovic, J. D. Ashall, K. B. Axon, R. A. Bamford, C. A. Bunting, T. Edlington, A. M. Edwards, J. G. Ferreira, S. J. Manhood, R. O'Connell, M. A. Singleton, K. Stammers, J. Tomas, and D. L. Trotman. Characteristics of ohmic H-modes in COMPASS-D. *Plasma Physics and Controlled Fusion*, 36(7A):A111, 1994.

[14] R. Panek, J. Stockel, J. Havlicek, F. Janky, M. Hron, V. Weinzettl, P. Bilkova, M. Dimitrova, P. Hacek, R. Dejarnac, M. Aftanas, P. Bohm, P. Cahyna, M. Imrisek, E. Stefanikova, J. Varju, and the COMPASS team. Characterization of Ohmic and NBI heated H-mode in the COMPASS tokamak. In *EPS Conference on Plasma Physics, 2013 (Papers)*, pages 1–4, P4.103, July 2013.

[15] H. Zohm. *Magnetohydrodynamic Stability of Tokamaks*. Wiley-VCH, 1 edition, December 2014.

[16] H. Zohm. The physics of edge localized modes (ELMs) and their role in power and particle exhaust. *Plasma Physics and Controlled Fusion*, 38(8):1213, 1996.

[17] G. L. Falchetto, D. P. Coster, R. Coelho, B. D. Scott, L. Figini, D. Kalupin, E. Nardon, S. Nowak, L. L. Alves, J. F. Artaud, V. Basiuk, J. P.S. Bizarro,

C. Boulbe, A. Dinklage, D. Farina, B. Faugeras, J. G. Ferreira, A. Figueiredo, P. Huynh, F. Imbeaux, I. I. Stanik, T. Jonsson, H. J. Klingshirn, C. Konz, A. Kus, N. B. Marushchenko, G. Pereverzev, M. Owsiak, E. Poli, Y. Peysson, R. Reimer, J. Signoret, O. Sauter, R. Stankiewicz, P. Strand, I. Voitsekhovitch, E. Westerhof, T. Zok, W. Zwingmann, ITM-TF Contributors, the ASDEX Upgrade Team, and JET-EFDA Contributors. The European Integrated Tokamak Modelling (ITM) effort: achievements and first physics results. *Nuclear Fusion*, 54(4):043018, 2014.

[18] F. Janky, J. Havlicek, D. F. Valcárcel, M. Hron, J. Horacek, O. Kudlacek, R. Panek, and B. B. Carvalho. Determination of the plasma position for its real-time control in the COMPASS tokamak. *Fusion Engineering and Design*, 86(6-8):1120–1124, OCT 2011. 26th Symposium on Fusion Technology (SOFT), Porto, Portugal, SEP 27-OCT 01, 2010.

[19] F. Janky, J. Havlicek, A. J. N. Batista, O. Kudlacek, J. Seidl, A. C. Neto, J. Pipek, M. Hron, O. Mikulin, A. S. Duarte, B. B. Carvalho, J. Stockel, and R. Panek. Upgrade of the COMPASS tokamak Real-Time Control System. *Fusion Engineering and Design*, 89(3):186–194, March 2014.

[20] F. Janky, M. Hron, J. Havlicek, M. Varavin, F. Zacek, J. Seidl, and R. Panek. Plasma density control in real-time on the COMPASS tokamak. *Fusion Engineering and Design*, 96-97:637–640, 2015.

[21] M. Hron, F. Janky, J. Pipek, J. Sousa, B. B. Carvalho, H. Fernandes, P. Vondracek, P. Cahyna, J. Urban, R. Paprok, O. Mikulín, M. Aftanas, R. Panek, J. Havlicek, J. C. Fortunato, A. J. N. Batista, B.A. Santos, A. S. Duarte, T. Pereira, and D. F. Valcárcel. Overview of the COMPASS CODAC system. *Fusion Engineering and Design*, 89(3):177–185, March 2014. submitted to Fusion Engineering and Design - SI on Design and implementation of real-time systems for magnetic confined fusion.

[22] Continuous Computing Corporation. *FlexChassis ATCA-SH141 (13U, 14-slot AC/DC Chassis) User Manual*, December 2010.

[23] D. F. Valcárcel, A. C. Neto, J. Sousa, B. B. Carvalho, H. Fernandes, J. C. Fortunato, A. S. Gouveia, A. J. N. Batista, A. Fernandes, M. Correia, T. Pereira, I. S. Carvalho, A. S. Duarte, C. A. F. Varandas, M. Hron, F. Janky, and J. Pisacka. An ATCA Embedded Data Acquisition and Control System for the COMPASS tokamak. *Fusion Engineering and Design*, 84(7-11):1901–1904, JUN 2009. 25th Symposium on Fusion Technology, Rostock, Germany, SEP 15-19, 2008.

[24] A. J. N. Batista, A. C. Neto, M. Correia, A. Fernandes, B. B. Carvalho, J. C. Fortunato, J. Sousa, C. A. F. Varandas, F. Sartori, M. Jennison, and JET-EFDA Contributors. ATCA Control System Hardware for the Plasma Vertical Stabilization in the JET Tokamak. In *2009 16th IEEE-NPSS Real-Time Conference*, pages 308–313. IEEE; NPSS, 2009. 16th IEEE/NPSS Real-Time Conference, Beijing, Peoples R China, May 10-15, 2009.

[25] A. J. N. Batista, J. Sousa, and C. A. F. Varandas. ATCA digital controller hardware for vertical stabilization of plasmas in tokamaks. *Review of Scientific Instruments*, 77(10):–, 2006.

[26] R. C. Pereira, A. Fernandes, A. C. Neto, J. Sousa, A. J. N. Batista, B. B. Carvalho, C. M. B. A. Correia, C. A. F. Varandas, and JET-EFDA Contributors. ATCA Fast Data Acquisition and Processing System for JET Gamma-Ray Cameras Upgrade Diagnostic. *IEEE Transactions on Nuclear Science*, 57(2, Part 1):683–687, APR 2010. 16th IEEE/NPSS Real-Time Conference, Beijing, Peoples R China, May 10-15, 2009.

[27] I. S. Carvalho, P. Duarte, H. Fernandes, D. F. Valcárcel, P. J. Carvalho, C. Silva, A. S. Duarte, A. C. Neto, J. Sousa, A. J. N. Batista, and B. B. Carvalho. ISTTOK control system upgrade. *Fusion Engineering and Design*, 88(6–8):1122 – 1126, 2013. Proceedings of the 27th Symposium On Fusion Technology (SOFT-27); Liège, Belgium, September 24-28, 2012.

[28] P. J. Carvalho, H. Thomsen, R. Coelho, P. Duarte, C. Silva, and H. Fernandes. ISTTOK plasma control with the tomography diagnostic. *Fusion Engineering and Design*, 85(2):266 – 271, 2010.

[29] I. S. Carvalho, P. Duarte, H. Fernandes, D. F. Valcárcel, P. J. Carvalho, C. Silva, A. S. Duarte, A. C. Neto, J. Sousa, A. J. N. Batista, T. Hekkert, and B. B. Carvalho. ISTTOK real-time architecture. *Fusion Engineering and Design*, 89(3):195–203, March 2014.

[30] B. Gonçalves, J. Sousa, B. B. Carvalho, A. P. Rodrigues, M. Correia, A. J. N. Batista, J. Vega, M. Ruiz, J. M. Lopez, R. Castro, A. Wallander, N. Utzel, P. Makijarvi, S. Simrock, A. C. Neto, D. Alves, D. F. Valcárcel, P. Lousa, F. Piedade, and L. Fernandes. ITER prototype fast plant system controller. *Fusion Engineering and Design*, 86:556–560, 2011.

[31] B. Gonçalves, J. Sousa, B. B. Carvalho, A. J. N. Batista, A. C. Neto, B. Santos, A. S. Duarte, D. F. Valcárcel, D. Alves, M. Correia, A. P. Rodrigues, P.F. Carvalho, M. Ruiz, J. Vega, R. Castro, J. M. Lopez, N. Utzel, and P. Makijarvi. ITER fast plant system controller prototype based on ATCA platform. *Fusion Engineering and Design*, 87(12):2024 – 2029, 2012. Proceedings of the 8th IAEA Technical Meeting on Control, Data Acquisition, and Remote Participation for Fusion Research.

[32] Wikipedia. FPGA. `https://en.wikipedia.org/wiki/Field-programmable_gate_array`, July 2013.

[33] A. C. Neto, F. Sartori, F. Piccolo, R. Vitelli, G. De Tommasi, L. Zabeo, A. Barbalace, H. Fernandes, D. F. Valcárcel, A. J. N. Batista, and JET-EFDA Contributors. MARTe: A Multiplatform Real-Time Framework. *IEEE Transactions on Nuclear Science*, 57(2, Part 1):479–486, APR 2010. 16th IEEE/NPSS Real-Time Conference, Beijing, Peoples R China, May 10-15, 2009.

[34] D. F. Valcárcel, A. S. Duarte, A. C. Neto, I. S. Carvalho, B. B. Carvalho, H. Fernandes, J. Sousa, F. Sartori, F. Janky, P. Cahyna, M. Hron, and R. Panek. Real-time software for the COMPASS tokamak plasma control. *Fusion Engineering and Design*, 85(3-4):470–473, JUL 2010. 7th IAEA Technical Meeting on Control, Data Acquisition and Remote Participation for Fusion Research, Aix-en-Provence, France, May 15-JUN 19, 2009.

[35] J. C. Fortunato, A. J. N. Batista, J. Sousa, H. Fernandes, and C. A. F. Varandas. Event and Pulse Node Hardware Design for Nuclear Fusion Experiments. *Nuclear Science, IEEE Transactions on*, 55(2):679–682, 2008.

[36] J. Zajac, R. Panek, F. Zacek, J. Vlcek, M. Hron, A. Krivska, R. Hauptmann, M. Danek, J. Simek, and J. Prosek. Power supply system for the COMPASS tokamak re-installed at the IPP, Prague. *Fusion Engineering and Design*, 84(7-11):2020–2024, JUN 2009. 25th Symposium on Fusion Technology, Rostock, Germany, SEP 15-19, 2008.

[37] J. Zajac, F. Zacek, V. Lejsek, and Z. Brettschneider. Short-term power sources for tokamaks and other physical experiments. *Fusion Engineering and Design*, 82(4):369 – 379, 2007.

[38] J. Pavelka, R. Hauptmann, J. Šimek, and P. Pavelka. Tokamak. *Elektro, odborný časopis pro eletrotechniku*, 2:6–13, 2015.

[39] Electronic Industries Association. Engineering Department. *Interface between data terminal equipment and data communication equipment employing serial binary data interchange.* Electronic Industries Association, Engineering Dept, Washington, USA, 1969.

[40] RS-232. `http://en.wikipedia.org/wiki/RS-232`, 2013.

[41] Mitsubishi. Mosfet Module FM600TU-3A High Power Switching use Insulated Package. `http://www.mitsubishielectric.com/semiconductors/content/product/powermod/powmod/mosfetmod/mosfetmod_lv4/fm600tu-3a_e.pdf`, Jan. 2013.

[42] J. Havlicek, R. Hauptmann, O. Peroutka, M. Tadros, M. Hron, F. Janky, P. Vondracek, P. Cahyna, O. Mikulín, D. Šesták, P. Junek, and R. Pánek. Power supplies for plasma column control in the COMPASS tokamak. *Fusion Engineering and Design*, 88(9-10):1640–1645, 2013. accepted for publication.

[43] Infineon. Technical Information FZ3600R17HP4. `http://www.infineon.com/dgdl/DS_FZ3600R17HP4_2_2.PDF?folderId=db3a304412b407950112b4095b0601e3&fileId=db3a30432313ff5e01235601c5db1610`, Jan. 2013.

[44] Tms320c6414, tms320c6415, tms320c6416 fixed-point digital signal processors. `http://www.ti.com/lit/ds/symlink/tms320c6416.pdf`, Texas Instruments 2005.

[45] Digital signal processor. http://en.wikipedia.org/wiki/Digital_signal_processor, 2015.

[46] Intel. ATX Specification - Version 2.2. http://www.formfactors.org/developer/specs/atx2_2.pdf, 2004.

[47] PCI-SIG. PCI Express Base 3.1 Specification. https://members.pcisig.com/wg/PCI-SIG/document/download/8257, 2014.

[48] A. C. Neto, H. Fernandes, A. S. Duarte, B. B. Carvalho, J. Sousa, D. F. Varcarcel, M. Hron, and C. A. F. Varandas. FireSignal - Data acquisition and control. *Fusion Engineering and Design*, 82(5-14):1359–1364, OCT 2007. 24th Symposium on Fusion Technology (SOFT-24), Warsaw, POLAND, SEP 11-15, 2006.

[49] Inc. Object Management Group. CORBA. http://www.corba.org, 2015.

[50] Microchip Technology Inc. Data Sheet - dsPIC30F4011/4012. http://ww1.microchip.com/downloads/en/devicedoc/70135c.pdf, Jan. 2013.

[51] A. C. Neto, D. Alves, L. Boncagni, P. J. Carvalho, D. F. Valcárcel, A. Barbalace, G. De Tommasi, H. Fernandes, F. Sartori, E. Vitale, R. Vitelli, and L. Zabeo. A Survey of Recent MARTe Based Systems. *Nuclear Science, IEEE Transactions on*, 58(4):1482–1489, aug. 2011.

[52] I. S. Carvalho, P. Duarte, H. Fernandes, D. F. Valcárcel, P. J. Carvalho, C. Silva, A. S. Duarte, A. C. Neto, J. Sousa, A. J. N. Batista, T. Hekkert, B. B. Carvalho, and R. B. Gomes. Real-time control for long ohmic alternate current discharges. *Fusion Engineering and Design*, 89(5):576 – 581, 2014. Proceedings of the 9th IAEA Technical Meeting on Control, Data Acquisition, and Remote Participation for Fusion Research.

[53] L. Boncagni, R. Vitelli, D. Carnevale, Cristian Galperti, G. Artaserse, and D. Pucci. An overview of the software architecture of the plasma position, current and density realtime controller of the FTU. *Fusion Engineering and Design*, 89(3):204–213, March 2014.

[54] L. Boncagni, D. Pucci, F. Piesco, E. Zarfati, G. Mazzitelli, and S. Monaco. A control approach for plasma density in tokamak machines. *Fusion Engineering and Design*, 88(6–8):1097 – 1100, 2013. Proceedings of the 27th Symposium On Fusion Technology (SOFT-27); Liège, Belgium, September 24-28, 2012.

[55] L. Boncagni, Y. Sadeghi, D. Carnevale, A. Di Geronimo, G. Varano, R. Vitelli, C. Galperti, E. Zarfati, and D. Pucci. MARTe at FTU: The new feedback control. *Fusion Engineering and Design*, 87(12):1917 – 1920, 2012. Proceedings of the 8th IAEA Technical Meeting on Control, Data Acquisition, and Remote Participation for Fusion Research.

[56] L. Boncagni, C. Centioli, C. Galperti, E. Alessi, G. Granucci, L. A. Grosso, C. Marchetto, M. Napolitano, S. Nowak, M. Panella, C. Sozzi, B. Tilia, and V. Vitale. Hardware and software architecture for the integration of

the new EC waves launcher in FTU control system. *Fusion Engineering and Design*, 88(6–8):1050 – 1054, 2013. Proceedings of the 27th Symposium On Fusion Technology (SOFT-27); Liege, Belgium, September 24-28, 2012.

[57] C. Galperti, L. Boncagni, E. Alessi, C. Sozzi, S. Nowak, G. Granucci, D. Minelli, and C. Marchetto. Testing and commissioning the multinode ECRH realtime control system on the FTU tokamak. *Fusion Engineering and Design*, 89(3):214–223, March 2014.

[58] A. Luchetta, G. Manduchi, and C. Taliercio. Fast control and data acquisition in the neutral beam test facility. *Fusion Engineering and Design*, 89(5):663 – 668, 2014. Proceedings of the 9th IAEA Technical Meeting on Control, Data Acquisition, and Remote Participation for Fusion Research.

[59] G. Manduchi, A. Luchetta, A. Soppelsa, and C. Taliercio. From distributed to multicore architecture in the RFX-mod real time control system. *Fusion Engineering and Design*, 89(3):224–232, March 2014.

[60] G. Manduchi, A. Barbalace, A. Luchetta, A. Soppelsa, C. Taliercio, and E. Zampiva. Upgrade of the RFX-mod real time control system. *Fusion Engineering and Design*, 87(12):1907 – 1911, 2012. Proceedings of the 8th IAEA Technical Meeting on Control, Data Acquisition, and Remote Participation for Fusion Research.

[61] T. Bellizio, G. De Tommasi, N. Risoli, R. Albanese, and A. C. Neto. A MARTe based simulator for the JET vertical stabilization system. *Fusion Engineering and Design*, 86(6–8):1026 – 1029, 2011. Proceedings of the 26th Symposium of Fusion Technology (SOFT-26).

[62] G. De Tommasi, F. Maviglia, A. C. Neto, P. J. Lomas, P. McCullen, and F. G. Rimini. Plasma position and current control system enhancements for the JET ITER-like wall. *Fusion Engineering and Design*, 89(3):233–242, March 2014.

[63] F. G. Rimini, F. Crisanti, R. Albanese, G. Ambrosino, M. Ariola, G. Artaserse, T. Bellizio, V. Coccorese, G. De Tommasi, P. C. de Vries, P. J. Lomas, F. Maviglia, A. C. Neto, I. Nunes, A. Pironti, G. Ramogida, F. Sartori, S. R. Shaw, M. Tsalas, R. Vitelli, and L. Zabeo. First plasma operation of the enhanced JET vertical stabilisation system. *Fusion Engineering and Design*, 86(6–8):539 – 543, 2011. Proceedings of the 26th Symposium of Fusion Technology (SOFT-26).

[64] A. Fernandes, R. C. Pereira, D. F. Valcárcel, D. Alves, B. B. Carvalho, J. Sousa, V. Kiptily, C. M. B. A. Correia, and B. Gonçalves. Real-time algorithms for JET hard X-ray and gamma-ray profile monitor. *Fusion Engineering and Design*, 89(3):259–266, March 2014.

[65] D. F. Valcárcel, D. Alves, P. Card, B. B. Carvalho, S. Devaux, R. Felton, A. Goodyear, P. J. Lomas, F. Maviglia, P. McCullen, C. Reux, F. G. Rimini, A. Stephen, L. Zabeo, and K-D. Zastrow. The JET real-time plasma-wall load monitoring system. *Fusion Engineering and Design*, 89(3):243–258, March 2014.

[66] A. Barbalace. *MARTe/BaseLib2 Software Design Analysis Code Development Guide*, June 2009.

[67] `atca1:/root/code/JET_Control/BaseLib2/Documentation/images/MARTeComponents.svg`.

[68] M. Hron, J. Sova, J. Siba, J. Kovar, J. Adamek, R. Panek, J. Havlicek, J. Pisacka, J. Mlynar, and J. Stockel. Interlock system for the COMPASS tokamak. *Fusion Engineering and Design*, 85(3-4):505–508, JUL 2010. 7th IAEA Technical Meeting on Control, Data Acquisition and Remote Participation for Fusion Research, Aix-en-Provence, France, May 15-JUN 19, 2009.

[69] O. Mikulin, M. Hron, P. Bohm, G. Naylor, P. Bilkova, F. Janky, J. Salasek, and R. Panek. Timing and triggering of the Thomson scattering diagnostics on the COMPASS tokamak. *Fusion Engineering and Design*, 89(5):693 – 697, 2014. Proceedings of the 9th IAEA Technical Meeting on Control, Data Acquisition, and Remote Participation for Fusion Research.

[70] P. Bilkova, M. Aftanas, P. Bohm, V. Weinzettl, D. Sestak, R. Melich, J. Stockel, R. Scannell, and M. J. Walsh. Design of new Thomson scattering diagnostic system on COMPASS tokamak. *Nuclear Instruments and Methods in Physics Research Section A: Accelerators, Spectrometers, Detectors and Associated Equipment*, 623(2):656 – 659, 2010. 1rs International Conference on Frontiers in Diagnostics Technologies.

[71] M. Aftanas, P. Bohm, R. Scannell, M Tripsky, V. Weinzettl, M. Hron, R. Panek, J. Stockel, M. J. Walsh, and P. Bilkova. Thomson scattering on COMPASS — commissioning and first data. *Journal of Instrumentation*, 7(01):C01074, 2012.

[72] P. Bohm, M. Aftanas, P. Bilkova, E. Stefanikova, O. Mikulin, R. Melich, F. Janky, J. Havlicek, D. Sestak, V. Weinzettl, J. Stockel, M. Hron, R. Panek, R. Scannell, L. Frassinetti, A. Fassina, G. Naylor, and M. J. Walsh. Edge Thomson scattering diagnostic on COMPASS tokamak: Installation, calibration, operation, improvements. *Review of Scientific Instruments*, 85(11):1–3, 2014.

[73] M. Berta, G. Anda, M. Aradi, A. Bencze, C. Buday, I. G. Kiss, S. Tulipan, G. Veres, S. Zoletnik, J. Havlicek, and P. Hacek. Development of atomic beam probe for tokamaks. *Fusion Engineering and Design*, 88(11):2875–2880, 2013.

[74] F. Janky, H. Fernandes, I. S. Carvalho, J. Sousa, and T. V. Pereira. *Current Control Protocol (CCP) v 1.0.2.*, March 2008.

[75] J. Stockel, J. Brotankova, R. Dejarnac, J. Havlicek, M. Hron, D. Naydenkova, R. Panek, V. Weinzettl, J. Zajac, F. Zacek, M. Berta, A. Szappanos, Sz. Tulipán, G. Veres, S. Zoletnik, D. F. Valcárcel, T. V. Pereira, I. Cavalho, A. S. Duarte, A. C. Neto, Fernandes H., and the COMPASS Team. Plasma breakdown studies on COMPASS. In *36th EPS Conference on Plasma Physics*, volume 33E, pages P–5.141, Sofia, 2009.

[76] Chen F. F. *Úvod do fyziky plasmatu.* Academia Praha, 1984.

[77] J. Havlicek. *Study of Equilibrium Magnetic Configuration in Tokamak Type Devices.* PhD thesis, Department of Surface and Plasma Science, Faculty of Mathematics and Physics, Charles Universtity in Prague, 2015.

[78] G. Casini, F. C. Schüller, and A. A. M. Oomens. Plasma engineering aspects of large tokamak operation. *Fusion Engineering and Design*, 22(1):35 – 55, 1993.

[79] J. A. Wesson, R. D. Gill, M. Hugon, F. C. Schüller, J. A. Snipes, D. J. Ward, D. V. Bartlett, D. J. Campbell, P. A. Duperrex, A. W. Edwards, R. S. Granetz, N. A. O. Gottardi, T. C. Hender, E. Lazzaro, P. J. Lomas, N. L. Cardozo, K. F. Mast, M. F. F. Nave, N. A. Salmon, P. Smeulders, P. R. Thomas, B. J. D. Tubbing, M. F. Turner, and A. Weller. Disruptions in JET. *Nuclear Fusion*, 29(4):641, 1989.

[80] P. C. de Vries, M. F. Johnson, B. Alper, P. Buratti, T. C. Hender, H. R. Koslowski, V. Riccardo, and JET-EFDA Contributors. Survey of disruption causes at JET. *Nuclear Fusion*, 51(5):053018, 2011.

[81] Pautasso, G. and de Vries, P. C. and the ASDEX Upgrade team. Disruption causes in ASDEX Upgrade. *Europhysics Conference Abstracts*, 38F:P2.015, 2014.

[82] M. Kikuchi. *Fusion Physics.* International Atomic Energy Agency, 2012.

[83] C. M. Braams and P. E. Stott. *Nuclear Fusion: Half a Century of Magnetic Confinement Fusion Research.* CRC Press, 2002.

[84] J. P. Freidberg. *Plasma Physics and Fusion Energy.* Cambridge University Press, 2007. Cambridge Books Online.

[85] P. Kudlacek. Řízení polohy plazmatu tokamaku COMPASS s přihlédnutím k tlmumícimu efektu vodivé komory zařízení. Master's thesis, České vysoké učení technické v Praze Fakulta jaderná a fyzikálně inženírská Katedra fyziky, Prague, Czech Republic, 2011.

[86] P. R. Thomas, J. A. Wesson, F. Alladio, D. V. Bartlett, K. Behringer, R. J. Bickerton, M. Brusati, D. J. Campbell, J. P. Christiansen, J. G. Cordey, A. E. Costley, F. Crisanti, K. J. Dietz, P. A. Duperrex, W. Engelhardt, A. Gibson, R. D. Gill, N. A. O. Gottardi, C. W. Gowers, B. J. Green, J. L. Hemmerich, C. A. Hugenholz, M. Huguet, R. Keller, L. de Kock, H. Krause, J. Last, E. Lazzaro, F. K. Mast, P. D. Morgan, A. W. Morris, H. Niedermeyer, P. Noll, M. Pick, A. Pochelon, P. H. Rebut, D. C. Robinson, R. T. Ross, G. J. Sadler, F. C. Schüller, T. E. Stringer, D. Summers, A. Tanga, G. Tonetti, and P. van Belle. MHD behaviour and discharge optimization in JET. *Phys. Contr. Nucl. Fusion Research*, 1:353, 1985.

[87] P. Vyas. *Plasma vertical position control in COMPASS-D tokamak.* PhD thesis, University of Oxford, Oxford, U.K., 1996.

[88] L. C. Appel, G. T. A. Huysmans, L. L. Lao, P. J. McCarthy, D. G. Muir, E. R. Solano, J. Storrs, D. Taylor, and W. Zwingmann. A Unified Approach to Equilibrium Reconstruction. In *Europhysics Conference Abstract*, volume 30I, pages P–2.184, 2006.

[89] V. D. Shafranov. Equilibrium of a toroidal pinch in a magnetic field. *Soviet Atomic Energy*, 13(6):1149–1158, November 1963.

[90] J. Urban, J. Pipek, M. Hron, F. Janky, R. Paprok, M. Peterka, and A. S. Duarte. Integrated data acquisition, storage, retrieval and processing using the COMPASS DataBase (CDB). *Fusion Engineering and Design*, 89(5):712 – 716, 2014. Proceedings of the 9th IAEA Technical Meeting on Control, Data Acquisition, and Remote Participation for Fusion Research.

[91] Bilinear Interpolation. `https://en.wikipedia.org/wiki/Bilinear_interpolation`, November 2015.

[92] Electronic Industries Association. Engineering Department. *Interface between data terminal equipment and data communication equipment employing serial binary data interchange*. Electronic Industries Association, Engineering Deptartment, Washington, 1969.

[93] Xilinx. Aurora. http://www.xilinx.com/products/design
_resources/conn
_central/grouping/aurora.htm, July 2013.

[94] O. Mikulin and F. Janky. *VKPS and FA regulator communication protocol v0.3*, 2014.

[95] Radek Beňo. Řízení Tokamaku COMPASS. Master's thesis, České vysoké učení technické v Praze Fakulta elektrotechnická, January 2011.

[96] M. Hron, J. Havlicek, O. Mikulin, M. Tadros, F. Janky, J. Stockel, A. J. N. Batista, M. Imrisek, V. Weinzettl, J. Krbec, and R. Panek. ELM control using vertical kicks on the COMPASS tokamak. In *21st IAEA TM on Research Using Small Fusion Devices, 27-29 January 2014, San José, Costa Rica*, 2014.

[97] A. Kostic. Physics of the L-H transition with different X-point heights in the COMPASS tokamak. Master's thesis, Universiteit Ghent, July 2015.

[98] J. Horacek, P. Vondracek, R. Panek, R. Dejarnac, M. Komm, R. A. Pitts, M. Kocan, R. J. Goldston, P. C. Stangeby, E. Gauthier, P. Hacek, J. Havlicek, M. Hron, M. Imrisek, F. Janky, and J. Seidl. Narrow heat flux channels in the COMPASS limiter scrape-off layer. *Journal of Nuclear Materials*, 463:385 – 388, 2015. Plasma-Surface Iinteractions 21Proceedings of the 21st International Conference on Plasma-Surface Interactions in Controlled Fusion Devices Kanazawa, Japan May 26-30, 2014.

[99] M. Kocan, R. A. Pitts, G. Arnoux, I. Balboa, P. C. de Vries, R. Dejarnac, I. Furno, R. J. Goldston, Y. Gribov, J. Horacek, M. Komm, B. Labit, B. Labombard, C. J. Lasnier, R. Mitteau, F. Nespoli, D. Pace, R. Panek,

P. C. Stangeby, J. L. Terry, C. Tsui, and P. Vondracek. Impact of a narrow limiter SOL heat flux channel on the ITER first wall panel shaping. *Nuclear Fusion*, 55(3):033019, 2015.

[100] O. Motojima. The ITER project construction status. *Nuclear Fusion*, 55(10):104023, 2015.

[101] M. Keilhacker. H-mode confinement in tokamaks. *Plasma Physics and Controlled Fusion*, 29(10A):1401, 1987.

[102] J. A. Wesson and A. Sykes. Tokamak Beta Limit. *Nuclear Fusion*, 25(1):85–88, 1985.

[103] F. Troyon, R. Gruber, H. Saurenmann, S. Semenzato, and S. Succi. MHD-Limits to Plasma Confinement. *Plasma Physics and Controlled Fusion*, 26(1A):209–215, 1984.

[104] A. L. Peratt. Advances in Numerical Modeling of Astrophysical and Space Plasmas. *Astrophysics and Space Science*, 242:93–163, March 1996.

[105] M. Greenwald, J. L. Terry, S. M. Wolfe, S. Ejima, M. G. Bell, S. M. Kaye, and G. H. Neilson. A new look at density limits in tokamaks. *Nuclear Fusion*, 28(12):2199, 1988.

[106] M. Greenwald. Density limits in toroidal plasmas. *Plasma Physics and Controlled Fusion*, 44(8):R27, 2002.

[107] M. Bernert, T. Eich, A. Kallenbach, D. Carralero, A. Huber, P. T. Lang, S. Potzel, F. Reimold, J. Schweinzer, E. Viezzer, and H. Zohm. The H-mode density limit in the full tungsten ASDEX Upgrade tokamak. *Plasma Physics and Controlled Fusion*, 57(1):014038, 2015.

[108] M. A. Mahdavi, T. H. Osborne, A. W. Leonard, M. S. Chu, E. J. Doyle, M. E. Fenstermacher, G. R. McKee, G. M. Staebler, T. W. Petrie, M. R. Wade, S. L. Allen, J. A. Boedo, N. H. Brooks, R. J. Colchin, T. E. Evans, C. M. Greenfield, G. D. Porter, R. C. Isler, R. J. La Haye, C. J. Lasnier, R. Maingi, R. A. Moyer, M. J. Schaffer, P. G. Stangeby, J. G. Watkins, W. P. West, D. G. Whyte, and N. S. Wolf. High performance H-mode plasmas at densities above the Greenwald limit. *Nuclear Fusion*, 42(1):52, 2002.

[109] O. Gruber, V. Mertens, J. Neuhauser, F. Ryter, W. Suttrop, M. Albrecht, M. Alexander, K. Asmussen, G. Becker, K. Behler, K. Behringer, A. Bergmann, M. Bessenrodt-Weberpals, K. Borras, H. S. Bosch, B. Braams, M. Brambilla, F. Braun, H. Brinkschulte, K. Büchl, A. Buhler, A. Carlson, R. Chodura, D. P. Coster, L. Cupido, H. J. De Blank, S. De Pena Hempel, S. Deschka, C. Dorn, R. Drube, R. Dux, W. Engelhardt, J. Engstler, H. U. Fahrbach, H. U. Feist, S. Fiedler, P. Franzen, J. C. Fuchs, G. Fussmann, J. Gafert, O. Gehre, J. Gernhardt, S. Günter, G. Haas, K. Hallatschek, J. Hartmann, B. Heinemann, G. Herppich, A. Herrmann, W. Herrmann, S. Hirsch, M. Hoek, F. Hoenen, F. Hofmeister, H. Hohenoecker, E. Holzhauer, P. Ignacz, D. Jacobi, W. Junker, M. Kakoulidis,

A. Kallenbach, N. Karakatsanis, O. Kardaun, T. Kass, M. Kaufmann, A. Khutoretski, H. Kollotzek, W. Koeppendoerfer, W. Kraus, K. Krieger, B. Kurzan, G. Kyriakakis, K. Lackner, P. T. Lang, R. S. Lang, M. Laux, L. Lengyel, F. Leuterer, M. Maraschek, M. Markoulaki, K. F. Mast, P. J. McCarthy, D. Meisel, H. Meister, R. Merkel, H. W. Mueller, M. Muenich, H. Murmann, B. Napiontek, G. Neu, R. Neu, M. Niethammer, J. M. Noterdaeme, E. Pasch, G. Pautasso, A. G. Peeters, G. Pereverzev, C. S. Pitcher, W. Poschenrieder, G. Raupp, K. Reinmueller, R. Riedl, V. Rohde, H. Roehr, J. Roth, H. Salzmann, W. Sandmann, H. B. Schilling, M. Schittenhelm, D. Schloegl, H. Schneider, R. Schneider, W. Schneider, G. Schramm, J. Schweinzer, S. Schweizer, R. Schwoerer, B. D. Scott, U. Seidel, F. Serra, S. Sesnic, A. Silva, M. Sokoll, E. Speth, A. Staebler, K. H. Steuer, J. Stober, B. Streibl, A. Thoma, W. Treutterer, M. Troppmann, N. Tsois, M. Ulrich, P. Varela, H. Verbeek, O. Vollmer, H. Wedler, M. Weinlich, U. Wenzel, F. Wesner, R. C. Wolf, R. Wunderlich, N. Xantopoulus, Q. Yu, D. Zasche, T. Zehetbauer, H. P. Zehrfeld, H. Zohm, and M. Zouhar. Divertor tokamak operation at high densities on ASDEX Upgrade. *Plasma Physics and Controlled Fusion*, 39(12B):B19, 1997.

[110] A. V. Melnikov, T. Markovic, L. G. Eliseev, J. Adamek, M. Aftanas, P. Bilkova, P. Bohm, M. P. Gryaznevich, M. Imrisek, S. E. Lysenko, S. Y. Medvedev, R. Panek, M. Peterka, J. Seidl, E. Stefanikova, J. Stockel, V. Weinzettl, and the COMPASS team. Quasicoherent modes on the COMPASS tokamak. *Plasma Physics and Controlled Fusion*, 57(6):065006, 2015.

[111] Pfeiffer vacuum. Compact fullrange gauge. `http://www.idealvac.com/files/brochures/Pfeiffer_PKR_251_Pirani_ColdCathode.pdf`, APR 2008.

[112] M. Varavin, J. Zajac, F. Zacek, S. Nanobashvili, G. P. Ermak, A. Varavin, A. Vasilev, M. Stumbra, A. Vetoshko, A. S. Fateev, and V. Shevchenko. New Design of Microwave Interferometer for tokamak COMPASS. *Telecommunications and Radio Engineering*, 73(10):571–575, 2014.

[113] M. Varavin, J. Zajac, F. Zacek, S. Nanobashvili, G. P. Ermak, A. Varavin, A. Vasilev, M. Stumbra, A. Vetoshko, A. S. Fateev, and V. Shevchenko. Modernization and calibration of intrferometer of tokamak COMPASS;. In *Physics and Engineering of Microwaves, Millimeter and Submillimeter Waves (MSMW)*, pages 571–575, June 2013.

[114] A. Mlynek, L. Casali, O. Ford, H. Eixenberger, and ASDEX Upgrade Team. Fringe jump analysis and implementation of polarimetry on the ASDEX Upgrade DCN interferometer. *Review of Scientific Instruments*, 85(11), 2014.

[115] D. Shiner, J. M. Gilligan, B. M. Cook, and W. Lichten. H_2, D_2, and HD ionization potentials by accurate calibration of several iodine lines. *Phys. Rev. A*, 47:4042–4045, May 1993.

[116] D. R. Lide. *Ionization potentials of atoms and atomic ions*. CRC Press, Boca Raton, FL, 2005.

List of Tables

List of Figures

List of Abbreviations

ČKD Communication Unit (ČKD-CU) Communication and timing unit for controlling main power supplies. 8, 76, 112

Advance Telecommunications Computing Architecture (ATCA) A data acquisition system based on standard telecommunication architecture. 6, 68

Advanced Technology eXtended (ATX) A motherboard configuration specification developed by Intel. 11

Analog Digital Converter (ADC) Converts analog signal to digital. 24

Central Processing Unit (CPU) An electronic circuitry within a computer that carries out the instructions of a computer program by performing the basic arithmetic, logical, control and input/output (I/O) operations specified by the instructions. 12

Central Solenoid (CS) Solenoid in the centre of tokamak mainly used for current drive and ohmic plasma heating. 8, 22, 127

Common Object Request Broker Architecture (CORBA) A communication protocol. 12

COMPASS DataBase (CDB) A database for storing signals. It was developed at COMPASS. 52

Current Control Protocol (CCP) Communication protocol for communicating between main power supplies (EFPS, MFPS, TFPS and SFPS) and real-time control framework MARTe. 29

Data Acquisition System (DAS) Data acquisition system used for acquiring data from experiment. 6, 24, 112

Digital Signal Processor (DSP) A specialised microprocessor, with its architecture optimised for the operational needs of digital signal processing. 11

Digitizer-Generator-Processor (DGP) Card equipped with 32 ADC; 8 DAC; 1 FPGA to control the module inputs and outputs and perform fast data processing; 512 MB DDR2 memory for data buffering; 11 serial links (Aurora) to connect to other similar boards through the crate backplane; 8 RS485 serial links to connect to external devices; 1 SFP transceiver for an Aurora serial link to connect to the timing and event processing boards. 6

Direct Memory Access (DMA) Direct memory access is a feature of computer systems that allows certain hardware subsystems to access main system memory (RAM) independently of the central processing unit (CPU).. 7

Double Null Divertor (DND) Plasma shape with two divertors (up and down) inside the tokamak vacuum vessel. 74

Dynamic Data Buffer (DDB) A memory bus in MARTe. 14, 109

Edge Localised Mode (ELM) A disruptive instability occurring in the edge region of a tokamak plasma due to the quasi-periodic relaxation of a transport barrier. 4, 71, 79, 106, 110, 128

Electron Cyclotron Resonant Heating (ECRH) A system heating the electrons in the plasma with a high-intensity beam of electromagnetic radiation. 12

Equilibrium and Reconstruction Fitting Code (EFIT) A computer code developed to translate measurements from plasma diagnostics into useful information like plasma geometry, stored energy and current profiles. 41

Equilibrium Field (EF) A vertical magnetic field establishing equilibrium and powered by Equilibrium Field Power Supply. 8, 35

Equilibrium Field Power Supply (EFPS) A power supply for establishing equilibrium. 8, 27, 35, 76, 106, 109, 126

Error Field Current Coils (EFCC) A set of coils specified to compensate the main harmonic contribution to error field induced modes. 13

Event and Pulse Node (EPN) A node distributing triggers and synchronising clock. 11

External Partial Rogowski (EPR) Part of a Rogowski coil placed outside of the vacuum vessel. 41

Fast Amplifier for Radial Magnetic Field (FABR) A power supply for vertical stabilisation. 10, 36, 87, 107, 126

Fast Amplifier for Vertical Magnetic Field (FABV) A power supply for horizontal stabilisation. 10, 35, 87, 106, 109, 126

Field Programmable Gate Array (FPGA) An integrated circuit designed to be configured by a customer or a designer after manufacturing. 6, 57, 107, 113

Finite Input Response (FIR) Filtering method. 6

Flux Loop (FL) A loop of wire placed measuring magnetic flux. 41

Frascati Tokamak Upgrade (FTU) A tokamak operating at Frascati, Italy. 12

Generic Application Module (GAM) A defined block of software, that is executed by the real-time scheduler in MARTe. 13, 28, 58, 75, 99, 107, 109, 128

Graphical User Interface (GUI) Graphical interface for interaction with user. 12, 93, 112

High Field Side (HFS) An inner side of the tokamak vessel with higher magnetic field. 8, 21, 58

HyperText Markup Language (HTML) A standard markup language used to create web pages. 15

Input Output Generic Application Module (IOGAM) A module providing a unique high-level interface to any kind of hardware in MARTe. 13

Instituto Superior Técnico TOKamak (ISTTOK) A tokamak operating at Instituto Superior Técnico, in Lisabon, Portugal. 12

Integrated Tokamak Modelling (ITM) Activity to integrate all models describing tokamaks' physic in one framework. 5

Internal Partial Rogowski (IPR) Part of a Rogowski coil placed in the vacuum vessel. 41, 88, 109, 130

ITER-like wall (ILW) A tokamak wall composed with the same material as will be used at ITER tokamak. 13, 23

Joint European Torus (JET) The world's largest operational tokamak, located at Culham Centre for Fusion Energy in Oxfordshire, UK.. 6

Last Closed Flux Surface (LCFS) Last closed magnetic field line. 23

Low Field Side (LFS) An outers side of the tokamak vessel with lower magnetic field. 8, 21, 58, 79

Magnetising Field (MF) A magnetic field for ohmic heating and plasma current drive. It is powered by Magnetising Field Power Supply. 8, 22, 36

Magnetising Field Power Supply (MFPS) A power supply for ohmic heating and plasma current drive. 8, 22, 36, 75, 88, 106, 110, 126

MagnetoHydroDynamic (MHD) A study of the magnetic properties of electrically conducting fluids. 13, 23, 34, 73, 79

Multi-Threaded Real-Time executor (MARTe) A real-time framework built over a multi-platform library that allows the execution of the same code in different operating systems.. 12

Multiple Input Multiple Output (MIMO) Controller with multiple inputs and outputs. 106, 111

Neautral Beam Injection (NBI) External heating using neutral beam injection. 4, 27, 79, 127

Ohmic Heating (OH) Heat the plasma by inducing a current through it. It is done by driving current in Magnetising Field coils using Magnetising Field Power Supply. 8, 23

Operating System (OS) System software that manages computer hardware and software resources and provides common services for computer programs. 12

Peripheral Component Interconnect Express (PCIe™) A high-speed serial computer expansion bus. 11

Personal Computer (PC) A personal computer is a general-purpose computer whose size, capabilities and original sale price make it useful for individuals, and is intended to be operated directly by an end-user with no intervening computer operator.. 11

Proportional Integral (PI) Controller with proportional and integral component.. 19, 29, 40, 93, 107, 109

Proportional-Integral-Derivative (PID) A control loop feedback mechanism (controller) which continuously calculates an error value as the difference between a desired value and a measured process variable. 19, 60

Pulse Width Modulation (PWM) A modulation technique used to encode a message into a pulsing signal. 93

Radial Field (BR) A magnetic horizontal field for stabilising plasma in vertical direction powered by Fast Amplifier for Radial Field. 10, 36, 131

Real-Time Board (RTB) Board used by MARTe for acquiring data in real-time. 6

Rear Transition Module (RTM) Board assembled with FPGA attached to an ATCA crate used for triggering, synchronisation and communication via Aurora, and assembled with 8 digital analog converters and ouputs. 7, 68, 93

Resonant Magnetic Perturbation (RMP) Resonant magnetic perturbation. 4, 49, 87, 106, 126

Reversed Field eXperiment (RFX) A nuclear fusion test machine in Padova, Italy. 13

Scrape of Layer (SOL) The plasma region characterised by open field lines beginning or ending on a material surface. 5, 106

Shaping Field (SF) A magnetic field for changing plasma shape. It is powered by Shaping Field Power Supply. 8, 36, 74, 110

Shaping Field Power Supply (SFPS) A power supply for creating diverted and elongated plasma. 8, 22, 36, 74, 99, 106, 110, 126

Single Null Divertor (SND) Plasma shape with a divertor. 3, 74

Single Null Divertor with high Triangularity (SNT) Plasma shape with a divertor and high triangularity. 3, 74

Standard Cubic Centimeters per Minute (SCCM) A flow measurement term indicating cubic centimetres per minute at a standard temperature and pressure.. 95, 133

Thomson Scattering (TS) Diagnostic using a laser for measuring electron density and electron temperature profile along a laser chord. 12, 70, 100, 110, 112

Timing Unit (TU) Timing unit providing clocks for synchronising data acquisition systems and reflectometry diagnostic, triggers for diagnostics and MARTe configurable outputs. 7, 113

Toroidal Field (TF) A magnetic field in toroidal direction powered by Toroidal Field Power Supply. 8

Toroidal Field Power Supply (TFPS) A power supply for creating toroidal magnetic field. 8

Transistor–transistor logic (TTL) A class of digital circuits. 12

Vertical Displacement Event (VDE) Fast uncontrolled movement of plasma column in vertical direction. 40, 77, 107

Vertical Field (BV) A magnetic vertical field for stabilising plasma in horizontal direction powered by Fast Amplifier for Vertical Field. 10, 35

Vertical Kick Power Supply (VKPS) Power supply for fast vertical plasma column displacement. 4, 57, 107, 110, 126

Attachments

Fusion Engineering and Design 86 (2011) 1120–1124

Contents lists available at ScienceDirect

Fusion Engineering and Design

journal homepage: www.elsevier.com/locate/fusengdes

Determination of the plasma position for its real-time control in the COMPASS tokamak

F. Janky[a,c,*], J. Havlicek[a,c], D. Valcárcel[b], M. Hron[a], J. Horacek[a], O. Kudlacek[d], R. Panek[a], B.B. Carvalho[b]

[a] Institute of Plasma Physics, AS CR, v.v.i., Association EURATOM/IPP.CR, Za Slovankou 3, 182 00 Prague, Czech Republic
[b] Associação EURATOM/IST, Instituto de Plasmas e Fusão Nuclear - Laboratório Associado, Instituto Superior Técnico, P1049-001 Lisboa, Portugal
[c] Charles University in Prague, Faculty of Mathematics and Physics, V Holesovickach 2, CZ-18000 Prague, Czech Republic
[d] Czech Technical University, Faculty of Nuclear Sciences and Physical Engineering, Technicka 2, 166 27 Prague, Czech Republic

ARTICLE INFO

Article history:
Available online 3 March 2011

Keywords:
Real-time
Plasma position
Feedback

ABSTRACT

An efficient horizontal and vertical stabilization of the plasma column position are essential for a reliable tokamak operation. Plasma position is generally determined by plasma current, plasma pressure and external vertical and horizontal magnetic fields. Such fields are generated by poloidal field coils and proper algorithm for the current control have to by applied, namely, in case of fast feedback loops.

This paper presents a real-time plasma position reconstruction algorithms developed for the COMPASS tokamak. Further, its implementation in the MARTe (Multithreaded Application Real-Time executor) is described and the first results from test of the algorithm for real-time control of horizontal plasma positions are presented.

1. Introduction

Efficient systems for plasma position stabilization form one of the key elements of tokamak operation, especially in case of increasing plasma performance. Such a new digital system has been built for the COMPASS tokamak [1], which has been recently put in a test operation [2]. The COMPASS tokamak is a small size device with main parameters listed in Table 1. Its feedback system is based on a real-time plasma position reconstruction algorithms implemented in the MARTe (Multithreaded Application Real-Time executor) [3]. The COMPASS tokamak is currently being operated with a circular limiter plasma. A model and first results of the real-time control of the radial plasma position are presented.

The paper is organized as follows: Section 1 is an introduction. Section 2 presents the model of plasma used for plasma position calculation. In addition, an appropriate set of magnetic diagnostic coils and a criteria of their selection are described. Section 3 is devoted to the structure of the real-time executor and presents the first results of the horizontal position control in the COMPASS tokamak.

2. Model of plasma and plasma position detection

In order to create an algorithm for plasma position determination a suitable set of magnetic diagnostic coils must be selected. The selection was performed by computing the magnetic field in all magnetic diagnostic coils from modelled plasma with various parameters like plasma shape and plasma current profile. Then two sets of diagnostic coils have been selected for radial and vertical plasma position determination. The main selection criteria were both high sensitivity to the plasma movement and low sensitivity to the different plasma parameters. The final step in the modeling was the computation of look-up tables containing plasma position coordinates in a dependence on signals from both selected sets of diagnostic coils.

An ellipse with different current profiles and "limiter" or "divertor" configuration was used in the modeling as the plasma approximation. The plasma shape was selected to be an ellipse with three different value of elongations $k = 1.0$ (circular plasma cross-section), 1.5 and 2.0. The plasma current profile was described by Eq. (1) [4]

$$j(r) = j(0)\left(1 - \frac{r^2}{a^2}\right)^p \quad (1)$$

where $j(0)$ is current density in the centre, r is the distance from the current profile centre, a is minor radius and p is the peaking

* Corresponding author at: Institute of Plasma Physics, AS CR, v.v.i., Association EURATOM/IPP.CR, Za Slovankou 3, 182 00 Prague, Czech Republic.
Tel.: +420 266053575; fax: +420 286586389.
E-mail addresses: jankyf@ipp.cas.cz, filip.janky@gmail.com (F. Janky).

0920-3796/$ – see front matter © 2011 EURATOM/IPP.CR. Institute of Plasma Physics. Published by Elsevier B.V. All rights reserved.
doi:10.1016/j.fusengdes.2011.01.143

Table 1
COMPASS parameters.

Major radius	0.56m
Minor radius	0.18–0.23 m
Plasma current	<400 kA
Magnetic field	0.9 T–2.1 T
Triangularity	0.5–0.7
Elongation	1.8
Pulse length	<1 s
P_{NBI}	2 × 0.3 MW

factor. Eq. (1) is valid for circular plasma and can be easily adapted for vertically elongated plasma current profile by Eq. (2):

$$j(r,\theta) = j(0)\left(1 - r^2\frac{1-\varepsilon^2\cos^2\theta)}{b^2}\right)^p \quad (2)$$

where ε is eccentricity given by $\varepsilon = \sqrt{1-(1/\kappa^2)}$ and k is elongation, θ is poloidal angle and b is semiminor axis. The peaking factor p was selected to be either 2 or 3. The configuration of the plasma was selected to be either "limiter", i.e. minor radius r is determined by the nearest limiter point or "divertor", i.e. minor radius is set to be smaller than the distance to the nearest limiter point. The minor radius for the "divertor" configuration and for the three different elongations k = 1.0, 1.5 and 2.0 was selected to be a = 0.16 m, 0.15 m and 0.14 m.

The elliptical plasma approximation does not include the Shafranov shift and realistic plasma shape, nevertheless, the twelve used different plasma approximations (all combinations of three elongations, two current profiles and two configurations) allow to decide which diagnostic coils are less sensitive to different plasma parameters and are suitable for plasma position determination (Fig. 1).

Three types of diagnostic coils installed at the COMPASS tokamak (8 flux loops, 24 Mirnov coils and 16 Internal Partial Rogowski (IPR) coils) were taken into account in this simulation. Flux loops are winded around vessel in the toroidal direction at 8 different positions and measure the poloidal flux function Ψ. The 24 Mirnov coils and 16 IPR coils measure the poloidal magnetic field. The IPR coils are 37 mm long while the Mirnov coils have negligible dimension. In order to compute the magnetic field response in the diagnostic coils the poloidal plane was divided into 50 × 50 points. The magnetic field from each of these points to the Mirnov coils and to the IPR coils was calculated using Biot–Savart law.

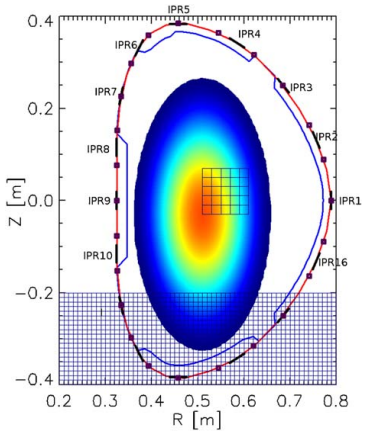

Fig. 1. Position of IPR coils used for simulation and for determination of plasma position.

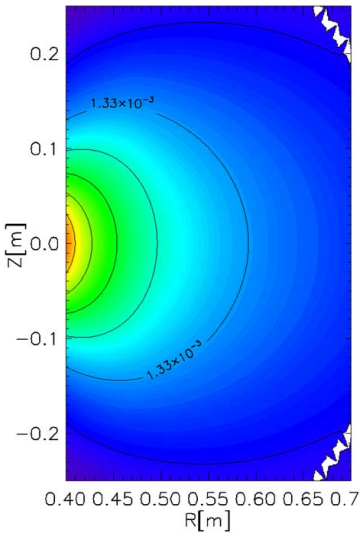

Fig. 2. Magnetic field in mT per 1 kA of plasma current measured from modelled plasma in IPR9 for "divertor" configuration, a = 0.15 m, p = 2.0, k = 1.5.

The poloidal flux measured by flux loops was calculated using mutual inductance. Then the current profile normalized to 1 kA with given plasma parameters and plasma centre was placed into this grid and the response signal (either in mT/kA or in V s/kA) in the diagnostic coils was computed. The centre of the plasma was moved in another grid (300 × 500) from 0.4 m to 0.7 m in horizontal direction and from −0.25 m to 0.25 m in vertical direction to create the dependence of the diagnostic coils signals on the plasma position. Plasma centre was moved with step 1 mm. As an example the resulting matrix of signal measured in IPR9 (located on the high field side on the midplane) coil is shown in Fig. 2.

Fig. 2 shows that the IPR9 coil signal can be used for horizontal plasma position determination for vertical position in the range $Z = \pm 7$ cm. The cut from Fig. 2 for Z = 0 m for all twelve possible plasma approximations is in Fig. 3.

According to Fig. 3 the slope of the signal in the IPR9 is almost the same for all twelve possible approximations of the plasma shape, although the absolute plasma positions can be different. This result justifies use of the Eq. (1) for description of different plasma shapes and current profiles instead of more elaborate and realistic mod-

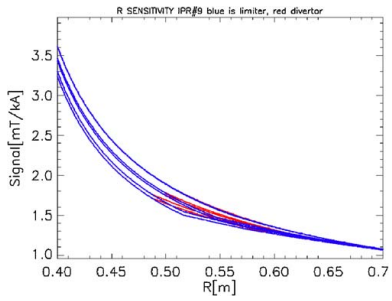

Fig. 3. Horizontal sensitivity of IPR9 – a cut from Fig. 1 for Z = 0 m (midplane) and for all twelve used plasma approximations.

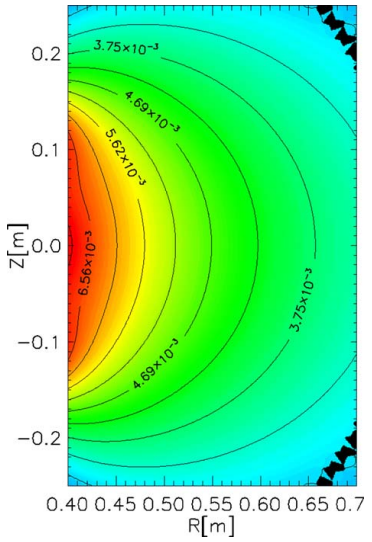

Fig. 4. Magnetic field calculated for determining horizontal plasma position for "limiter" configuration, $p = 2.0$, $k = 1.0$.

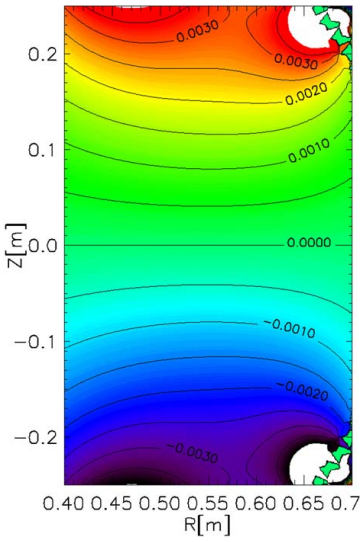

Fig. 5. Magnetic field calculated for determining vertical plasma position for "limiter" configuration, $p = 2.0$, $k = 1.0$.

els based on MHD equations as in [5–7]. The error in the absolute plasma position can be mitigated by changing the set point of the PID controller by given offset. The offset for particular plasma shape can be determined offline between shots from EFIT++ [8] equilibrium reconstruction.

The following two combinations of IPR coils have been chosen to gain sensitivity to plasma movement only in one direction for horizontal position (3) and for vertical position (4).

$$B_{hor} = 3 \cdot \mathrm{IPR}_5 + \mathrm{IPR}_3 - 3 \cdot \mathrm{IPR}_{13} - \mathrm{IPR}_{15} \quad (3)$$

$$B_{ver} = 1.2 \cdot \mathrm{IPR}_8 + \mathrm{IPR}_9 + 1.2 \cdot \mathrm{IPR}_{10} \quad (4)$$

Mirnov coils have worse signal/noise ratio when compared with IPR coils. Fig. 4 shows the magnetic field calculated from model using the set of IPR coils described by Eq. (4). This set of IPRs coils is sensitive to movement in the horizontal direction and moving plasma in the vertical direction has less significant effect. Fig. 5 shows magnetic field from set of IPR described by Eq. (3) which is used for determination of vertical position.

Magnetic signal from the individual IPR coils (i.e. magnetic field from the poloidal field coils and vessel eddy currents are subtracted from measured value) normalized to 1 kA plasma current is combined according to the Eqs. (3) and (4) providing two signals B_{hor} and B_{ver}. These two signals correspond to equipotentials in Fig. 5 and in Fig. 4. The cross-section of these equipotentials gives us the plasma position. The selected set of coils has only one unique cross-section of equipotentials for all reasonable plasma centre positions (Z in the range ±0.2 m and R in the range 0.4 m–0.7 m).

In order to perform the plasma position determination in the real-time it is necessary to speed up the code execution. Figs. 4 and 5 contain the signal in the sets of coils in dependency on the plasma centre position $B_{hor} = B_{hor}(R, Z)$ and $B_{ver} = B_{ver}(R, Z)$. It is possible to create a look-up tables $R = R(B_{hor}, B_{ver})$ and $Z = Z(B_{hor}, B_{ver})$ by finding the plasma position for each B_{hor} and B_{ver} value in Figs. 4 and 5. These look-up tables are used in the real-time algorithm to calculate quickly the plasma position [9,10].

3. Real-time calculation of plasma position

Control and calculation of plasma position has to be performed in real-time. Calculation of plasma position was implemented in the MARTe real-time software. MARTe – Multi-threaded Application Real-Time executor is a software which can run the same code on several operating system. Its main advantage is portability to several operating systems, re-usability to different projects and maintainability. It is written in C++ so it is easy to add a new parts of the code.

The basic parts of MARTe are GAMs (Generic Application Module). GAM is a piece of a code which has three points for communication: configuration, data input and data output. GAM usually processes input data to modified outputs according to the specification in a configuration file which has to be loaded during the MARTe startup. Each GAM at startup, during initialization, declares which data it expects as an input and which data will be created in an output. The inputs and the outputs are declared by writing a variable signal name and data type into the configuration file. After initialization there is an execution of each GAM. During the execution the input data are processed with defined operation in GAM. GAMs in MARTe are running one by one in the order which is defined in the configuration file. Sequence of the configured GAMs runs during the shots in a loop.

COMPASS real time control is running in two threads with two different speeds. First – *fast thread* – (sequence of GAMs takes 50 μs in a loop) operates with GAMs for collecting and measuring analogue signals (ATCAAdcGAM), for timing (TimingGAM) and triggering (GPIOTriggerGAM), subtracting drift from integrators from measured data (DriftRemoverGAM), plasma current calculator (CurrentCalculatorGAM), plasma position calculation (PlasmaPositionCalculationGAM) and data collection GAM for collecting and storing data (DataCollectionGAM). Some of the collected or calculated data are transmitted with OutputGAM to the *slow thread* (which runs in a loop of 500 μs).

The *slow thread* is used mostly for communication with Main Power Supplies (CkdCommunicatorGAM) which control currents

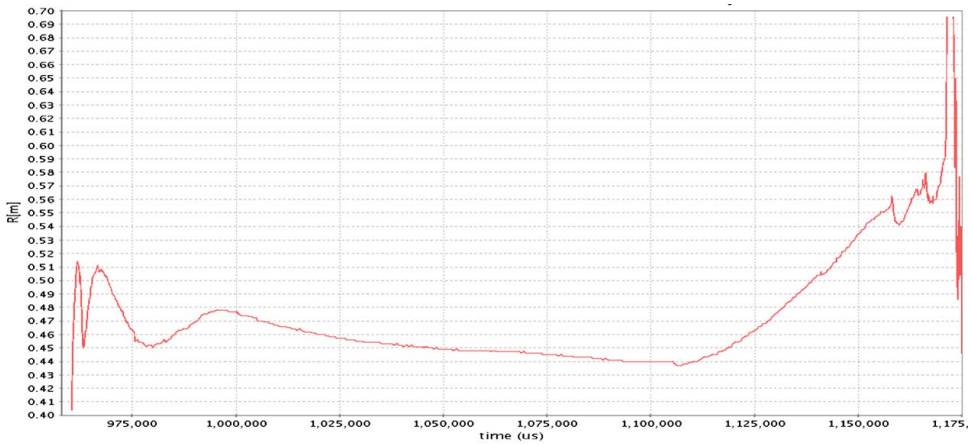

Fig. 6. Plasma column horizontal position calculated in real-time in shot #1559.

in Magnetizing, Equilibrium, Toroidal and Shaping Fields circuits. Currents for these windings are programmed in specific waveforms (WaveformGAM) written in configuration file or uploaded to MARTe via HTTP protocol. These two threads are running in parallel – *dual thread* – on two different CPUs and each thread is synchronized with precision of a microsecond. Timing clocks are provided by MARTe based on the CPU time. MARTe runs on so called ATCA (Advanced Telecommunications Computing Architecture). ATCA is connected to the timing node (providing clocks and triggers) and CODAC [11] central server (FireSignal server) [11].

Signals from IPR coils 3, 5, 8, 9, 10, 13 and 15 (see Fig. 1) are provided after analogue integration (i.e. it is not necessary to perform digital integration to obtain signal directly proportional to measured magnetic field). These signals are measured and digitized in the ATCA board with 20 kS/s. Drifts from integration are in real-time subtracted in DriftRemoverGAM. This modified signal from IPRs creates an input to the PlasmaPositionCalculationGAM and, consequently, the magnetic field in the coils set is calculated using Eqs. (3) and (4). The summed signals from Eqs. (3) and (4) consist of a signal from plasma as well as signal induced by other magnetic fields. The signal of magnetic field from Magnetizing, Shaping and Equilibrium field circuits is subtracted using currents measured at the Power Supply outputs. The magnetic field originating from the vacuum vessel current is assumed to be proportional to the measured loop voltage. This approximation allows subtraction of this magnetic field. The approximation is valid for high field side coils IPR 8, 9 and 10. The up-down symmetry of coils IPR 3, 5, 13 and 15 means that the vacuum vessel magnetic field can be neglected. The remaining signal is generated only by plasma. The signal is then divided by measured plasma current and used to find the plasma centre position in the look-up tables described in Section 2.

Before using the code during a COMPASS discharge, calculation was tested using WaveformGAM where measured data from IPR was used as input, then transmitted to the PlasmaPositionCalculationGAM and then R and Z position was sent to the DataCollectionGAM. Results were compared with data analyzed offline.

The procedure has been tested first at the *slow thread* and, afterwards, the *fast thread* and using *dual thread*. Z position of plasma was qualitatively verified with a bolometry [12] and R position with a fast visible camera [13]. The results shows a qualitative agreement, howerer, the plasma position calibration has to be improved and optimized.

Fig. 6 shows one of the first tests of the real-time plasma position reconstruction using slow EFPS feedback regulation during a COMPASS discharge. In the shot #1559 plasma position was controlled by a proportional controller on the plasma current using BasicControllerCoreGAM [10]. Plasma discharge starts at 958 ms and is unstable untill 980 ms. Afterwards, the plasma column moves to the low field side (LFS) followed by movement to high field side then plasma collapse slowly at low field side during plasma current ramp-down. Several tests were already done to control the EFPS with PID controller on actual plasma position. These tests proved that the plasma position calculation algorithm executes in approximately 0.8 μs which is fast enough to run it in 50 μs *fast thread*.

In a near future the plasma position algorithm will be optimized for the slow EFPS position feedback. The same algorithm will be implemented in the fast plasma position feedback system. The robustness and the precision of the algorithm will be increased by adding a signal from the flux loops.

4. Conclusion

The algorithm for plasma position determination used in COMPASS tokamak was described. Plasma position was calculated with GAM which runs in the real-time code MARTe. Results show that trends of plasma column movement are correctly computed but exact position is not correctly determined. Calculation is sufficiently fast to be executed in real-time.

Acknowledgements

This work was supported by Czech Science Foundation, grant 202/08/H057, the Academy of Sciences of the Czech Republic IRP #AV0Z20430508, the Ministry of Education, Youth and Sports CR #7G10072 and European Communities under the contract of Association between EURATOM/IPP.CR and EURATOM/IST. The work at IST also received financial support from "Fundação para a Ciência e Tecnologia" in the frame of the Contract of Associated Laboratory. The views and opinions expressed herein do not necessarily reflect those of the European Commission.

References

[1] R. Pánek, O. Bilyková, V. Fuchs, M. Hron, P. Chráska, P. Pavlo, J. Stöckel, J. Urban, V. Weinzettl, J. Zajac, F. Žáček, Reinstallation of the COMPASS-D tokamak in IPP ASCR, Czechoslovak Journal of Physics 56 (2006) B125–B137.

[2] R. Panek, P. Cahyna, R. Dejarnac, V. Fuchs, J. Havlicek, J. Horacek, M. Hron, O. Hronova, F. Janky, J. Mlynar, J. Stockel, J. Urban, V. Weinzettl, J. Zajac, F. Zacek, the COMPASS team, Status of the COMPASS tokamak reinstallation in institute of plasma physics AS CR, in: Proceedings of the 35th EPS Conference on Plasma Physics, vol. 33E of Europhysics Conference Abstracts, p. P-5.140.

[3] A.C. Neto, F. Sartori, F. Piccolo, R. Vitelli, G. de Tommasi, L. Zabeo, A. Barbalace, H. Fernandes, D.F. Valcarcel, A.J.N. Batista, MARTe: a multiplatform real-time framework, IEEE Transactions on Nuclear Science 57 (2010) 479–486.

[4] J. Wesson, Tokamaks, 3rd ed., Clarendon Press, Oxford, UK, 2004.

[5] J. Ferron, M.L. Walker, L.L. Lao, H.E.S. John, D.A. Humphreys, J.A. Leuer, Real tokamak equilibrium reconstruction for tokamak discharge control, Nuclear Fusion 38 (1998) 1055–1066.

[6] J. Blum, J.L. Foll, B. Thooris, The self-consisted equilibrium and diffusion code SCED, Computer Physics Communications 24 (1981) 235–254.

[7] S.C. Jardin, N. Pomphrey, J. DeLucia, Dynamic modeling of transport and positional control of tokamaks, Journal of Computational Physics 66 (1986) 481–507.

[8] L.C. Appel, G.T.A. Huysmans, L.L. Lao, P.J. McCarthy, D.G. Muir, E.R. Solano, J. Storrs, D. Taylor, W. Zwingmann, A unified approach to equilibrium reconstruction, in: Proceedings of the 33th EPS Conference on Plasma Physics, vol. 33E of Europhysics Conference Abstracts, p. P-2.184.

[9] D. Valcárcel, A. Neto, I. Carvalho, B. Carvalho, H. Fernandes, J. Sousa, F. Janky, J. Havlicek, R. Beňo, J. Horacek, M. Hron, R. Panek, The COMPASS tokamak plasma control software performance, in: Presented at 17th Real Time Conference, in press.

[10] D. Valcárcel, A. Duarte, A. Neto, I. Carvalho, B. Carvalho, H. Fernandes, J. Sousa, F. Sartori, F. Janky, P. Cahyna, M. Hron, R. Panek, Real-time software for the COMPASS tokamak plasma control, Fusion Engineering and Design 85 (2010) 470–473 (Proceedings of the 7th IAEA Technical Meeting on Control, Data Acquisition, and Remote Participation for Fusion Research).

[11] D. Valcárcel, A. Neto, J. Sousa, B. Carvalho, H. Fernandes, J. Fortunato, A. Gouveia, A. Batista, A. Fernandes, M. Correia, T. Pereira, I. Carvalho, A. Duarte, C. Varandas, M. Hron, F. Janky, J. Pisacka, An ATCA embedded data acquisition and control system for the COMPASS tokamak, Fusion Engineering and Design 84 (2009) 1901–1904 (Proceeding of the 25th Symposium on Fusion Technology (SOFT-25)).

[12] V. Weinzettl, D. Naydenkova, D. Sestak, J. Vlcek, J. Mlynar, R. Melich, D. Jares, J. Malot, D. Sarychev, V. Igochine, Design of multi-range tomographic system for transport studies in tokamak plasmas, Nuclear Instruments and Methods in Physics Research Section A: Accelerators, Spectrometers, Detectors and Associated Equipment 623 (2010) 806–808.

[13] A. Szappanos, M. Berta, M. Hron, R. Panek, J. Stockel, S. Tulipán, G. Veres, V. Weinzettl, S. Zoletnik, EDICAM fast video diagnostic installation on the COMPASS tokamak, Fusion Engineering and Design 85 (2010) 370–373 (Proceedings of the 7th IAEA Technical Meeting on Control, Data Acquisition, and Remote Participation for Fusion Research).

Fusion Engineering and Design 89 (2014) 186–194

Contents lists available at ScienceDirect

Fusion Engineering and Design

journal homepage: www.elsevier.com/locate/fusengdes

Upgrade of the COMPASS tokamak real-time control system

F. Janky[a,c,*], J. Havlicek[a,c], A.J.N. Batista[b], O. Kudlacek[a], J. Seidl[a], A.C. Neto[b], J. Pipek[a], M. Hron[a], O. Mikulin[a,d], A.S. Duarte[b], B.B. Carvalho[b], J. Stockel[a], R. Panek[a]

[a] Institute of Plasma Physics, AS CR, v.v.i., Association EURATOM/IPP.CR, Za Slovankou 3, 18200 Prague, Czech Republic
[b] Associação EURATOM/IST, Instituto de Plasmas e Fusão Nuclear, Instituto Superior Técnico, Universidade Técnica de Lisboa, 1049-001 Lisboa, Portugal
[c] Charles University in Prague, Faculty of Mathematics and Physics, V Holesovickach 2, 18000 Prague, Czech Republic
[d] Czech Technical University, Faculty of Nuclear Sciences and Physical Engineering, V Holesovickach 2, 18000 Prague, Czech Republic

HIGHLIGHTS

- An upgrade of the COMPASS real-time system has been made to generally improve the plasma performance.
- Stability of discharges in SNT configuration has been increased.
- Plasma flat-top phase length has been extended.
- Central solenoid protection has been developed.
- Plasma position estimation has been improved.

ARTICLE INFO

Article history:
Received 30 April 2013
Received in revised form
13 December 2013
Accepted 16 December 2013
Available online 23 January 2014

Keywords:
Real-time
Feedback control
Real-time framework
MARTe
COMPASS tokamak

ABSTRACT

The COMPASS plasma control system is based on the MARTe real-time framework. Thanks to MARTe modularity and flexibility new algorithms have been developed for plasma diagnostic (plasma position calculation), control (shaping field control), and protection systems (central solenoid protection). Moreover, the MARTe framework itself was modified to broaden the communication capabilities via Aurora.

This paper presents the recent upgrades and improvements made to the COMPASS real-time plasma control system, focusing on the issues related to precision of the real-time calculations, and discussing the improvements in terms of discharge parameters and stability. In particular, the new real-time system has given the possibility to analyze and to minimize the transport delays of each control loop.

1. Introduction

COMPASS [1] is a tokamak with an ITER-like magnetic configuration, which currently operates with the parameters listed in Table 1.

The simplified scheme of the poloidal field coils and of the corresponding power supplies [2] is shown in Fig. 1.

The Magnetizing Field Power Supply (MFPS) is used to drive the current in the central solenoid made by the MA and MB windings reported in Fig. 1). The central solenoid generates the loop voltage needed to drive the plasma current. The shaping magnetic field elongates and shapes the plasma, in order to achieve different configurations. This additional field is generated by the Shaping Field Power Supply (SFPS). The horizontal magnetic field, which vertically stabilizes the plasma is generated by the Fast Amplifier for Radial Field (FABR), while the vertical magnetic field used to horizontally control the plasma has two different sources. The "slow" one generated by the Equilibrium Field Power Supply (EFPS) and the "fast" one is generated by Fast Amplifiers for the Vertical Magnetic field (FABV). Both fast amplifiers (FABR and FABV) operate with a frequency response of 40 kHz.

1.1. Feedback control

Present-day tokamaks, in particular those with divertor configuration, need a robust real-time control system to keep a predefined and stable magnetic configuration. Fig. 2 shows the block scheme of the COMPASS real-time control system. All power supplies are

* Corresponding author at: Institute of Plasma Physics, AS CR, v.v.i., Association EURATOM/IPP.CR, Za Slovankou 3, 18200 Prague, Czech Republic.
Tel.: +420 266053575.
E-mail address: filip.janky.work@gmail.com (F. Janky).

0920-3796/$ – see front matter © 2014 Institute of Plasma Physics AS CR.. Published by Elsevier B.V. All rights reserved.
http://dx.doi.org/10.1016/j.fusengdes.2013.12.042

Table 1
COMPASS parameters.

Major radius	0.56 m
Minor radius	0.18–0.23 m
Plasma current	<300 kA
Magnetic field	0.9–2.1 T
Triangularity	0.5–0.7
Elongation	1.8
Pulse length	<0.5 s
P_{NBI}	2 × 0.3 MW

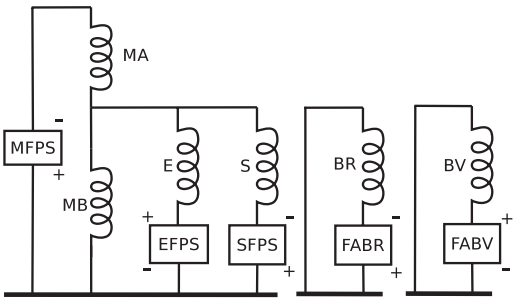

Fig. 1. Simplified scheme of coils connection between magnetizing, equilibrium and shaping filed power supplies.

controlled in real-time by using the Multi-threaded Application Real-Time executor (MARTe) [3,4]. The MARTe system runs on two Advanced Telecommunications Computing Architecture (ATCA) crates [5]. Each ATCA crate is equipped with Data Acquisition (DAQ) boards having a Field-Programmable Gate Array (FPGA) [6], whose firmware can be programmed either to acquire data at 2 Msps, or to control experiments in real-time with MARTe. Data are digitized by the analogue–digital converters assembled on the DAQ boards. For real-time control, the data are down-sampled by the on-board FPGA and then streamed to MARTe in 50 μs cycles. The ATCA crate has a carrier board which connects every DAQ board to the mother-board, where MARTe runs at dedicated isolated CPU cores, via the Peripheral Component Interconnect Express cable (PCIe) [7].

Each ATCA crate is synchronized by the timing unit with 2 MHz clocks. The timing unit sends triggers to each ATCA crate to start acquiring data and provides triggers for diagnostics to start measurements, when required.

The real-time control on COMPASS operates in two different ways. Parameters can be controlled either with predefined waveforms or with a feedback control loop applied to the measured

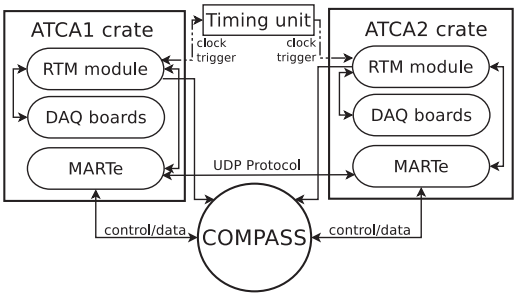

Fig. 2. Block scheme of the real-time control. Timing unit sends triggers and clocks to synchronize the ATCA boards. MARTe analyses data from COMPASS and controls the experiment according to measured signals.

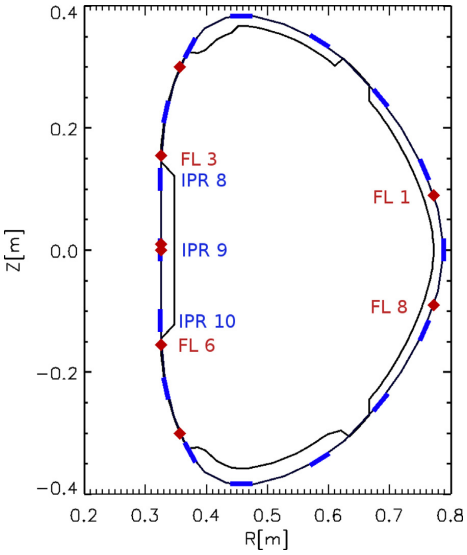

Fig. 3. Position of sixteen internal partial Rogowski coils (IPR1–IPR16) and eight flux loops (FL1–FL8) used as magnetic sensors for real-time control. Named IPR coils and flux loops are used for calculating horizontal position.

signal. These two methods can be combined for any controlled parameter.

1.2. Recent upgrades

During the commissioning phase, the COMPASS tokamak was successfully operated with a circular plasma cross-section by using the control system already described in [8,5,9]. However, the existing control system appeared not to be fully efficient in broadening the operational scenarios to D-shaped plasmas, which are required in order to achieve the H-mode. In particular, the vertical stability of elongated plasmas was rather poor, mainly because of the vertical displacement events (VDE) [10–12], and development of a more robust feedback system appeared to be urgent.

Several improvements have recently been implemented to ensure plasma stability and consequently the reproducibility of the plasma discharges. These upgrades are described in the following sections. Improved estimation of the horizontal plasma position is described in Section 2. An upgrade of the EFPS control, which suppresses oscillations in the horizontal plasma position is mentioned in Section 3. The main problem with vertical plasma position stability, caused by time delays between measurements of the data and acting on plasma with the actuators, is treated in Section 4. Overshooting of a controlled parameter and connection between feedback and the predefined control system is described in Section 5. Newly developed plasma shape control is described in Section 6. Furthermore, protection of the central solenoid against overheating during the discharge is discussed in Section 7. The last Section 8 is devoted to the upgrade of the real-time control MARTe software and the control FireSignal software.

2. Improved calculation of the horizontal plasma position

The location of the magnetic sensors, which are used for real-time control is shown in Fig. 3. The setup is made of sixteen internal

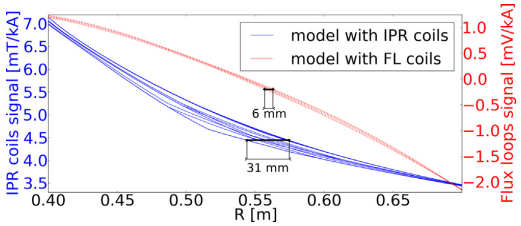

Fig. 4. Estimation of the horizontal plasma position modelled by algorithm using IPR coils (full blue lines) and the algorithm using flux loops (dotted red lines). Horizontal lines show scatter in the plasma position calculation for the different plasma scenarios. (For interpretation of the references to color in this figure legend, the reader is referred to the web version of this article.)

partial Rogowski (IPR) coils, which measure the poloidal magnetic field, and eight toroidal flux loops. Originally, the horizontal plasma position was calculated just from signals of four IPR coils [8]. However, this algorithm had systematic errors depending on the plasma shape and artificial ramp-ups and offsets had to be applied to keep the horizontal plasma position stable. Furthermore, the resulting position derived by this algorithm was not in agreement with the EFIT reconstruction [13]. Therefore, a new control algorithm based on the signals of the flux loops was developed. The most suitable flux loops were selected according to the model which is described below.

2.1. Model

The response of the all flux loops was modelled for several plasma shapes and current density profiles. In the case of circular plasmas, the current density profile is described as

$$j(r) = j(0)\left(1 - \frac{r^2}{a^2}\right)^p \quad (1)$$

where $j(0)$ is the central current density, r is the distance from the current profile centre, a is the minor radius and p is the peaking factor. Eq. (1) is adapted for vertically elongated plasmas as

$$j(r,\theta) = j(0)\left(1 - r^2\frac{1-\varepsilon^2 cos2\theta}{b^2}\right)^p \quad (2)$$

where $\varepsilon = \sqrt{1-(1/\kappa^2)}$ is the eccentricity and κ is the elongation, θ is the poloidal angle and b is the semi-minor axis. Two different peaking factors of the plasma current profiles ($p = 2$ and 3) and three elongations ($\kappa = 1$, 1.5 and 2) are assumed in the modelling.

The modelled plasma was moved in the horizontal direction and signals of the flux-loops in their real positions were calculated using mutual inductances between them and the plasma column. A proper combination of the flux-loops was selected to be mainly sensitive to the horizontal displacement of the plasma column and non-sensitive to its vertical displacement. The results from the model are inserted in a look-up table which is used in real-time for the calculation of the plasma position in the feedback control loop. The combination of flux-loops is evident from the equation

$$S = 2.5\cdot(FL3 + FL6) - (FL1 + FL8) \quad (3)$$

where FL denotes the integrated flux-loop voltage and S is the resulting signal which is used as input to the look-up table.

A comparison between the new algorithm and the old one which used the array of IPR coils and the flux loops is shown in Fig. 4. Each set of lines represents three different elongations, two different current profiles, and the limiter or diverted plasma configuration. Dotted lines denote results of modelling with the flux loops and the solid lines correspond to the model with the IPR coils [8]. Horizontal lines, plotted around the major radius of the tokamak vessel ($R = 0.56$ m), show how much the plasma centre may move horizontally if the elongation and the peaking factor of the plasma current density change. In the case of the flux loops, the expected error at typical position of the plasma centre is around 6 mm, while it is 31 mm, when the IPR coils are exploited in the feedback loop. It is evident from the figure that the flux loop algorithm is less dependent on variation of the plasma parameters and therefore it is more suitable for real-time control.

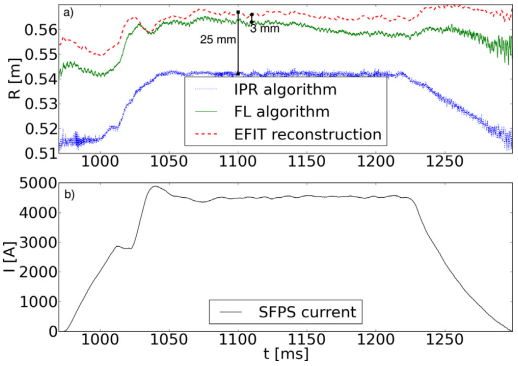

Fig. 5. (a) Comparison of the horizontal position calculated from the EFIT reconstruction (red dashed line) and from the model using either the IPR coil (blue dotted line) or the flux loops (green solid line) for the discharge #4141. (b) Evolution of the shaping current. (For interpretation of the references to color in this figure legend, the reader is referred to the web version of this article.)

2.2. Experiment

As already mentioned, during a discharge the obtained look-up table is used to compute an estimation of the plasma position.

It is important to note that the horizontal position obtained from flux loops is also in a good agreement with the EFIT reconstruction. Fig. 5 compares the position of the plasma centre calculated by using the IPR coils [8] and the flux loops, with the plasma centre position computed by EFIT. It can be noticed that the difference between the EFIT and the IPR coil model is about 25 mm, while the difference with the flux loop model is about 3 mm during the flat-top phase of the discharge.

Since the EFIT is an equilibrium code, main differences are observed during the ramp-up and ramp-down phases of the shaping current.

3. Upgrade of the equilibrium position control

In tokamaks, a vertical magnetic field has to be applied to keep the plasma column in a pre-defined equilibrium position.

On COMPASS, the vertical magnetic field is generated by two power circuits connected to the EFPS and the fast amplifier FABV. However, non-optimized control may cause oscillations in the horizontal plasma position, as reported in Fig. 6 sometimes, such oscillations, may lead to a plasma disruption.

The old algorithm stabilized plasma with a standard Proportional-Integral-Derivative (PID) controller where only the proportional part was applied either on the plasma current $I_{EFPS} = K_p^{Ipl}\cdot I^{pl}$ or on the plasma position $I_{EFPS} = K_p^{pos}\cdot e^{pos}$, where I_{EFPS} is EFPS current, K_p is the proportional constant from PID regulator and e is the error between the measured and the requested

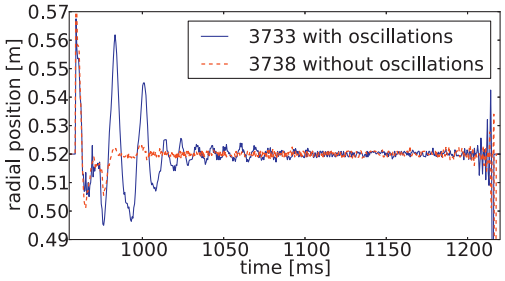

Fig. 6. Temporal evolution of the horizontal plasma position in two discharges. #3733 (blue solid line) – plasma oscillates in the radial position, when the wrong constants in the PID controller are chosen. #3738 (red dashed line) – the plasma position is stable with the correct PID constants implemented in the control of the EFPS. (For interpretation of the references to color in this figure legend, the reader is referred to the web version of this article.)

value. Note that the upper-script *pos* stands for plasma position, while I^{pl} stands for measured plasma current.

In this paper we present the new algorithm that has been implemented for the EFPS to suppress these oscillations. The new EFPS control is developed by using a sum of three different controllers applied on three different signals – plasma current, plasma centre position and the current from FABV amplifier according to the equation:

$$I_{EFPS} = K_p^{Ipl} \cdot I^{pl} + K_p^{pos} \cdot e^{pos} + \int_{t_0}^{t} K_i^{pos} \cdot e^{pos} dt + K_p^{FABV} \cdot \frac{1}{N} \sum_{j=1}^{N} I_j^{FABV} \quad (4)$$

where, K_i is the integral constant and the integral is evaluated as a sum over intervals of the 500 μs MARTe loop cycles, I_j^{FABV} is last "jth" current driven by the FABV power supply, and $N = 38$, which together with the loop cycle gives an average FABV current over 19 *ms*. All these algorithms are implemented in the real-time MARTe framework.

The first term is a proportional (P) controller according plasma current which represents the dominant contribution to the total EFPS current. The second and third term are respectively proportional and integral (PI) controllers of the plasma position, calculated from flux loop sensors in GAM in MARTe [8], (see Sections 2 and 8). The fourth term is the proportional control which reacts to current driven by FABV, which creates the vertical magnetic field. The last term in Eq. (4) helps the fast amplifier FABV to stay close to the zero current which gives almost the same dynamic range for changing the current in both directions. This allows fast reaction of the FABV to the horizontal displacements of the plasma column. However, the strong proportional part of this current created the oscillations (Fig. 6) and averaging over 19 ms of the measured FABV current has to be used. The range for each controller parameter has been first estimated using simple models, and then an experimental scan has been performed to choose the optimal values.

The upgrade of the EFPS controller and the proper set of control parameters stabilizes the horizontal plasma position in circular as well as in D-shaped plasmas and also during H-modes with Edge Localized Modes (ELMs) instabilities.

4. Suppression of time delays and vertical and radial stability

Digital control suffers from time delay between the measurement of signals by sensors and actuator response. Although the COMPASS vacuum vessel stabilizes events with characteristic time scale up to 0.5 ms [14] and the control loop is about ten times shorter, the time delays in the feedback loop cause problems, in particular in elongated plasmas with enhanced triangularity. To be able to address the diverted H-mode scenarios it was necessary to reduce the time delay.

We found that the main problem is the measurement delay prior to closing the feedback loop, which is between 90 μs and 140 μs, and it is composed of:

1. Processing and calculation delay – 12 μs
2. Digital filter delay – 40 μs
3. Serial communication delay – 24 μs + 6 μs to 30 μs delay needed for communication with the serial communication driver
4. Delay caused by switching the fast amplifiers FABR and FABV – 10–35 μs

In the following we describe how some of the above mentioned delays have been eliminated or reduced.

4.1. Processing and calculation

The 12 μs time delay consists mainly of the time needed for various manipulations. Specifically, acquiring data, removing drifts from integrators and estimating the plasma position (see Section 2), calculation of current set points for FABR and FABV amplifiers, and sending requests to them. This time delay is inherent and cannot be reduced.

4.2. Digital filter

The signals from COMPASS diagnostics are digitized at 2 Msps and pre-processed with an FPGA assembled at the real-time DAQ board located within the ATCA crate. Originally, during preprocessing the data were filtered with the 99th order Finite Impulse Response filter (FIR) to suppress frequencies higher than 10 kHz and then the sampling rate was decreased to 20 ksps. These decimated and filtered data are used in MARTe to control discharge in real-time. The total time delay was measured with and without the filter. From the time differences between these two measurements the digital filter delay was estimated. This filter caused a delay of 40 μs in the reaction time. We have attempted to remove this filter.

To ensure that the filter can be avoided, the frequency spectra of the control signals were analyzed. Most of the signals used for real-time control come from magnetic diagnostic (e.g. Rogowski coils, IPR coils, flux-loops, etc.). Frequencies measured with these sensors are below 1 kHz in steady-state. Only when magnetohydrodynamic (MHD) [10] activity occurs, the measured frequencies rise up to 20 kHz. This MHD activity is caused by the rotation of magnetic islands inside the plasma column. MHD oscillations are visible mainly on the IPR1 signal used for plasma position estimation [8] as it is evident from Figs. 7(a) and 8(a)

Fig. 7(b) shows the temporal evolution of the plasma position calculated with IPR algorithm before and after MHD activity when FPGA with the filter was used. A significant MHD activity is observed after 978 ms of the discharge. Differences can be seen due to the increased noise level, which can have a negative influence on the plasma stability. The effect of the noise on the plasma position is about 3 mm. When the filter is removed the effect of the noise rises up to 6 mm with the algorithm which uses IPR coils as seen at in Fig. 8(b).

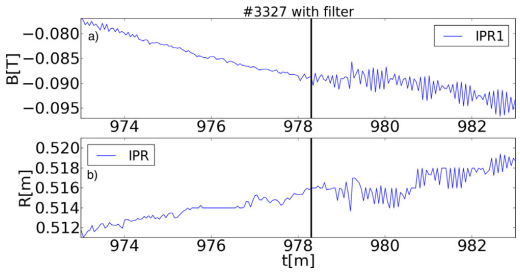

Fig. 7. (a) MHD activity measured by the IPR1 coil. (b) Evolution of the plasma position for discharge: #3327. Black vertical lines show the time when the MHD activity occurs.

On the other hand, these MHD oscillations are not observed with the algorithm which uses flux loops. Hence, the change of the plasma position estimation algorithm (see Section 2) implies also a reduction of the noise. The difference between these algorithms during MHD activity is clearly shown in Fig. 8(b). Therefore, the 99th order FIR filter has been removed which allowed us to react faster to the changes in the signals related to displacement of the plasma. Reaction of the feedback loop is faster by 40 μs and the D-shaped plasma becomes more stable including H-mode with ELMs [15].

4.3. Serial communication delay

As already mentioned, there is a further 24 μs delay caused by the serial communication between the MARTe and the FABR and FABV amplifiers [16] via the RS-232 protocol [17]. At present, the serial communication has a speed 921,600 bit/s, hence 23.8 μs are needed to transfer 16 bits. The total amount of transferred bits is 22 (16 data bits + 2 start bits + 2 stop bits + 2 parity check). This serial communication uses a serial PCIe card with four outputs: two outputs are used for communication with FABR and FABV, the third output is used for communication with controllers of the EFPS, MFPS, SFPS and the toroidal magnetic field power supply. The last one is used for the communication with the pre-triggering unit.

If the serial communication is replaced with an Aurora communication [18], transmission of the 32 useful bits is done in 1 μs. Moreover, this modification also reduces the time needed for transmission of the data from the Linux kernel to the serial card. Detailed description of the Aurora implementation in MARTe is presented in Section 8.1.

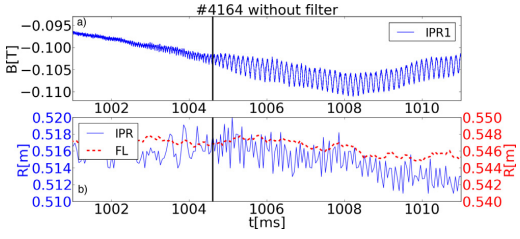

Fig. 8. (a) MHD activity measured by the IPR1 coil. (b) MHD oscillation impact on the IPR (blue solid line) and FL (red dashed line) algorithm for the plasma position. Black vertical lines show the time when the MHD activity occurs. (For interpretation of the references to color in this figure legend, the reader is referred to the web version of this article.)

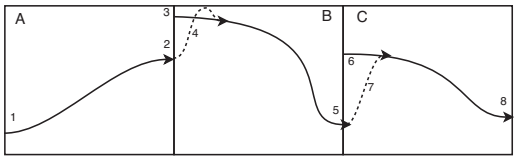

Fig. 9. Scheme of the connection of time intervals controlled by pre-defined waveform and by the real-time feedback (or optionally of two intervals with different algorithms applied).

4.4. Time delay caused by control of fast amplifiers

The control of the FABR and FABV amplifiers is performed by using micro-controllers [16], which generate a time delay in the range of 10–35 μs. The delay of 10 μs is needed to process data received from MARTe. The rest of the time delay is caused by the switching frequency of transistors of the fast amplifiers, which is 40 kHz. This means that the fast amplifiers can change their current in not less than 25 μs.

5. Connection between pre-programmed waveforms and feedback activation

The COMPASS real-time control system is based on GAMs – small pieces of codes written in C++ programming language. Each GAM implements a specific function (e.g. calculates the plasma position, communicates with power supplies, calculates the plasma density, acquires data, etc.). These GAMs run in series in loops managed by MARTe.

Some of the GAMs are used to control specific parameters like plasma current, plasma shape (see Section 6), plasma position, etc. As already mentioned, parameters can be controlled either by a predefined waveform or within a feedback loop. In the first case, the requested value of the parameter is predefined as a specific value at a given time. In the second case, requested values are calculated from measured signals according to given algorithms in real-time. Each parameter can be also controlled by a combination of these two approaches.

Connection of the two different set points always caused an overshoot of the controlled variable (either too high, or too low), in particular when the predefined value given by the waveform control is far away from the requested value given by the feedback control. A special algorithm has been developed to make a smooth transition between the two different controls, see Fig. 9.

Request between the set-point in the window “A” simply jumps to the set-point in the following window “B” which the feedback control cannot follow and thus creates overshoot. In contrast, the transition between “B” and “C” uses the new algorithm which requests set-points reasonably close to actual measured value and leads it, according to a predefined ramp in the code, to the requested value in the configuration file. This solution avoids overshooting of the controlled variable. Dotted lines 4 and 7 show the difference between the two approaches. Solid black lines show predefined requests; numbers 1 and 2, 3 and 5, 6 and 8 show requested set-points at the start/end of each interval. This algorithm helps the feedback system to control plasma current at requested value without overshoot caused by the integral term of the controller.

A detailed description of this algorithm is provided in the example of the plasma current control. The plasma current is controlled by the time derivative of the current in the magnetizing circuit, driven by the MFPS. The evolution of the magnetizing current is plotted in Fig. 10(a).

MARTe controls the magnetizing current in two time intervals. First, a pre-programmed waveform is applied to assure

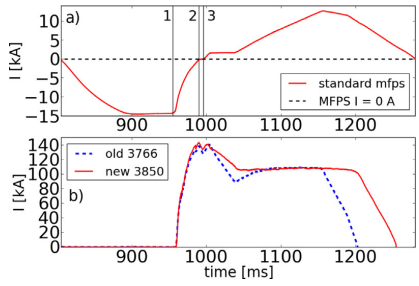

Fig. 10. (a) Typical MFPS current. (b) Plasma current: discharge with label 'old' is only with feedback algorithm. Discharge with label 'new' is with algorithm to connect different scenario windows.

reproducible plasma break-down. The negative current is ramped down typically from zero to −14 kA between 800 ms and 950 ms. When the magnetizing current reaches requested value, it is kept constant for several tens of ms to ensure that the current induced in tokamak vessel $I_{vessel} = dI_{MFPS}/dt = 0$. After that, at about $t = 950$ ms (Fig. 10(a) line #1), zero magnetizing current is requested and starts rising towards zero. A sufficiently high loop voltage is created and plasma breakdown occurs. The ramp-up of the plasma current remains uncontrolled during this phase and its evolution depends on the shaping current, pressure of the working gas, status of the first wall elements, etc.

When the magnetizing current reaches zero at about $t = 980$ ms (Fig. 10(a) line #2), the MFPS power supply changes polarity, which usually takes 8–12 ms. The loop voltage is zero during this period and the plasma current decreases in an uncontrolled way. When the polarity of the magnetizing current is changed (Fig. 10(a) line #3), the feedback loop overtakes the control and tries to reach the requested value of plasma current. A large difference between the actual and requested value causes overshooting of the plasma current due to the integral part of the regulator in the old algorithm, as seen from Fig. 10(b).

The resetting and changing of set point smoothly from its actual value to value requested before the discharge, has been applied to connect these two controls and to make plasma current changes smooth and better controlled. The difference between the old algorithm and the new algorithm using feedback and resetting of the set point is shown in Fig. 10(b). After the MFPS crossing zero requested current for both discharges is 110 kA. The control algorithm for discharge #3766 tries to reach 110 kA immediately but overshoots. A smooth transition attempts to reach the requested value with maximum derivative 2 kA/ms, as can be seen in discharge #3850. We clearly see that the steady state phase of the discharge is longer, the overshoot does not occur and the control of the plasma current is better in general. We note that this new control can be applied for any of the controlled parameters.

6. Control of plasma shape

The COMPASS tokamak has been routinely operating in single null divertor with higher triangularity (SNT) since the filter was removed at the FPGA, as was already described in Section 4. Previously, the duration of the plasma discharge from the start to the end was approximately 200 ms, where the ramp-up was about 70 ms and the ramp-down 50 ms. Originally, when the circular plasma reached a flat-top phase, the pre-defined waveform of the shaping current was requested. Thus, the ramp-up of the shaping field took approximately another 40 ms. Consequently, the steady-state phase with the fully shaped SNT plasma lasted only 40 ms.

Moreover, strong MHD activity usually occurred during plasma current ramp-up of the circular plasma. Since change of the q profile can suppress and/or prevent rising of the magnetic islands, the shaping field is being applied during the plasma current ramp-up phase and the MHD activity disappears. Furthermore, starting the shaping before the plasma current reaches the requested flat-top current phase helps not only to suppress the MHD activity but it also extends the steady-state phase in the SNT configuration. However, the shaping of the plasma cross-section causes oscillations of the plasma current and the horizontal position, which are caused mainly by mutual inductances between the EF, MF and SF power circuits. Also the EF, MF and SF are bound through plasma and have one common coil MB (see Fig. 1). The SFPS has stronger voltage control than the EFPS and the MFPS, therefore its reaction is faster than the reaction of the EFPS and MFPS. Therefore the SFPS current also induces a signal in the EFPS and the MFPS circuits and their controllers have to react to it.

The control of the SFPS is programmed in GAM in MARTe. First, a pre-programmed waveform is used for the SFPS before the MFPS crosses zero current. Feedback control for the SFPS tries to reach the requested SNT configuration after the MFPS changes polarity. The feedback constants for PI regulator change smoothly in time in order not to create overshoot.

To suppress these oscillations, massive smoothing of the plasma current over 53 ms for the control of the shaping field has to be used. This smoothing slows down the speed of the SFPS, currents induced in the EFPS and MFPS are not so large and oscillations are suppressed.

Better control of the SFPS with smoothing helps to keep plasma stable and the early start and feedback control of SFPS extended the plasma flat-top phase in SNT configuration for 50 ms.

7. Protection of the central solenoid from overheating

The MA and MB coils of the central solenoid are heated up with currents of the MF, EF and SF power supplies as is clear from Fig. 1. The inner-turn insulation is rated for temperature 80 °C, therefore, the central solenoid has to be protected from overheating. Maximum allowed energy dissipated in the central solenoid is calculated according to Eq. (5).

$$I^2t = c \cdot m \cdot \frac{dT}{R} = 178 \quad \mathrm{kA^2s} \tag{5}$$

where I is total current in the MA and MB coils of the central solenoid with resistance $R = 9.2\,\mathrm{m\Omega}$, c is the specific heat capacity of the copper winding $384.5\,\mathrm{JK^{-1}kg^{-1}}$, dT is the maximum allowed temperature difference 50 K and $m = 170$ kg is the total mass of coils MA and MB. Protection of the central solenoid has been implemented in real-time control in GAM in MARTe (Eq. (6)). If the value of I^2t in the MA coil or in the MB coil prevails 80% of 178 $\mathrm{kA^2s}$, all requested currents are set to zero and the discharge is terminated.

$$\begin{aligned} I_{MB} &= \int (I_{MFPS} + I_{SFPS} - I_{EFPS})^2 dt \\ I_{MA} &= \int I_{MFPS2} dt \end{aligned} \tag{6}$$

8. Upgrade of the MARTe and FireSignal

The ATCA crate can have up to 12 Data Acquisition boards (DAQ) with 32 ADC (analogue–digital converters) channels, one carrier board and one motherboard with 4 CPU cores. One CPU core is dedicated to running the Linux operating system and the remaining cores can be used for real-time control. Each DAQ board has a FPGA with firmware where data from 32 ADC channels are sampled at 2 Msps. Zero, one or more acquisition boards from ATCA can be used

as acquisition boards for real-time framework MARTe. This FPGA has different firmware where data are decimated by one hundred samples which are used for real-time control.

Each ATCA crate has one Rear Transition Module (RTM) with 8 digital inputs, 8 analogue outputs and one Aurora communication link. The RTM module provides clock for synchronization of boards and a trigger for the start of acquiring data (see Fig. 2).

At present, two ATCA crates are used for the control of plasma on the COMPASS tokamak. The first one, labelled as ATCA1 is used to acquire data from diagnostics which are grounded to the tokamak vessel (IPR coils, flux-loops, Mirnov coils) and to record currents from power supplies (measured by Rogowski coils).

The second crate, labelled as ATCA2, acquires data from optical diagnostics [19] and it is insulated from the tokamak vessel via optical fibres.

Originally, the MARTe run only at ATCA1 at CPU (Intel® Core™ 2 Quad CPU Q9550 @2.83 GHz), therefore data from optical diagnostics, recorded by ATCA2, could not be used for real-time control. The second MARTe2 has recently been installed at ATCA2 and runs at 4 core CPU (Intel® Core™ i7-3770K CPU @3.50 GHz) and, therefore, data from optical diagnostics can be also exploited for real-time control. MARTe1 and MARTe2 are connected together via the UDP protocol, and can transfer measured data or calculated values between them using Input/Output GAMs.

8.1. Upgrade of communication

MARTe communicates with the main power supplies (EFPS, SFPS, MFPS, and the toroidal magnetic field power supply), the FABR and FABV amplifiers and the pre-plasma trigger unit used for synchronization of diagnostics (such as the Li-beam diagnostics, Thomson-scattering laser and integrators) with the 4 port serial card connected to the PCIe slot at the motherboard inside ATCA1. MARTe also uses an Aurora communication link installed at RTM at ATCA1. MARTe communicates with the timing unit via Aurora, which could be used only on the real-time board.

The communication speed of a serial card goes only up to a maximum of about 1 Mb/s. However, in our case, Aurora can transfer 32 Mb/s. For this reason, the Aurora communication protocol has been included in the FPGA firmware on every DAQ board at ATCA1 and ATCA2. Therefore each DAQ board can have one RTM module and can communicate via the Aurora link. Also a driver accessing Aurora at FPGA has been developed to ensure MARTe's possibility to access Aurora at the RTM on each DAQ board (up to 12 per each ATCA crate). Furthermore, each RTM has 8 digital inputs and 8 DAC (Digital Analogue Converter). This solution is now used for communication with the FABR and FABV amplifiers (Section 4.3).

8.2. MARTe performance

MARTe runs GAMs in series in a specific order according to a configuration file read during its star-up. Each series of GAMs (thread) can run at one dedicated CPU with different loop cycle. COMPASS implementation uses two different threads. The first one runs in 50 μs loop cycle, used mainly for calculating plasma position and for communication with the FABR and FABV amplifiers. The second thread runs at 500 μs cycle and communicates mostly with the main power supplies. GAMs which are executed in the first fast main thread are ATCAAdc for acquiring data, TimingGAM for synchronizing and triggering, DriftRemover for subtracting drifts which come from integrators, PlasmaPositionCalculation, which calculates horizontal and vertical plasma position according to Section 2 and Ref. [8], FABRCurrentController, FABRCommunicatorGAM, FABVCurrentController and FABVCommunicatorGAM calculate current requests for fast power supplies and communicate

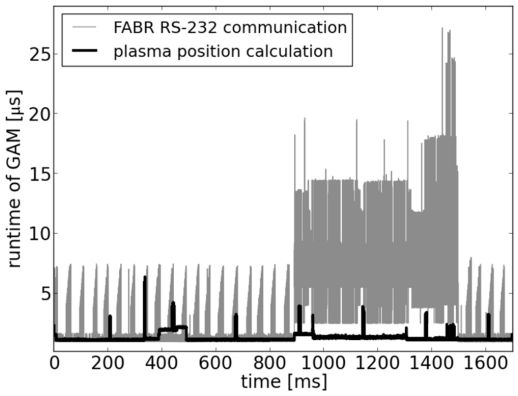

Fig. 11. Runtime of GAM for calculation plasma position and for communication with FABR for discharge #5711.

with them. These GAMs are followed with GAMs responsible for data acquisition and synchronization with slow thread.

The slow thread is mainly used for controlling main currents and communication with main power supplies (EFPS, SFPS, MFPS and toroidal magnetic field power supply) and for controlling plasma density and for protection of central solenoid (see Section 7).

MARTe has to execute all GAMs in one thread within one loop cycle. If the time needed for executing all GAMs in sequence in one loop cycle exceeds time specified in configuration file, MARTe will finish the sequence of GAMs as it is specified in the thread and will wait until the next loop cycle starts. For instance, if MARTe runs at a 50 μs cycle and execution of all GAMs in one thread takes 60 μs instead of 50 μs to process all data in one cycle, MARTe will wait till the start of the next cycle. That means waiting for 40 μs and skipping one control cycle.

From time to time, the MARTe cycle exceeds the 50 μs cycle loop and looses control with FABR and FABV for one cycle. This happens mainly because of communication between MARTe and the fast amplifiers via the RS-232 protocol, where the longest time was needed to access ports in the Linux kernel.

The difference in the running time of the two GAMs are shown in Fig. 11. The first GAM calculates the horizontal plasma position from four flux loops according to the description in Section 2, and

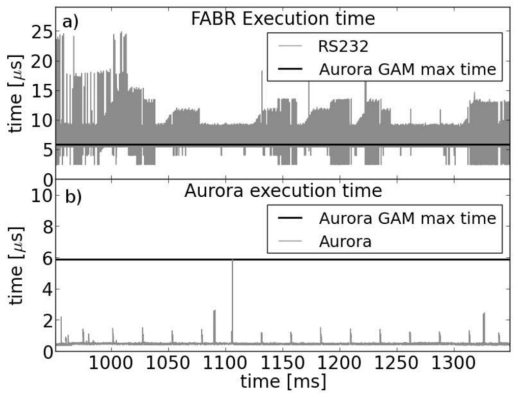

Fig. 12. (a) Time needed for running the FABR GAM using RS-232 protocol. (b) Time needed for running the FABR GAM using Aurora protocol.

Table 2
Comparison of RS-232 and Aurora driver.

	Max [μs]	Average [μs]
RS-232	25	6.6
Aurora	6	0.5

vertical position from four IPR coils [8]. All these calculations need approximately 1 μs. However, the second GAM writes only to the serial card using the Linux kernel input/output port instructions and usually takes 5–10 μs, but up to 25 or 30 μs in the worst case.

Changing the means of communication with the fast amplifiers from the RS-232 protocol to Aurora communication can decrease time of execution of GAMs which communicate with the FABR and FABV amplifiers. Fig. 12 shows differences in GAM execution time needed to send and to receive data from the FABR power supply. The black lines in both graphs show maximal value of time needed for execution of the GAM which uses Aurora communication protocol. Differences in average and maximal values between the RS-232 driver and Aurora driver are listed in Table 2

8.3. FireSignal upgrade

The initial impulse for MARTe to get prepared and start a new discharge comes from FireSignal [20], the off-line data acquisition management system used on COMPASS. This system (based on the client-server architecture) is used to configure data acquisition systems, to initiate the discharges, and to store and overview collected data. MARTe is represented in this system as a node (MARTeNode) which communicates with MARTe through web service interface and proxies both status change requests and data acquisition. It should be noticed that FireSignal does not itself participate in the real-time work-flow and this communication happens only before and after discharge with no strict requirements on speed.

FireSignal provides a graphical user interface (GUI) – a light-weight client that connects to the central server and does not communicate directly with MARTe, or any other data acquisition system. This GUI was adapted to better serve tokamak operators in a number of ways, the most important being the inclusion of checks that are made before the discharge is initiated – if any of them fails, it means that the discharge cannot proceed successfully, and the operator is given a choice whether or not to continue. The following conditions are checked: whether all nodes are present (particularly the MARTe one); whether all nodes are in the stand-by status; whether all waveforms were loaded; and whether the energetics is operable. After these checks were introduced, the number of unsuccessful discharges due to human error dramatically decreased.

9. Conclusion

Recent upgrades and improvements to the COMPASS real-time control addressed several issues related to improvement of discharge parameters and plasma performance. These upgrades contributed significantly to the successful mastering of the H-mode discharges on COMPASS.

A new algorithm was implemented for more precise calculation of the horizontal plasma position using 4 toroidal flux loops instead of 3 IPR coils. This algorithm is also less sensitive to the noise in the measured signals.

The control of the equilibrium power supply was improved, and is now based on a complex controller, which includes plasma current, plasma centre position, and current driven by the FABV amplifier. This approach gives better control of the plasma equilibrium and helps to keep the maximum dynamic range of the FABV, which controls the horizontal position.

Furthermore, two causes of plasma position instability were found, and their effect was significantly reduced: (1) delays within the digital control loop were analyzed and key parts were improved, with the result of shortening the reaction time and significantly improving vertical stability. (2) There are periods during the discharge controlled by pre-programmed waveforms and by real-time feedback. Smooth transition between these phases was implemented, which significantly reduced oscillations of the controllers in the feedback phase. Solving both these issues broadened the operational space of COMPASS scenarios. Moreover, optimization of the start-up phase of the plasma shaping was addressed, thus achieving a longer flat-top phase of the discharge.

In order to estimate the power dissipated in the central solenoid, a GAM that controls the I^2t was developed, and included into the control loop to protect the COMPASS primary winding against overheating.

Last but not least, issues related to communication and performance were addressed within MARTe and the operator FireSignal interface was upgraded.

Acknowledgements

This work has been carried out within the framework of the Contract of Association between EURATOM and the IPP.CR. The views and opinions expressed herein do not necessarily reflect those of the European Commission.

The work at the Institute of Plasma Physics AS CR, v.v.i. was supported by projects MSMT 7G10072 and MSMT LM2011021 and partly by ASCR.

The work related to discharge performance and communication were supported by Czech Science Foundation grant P205/11/2470.

Authors are very grateful to Vladimir Fuchs for valuable comments on the manuscript.

References

[1] R. Panek, O. Bilykova, V. Fuchs, M. Hron, P. Chraska, P. Pavlo, et al., Reinstallation of the COMPASS-D tokamak in IPP ASCR, Czechoslovak Journal of Physics 56 (Suppl. B) (2006) B125–B137, 22nd Symposium on Plasma Physics and Technology, Prague, Czech Republic, June 26–29, 2006.
[2] J. Zajac, R. Panek, F. Zacek, J. Vlcek, M. Hron, A. Krivska, et al., Power supply system for the COMPASS tokamak re-installed at the IPP Prague, Fusion Engineering and Design 84 (7–11) (2009) 2020–2024, http://dx.doi.org/10.1016/j.fusengdes.2008.11.092, 25th Symposium on Fusion Technology, Rostock, Germany, September 15–19, 2008.
[3] A.C. Neto, F. Sartori, F. Piccolo, R. Vitelli, G. De Tommasi, L. Zabeo, et al., MARTe: a multiplatform real-time framework, IEEE Transactions on Nuclear Science 57 (2 Part 1) (2010) 479–486, http://dx.doi.org/10.1109/TNS.2009.2037815, 16th IEEE/NPSS Real-Time Conference, Beijing, Peoples Republic of China, May 10–15, 2009.
[4] A. Neto, D. Alves, L. Boncagni, P. Carvalho, D. Valcarcel, A. Barbalace, et al., A survey of recent marte based systems, IEEE Transactions on Nuclear Science 58 (4) (2011) 1482–1489, http://dx.doi.org/10.1109/TNS.2011.2120622.
[5] D.F. Valcarcel, A. Neto, J. Sousa, B.B. Carvalho, H. Fernandes, J.C. Fortunato, et al., An ATCA embedded data acquisition and control system for the COMPASS tokamak, Fusion Engineering and Design 84 (7–11) (2009) 1901–1904, http://dx.doi.org/10.1016/j.fusengdes.2008.12.011, 25th Symposium on Fusion Technology, Rostock, Germany, September 15–19, 2008.
[6] Wikipedia, FPGA, July 2013 http://en.wikipedia.org/wiki/Field-programmable_gate_array
[7] PCI-SIG, PCI Express Base 3.0 Specification. http://www.pcisig.com/specifications/pciexpress/base3/
[8] F. Janky, J. Havlicek, D. Valcarcel, M. Hron, J. Horacek, O. Kudlacek, et al., Determination of the plasma position for its real-time control in the COMPASS tokamak, Fusion Engineering and Design 86 (6–8) (2011) 1120–1124, http://dx.doi.org/10.1016/j.fusengdes.2011.01.143, 26th Symposium on Fusion Technology (SOFT), Porto, Portugal, September 27–October 01, 2010.
[9] M. Hron, F. Janky, J. Pipek, J. Sousa, B.B. Carvalho, H. Fernandes, et al., COMPASS Team, Overview of the COMPASS CODAC system, Fusion Eng. Des. (2013), http://dx.doi.org/10.1016/j.fusengdes.2013.09.010, In print.
[10] J. Wesson, Tokamaks, 3rd ed., Clarendon Press, Oxford, UK, 2004.
[11] M. Kikuchi, Fusion Physics, International Atomic Energy Agency, 2012 http://books.google.cz/books?id=herWMgEACAAJ

[12] G. Ambrosino, M. Ariola, G. De Tommasi, A. Pironti, Plasma vertical stabilization in the ITER tokamak via constrained static output feedback, IEEE Transactions on Control Systems Technology 19 (2) (2011) 376–381, http://dx.doi.org/10.1109/TCST.2010.2042601.
[13] L.C. Appel, G.T.A. Huysmans, L.L. Lao, P.J. McCarthy, D.G. Muir, E.R. Solano, et al., A Unified Approach to Equilibrium Reconstruction, 30I, 2006, P-2.184.
[14] P. Vyas, Plasma Vertical Position Control in COMPASS-D Tokamak, University of Oxford, Oxford, UK, 1996, Ph.D. thesis.
[15] R. Panek, J. Stockel, J. Havlicek, F. Janky, M. Hron, V. Weinzettl, et al., Characterization of ohmic and nbi heated h-mode in the compass tokamak, in: Europhysics Conference Abstract, 2013, P-4.103 http://ocs.ciemat.es/EPS2013PAP/pdf/P4.103.pdf
[16] J. Havlicek, R. Hauptmann, O. Peroutka, M. Tadros, M. Hron, F. Janky, et al., Power supplies for plasma column control in the COMPASS tokamak, Fusion Engineering and Design 88 (2013) 1640–1645, http://dx.doi.org/10.1016/j.fusengdes.2013.02.040.
[17] E.I.A.E. Department, Interface Between Data Terminal Equipment and Data Communication Equipment Employing Serial Binary Data Interchange., Electronic Industries Association, Engineering Dept., WA, USA, 1969.
[18] Xilinx, Aurora (July 2013). http://www.xilinx.com/products/design_resources/conn_central/grouping/aurora.htm
[19] V. Weinzettl, R. Panek, M. Hron, J. Stockel, F. Zacek, J. Havlicek, et al., Overview of the COMPASS diagnostics, Fusion Engineering and Design 86 (6–8) (2011) 1227–1231, http://dx.doi.org/10.1016/j.fusengdes.2010.12.024, 26th Symposium on Fusion Technology (SOFT), Porto, Portugal, September 27–October 01, 2010.
[20] A. Neto, H. Fernandes, A. Duarte, B.B. Carvalho, J. Sousa, D.F. Varcarcel, et al., FireSignal – data acquisition and control, Fusion Engineering and Design 82 (5–14) (2007) 1359–1364, http://dx.doi.org/10.1016/j.fusengdes.2007.02.016, 24th Symposium on Fusion Technology (SOFT-24), Warsaw, Poland, September 11–15, 2006.

Fusion Engineering and Design 96–97 (2015) 637–640

Contents lists available at ScienceDirect

Fusion Engineering and Design

journal homepage: www.elsevier.com/locate/fusengdes

Plasma density control in real-time on the COMPASS tokamak

F. Janky[a,b,*], M. Hron[a], J. Havlicek[a,b], M. Varavin[a], F. Zacek[a], J. Seidl[a], R. Panek[a], COMPASS Team

[a] Institute of Plasma Physics AS CR, v.v.i., Association EURATOM/IPP.CR, Za Slovankou 3, 182 00 Praha 8, Czech Republic
[b] Department of Surface and Plasma Science, Faculty of Mathematics and Physics, Charles University in Prague, V Holešovičkách 2, 180 00 Praha 8, Czech Republic

HIGHLIGHTS

- We fitted length of the chord of the interferometry crossing plasma in the different plasma scenarios.
- We add correction to the actual length of the chord of the interferometry according to plasma shape and position in real-time code.
- We used this correction to control plasma density in real-time.

ARTICLE INFO

Article history:
Received 5 October 2014
Received in revised form 14 April 2015
Accepted 29 April 2015
Available online 30 May 2015

PACS:
52.55.Fa

Keywords:
COMPASS tokamak
Real-time control
Density control
MARTe
Interferometer
Stickiness of the valve

ABSTRACT

The electron density on COMPASS is measured using 2 mm microwave interferometer. Interferometer signal is used as an input for the feedback control loop, running under the MARTe real-time framework. Two different threads are used to calculate (fast 50 μs thread) and to control (slow 500 μs thread) the electron density. The interferometer measures a line averaged density along a measurement chord.

This paper describes an approach to control the line-averaged electron density in a real-time loop, using a correction to the real plasma shape, the plasma position, and non-linear effects of the electron density measurement at high densities.

Newly developed real-time electron density control give COMPASS the chance to control the electron density more accurately which is essential for parametric scans for diagnosticians, for physics experiments and also for achieving plasma scenarios with H-mode.

1. Introduction

The control of electron density plays an important role in the tokamak operation. The density in a tokamak is influenced by plasma confinement, interaction of the plasma with the wall and the wall conditions in general, active gas feeding, and pumping. Among these, a prospective actuator for electron density control is the gas feeding: pellets, gas injection, and Neutral Beam Injection (NBI). On the other hand, the control of the plasma confinement, plasma-wall interaction, and wall conditions cannot be used directly for density feedback since these tools either change the discharge scenario or cannot be controlled on the time scale of the COMPASS discharges. Similarly, the pumping speed is a given steady-state quantity which cannot be significantly changed.

Due to its size, COMPASS [1] does not use (and need) the pellet injection to feed the core plasma by the working gas. The NBI [2] power typically brings the COMPASS plasma to the H-mode [3] and then the density rapidly increases and can be controlled only by changing the discharge scenario, particularly by changing the ELM types. Therefore, the most suitable actuator for density control on COMPASS remains the gas injection.

In this paper, we describe the electron density measurement and available control tools (Section 2), the real-time data evaluation and control (Section 3), and finally we present the calibration and results (Section 4).

* Corresponding author at: Max-Planck-Institut für Plasmaphysik, Boltzmannstr. 2, 85748 Garching, Germany. Tel.: +49 89 3299 1327.
E-mail address: filip.janky.work@gmail.com (F. Janky).

http://dx.doi.org/10.1016/j.fusengdes.2015.04.065
0920-3796/

2. Electron density measurement and control

COMPASS uses interferometer [4,5] operating with 2 mm electromagnetic wave using two near frequencies 139.3 and 140 GHz. A phase shift that appears between the both waves passing through the plasma along the same chord corresponds to the electron density. This phase shift is processed by measuring circuits, which have a voltage output giving a linear function of the phase shift. Whenever the electron density increases, phase shift increases too.

2.1. Influence of the plasma shape and the plasma position on the electron density

The interferometry diagnostic measures the electron density as a line integrated quantity along the chord passing through the plasma. This signal is normalised to the standard circular shape with diameter 0.4 m and then stored in COMPASS Database (CDB) [6] or used as a measured signal for feedback controller. Therefore, when the plasma shape is changed from circular to elongated D-shaped plasma [7] and/or the radial or vertical plasma position is moved [8], the path of the interferometer chord through the plasma changes as well as the line integrated density measured along this chord. Due to these effects, the measured density has to be corrected accordingly. Several different discharge scenarios when shape and vertical and horizontal positions were changing were chosen. Then least square fitting method was used to calculate coefficients offline for these scenarios and results were compared with the EFIT reconstruction. Correction to the interferometry chord length according to the plasma position and the plasma shape is calculated according to Eq. (1).

$$n_{cor} = \frac{n_0}{\left(\sum_i^{n=5} c_i \cdot \left(\frac{I_{SF}}{I_{pl}}\right)^i + c_R \cdot R + c_Z \cdot Z + c_C\right)} \cdot 0.4 \quad (1)$$

where n_{cor} is the corrected density according to plasma shape, n_0 is measured density, I_{SF} is current driven in the shaping field coils and I_{pl} is plasma current, R is radial plasma position, and Z is vertical plasma position. c_i, c_R, c_Z, c_C are multiplying constants calculated from the fitting.

2.2. Correction to the interferometer non-linearity

The interferometer can measure density up to the critical density of $n_{crit} = 24.08 \times 10^{19}\ \mathrm{m}^{-3}$. However, if the electron density somewhere inside the plasma becomes not negligible compared to the critical density (i.e. the plasma frequency becomes comparable to the probing wave frequency), the measured phase shift does not increase linearly with the increasing averaged density anymore, but faster. In an extreme case, if the linearised form is used, even density value higher than the critical one can be evaluated (clearly incorrect from the physics point of view). It is evident that the effect of non-linearity must be taken into account, if the density exceeds value of about 20% of the critical one (which is a common case of the COMPASS tokamak).

Moreover, the problem is still more complex taking into account the fact that plasma is not homogeneous. As a consequence the local non-linear enhancement of the phase shift is radially dependent and the measured phase shift averaged along the radius is, therefore, not only function of the average density but also function of a density profile.

To estimate the influence of the non-linearity effect on the phase shift in the case of an inhomogeneous plasma, the real (i.e. taking into account non-linearity) local values of the phase shift have been modelled. The phase shift was modelled for homogeneous plasma and for five axially symmetric parabolic density profiles

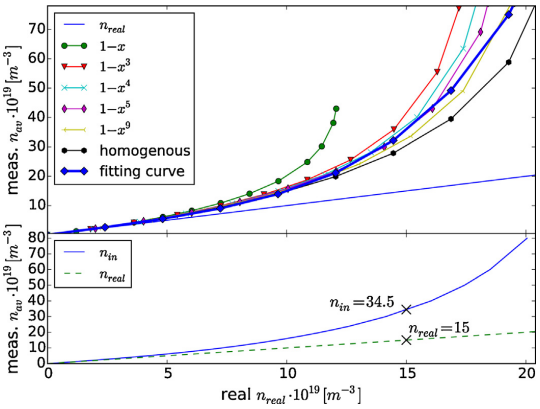

Fig. 1. Top: Different conversions between real densities and measured densities assuming different density profiles. Bottom: Conversion between real density and measured density. Dashed line shows density when non-linearity is considered. Example values for the case of $n_{real} = 15$ are shown.

$n = n_0 \cdot (1 - (r/a)^p)$ ($p = 1$ – triangle, $p = 3, 4, 5$ and $p = 9$ – approaching the homogeneous one) and numerically integrated along the radius r. For each profile we increased the central density n_0 step by step from zero to the critical one (till probing wave cut-off was reached). The incorrectly evaluated averaged densities n_{in} (i.e. enhanced due to the linearised approximation used) are displayed (y axis) for all mentioned profiles in dependence on the real averaged density (x axis) on the top part of Fig. 1. Surprisingly, it has been found that the form of the profile does not play any decisive role (except the non-physical triangle profile), at least for the averaged density lower than approx. one half of the critical density. Therefore we approximate the relation between n_{in} and the real density for all values of p between 3 (inhomogeneous plasma) and infinity (homogeneous plasma) by a single fitting curve.

In this way, we elaborated a graph, where for every density value n_{in} there are two values of the averaged densities. The smaller one corresponds to the real averaged density n_{real}. The greater one corresponds to the value n_{in}, evaluated incorrectly from the phase linear approximation. In this way, a following simple transformation formula from the erroneously "evaluated" n_{in} to the correct real averaged density n_{real}, has been obtained (again numerically):

$$n_{real} = \frac{n_{in}}{[1 + 0.9 \cdot (n_{in}/n_{crit})]} \quad (2)$$

Differences between the incorrectly evaluated (measured, neglecting non-linear effects – dashed line) electron density and the real electron density (solid line) can be seen on the bottom Fig. 1.

3. Real-time control

Real-time control on the COMPASS tokamak [9] is done using a real-time framework MARTe (Multi-threaded Application Real-Time executer) [10,11]. MARTe at present runs at two isolated cores at a four core CPU assembled in a motherboard placed in the ATCA (Advanced Telecommunications Computing Architecture) crate [12–14]. One CPU is used for a fast thread which is executed in a 50 μs loop, second one is used for a slow thread which is executed in a 500 μs loop. One of the remaining cores is dedicated to carry out the management tasks of Linux. The threads are composed of the generic application modules (GAMs), blocks of the code

that perform specific tasks. Sequence of following tasks is used for electron density control.

At the beginning of the process, output voltage from the interferometry is measured with the MARTe GAM. Then offset of the voltage is subtracted from measured signal with drift removing GAM. Afterwards, GAM for calculation of real electron density is performed. Firstly, electron density is calculated according to Eq. (1) where the length and the plasma position and the shape are taken into account. Then, the n_{cor} from Eq. (1) is used in Eq. (2) as n_{in} (i.e. $n_{in} \equiv n_{cor}$) and linearisation is performed. After proper calculation of the electron density, GAM for feedback control uses proportional and integral part of a PID (Proportional–Integral–Derivative) controller to calculate requests for the valve. The PI controller controls the gas-puff valve opening and thus controls the amount of the gas inlet to the tokamak vessel as described in Section 3.1. Finally, control of the piezo-electric gas-puff valve is programmed in dedicated GAM for converting requests to the voltage.

3.1. Stickiness of piezo-electric valve

There are two piezoelectric valves currently installed on COMPASS, one on the low field side, other on the high field side of the torus. This gives us the opportunity to study the influence of the gas inlet location. As noted above, the electron density is controlled by controlling the amount of the injected working gas, in a feedback loop, which uses the interferometer measurement of the electron density as an input and returns requested values for the voltage to open the selected valve. Thus, either one gas-puff location can be selected or, optionally, the other valve can be (a) controlled with a pre-defined feedforward wave-form throughout the whole discharge or (b) used for experiments with gas-puff imaging. In principle, both valves can be connected to feedback control loop in future.

The piezo-electric valves may suffer from a stickiness. To suppress the stickiness of the valve and to open the valve fast, maximum voltage of 100 V has to be used for several milliseconds (usually around 5 ms) at the first opening. It is typically done using a predefined waveform for the piezo-electric valve at the beginning of the discharge (approximately 30 ms before breakdown). This fills the tokamak vessel at pressure around $1-4\times10^{-2}$ Pa. The feedback control loop then overtakes the gas-puffing approximately 10 ms after breakdown (usually 980 ms). If the maximum voltage is applied for less than 5 ms, the valve may not open or amount of gas filled into the tokamak vessel will not be sufficient for the plasma breakdown.

Once the valve is fully opened, it can be controlled easily and fast. If the valve is fully closed during a discharge and then there is a new request to open the valve again, additional time is needed and this causes delay in control. According to characteristics of the valves, typically voltage between 30 and 50 V (i.e. 30–50% of the maximum) can be required to keep the valve open. Lower voltage, approx. 20–30 V, keeps valve closed but the feedback reaction remains fast.

3.2. Calibration

Piezo-electric valves can have different characteristic for the opening. Ranges of characteristics are different for every single valve, therefore calibration of our valve had to be done, before using it in real-time control loop. First, we opened valve at 100% with 100 V amplifier for a short time of 5–9 ms and measured pressure in the vacuum vessel. Fig. 2 shows that first 5 ms gas puff was smaller than two others 5 ms pulses. This was caused by stickiness at the first opening of the valve after several hours without operation.

After this measurements 6 ms long pulse was chosen, because amount of gas puffed during such pulse was suitable for plasma

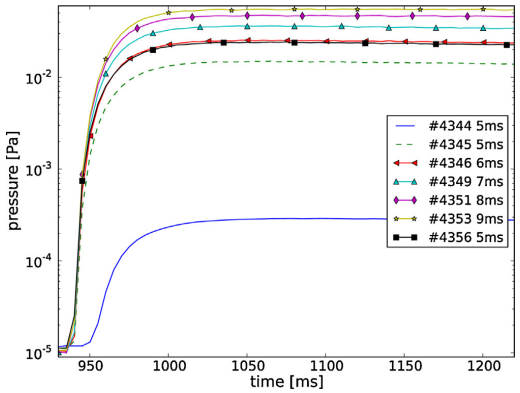

Fig. 2. Hydrogen gas-puffing for calibration of the valve. Valve was opened at maximum (100 V) at the same time for different lengths 5–9 ms.

breakdown. This 6 ms pulse was followed by 300 ms pulse with different level of opening between 10 and 50 V. The applied voltage used after first 6 ms pulse is marked in the legend of Fig. 3 after the shot number. We can see how pressure in the vessel decreases if voltage is less than 20 V. Voltage even higher than 30 V has to be used to increase pressure in the vessel. Therefore, we set lowest voltage during experiment to 20 V to keep valve closed, but not to loose its fast reactions in the feedback control.

4. Results

In Fig. 4 we can see different phases of feedback controlled electron density and advantages of the digital control. At the beginning of the discharge we can see controlled electron density, with feedback starting at 970 ms (first vertical black dashed line). Electron density follows predefined waveform and follows density ramp-up. Feedback on density is switched off at 1050 ms (second black dashed line) and experiment with gas puff imaging followed. During this experiment, plasma density was not controlled and high inlet of gas was used. Therefore, electron density kept rising despite the fact that the main piezo-electric valve was closed. Control

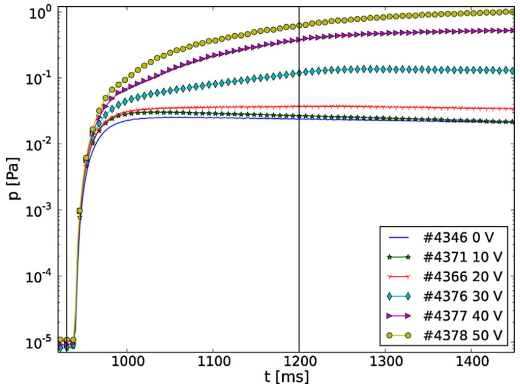

Fig. 3. Hydrogen gas-puffing for calibration of the valve. Valve was opened at 930 ms till 1200 ms for 0–50 V after 6 ms long pulse at the maximum voltage (100 V). Vertical lines show when valve was open and closed.

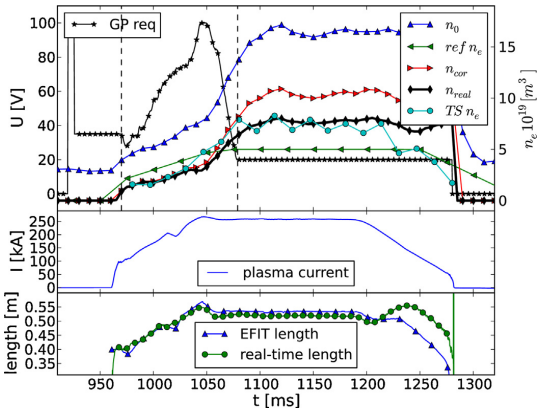

Fig. 4. Top graph: The measured n_0, corrected n_{cor}, requested density $ref\ n_e$ and density from Thomson Scattering diagnostic $TS\ n_e$ and the output signal of the feedback system from the gas puff valve – GP req. The black dashed vertical lines show time interval when the feedback control was used. Middle graph: The plasma current during the discharge. Bottom graph: Comparison between chord length calculated in real-time according to Eq. (1) and EFIT reconstruction after the discharge.

output from real-time calculation for the valve opening (analogue request) is shown in the top of the figure. Measured plasma current is in the middle of the figure.

The bottom part of Fig. 4 shows length of plasma calculated on $R = 0.56$ m in real time and comparison with EFIT reconstructed length of plasma at the same position. We can see nice agreement with difference less than 5%.

5. Conclusion

Controlling of electron density is necessary for investigation of the plasma physics in tokamaks. Newer precise calculation of interferometer chord length and non-linearity was introduced, which give us chance to control electron density more accurately. Better calculated density in real-time is essential for parametric scans for diagnosticians and for physics experiments. Also H-mode could be achieved only with feedback controlled density [3]. Also the measured electron density from the interferometer is in very good agreement with measurement from the Thomson scattering measurement.

Acknowledgements

The work at the Institute of Plasma Physics AS CR, v.v.i. was supported by project MSMT LM2011021. This project has received funding from the European Union's Horizon 2020 research and innovation programme under grant agreement number 633053. The views and opinions expressed herein do not necessarily reflect those of the European Commission.

References

[1] R. Panek, O. Bilykova, V. Fuchs, M. Hron, P. Chraska, P. Pavlo, et al., Reinstallation of the COMPASS-D tokamak in IPP ASCR, Czechoslov. J. Phys. 56 (2006) B125–B137.
[2] P. Deichuli, V. Davydenko, V. Belov, A. Gorbovsky, A. Dranichnikov, A. Ivanov, et al., Commissioning of heating neutral beams for COMPASS-D tokamak, Rev. Sci. Instrum. 83 (2012) 02B114.
[3] R. Panek, J. Stockel, J. Havlicek, F. Janky, M. Hron, V. Weinzettl, et al., Characterization of ohmic and NBI heated H-mode in the COMPASS tokamak, in: EPS Conference on Plasma Physics, 2013, pp. 1–4 (Papers), P4.103.
[4] V. Weinzettl, R. Panek, M. Hron, J. Stockel, F. Zacek, J. Havlicek, et al., Overview of the COMPASS diagnostics, Fusion Eng. Des. 86 (2011) 1227–1231.
[5] M. Varavin, J. Zajac, F. Zacek, S. Nanobashvili, G.P. Ermak, A.V. Varavin, et al., New design of microwave interferometer for tokamak COMPASS, Telecommun. Radio Eng. 73 (2014) 571–575.
[6] J. Urban, J. Pipek, M. Hron, F. Janky, R. Paprok, M. Peterka, et al., Integrated data acquisition, storage, retrieval and processing using the COMPASS DataBase (CDB), Fusion Eng. Des. 89 (2014) 712–716.
[7] F. Janky, J. Havlicek, A. Batista, O. Kudlacek, J. Seidl, A. Neto, et al., Upgrade of the COMPASS tokamak real-time control system, Fusion Eng. Des. 89 (2014) 186–194.
[8] F. Janky, J. Havlicek, D. Valcarcel, M. Hron, J. Horacek, O. Kudlacek, et al., Determination of the plasma position for its real-time control in the COMPASS tokamak, Fusion Eng. Des. 86 (2011) 1120–1124.
[9] M. Hron, F. Janky, J. Pipek, J. Sousa, B. Carvalho, H. Fernandes, et al., Overview of the COMPASS CODAC system, Fusion Eng. Des. 89 (2014) 177–185.
[10] A.C. Neto, F. Sartori, F. Piccolo, R. Vitelli, G. De Tommasi, L. Zabeo, et al., EFDA JET contributors, MARTe: a multiplatform real-time framework, IEEE Trans. Nucl. Sci. 57 (2010) 479–486.
[11] A. Neto, D. Alves, L. Boncagni, P. Carvalho, D. Valcarcel, A. Barbalace, et al., A survey of recent MARTe based systems, IEEE Trans. Nucl. Sci. 58 (2011) 1482–1489.
[12] D.F. Valcarcel, A. Neto, J. Sousa, B.B. Carvalho, H. Fernandes, J.C. Fortunato, et al., An ATCA embedded data acquisition and control system for the COMPASS tokamak, Fusion Eng. Des. 84 (2009) 1901–1904.
[13] D.F. Valcarcel, A.S. Duarte, A. Neto, I.S. Carvalho, B.B. Carvalho, H. Fernandes, et al., Real-time software for the COMPASS tokamak plasma control, Fusion Eng. Des. 85 (2010) 470–473.
[14] D.F. Valcárcel, A. Neto, I.S. Carvalho, B.B. Carvalho, H. Fernandes, J. Sousa, et al., The COMPASS tokamak plasma control software performance, IEEE Trans. Nucl. Sci. 58 (2010) 1490–1496.